Plasma Sheath Formation Around Moon and Its Implications

A thesis submitted in partial fulfillment of
the requirements for the degree of

Doctor of Philosophy

by

Trinesh Sana

(Roll No. 20330018)

Under the supervision of

Dr. Sanjay K. Mishra
Planetary Sciences Division
Physical Research Laboratory, Ahmedabad, India.

DEPARTMENT OF PHYSICS

INDIAN INSTITUTE OF TECHNOLOGY GANDHINAGAR

2025

Dedication

to
the loving memories of my
mother

THESIS APPROVAL

Certified that the thesis titled

Plasma Sheath Formation Around Moon and Its Implications,

submitted by **Trinesh Sana** (IITGN Roll No. **20330018**) to the I**ndian Institute of Technology Gandhinagar,** is approved for the degree of *Doctor of Philosophy.*

Date: November 03, 2025

Place: Gujarat, India

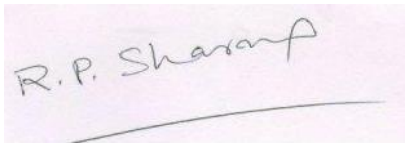

03.11.2025

Prof. R.P. Sharma
External Examiner,
IIT Delhi

03.11.2025

Prof. Sudipta Sarkar
FDC Member,
IIT Gandhinagar

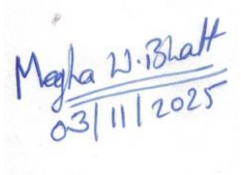

Dr. Megha Upendra Bhatt
DSC and FDC Member,
PRL Ahmedabad

03 November 2025

Prof. Dibyendu Chakrabarty
DSC and FDC Member,
PRL Ahmedabad

03-11-2025

Prof. Varun Sheel
DSC and FDC Member,
PRL Ahmedabad

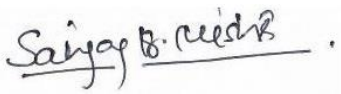

Nov.03, 2025

Dr. Sanjay K. Mishra
PhD Supervisor and FDC member,
PRL Ahmedabad

DECLARATION

I declare that this written submission represents my ideas in my own words, and where others' ideas or words have been included, I have adequately cited and referenced the original sources. I also declare that I have adhered to all principles of academic honesty and integrity and have not misrepresented or fabricated or falsified any idea/data/fact/source in my submission. I understand that any violation of the above will be cause for disciplinary action by the Institute and can also evoke penal action from the sources which have thus not been properly cited or from whom proper permission has not been taken when needed.

(Name: Trinesh Sana)

(Roll No: 20330018)

CERTIFICATE

It is certified that the work contained in the thesis entitled **"Plasma Sheath Formation Around Moon and Its Implications"** submitted by **Trinesh Sana** (Roll no: 20330018), to Indian Institute of Technology, Gandhinagar, has been carried out under my supervision at the Planetary Sciences Division, Physical Research Laboratory, Ahmedabad, and that this work has not been submitted elsewhere for any degree or diploma.

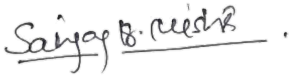

Dr. Sanjay K. Mishra
(Thesis Supervisor)
Associate Professor
Planetary Sciences Division
Physical Research Laboratory
Ahmedabad, India

Acknowledgements

First of all, I would like to express my sincere gratitude to my thesis supervisor, Dr. Sanjay K. Mishra. I am grateful to him for introducing me to the exciting field of space plasma physics. Without his constant encouragement, help, and support, this work would not have been transformed into a thesis. Right from the beginning of the thesis, he was always by my side through all my ups and downs, in any situation. I truly feel that I can never fully repay the debt of gratitude I owe him for his mentorship and belief in my capabilities.

I would like to express my gratitude to my DSC members, Dr. Megha Upendra Bhatt, Prof. Varun Sheel, and Prof. Dibyendu Chakrabarty, for their constructive feedback, valuable suggestions, and unwavering support throughout this journey. I also extend my appreciation to all the coursework instructors: Prof. D. Banerjee, Prof. Kuljeet Kaur Marhas, Prof. Jayesh P. Pabari, Dr. K. Durga Prasad, Dr. S. Vijayan, Dr. Megha Upendra Bhatt, Prof. Varun Sheel, Dr. Neeraj Srivastava, and Mr. R. R. Mahajan, for introducing me to the fascinating subject of Planetary Sciences. Also, I am thankful to Dr. Naveen Chauhan for teaching the Research Methodology course. I am deeply grateful to my coursework project supervisors: Prof. Jayesh P. Pabari, Prof. Varun Sheel, Dr. Kinsuk Acharyya, and Prof. Dibyendu Chakrabarty. Their guidance provided me with invaluable research experience and prepared me to take on significant responsibilities, such as working on my thesis. Additionally, I sincerely thank Dr. Dwijesh Ray, Dr. Deepak K. Panda, Dr. Rajiv Ranjan Bharti, and Dr. Rishitosh Kumar Sinha.

I express my profound gratitude to the Director, PRL, Prof. Anil Bhardwaj, the Dean, PRL, Prof. Pallam Raju, the Head, Academic Services, PRL, Dr. Bhushit G. Vaishnav, the division head, PSDN, PRL, Prof. Varun Sheel, the deputy head, Prof. D. Banerjee, and all the academic committee members for their support. I would like to express my sincere gratitude to the Science and Engineering Research Board (SERB), now known as the Anusandhan National Research Foundation, as well as the Department of Science and Technology (DST) and the Council of Scientific & Industrial Research (CSIR) under the Ministry of Science and Technology, Government of India, for providing me with the necessary funding for my international travel. This support enabled me to attend the 4th Dust, Atmosphere, and Plasma Environment of the Moon and Small Bodies workshop at the University of Colorado and the 55th Lunar and Planetary Science Conference (LPSC) in The Woodlands, Texas, United States of America. I am grateful to Prof. Anil Bhardwaj, Director of PRL, and the Department of Space, Government of India, for the opportunity to participate in this international conference. I am also thankful to IITGN and PRL Administration, PRL Library, PRL Computer Center, PRL Purchase and Stores, PRL Canteen, and PRL Account Section. I would like to extend my heartfelt appreciation to Dr. Samir Dani and Dr. Shital Patel, Medical Officer at PRL Dispensary, for their

exceptional care and support regarding my health during a critical time. Their professionalism and dedication made a significant difference in my recovery. Thank you for your invaluable assistance.

Reflecting on my memories from the beginning of 2020, I was an enthusiastic M.Sc. student aspiring to become a particle physicist. I was working on my master's project under the supervision of Prof. Palash B. Pal. I am sincerely grateful for his constant mentorship during the challenges posed by COVID-19. He encouraged me to not solely pursue my original dreams but to seize the opportunities that arose. Following his guidance, I embarked on a completely new path in planetary science and joined PRL. Joining PRL not only gave me the opportunity to work under the guidance of Dr. Sanjay K. Mishra, but also to write the most exciting, fascinating, challenging, and eye-opening chapters of my life. I am grateful to many people; without them, this journey might have been very different. It is time to express my sincere gratitude to them.

To my batchmates Aditya, Sanjay, Arup M, Arup C, Malika, Wafikul, Kamran, Dharmendra, Mansi, Akanksha, Chandrima, Debashis, Gurucharan, Ananya, and Sandeep.

To my super-seniors, Dr. Shefali Uttam, Dr. Harish, Dr. Sana Ahmed, Dr. Shivani Baliyan, Dr. Alka Rani, Dr. Yash Srivastava, Dr. Akanksha Khandelwal, Dr. Namita Uppal, Dr. Naval Kishor Bhadari, and Dr. Vikas Soni, for sharing their experience and invaluable help in making big decisions during the tenure.

To my seniors, Dr. Vineet Rawat, Dr. Saumya Jyoti Sarkar, Dr. Birendra Chhotaray, Dr. Neha Panwar, and Dr. Kimi Khungree Basumatary, and Dr. Vardaan Mongia, for the helpful suggestions, memories, and entertainment. They never hesitated for any help in any kind of situation.

To Kiran, Anupam, Varsha, Chahat, Aarti, Naren, Goldy, Arijit, Dibyendu, Soumik, Antarikhsa, for being good juniors.

Again, to Dr. Vineet Rawat, Dr. Saumya Jyoti Sarkar, Anupam, Aditya, Soumik, Arijit, Dibyendu, for the sleepless nights with clouded thoughts.

To my painkillers, Kiran and Sanjay, for being with me during all my highs and lows and for getting stuck in the endless loop of Instagram reels.

To Aditya, for educating me in Geology and other subjects that were beyond my imagination.

Again, to Arup C, Wafikul, Kiran, and Sanjay for being the friends in need. You stood like anchors when everything else drifted.

To Dr. Subham Sarkar, Dr. Narayan Bose, Dr. Sumit Pathak, and Dr. Deepali Singh for everything. Words truly fall short in conveying the depth of my appreciation for all that you have done. Thank you for being such remarkable pillars in my life.

To my elder brother, zoologist Trideb, for teaching me to be steadfast in my deter-

mination.

To my father, who taught me to accept what cannot be changed and how to live with it.

Lastly, to my mother, for her love, compassion, care, teachings, poetry, and the loving memories she left behind. May her soul rest in peace in the land of eternal freedom.

Trinesh Sana

Contents

Abstract

This thesis investigates plasma sheath formation over the Moon. The sheath on the sunlit side of the Moon is identified as very different from the nightside. Photoelectrons are an integral part of the plasma sheath at sunlit locations, which is referred to as the lunar photoelectron sheath. This thesis formulates the characteristic velocity distribution of the emitted photoelectrons over the sunlit Moon. As an advancement, Fowler's photoemission theory has been coupled with observed solar spectra, photoelectric quantum yield, and latitude-dependent surface temperature in deriving the velocity distribution function (VDF) of the photoelectrons. It is noticed that the dominant contribution in the photoelectron VDF comes from extreme ultraviolet photons of the solar spectra, and it significantly deviates from the Maxwellian nature. Moreover, within a photoelectron sheath, which refers to a finite surface potential, the velocity distributions significantly differ from that of the uncharged surface — VDF has been evaluated in terms of free and trapped photoelectron population densities. The derived VDF is found in close agreement with the measured photoelectron velocity distribution.

This VDF has been further used in analytical investigations of the sheath formation on the sunlit moon, influenced by observed solar UV/EUV radiation as well as solar wind plasma. Poisson's equation is coupled with the duly derived novel characteristics of photoelectrons, non-Maxwellian solar wind electrons, and cold ions to derive the electric potential, electric field, and population density profiles within the photoelectron sheath. Results show that a traditional Debye (Type C) sheath forms around the terminator due to dominant plasma electron accretion and marginal photoemission. While moving towards the equator, the photoelectron contribution increases, yielding monotonic (Type B) and non-monotonic (Type A) sheath solutions over sunlit locations. The calculations show that the non-monotonic potential structures are more stable near the terminator region, while both types of potential structures are probable near the equator region for the nominal solar wind plasma. A vertical sheath extension of $\sim$ 60 m and $\sim$ 12 m is predicted for typical solar wind plasma at the equator corresponding to Type A and Type B sheath, respectively. Under exotic plasma conditions (e.g. Earth's magnetospheric tail lobe, plasma sheet), non-monotonic solutions become stable for the photoemission-dominated region, and the entire sunlit lunar surface may acquire negative potential.

The capability of this comprehensive model has been showcased by predicting the sheath structure around the Chandrayaan-3 landing site during a 14-day sunlit passage.

As input parameters, the observed solar UV spectrum and realistic plasma parameters measured by THEMIS-ARTEMIS have been used in this case study. A dynamic variation of the potential structure around the sunlit landing site has been observed through the analysis. Exotic non-monotonic (Type A) potential structures are found to prevail during most of the sunlit passage. Model predicts a photoelectron density range between 10 and 40 cm^{-3} and a very dynamic variety of photoelectron populations with differing mean energies near the surface of the landing site.

Continuing to the lunar nightside, this thesis assesses the plasma sheath formation on the night side of the Moon when exposed to highly energetic ambient plasma. The calculations indicate that the secondary electron emission (SEE) due to highly energetic plasma electrons leads to the formation of the inverse sheath around the positively charged lunar surface on the night side, where a traditional Debye sheath with a high negative surface potential is anticipated. This thesis provides an analytical formulation of Debye sheath and inverse sheath formation, considering Maxwellian primary and secondary electrons and cold ions. For a given SEE yield, a temperature regime is predicted where the inverse sheath is possible.

Under the dynamic influence of these plasma sheath structures, intricate dynamics of lunar dust have been observed during the Surveyors and Apollo missions in the form of the Lunar horizontal glow. These dynamics are primarily driven by electrostatic forces generated by the continuous bombardment of solar wind and highly energetic UV photons on the lunar surface and dust particles. This thesis further investigates the phenomenon of dust charging within the lunar photoelectron sheath and subsequent dynamics using the duly derived comprehensive model of the lunar photoelectron sheath. A test dust particle is introduced into the sheath, and equilibrium charge and static levitation conditions are derived. The result of dynamical evolution suggests the existence of a narrow parametric regime corresponding to the periodic hopping trajectory of the dust particle over the lunar surface. In other cases, the dust particles are found to re-impact the surface after a single ballistic hop. We further identify that the discrete charging of the dust could be crucial in determining the dust dynamics, particularly in the tenuous plasmas. The analysis of the discrete dust charging model reveals significant discrepancies with the continuous dust charging model and suggests a lower likelihood of static dust levitation in the lunar environment. The present study is important for unraveling the fundamental processes governing surface evolution on the Moon and other airless bodies throughout the Solar System.

Further, going deeper into the microphysics of lunar dust detachment, a solution to the fundamental problem and physical mechanism of dust detachment from the lunar surface has been proposed in this thesis. It has been conceptualized that the electrostatic charge fluctuation at the microscopic scale could create a sufficient electric field and Coulomb force to overcome the dust-surface adhesive force and detach the dust particles. A Markovian process is manifested with a Monte Carlo scheme to simulate the concept. The simulation establishes the random generation and annihilation of fluctuating charged microscopic spots. The results demonstrate the existence of microscopic charged spots, capable of inducing sufficient electric field and Coulomb force of the order of a few MV m^{-1} and 10s of pN, respectively, which creates favorable conditions for lunar dust detachment. This concept fits the gap and puts forward a consistent mechanism describing dust dynamics and the generation of a dusty plasma scenario over the Moon.

Finally, this thesis addresses the influence of local surface topography on the plasma sheath structure, going beyond idealized flat-surface analyses. Analytically and using open-source Spacecraft Plasma Interaction Software, the effect of the simplest surface topography (a simple crater) in modifying the lunar photoelectron sheath has been investigated. Results highlighted the importance of local solar illumination angle varies around the crater's floor, and derived 3D electric potential and density profiles of various sheath populations.

Keywords: Moon, Plasma sheath, Photoelectrons, Secondary electrons, Solar wind, Lunar dust, Charge fluctuations

List of Publications

Included in this Thesis

1. **Trinesh Sana**, S K Mishra, Electrostatic Charging of Crater's Surface over Sunlit Moon, *Plasma Physics Reports*, Volume 49, Issue 1, March 2023, Pages 99–104, https://doi.org/10.1134/S1063780X22600943

2. **Trinesh Sana**, S K Mishra, Plasma sheath around sunlit moon: monotonic and non-monotonic structures, *Monthly Notices of the Royal Astronomical Society*, Volume 520, Issue 1, March 2023, Pages 233–246, https://doi.org/10.1093/mnras/stad155

3. **Trinesh Sana**, S K Mishra, Plasma Sheath around Chandrayaan-3 Landing Site: A Case Study, *The Planetary Science Journal*, Volume 4, Issue 9, September 2023, Page 158, https://dx.doi.org/10.3847/PSJ/acf1a1

4. **Trinesh Sana**, S K Mishra, Velocity Distribution of Photoelectrons over Sunlit Moon, *ICARUS*, Volume 412, April 2024, 115996, https://doi.org/10.1016/j.icarus.2024.115996.

5. **Trinesh Sana**, S K Mishra, Possibility of inverse sheath in the lunar nightside due to secondary electron emission, *Fundamental Plasma Physics*, Volume 10, June 2024, 100052, https://doi.org/10.1016/j.fpp.2024.100052

6. **Trinesh Sana**, S K Mishra, Revisiting Lunar Dust Charging And Dynamics, *Physics of Plasmas*, Volume 31, October 2024, 102901, https://doi.org/10.1063/5.0225693

7. **Trinesh Sana**, S K Mishra, Electrostatic Detachment of Dust from the Lunar Surface: Microscopic Fluctuations could be the key, *Earth and Planetary Science Letters*, Volume 668, October 2025, 119544, https://doi.org/10.1016/j.epsl.2025.119544

Conference Publication

1. **Trinesh Sana**, S. K. Mishra "Non-Monotonic Potential Structure Around Sunlit Moon" in 54th Lunar and Planetary Science Conference 2023 (LPI Contrib. No. 2806).

2. **Trinesh Sana**, S. K. Mishra "Dust Charging Within Lunar Photoelectron Sheath" in 55th Lunar and Planetary Science Conference 2024 (Abstract ID: 1042).

3. **Trinesh Sana**, S. K. Mishra "Effect of Solar Activity on The Lunar Plasma Environment" 43rd meeting of the Astronomical Society of India (ASI 2025).

Not included in this Thesis

1. S K Mishra, **Trinesh Sana**, Distribution of charge on floating dust particles over sunlit locations on Moon, *Monthly Notices of the Royal Astronomical Society*, Volume 508, Issue 3, December 2021, Pages 4332–4341, https://doi.org/10.1093/mnras/stab2862

2. S K Mishra, **Trinesh Sana**, Mitigating massive triboelectric charging of drill in shadowed region of Moon, *Monthly Notices of the Royal Astronomical Society*, Volume 512, Issue 4, June 2022, Pages 4730–4735, https://doi.org/10.1093/mnras/stac369

List of Figures

List of Tables

Chapter 1

Introduction

Moon, an airless planetary body, due to its small size and low gravity, exhibits a tenuous atmosphere (Urey and Korff, 1952; Hoffman et al., 1973; Vaniman et al., 1991; Heiken et al., 1991; Stern, 1999). The lunar surface is directly exposed to solar radiation, solar wind plasma, and other local plasma populations. Exposed to the flux of photons, solar wind ions, and electrons, solar energetic particles (SEP), Earth's magnetospheric plasmas, a complex electrical environment is produced near the surface of the Moon (Halekas et al., 2011b). The environment on the sunlit side of the Moon is very different from the dark side (Stubbs et al., 2007; Halekas et al., 2011b; Stubbs et al., 2014). Photons in the extreme ultraviolet (EUV) range primarily generate photoelectrons over the sunlit locations. In addition to that, solar wind and local plasma particles also accumulate on the lunar surface. The cumulative effect of these processes creates a positively charged lunar surface on the dayside — emitted photoelectrons near the surface form a photoelectron sheath over the lunar surface (Walbridge, 1973; Manka, 1973). Though the solar wind plasma is obstructed in the dayside, there are space plasma currents in the lunar nightside (currents from solar wind plasma expansion or currents from plasma of the Earth's magnetotail). Since electrons travel 42 times faster than ions, the faster rate of electron collection results in a negatively charged surface on the nightside. Plasma ions and electrons near the surface of the night side form a Debye sheath. The simple picture of the plasma sheath around the Moon is schematically shown in Figure 1.1. Moreover, highly energetic plasma electrons impacting the surface may produce secondary electron emission (Horányi, 1996). These emitted secondary electrons can also affect the characteristics of the lunar near-surface plasma environment (Vaverka et al., 2016). As the surface potential changes from dayside-positive to nightside-negative, it creates complex electrostatic

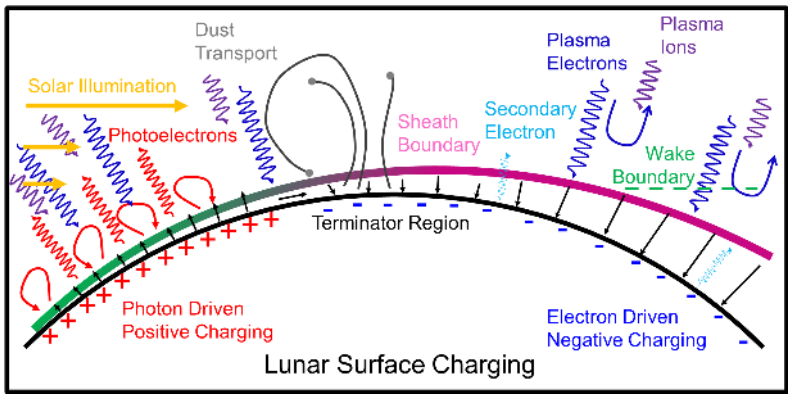

Figure 1.1: Simple picture of the Lunar plasma sheath. Various charging processes acting on the lunar surface are shown in this Figure. Photoelectrons are emitted from the lunar surface by solar UV and EUV-rays. Incident thermal plasma electrons and ions, and secondary emission of electrons are also shown. On the lunar dayside, the curled arrows represent photoelectrons that are unable to escape the positively charged surface. On the lunar nightside, the curled arrows represent plasma electrons that are reflected due to the negative surface potential. Modified from Stubbs et al. (2007).

features in the vicinity of the terminator (i.e., defined as the day and nightside boundary) (Farrell et al., 2007). Dust particles on the lunar surface, or just above it, undergo electrostatic charging through a similar mechanism. Their dynamical behavior is shaped by this electrostatically active plasma environment, leading to phenomena such as dust lofting and static levitation (Nitter et al., 1998; Colwell et al., 2007, 2009).

On a larger scale, the nightside of the Moon also produces an interesting plasma environment. As the solar wind plasma is absorbed in the dayside hemisphere of the Moon, a plasma void is created in the anti-sunward directions of the Moon. This trailing disturbance is called the lunar wake (Halekas et al., 2011b). This disturbance may propagate up to 25 lunar radius ($\sim$ 43000 km) (Clack et al., 2004). While filling this void, solar wind in the downstream region expands and gives rise to exciting plasma phenomena (Halekas et al., 2015). Non-trivial surface topography near the terminator and poles, especially (permanently) shadowed areas, also creates an electrically complex environment. The local solar wind flows tangentially to the surface near the terminator. While interacting with large-scale topographic features like mountains and big deep craters, the solar wind plasma is absorbed in the upstream surface, creating a plasma void on the leeward side, which may generate 'mini-wakes' like structures (Farrell et al., 2010). The expansion of solar wind plasma into such a void creates an ambipolar potential, which diverts ion flow into the void region. The solar wind plasma deviates from quasi-neutrality during expansion and creates an electron-rich (ion-free) region just behind the obstacle, followed by the ion front under the influence of the ambipolar field (Mishra and Bhardwaj, 2020).

Apart from that, the interaction of the lunar crustal magnetic anomalies with the solar wind and subsequent development of the plasma environment is also a potential problem (Bhardwaj et al., 2015). On the Moon, there are regions with strong surface remnant magnetic fields associated with high-albedo (bright) surface features called "lunar swirls" (Hood and Williams, 1989). This area appears to be relatively younger than the nearby non-swirl areas. This has been anticipated to be due to the shielding of incoming solar wind protons by the strong magnetic field in the swirl region.

The Moon, being the closest airless body to the Earth, exhibits a unique environment that allows us to explore its near-surface plasma environment (Halekas et al., 2011b). To effectively measure different characteristics of this environment, a solid theoretical foundation is essential. This foundation is also important for conceptualizing and designing experiments for future lunar missions. Additionally, the operation of instruments during lunar campaigns is significantly affected by the near-surface plasma environment. Therefore, it is important to conduct thorough assessments of these effects prior to the missions. This can be accurately achieved only with a better understanding of the near-surface plasma environment around the Moon (Farrell et al., 2008; Rhodes et al., 2020; Mishra and Sana, 2022). This thesis explores various aspects of the near-surface lunar plasma environment, highlights intriguing physics of plasma sheath formation over the Moon under different plasma conditions. The understanding developed can be further expanded to other airless planetary bodies like Mercury and asteroids.

This thesis primarily focuses on lunar surface charging, sheath formation, and the subsequent charging and dynamics of dust. The following sections review existing research on this topic, highlighting the gaps and unresolved issues that are addressed in this thesis.

1.1 Literature review

The notion of lunar surface charging and sheath formation is schematically shown in Figure 1.2: High-energy UV photons generate photoelectrons. Solar wind ions and electrons are collected on the surface. f_{pho} is the outgoing photoemission flux, whereas f_{sei} and f_{si} are the solar wind/ ambient plasma electron and ion fluxes, respectively. UV-induced photoelectron emission and solar wind/ ambient plasma ion collection yield the surface positively charged, while the electron collection from the solar wind/ ambient plasma makes the surface negatively charged. As a result, at steady state, a finite amount of

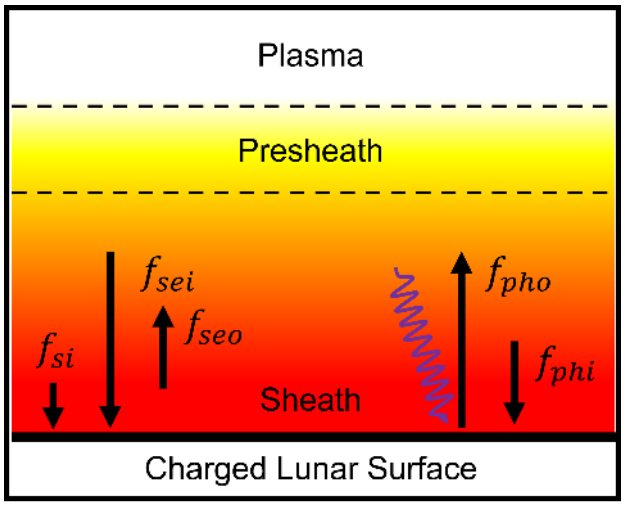

Figure 1.2: A schematic of the plasma sheath around the lunar surface.

electric potential is connected with the surface. This surface potential is screened by the emitted photoelectron and ambient plasma constituent, forming a sheath in the vicinity of the lunar surface. Depending on the surface potential and sheath structure, some of the incoming solar wind/ ambient plasma electrons are reflected back to space, while photoelectrons get trapped near the surface. As a result, there will be incoming photoelectron flux to the surface (f_{phi}) and outgoing solar wind electron flux (f_{seo}). The sheath possesses inherent electric potential and field structures that can influence the behavior of dust particles, which are electrostatically charged, within the sheath through the combined effects of electrostatic forces and gravity.

1.1.1 20th Century (between 1955-2000)

Gold (1955) for the first time discussed lunar surface charging and suggested that electrostatic forces may be responsible for the dust mobilization around the Moon. Though qualitative, he conceptualized the existence of photoelectron sheath in his later works (Gold, 1959, 1962). Thereafter, Singer and Walker (1962b) presented an approximate theoretical solution of the sheath electric field profile for the bodies in space exposed to solar UV flux using monoenergetic photoelectrons. They solved the Poisson equation with a constant photoelectron density. They have demonstrated photoelectron screening around flat space (Moon) and small spherical bodies. Although they have presented their calculations with some simplifying assumptions, this is one of the first theoretical attempts to explain this exciting photoelectronic screening phenomenon. Thereafter, they have argued that the sunlit lunar surface electric field is not sufficient to levitate dust, but if other mech-

anisms eject the dust, the electric field may determine its trajectory (Singer and Walker, 1962a). Grobman and Blank (1969) conducted analytical investigations to determine the steady-state electrostatic potential of the sunlit lunar surface by setting the net current to a small area on the lunar surface to zero. They considered the Moon as an electron-emitting body exposed to plasma and applied the probe theory to determine the surface potential. They emphasized the significance of work functions, quantum yield of the lunar surface, along with the illumination angle and solar activity. Along with that, they have incorporated the properties of solar wind plasma parameters in their calculations. Their calculations provided the prerequisite for theoretical studies of the electric potential and field determination at the lunar surface.

Grard and Tunaley (1971) presented photoelectron sheath formation around a photoemitting plate. Three different distributions of photoelectrons had been considered by them e.g.: i) monokinetic $\left(f(u) \propto \delta(u_0)\right)$, ii) rectangular $\left(f(u) \propto 1 \quad \text{for} \quad u < u_0\right)$, and iii) Maxwellian distribution $\left(f(u) \propto \exp(-u^2/u_{th}^2)\right)$. They have solved Poisson's equation considering energy conservation and continuity. They have analytically derived the electric potential, electric field, and photoelectron density above the surface in normalized form shown in Table 1.1.

VDF	Monokinetic	Rectangular	Maxwellian
$\frac{V(x)-V_0}{V_e}$	$\left(1-\frac{3x}{\sqrt{2}\lambda_s}\right)^{4/3}-1$	$\left(1-\frac{x}{3\sqrt{2}\lambda_s}\right)^{4}-3$	$-4\ln\left(1+\frac{x}{\sqrt{2}\lambda_s}\right)$
$\frac{E(x)}{E_0}$	$\left(1-\frac{3x}{\sqrt{2}\lambda_s}\right)^{1/3}$	$\left(1-\frac{x}{3\sqrt{2}\lambda_s}\right)^{3}$	$\left(1+\frac{x}{\sqrt{2}\lambda_s}\right)^{-1}$
$\frac{N(x)}{N_0}$	$\left(1-\frac{3x}{\sqrt{2}\lambda_s}\right)^{-2/3}$	$\left(1-\frac{x}{3\sqrt{2}\lambda_s}\right)^{2}$	$\left(1+\frac{x}{\sqrt{2}\lambda_s}\right)^{-2}$

Table 1.1: Analytical form of electric potential, field and photoelectron density profiles for different photoelectron velocity distribution function (VDF) obtained by Grard and Tunaley (1971). Here, $V(x)$, $E(x)$, $N(x)$ are electric potential, field and density at altitude x. The subscript "0" means at the surface. λ_s and V_e are the sheath thickness and mean photoelectron kinetic energy.

The monokinetic aspect of their study is unlikely to be relevant in realistic scenarios. This study, for the first time, highlighted the importance of different photoelectron velocity distribution functions in deriving the sheath features. Some studies have extensively utilized the Maxwellian part of their solution, which will be briefly discussed later. However, this work doesn't consider the contribution of the effect of ambient plasma in their analysis. Till then, within the photoelectron sheath, the electric potential profile is characterized by a monotonically decreasing trend from the positive surface potential to zero at the sheath edge.

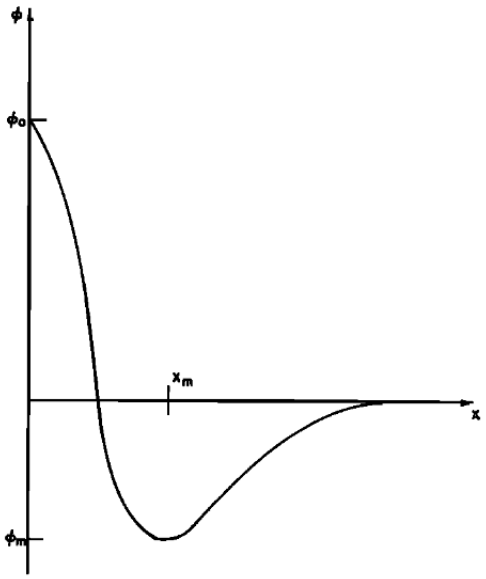

Fig. 1. Non-monotonic potential distribution.

Figure 1.3: Non-monotonic potential distribution. Taken from Guernsey and Fu (1970)

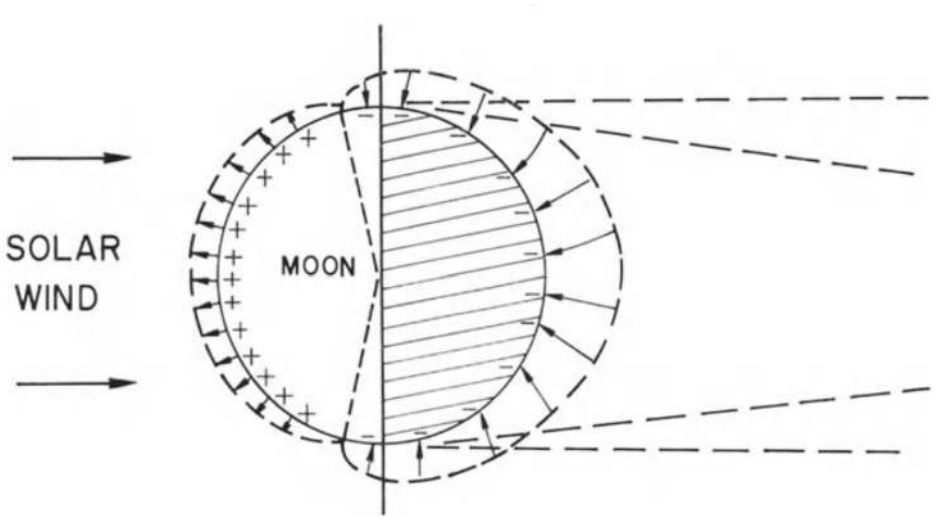

Figure 1.4: An expected potential and field distribution when the Moon is in the solar wind derived by Manka (1973). Taken from Manka (1973).

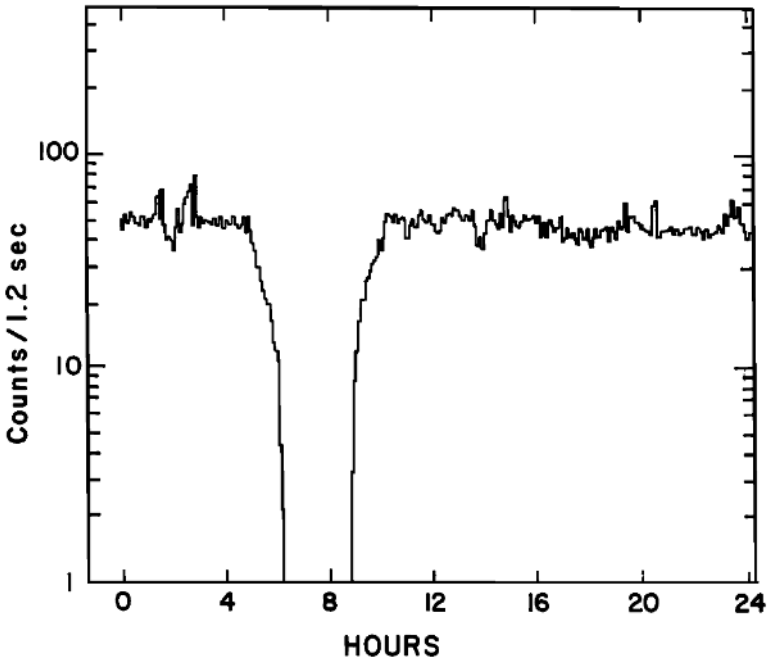

Figure 1.5: An Apollo 14 CPLEE instrument measurement of electron count rate during a solar eclipse. Taken from Reasoner and Burke (1972a).

The works of Guernsey and Fu (1969, 1970); Fu (1971) suggested the possibility of another potential profile as shown in Figure 1.3 for which the surface potential decreases to a negative maximum and then increases to zero. They have given an analytical formulation considering contributions from photoelectrons, plasma electrons, and ions (Guernsey and Fu, 1969, 1970). For Maxwellian photoelectrons, their calculation argued that this non-monotonic potential profile is more stable than the traditional monotonic potential profile.

Manka (1973) carried out a global study of lunar surface potential and electric field variation. Surface potential was determined using probe theory by setting the net current to zero, i.e.,

$$I_e + I_i + I_p + I_s = 0\,, \tag{1.1}$$

where "e","i","p", and "s" correspond to electron, ion, photoelectron, and secondary electron current, respectively. Manka (1973) solved Eq. 1.1 for different location on Moon under different plasma parameters. Subsequently, the electric potential was divided by the local Debye length, which was determined using the local density and temperature, to calculate the surface electric field under the assumption of exponential decay of electric potential above the surface. Although Manka (1973) sketched a typical global picture of the sheath structure (shown in Figure 1.4), the model is simplistic, and the use of the

Maxwellian nature of the charging constituent limits the applicability in a realistic scenario.

Another independent work by Walbridge (1973) tried to draw an analytical picture of the lunar photoelectron layer. He also suggested a different distribution of lunar photoelectrons. Walbridge (1973) reported a spectral variation of quantum yield, which increases linearly with photon energy up to 9 eV and takes a constant value (0.2) for high-energy photon radiation.

During the theoretical development of the photoelectron sheath, several instruments from the Apollo missions—including Apollo 12, 14, 15, and 17—provided important data. Specifically, the Suprathermal Ion Detector (SIDE) on Apollo 14 and 15 (Freeman Jr et al., 1970, 1972), the Charged Particle Lunar Environment Experiment (CPLEE) on Apollo 14 (O'Brien and Reasoner, 1971), the Solar Wind Spectrometer (SWS) on Apollo 12 and 15 (Neugebauer et al., 1972), and the Lunar Ejecta and Meteorites Experiment (LEAM) on Apollo 17 (Berg et al., 1973, 1974) all confirmed that the lunar surface plasma environment, when exposed to sunlight, is primarily dominated by the UV-generated photoelectron sheath. These references are cited from Poppe (2011).

One specific instance of the CPLEE instrument demonstrated a total loss of electrons during a total lunar eclipse, as illustrated in Figure 1.5. This observation confirms that the plasma environment on the lunar surface during the day is primarily influenced by photoelectrons (Reasoner and Burke, 1972a,b).

Numerous lunar samples were collected and brought back to Earth by various Apollo missions during this time. The experimental works by Feuerbacher et al. (1972) were one of the most significant studies in advancing the understanding of the lunar photoelectron sheath. They have showcased different photoelectric properties of lunar surface fines 14259,116. They measured the work function of the lunar sample to be 5 eV using the Fowler method. Also, they bombarded the sample with photons of wavelengths ranging from 50 nm to 250 nm, and measured the photoelectric yield of the lunar sample as shown in Figure 1.6. The yield value was noticed to peak at 90 nm. Combining this yield value with the relevant solar spectrum, they have reported typical photoemission flux from the lunar surface to be 4.5×10^{-6} A m^{-2} (Feuerbacher et al., 1972). This value has been widely used in subsequent literature. Their experiments also suggested a different photoelectron distribution from the Maxwellian.

Micron and sub-micron-sized dust particles lying on the lunar surface experience electrostatic charging through similar surface charging mechanisms. These particles can

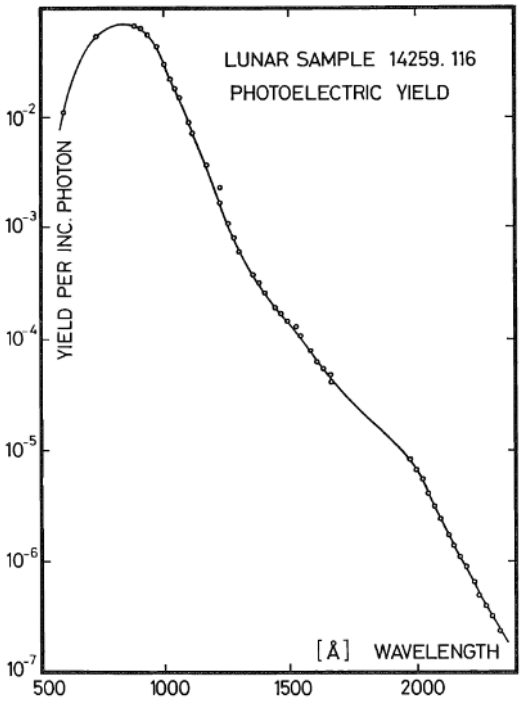

Figure 1.6: Photoelectric yield of the lunar sample. Taken from Feuerbacher et al. (1972).

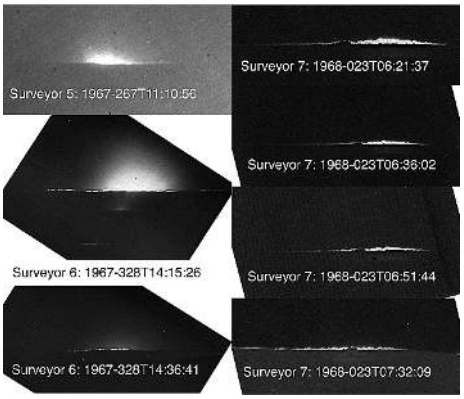

Figure 1.7: Unprocessed images of the Lunar Horizon Glow (LHG) from Surveyors 5, 6, and 7. Taken from Colwell et al. (2007).

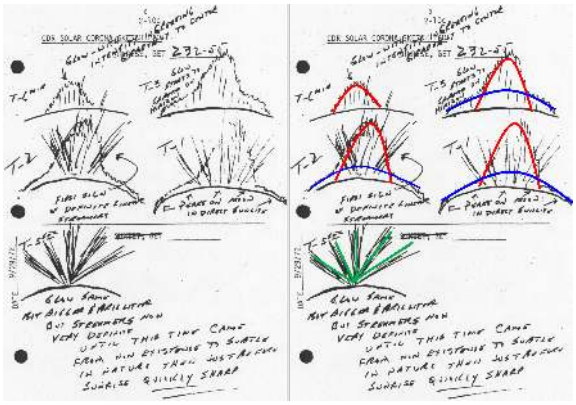

Figure 1.8: Sketches by Apollo 17 Commander E. Cernan. Different features are marked as (i) Red: coronal-zodiacal light, (ii) Green: streamers, and (iii) Blue: Lunar horizontal glow. Taken from Zook and McCoy (1991).

be lifted off the surface through various processes. Their charge and trajectory evolve over time due to the combined effects of the sheath electric field and gravity. These kinds of features have been observed during several Surveyor missions (5, 6, 7) in the form of a strange glow that was observed on the horizon of the Moon following the local sunset, as shown in Figure 1.7. This was named as "Lunar Horizontal Glow" (LHG), where sunlight was scattered by charged dust particles floating near the lunar surface (Criswell, 1972; Rennilson and Criswell, 1974). Optimal fits derived from scattering theory indicated that the average sizes of dust grains are roughly 5 μm at altitudes of around 30 cm (Criswell, 1972). Additional evidence of lunar dust dynamics comes from Apollo 17 Commander E. Cernan's series of sketches (shown in Figure 1.8). While carrying out their photographic campaign, astronauts E. Cernan sketched a number of unexpected visual phenomena. Among the most prominent were: (i) coronal-zodiacal light, (ii) time-varying 'streamers', and (iii) a faint horizontal glow. These observations offer qualitative insights into the plasma-driven behavior of dust near the lunar terminator (Zook and McCoy, 1991).

Near the end of the 20th century, three significant review works by Whipple (1981); Mendis and Rosenberg (1994); Horányi (1996), reviewed early works and provided a deep understanding of how surfaces and dust particles interact with their plasma environments and how these interactions influence a wide range of space and planetary phenomena throughout the solar system. Additionally, Horányi et al. (1998) studied the electrostatic properties of Apollo samples and lunar simulants. Nitter and Havnes (1992) have theoretically analyzed dust dynamics within a plasma sheath above the Moon and other asteroidal surfaces. Their work, however, is limited to the night side sheath structure of the airless bodies with zero photoemission.

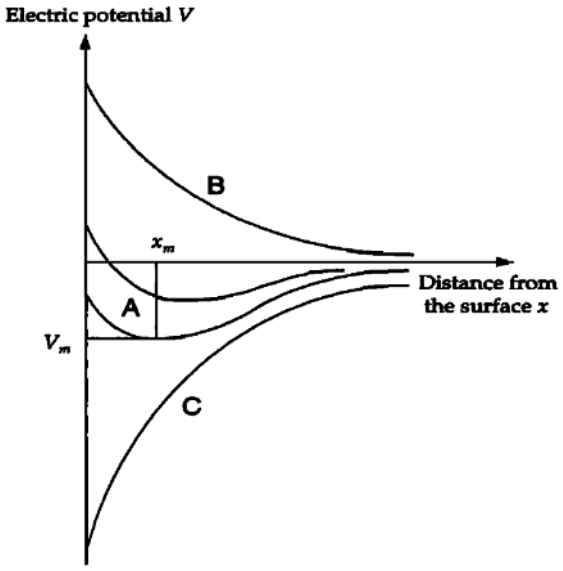

Figure 1.9: Shapes of the electric potential as a function of the distance from the surface suggested by Nitter et al. (1998).

A significant analysis of the photoelectron sheath formation considering incoming and outgoing photoelectrons was presented by Nitter et al. (1998). They suggested the possibility of three kinds of potential structures within the sheath. Two monotonic (Type B & C) and one non-monotonic (Type A) similar to Guernsey and Fu (1969, 1970); Fu (1971) — a schematic is illustrated in Figure 1.9, which is discussed in detail in the upcoming sections.

These studies, especially Nitter et al. (1998)'s works, have established a foundational understanding of the plasma environment surrounding airless planetary bodies, and they continue to influence research well into the 21st century. By outlining the basic principles of surface charging, sheath formation, dust charging, plasma-dust interactions, and the dynamics of charged dust in space, they have created the way for a diverse avenue of subsequent investigations. This includes theoretical calculations, computer simulations, laboratory experiments, space-based instrumentation, and mission design.

1.1.2 21st Century (between 2001-present)

The formation of the photoelectron sheath on the lunar surface and subsequent dust charging and dynamics has been vastly discussed in the 21st century via analytical/numerical/computational modeling, space observations, and laboratory experiments.

1.1.2.1 Theoretical works

In order to address the phenomenon of LHG, Stubbs et al. (2006) presented a dust fountain model where charged dust particles are accelerated upward by the surface electric field and follow a ballistic trajectory after crossing the sheath region. However, their model is oversimplified, as they consider the sheath field to be uniform up to one Debye length, and the dust charge is kept constant during its flight. Note, in a realistic scenario, the electric potential and field vary altitudinally within the sheath, and also, the dust particles collect the charges (sheath plasma) and emit photoelectrons as they move through the sheath. Since the population density varies within the sheath, the dust charge varies as its trajectory dynamically (temporally) evolves within the sheath. The study by Stubbs et al. (2007) examines how the latitudinal variation of plasma parameters, specifically density and temperature, measured by the Lunar Prospector, can be used to understand the global variation of lunar surface potential. It also emphasizes how changes in the surrounding plasma environment dynamically impact the charging of the lunar surface. In the later years, they conducted a comprehensive investigation of surface charging on the lunar dayside and near-terminator region, offering a detailed parametric analysis of various plasma, solar radiation, and lunar parameters (Stubbs et al., 2014). However, this was a simplistic study restricted only to the surface potential determination, considering Maxwellian photoelectrons as given by Manka (1973).

Sternovsky et al. (2008) highlighted the variation of lunar surface charging due to solar activity. They estimated various near-surface plasma parameters for solar Maxima, Minima, and X28 class solar flare data derived from the Flare Irradiance Spectral Model (FISM) (Chamberlin et al., 2008). However, their study restricted only to the determination of surface potential and surface electric field (dividing the surface potential by the local Debye length).

A series of papers authored by J. E. Colwell (Colwell et al., 2005, 2007; Hughes et al., 2008; Colwell et al., 2009) highlighted electrostatic dust transport over the Moon and asteroid 433 Eros. Colwell et al. (2005) had derived the surface potential of 433 Eros by balancing the outgoing photoemission flux with incoming solar wind electron flux. They used the electric potential, field, and density profiles derived by Grard and Tunaley (1971) for Maxwellian photoelectrons. Thereafter, they have carried out numerical estimation of dust transport within the sheath. They had discussed the results in the context of dust pond formation on Eros. Hughes et al. (2008) extended this work in the

3-dimensional scenario. Colwell et al. (2007) gave an extensive review on the mechanical properties of lunar dust and electrostatic charging. Colwell et al. (2009) extends their previous 433 Eros work in the lunar dusty plasma scenarios. Here, they have also used Maxwellian photoelectrons and used the work of Grard and Tunaley (1971). Additionally, they used the sheath profiles derived from commercial two-dimensional OOPIC Pro software but did not change the photoemission current from dust particles, which assumes Maxwellian photoelectrons. Popel's group (Golub' et al., 2012; Popel et al., 2013, 2018, 2022) modifies the expression of the sheath electric field derived by Grard and Tunaley (1971) (Maxwellian part shown in Table 1.1) for different solar illumination angles as

$$E(h,\theta) = \frac{2T_{pe}}{e}\frac{\sqrt{\cos\theta/2}}{\lambda_D + h\sqrt{\cos\theta/2}}, \tag{1.2}$$

where h is the altitude, θ is the subsolar angle, T_{pe}, photoelectron temperature and λ_D is the local Debye length. Moreover, they also modify the expression of the sheath's photoelectron density by accounting for the photoelectron contribution from the floating dust in addition to the lunar surface-generated photoelectrons, which can be written as

$$N(h,\theta) = N_0\frac{\cos\theta}{\left[1+(h/\lambda_D)\sqrt{\cos\theta/2}\right]^2} + N_e\left(\frac{h}{h_1}\right)^p, \tag{1.3}$$

where $h_1 = 1$ cm, $\lambda_D = \sqrt{T_{pe}/4\pi N_0 e^2}$, and p and N_e depend on the work function and subsolar angle. They argued that the 2nd term of the above equation becomes significant for the lunar dusty plasma scenario, where photoemission from the dust particles contributes to the sheath population. However, the model presumes a half-Maxwellian distribution of the sheath photoelectrons.

The theoretical analysis of Nitter et al. (1998) has been widely used in several studies. The most relevant studies are discussed in this thesis. Hartzell and Scheeres (2013) used this analytical model to study the dust dynamics near asteroids and the Moon. They used the non-monotonic potential profile of Nitter et al. (1998) and studied the dust charging and dynamics. They included a height-dependent gravity term to address the reduction of gravitational attraction with increasing altitude. They checked the stability and time scales of the dust particle motion about the static equilibrium position and constrained the velocity limit where a dust particle achieves levitation. Hartzell has extensively used Nitter et al. (1998)'s work in her subsequent studies related to the dust dynamics around asteroids and conceptualizing various payloads of lunar missions (Hartzell,

2019; Hartzell et al., 2022, 2023).

Burinskaya (2014, 2015) also used Nitter et al. (1998)'s model to study the effect of solar wind electron distribution on the sheath structure. These studies considered the shifted Maxwellian distribution of solar wind electrons and highlighted its importance in the parametric variation of solar wind plasma parameters in terms of density, temperature, and drift. Using Nitter et al. (1998)'s model, Li et al. (2016) carried out a global investigation of the sheath's potential and electric field structure and subsequent dust dynamics and transport around the Moon. They also commented about horizontal dust transport near the terminator. However, they all assumed a simplified Maxwellian velocity distribution for the emitted photoelectrons in deriving sheath characteristics and dust charging currents.

The works of Grard and Tunaley (1971) and Nitter et al. (1998) have been used to validate various results of particle-in-cell (PIC) simulation. In the analysis of Wang et al. (2008), a full-particle particle-in-cell (PIC) simulation model is used to derive the photoelectron sheath profiles. Their simulation produced a non-monotonic potential profile in the photoelectron-dominated region. But while addressing the dust dynamics, they have taken constant dust charge through the dynamical evolution of dust within the sheath, which limits its applicability in a realistic scenario. In the later studies, Zhao et al. (2021) improved the photoelectron sheath model via the Finite Difference (FD) Particle-in-Cell (PIC) scheme, but with a constant dust charge while addressing the dust dynamics (Zhao et al., 2022).

Lisin et al. (2014, 2015) investigated the importance of solar wind in shaping the photoelectron sheath profile. They have used a KARAT relativistic electromagnetic code based on the PIC method. They highlighted that in the absence of solar wind plasma, the solution is similar to Grard and Tunaley (1971), and when solar wind plasma was taken into account, non-monotonic features were observed in their simulation results similar to the results of Nitter et al. (1998). Another 1D PIC code of the lunar photoelectron sheath was developed by Poppe and Horányi (2010). In their work, they took the photoelectron distribution experimentally measured by Feuerbacher et al. (1972) and derived the sheath profiles as shown in Figure 1.10. Their PIC results showed a significant difference from Maxwellian photoelectrons. One significant effort of Poppe and Horányi (2010) was to incorporate the quantized and discrete nature of dust charging while deriving the dust dynamics within the sheath. They have used a Monte Carlo approach to tackle random dust charging, but they did not detail the specific protocol for assigning the random dust

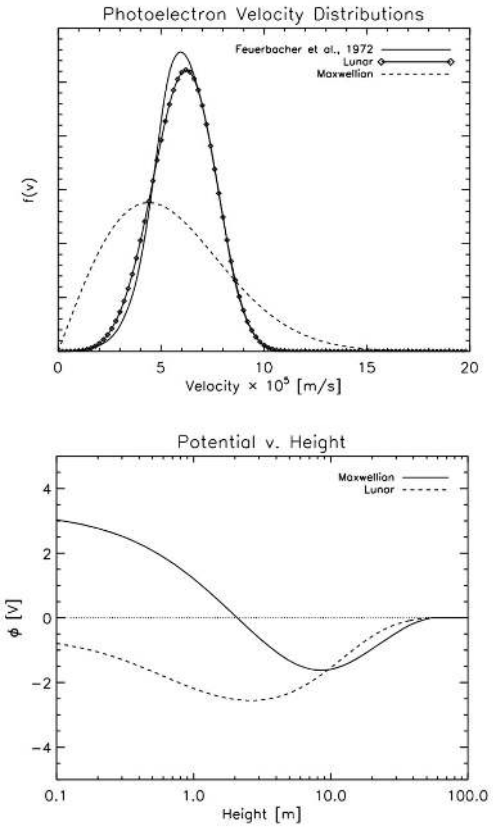

Figure 1.10: Top: Different velocity distributions of photoelectrons. The solid line represents the distribution obtained from lunar soil samples brought back by Apollo 17 (Feuerbacher et al., 1972), the diamonds denote the function fitted by Poppe and Horányi (2010), and the dashed line illustrates the corresponding Maxwellian distribution. Bottom: Non-monotonic potential structure above the lunar surface for the fitted (dashed) and Maxwellian (solid) photoelectron sheaths. Taken from Poppe and Horányi (2010); Poppe (2011).

charge. Additionally, while including the photoelectron contribution, they have assumed a photoelectron temperature without any proper justification. They have validated 1D PIC results with Nitter et al. (1998) model under the consideration of Maxwellian photoelectrons (Poppe, 2011). The 1D PIC results of Poppe and Horányi (2010) cannot explore the role of surface topography in modifying the spatial structure of the lunar photoelectron sheath, so they have used the commercial three-dimensional PIC simulation code VORPAL in their further study related to the sheath formation within a simple crater-like structure (Poppe et al., 2012b). On this note, Dyadechkin et al. (2015) developed a fully kinetic PIC model named HYBes aimed at studying the plasma environment above the surface of the Moon and other airless bodies in 1D, 2D, and 3D. They have validated their 1D results with the non-monotonic profiles of Nitter et al. (1998). However, they have assumed a Maxwellian distribution of emitted photoelectrons. As mentioned previously, Feuerbacher et al. (1972) showed that lunar photoelectrons exhibit a distribution that differs from the simplistic Maxwellian distribution. For the sake of simplicity, many studies have adopted the Maxwellian assumption. However, analytical attempts have been made by Senshu et al. (2015) to derive the photoelectron velocity distribution function. They have developed an angle-resolved velocity distribution function of photoelectrons from the laboratory-measured data of Feuerbacher et al. (1972) and used this distribution function in the model of Grard and Tunaley (1971) to derive the sheath potential structure. This model, however, considers the quasi-neutrality of the solar wind within the non-neutral sheath - this limits its utility to the real scenario.

From the above discussion, it is understood that a significant number of theoretical works have already been carried out specifically related to the lunar surface charging, sheath formation, subsequent dust charging, dynamics, and levitation. However, certain simplifications are noticed in the previous analyses, which limit their applicability to the realistic scenario, and need to be overcome in refining the understanding of the photoelectron sheath formation and a more precise estimate of the sheath features and their further implications. This is discussed in detail in section 1.2. Before that, let's review the relevant experimental and observational studies conducted in the 21st century.

1.1.2.2 Space observations

Theoretical attempts provided some estimates on the properties of the lunar photoelectron sheath. Halekas et al. (2008) reported the most relevant space observation utilizing the measurement of the Lunar Prospector Electron Reflectometer (ER) instrument. Figure

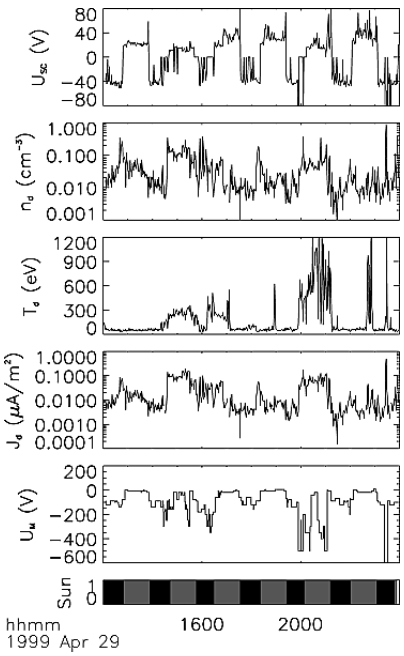

Figure 1.11: Lunar Prospector data in April 1999 while passing through the terrestrial plasma sheet. The panels show the spacecraft's potential, ambient electron density, electron temperature, electron current to the lunar surface, inferred lunar surface potential, and a sunlight/shadow indicator. Taken from Halekas et al. (2008)

1.11 shows time series data in April 1991, while Lunar Prospector passed through the geomagnetic tail and the terrestrial plasma sheet. They have measured the lunar surface potential with the method discussed in Halekas et al. (2008) using spacecraft potential, ambient plasma density, temperature, and the downward-going electron current to the surface. The Moon enters the plasma sheet around 20:00 as shown in the third panel of Figure 1.11 with increased electron temperature ($>$ 500 eV). Around -500 V electric potentials were seen in the photoemission-dominated locations of the sunlit lunar surface. These results contradicted the standard method of the surface charging model using the flux balance (Manka, 1973). Becasue the down going electron current towards the lunar surface ($\sim 0.1\,\mu\mathrm{A\,m^{-2}}$) was much smaller than the measured photoemission current ($\sim 4.5\,\mu\mathrm{A\,m^{-2}}$). They suggested the presence of non-monotonic potential structures above the sunlit lunar surface could explain these results, as theoretically predicted by Guernsey and Fu (1969, 1970); Fu (1971); Nitter et al. (1998).

As discussed by Fu (1971), for non-monotonic potential profiles, between the surface and potential minima, photoelectrons are getting trapped, and the negative potential minima reflect the incoming plasma electrons towards the surface. So the potential minima would be similar to the order of magnitude of the plasma electron temperature. And Lunar Prospector ER measured this potential minimum instead of the actual surface

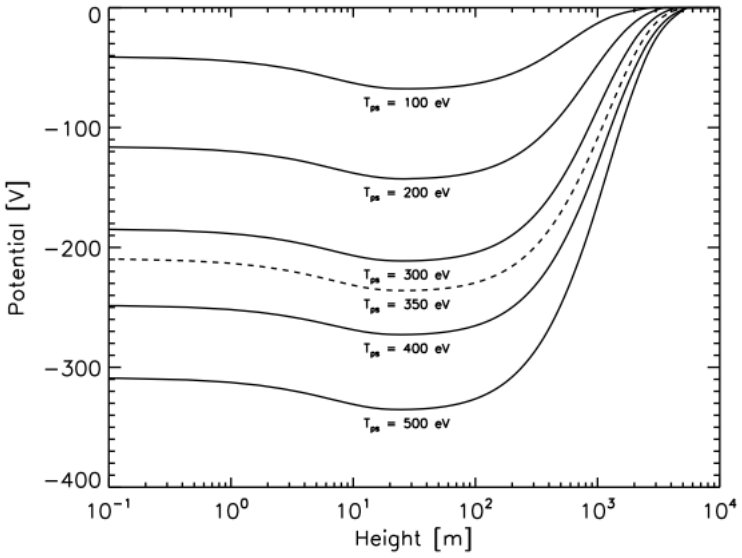

Figure 1.12: Non-monotonic potential structure above the lunar surface for different plasma sheet electron temperatures. Taken from Poppe (2011); Poppe et al. (2011).

potential. Nonetheless, the surface should not vary significantly from the potential minimum value, as the difference between the two potentials only needs to be adequate to capture most of the low-energy photoelectrons below the potential minima. Later, Poppe et al. (2011) compared Lunar Prospector ER measurements with their 1D PIC simulation (Poppe and Horányi, 2010) and derived stable non-monotonic potential structures around the Moon with high negative potential minima for the plasma parameter similar to Lunar Prospector measurements as shown in Figure 1.12.

The existence of non-monotonic potential structure has also been detected by ARTEMIS and reported in Halekas et al. (2011a); Poppe et al. (2012a). These space observations indicate that non-monotonic potentials are likely to be widespread throughout the solar system in various manifestations. It is crucial to incorporate these potential structures when modeling or interpreting observations of near-surface plasma environments, as they may significantly influence our understanding of these complex planetary plasma systems.

The direct implication of these potential structures around airless bodies is electrostatic dust transport. Significant computational and experimental studies of electrostatic dust dynamics have been carried out in the previous literature; however, observational evidence for electrostatic dust transport is perhaps the weakest of these investigations (Hartzell, 2012). After the observations of LHG during the Surveyor or Apollo Missions, there are no significant observations of electrostatic dust transport. The Lunar Dust Ex-

Figure 1.13: Lunar sunset captured by the Blue ghost lander. Taken from Firefly Aerospace (2025a,b).

periment (LDEX), which is part of NASA's Lunar Atmosphere and Dust Environment Explorer (LADEE), was created to assess the relative strengths of two distinct dust sources: a) dust generated from ejecta produced by the ongoing impact of interplanetary micrometeoroids on the lunar surface, and b) dust lifted due to its interactions with electric fields near the surface (Horanyi et al., 2015). These in-situ observations were unable to detect any electrostatically lifted particles above the lunar terminator within the altitude range of 3–250 km (Szalay and Horányi, 2015). Yan et al. (2019) reported fine dust deposits on lunar rocks up to a height of $\approx$ 30 cm from the distinct reflectance features of the rocks and regolith photographed by the Yutu rover of the Chang'E-3 mission. This height is similar to the height of LHG (Horányi et al., 2024). They argued that the electrostatic dust levitation process could explain this observation. In 2025, the Blue Ghost lunar lander, part of Firefly Aerospace's NASA-funded mission, successfully captured the image and video of sunset from the lunar surface (Firefly Aerospace, 2025c,a,b). As the Sun approached the lunar horizon on March 16, they captured high-resolution images of the lunar horizon glow as shown in Figure 1.13. Although analysis of these images is still going on, these can be regarded as the most recent (although indirect) evidence of electrostatic dust transport around the Moon (Wilcox, 2025). The relevant experimental works related to sheath formation and dust transport have been discussed in the next section.

1.1.2.3 Experimental works

Several laboratory experiments have been conducted to assess micron-sized dust charging exposed to a plasma environment. At the beginning of the 21st century, Sickafoose

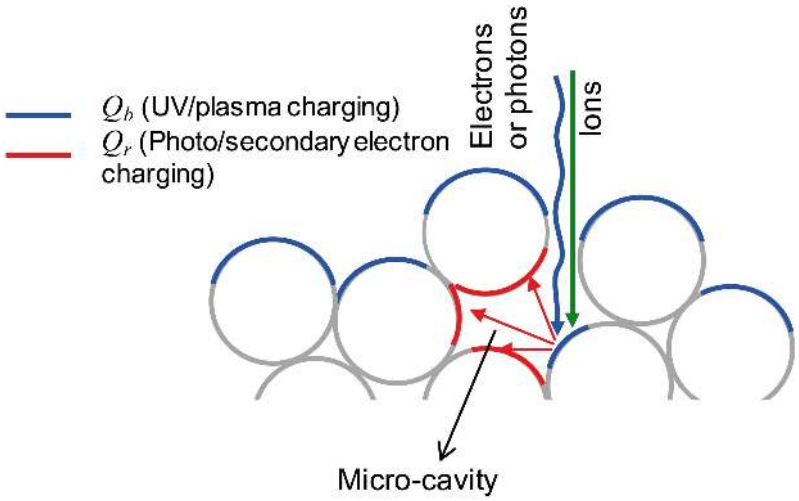

Figure 1.14: Schematic representations of the creation of charge patches within the micro-cavity. Taken from Wang et al. (2016b).

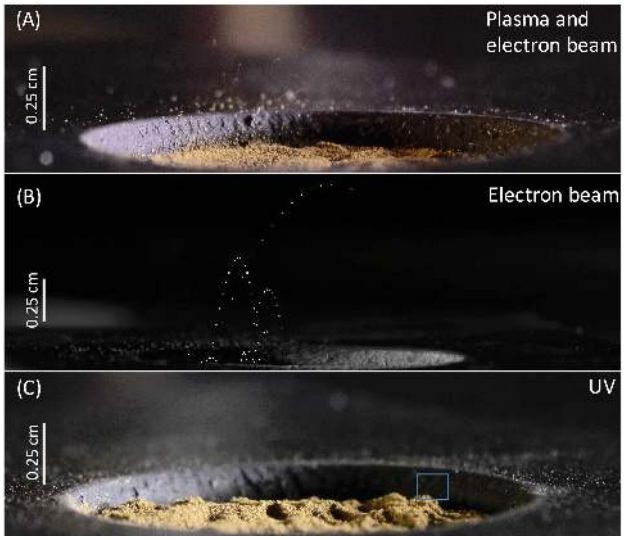

Figure 1.15: Images of dust mobilization under exposure to a) plasma and electron beam, b) electron beam, and c) UV irradiation. Taken from Wang et al. (2016b).

et al. (2001) experimentally analyzed the various charging properties (e.g., photoemission, plasma electron and ion collection, secondary emission, and triboelectric charging). Thereafter, they have assessed the possibility of electrostatic levitation of charged dust grains in a low-density plasma (Sickafoose et al., 2002). Flanagan and Goree (2006) carried out an experimental investigation on the dust lifting from the plasma-exposed surface. They assumed that the charges on a plasma-exposed dusty surface are uniformly distributed over the surface and the dust particle, as described by Gauss's law, and termed this the "shared charge model". Based on this assumption, each dust particle has charges of

$$Q = 4\pi\epsilon_0 a^2 E_s \,, \tag{1.4}$$

where a is the radius of the spherical dust particles and E_s is the surface electric field surrounding the dust. ϵ_0 is the permittivity in free space. Now, due to the random nature of the dust charging current, the dust charge fluctuates from this value. This creates a fluctuating electric force that can occasionally release dust particles, overcoming the adhesive van der Waals force. This model may be applicable for laboratory plasmas with high density, but in a typical lunar plasma scenario, a surface electric field typically around $5\,\mathrm{V\,m^{-1}}$ (Poppe and Horányi, 2010). Considering this field, the charge on micron-sized dust calculated from the above equation becomes less than unity. This suggests that most of the micron-sized and sub-micron-sized dust remains uncharged. However, dust released from the surface exposed to plasma and radiation has been observed in various experiments (Wang et al., 2009, 2010, 2011). Wang et al. (2016b) came up with "Patched Charged Model" and experimentally showed that within micro-cavities between adjacent dust particles below the surface, the emission and subsequent re-absorption of photoelectron and/or secondary electrons can generate significantly large negative charges and intense particle-particle repulsive forces that can launch the dust particles from the surface as shown in Figure 1.14. Here, these charge patches are created due to the dielectric nature of the material. As a result, deposited charges are concentrated within small patches rather than distributed uniformly. Figure 1.15 demonstrates the mobilization of dust particles under exposure to a) plasma and electron beam, b) electron beam, and c) UV irradiation. They have derived the maximum lofting height and initial vertical speed of the lofted dust from the combined frame photographs taken from the high-speed video camera. Based on that, they have determined the charge of the lofted dust. In their later experiments, they have demonstrated that under different illumination and plasma

conditions, the lofted dust was noticed to acquire negative charges Schwan et al. (2017). Hood et al. (2018), using the same experimental setup (Wang et al., 2016b), derived the rate of electrostatic dust lofting. Their measurement indicated that the electrostatic dust lofting rate is time-dependent, initially increasing before decreasing. The decrease is attributed to fewer microcavities and the removal of loose upper layers, while deeper layers are denser and exhibit stronger van der Waals forces. Additionally, Carroll et al. (2020) established a relationship between dust size and its initial lofting velocity using PCM results. In their experiments, the dust particles are observed to accumulate a significant net negative charge. Consequently, detached charged dust particles have less likelihood of undergoing periodic hopping trajectories within the photoelectron sheath (Yeo et al., 2021). However, the periodic hopping dust trajectories were widely predicted in various studies (Nitter et al., 1998; Wang et al., 2008; Poppe and Horányi, 2010; Li et al., 2016; Popel et al., 2022). They also examined how a magnetic field influences dust mobilization. They found that the magnetic field affects the movement of electrons and the processes of emission and reabsorption within micro-cavities and on dusty surfaces. This interaction leads to the formation of both active and inactive regions of dust mobilization (Yeo et al., 2022). Using the same experimental setup, Opp et al. (2024) demonstrated electrostatic dust sorting, which can alter the reflectance spectra of dusty surfaces. This effect may facilitate the global and local resurfacing of both small and large airless bodies. Further, using the concept of PCM, they have introduced dust mitigation technology and demonstrated that electron bombardment can remove dust particles from various surfaces Farr et al. (2020, 2021, 2022). Additionally, this concept was utilized to develop the Electrostatic Dust Analyzer (EDA) for upcoming lunar missions. The EDA will measure the charge, velocity, mass (size), and flux of dust that is electrostatically lofted on the lunar surface (Wang et al., 2024).

In their recent work (Pagán Muñoz et al., 2024), they extended PCM for single particles (PCM-SP) and conducted a comparative experimental investigation of electrostatic dust lofting for piled dust and isolated dust, focusing on spherical and jagged-shaped dust structures (Pagán Muñoz et al., 2025). This series of experiments has been carried out in the laboratory plasma environment. The plasma conditions in the lunar environment are considerably tenuous compared to those in a typical laboratory framework. Therefore, accumulating enough charge to detach dust particles may require a prolonged duration in space conditions. Moreover, under photo-illumination, the experiment suggests the requirement of significantly high-energy photoelectrons to accumulate enough charge for

dust detachment. Although solar soft X-ray radiation may create such photoelectrons under lunar conditions (Rennilson and Criswell, 1974), significant photon flux and quantum yield in the UV region yield UV-induced photoemission as the dominant source for the lunar surface charging over sunlit locations. Furthermore, as mentioned previously, all experiments conducted by Wang et al.'s group show that dust particles accumulate a significant net negative charge during detachment. In contrast, the most recent experiment by Pacaud et al. (2025) reported that the charges on the dust lying on the surface can be both positive and negative under direct exposure to VUV photons. These facts emphasize a critical need for further investigation into electrostatic dust detachment.

Apart from the investigation related to dust transport, Dove et al. (2012) carried out an experimental investigation of photoelectron sheath formation above a large Zr surface illuminated by a 172 nm photon lamp. They have used a Langmuir probe to determine the density profiles and compared their results with a 1D PIC code of Poppe and Horányi (2010). Thereafter, Wang et al. (2016a) experimentally demonstrated the sheath formation in the presence of Secondary Electron Emission (SEE). Experimentally, they have shown the possibility of three kinds of sheaths, viz., (i) Classical Debye type sheath with negative surface potential, (ii) Inverse sheath with positive surface potential, and (iii) Non-monotonic sheath with potential minima away from the solid surface. These experimental studies of sheath formation hold significant importance from both a scientific and a mission perspective. Furthermore, Dove et al. (2018) experimentally demonstrated that photoemission current above the lunar surface may reduce as the surface becomes rougher, which is likely due to the re-absorption of emitted photoelectrons at other locations on the surface. This study highlighted that the regional nature of the porosity/roughness properties of the regolith layer is a significant factor affecting the span and characteristics of the lunar photoelectron sheath. Wang et al. (2019) presented laboratory results showing that the plasma sheath structure inside a crater strongly depends on the ratio of the crater radius to the ambient plasma Debye length. Via this experiment, they have highlighted the complexity in the analytical formulation of crater charging exposed to plasma and radiation.

The experimental results strongly indicate the presence of a non-neutral space charge region (sheath) surrounding airless planetary bodies that are exposed to plasma and radiation. This intricate structure is influenced not only by plasma parameters but also by a variety of surface characteristics. Therefore, it is essential to establish a comprehensive theoretical, analytical, and computational framework to deepen our understand-

ing of the plasma environments around airless planetary bodies.

1.2 Research Gap and Thesis Objectives

As mentioned earlier, this thesis primarily focuses on lunar surface charging, sheath formation, and the subsequent charging and dynamics of dust. After an extensive review of the existing research on this topic, the research gaps and unresolved issues have been addressed in this section.

As discussed, the sheath is a non-neutral space charge region above the charged surface, which screens the effect of the surface potential. The sheath possesses inherent electric potential and field structures that are physically characterized by Poisson's equation. It influences the behavior of electrostatically charged dust particles within the sheath through the combined effects of electrostatic forces and gravity. Accounting for the large curvature of the Moon, any given location may be considered as of planar geometry, hence, Poisson's equation can be written as

$$\frac{d^2V}{dx^2} = -\frac{e}{\epsilon_0}\left[n_{\mathrm{si}} - n_{\mathrm{se}} - n_{\mathrm{pe}}\right], \tag{1.5}$$

where e is the electronic charge, ϵ_0 is the permittivity in free space, V is the electric potential at altitude x. n_{si}, n_{se}, and n_{pe} are the population densities of solar wind ions, solar wind electrons, and photoelectrons within the sheath, respectively. Poisson's equations connect the electric potential with the charge density. One needs to solve this equation with the boundary conditions $V(x = 0) = V_0$ and $V'(x \to \infty) = 0$ to quantitatively estimate the characteristics of the plasma sheath. To solve Poisson's equation, realistic estimates of number densities are essential. In the dayside of the Moon, photoelectrons dominantly contribute to the sheath formation along with solar wind plasma. As a result, the dayside plasma sheath around the Moon is often regarded as the lunar photoelectron sheath. On the nightside, one has to set the photoelectron density term (n_{pe}) to zero in Eq. 1.5, and sheath formation is governed by the plasma ions and electrons. While deriving the mathematical expressions of the n's in Eq. 1.5, for the photoelectron contribution, one has to incorporate accurate solar spectra and relevant lunar parameters like work function and photoelectric efficiency. For solar wind, it's necessary to include plasma parameters and velocity distribution functions that are consistent with the lunar plasma scenario.

The photoelectron sheath formation is widely discussed in the literature (Singer

and Walker, 1962b,a; Grard and Tunaley, 1971; Guernsey and Fu, 1970; Fu, 1971; Manka, 1973; Walbridge, 1973; Nitter et al., 1998; Stubbs et al., 2007; Wang et al., 2008; Poppe and Horányi, 2010; Poppe, 2011; Popel et al., 2013, 2014; Burinskaya, 2014, 2015; Dyadechkin et al., 2015; Sodha and Mishra, 2014; Li et al., 2016; Mishra and Bhardwaj, 2019; Mishra, 2020b; Zhao et al., 2021). One of the significant analysis of the lunar sheath formation considering incoming and outgoing photoelectrons was presented by Nitter et al. (1998). They suggested the possibility of three kinds of potential structures within the sheath — a schematic is illustrated in Figure 1.9. On the locations with negligible photoemission, the surface exhibits a negative surface potential due to dominant plasma electron collection that altitudinally increases to zero, forming a Type C sheath. This is a normal Debye-type potential structure. For significant photoemission, the surface potential takes positive values and monotonically decreases to zero to form a Type B sheath. The boundary conditions lead to another sheath solution where the surface potential decreases to a negative minimum and then increases to zero, giving rise to a non-monotonic potential structure (Type A sheath). However, their study's applicability is restricted by the inclusion of an isotropic Maxwellian distribution of emitted photoelectrons with an assumed photoelectron temperature.

Nitter et al. (1998)'s work has established a foundational understanding of the plasma sheath surrounding airless planetary bodies. Most studies based on Nitter et al. (1998)'s work, however, assume a preexisting photoelectron cloud above the surface, following a Maxwellian distribution with an arbitrary photoelectron temperature. Though this consideration simplifies the analytical formulation, it ignores the inherent physics and self-consistent mechanism of photoelectron generation from the surface and subsequent sheath formation. In order to find out the realistic estimate of photoelectrons, it is essential to consider significant mechanisms and parameters. First, the photoelectron population is sensitive to the photon flux, and hence, one must incorporate the incoming *Solar UV radiation spectra* adequately in the analysis. This spectrum significantly differs from Planck's distribution primarily because of strong emission lines, such as H-Lyman alpha (Bauer, 1973). The emitted photoelectron retains information about strong emission lines that cannot be identified in the Maxwellian distribution, which averages out these effects. The *regolith work function* is another significant parameter determining the effective solar spectra that give rise to photoemission. The *photoelectric efficiency or quantum yield* χ is another important parameter in determining the photoelectron characteristics. This χ for the lunar surface significantly depends on the energy of the incident photons

and the regolith work function. Feuerbacher et al. (1972) measured the photoelectric yield of the lunar samples and combined this yield value with the relevant solar spectrum; they reported typical photoemission flux from the lunar surface to be 4.5×10^{-6} A m^{-2}.

The considerable shortcomings of earlier studies are that they were restricted to using this photoemission flux measured by Feuerbacher et al. (1972). Because the fluxes of incoming high-energy photons undergo significant variation with solar activity, which might vary the near-surface lunar photoelectron flux and population (Sternovsky et al., 2008; Poppe and Horányi, 2010; Popel et al., 2014). Additionally, with the Maxwellian assumption, previous studies have assigned a photoelectron temperature without proper justification. The photoelectron temperature should be derived self-consistently from the inherent physics of photoelectron emission. In this aspect, the *regolith temperature* and the *velocity distribution of the electrons inside the surface lattice* are significant parameters in characterizing the photoelectron distribution within the sheath. The emitted photoelectrons carry information about these electrons inside the lunar surface lattice. The electrons inside the surface lattice follow Fermi-Dirac (FD) statistics, and the regolith temperature defines the number of electrons available for the emission inside the surface lattice (Fowler, 1967). Lunar Reconnaissance Orbiter (LRO) based Diviner observations suggest the temperature of the surface varies with the lunar latitude within the range 400—150 K over the equator to the terminator (Williams et al., 2017). The latitudinally varying regolith temperature must be considered when estimating the photoemission flux, which has often been overlooked in previous studies. As the lunar surface loses electrons in the process of photoemission, the surface acquires a finite positive charge and potential. It should be noted that the effective photoemission flux strongly depends on the surface potential, as it apparently affects the barrier height required for overcoming by the electrons for its emission from the surface (Fowler, 1929; Sodha, 2014), and hence, the effective photoemission flux.

For solar wind electrons, the Maxwellian nature has been considered in many previous studies; however, a non-Maxwellian Kappa distribution is a more consistent description of solar wind and ambient plasma electrons (Halekas et al., 2008, 2009b; Pierrard and Lazar, 2010), whereas due to low ion thermal speed compared to the solar wind drift speed, the ions population can be consider to be cold (Nitter et al., 1998; Lisin et al., 2014; Dyadechkin et al., 2015).

As discussed earlier, in the absence of photoemission, the nightside lunar surface acquires a negative potential due to dominant plasma electron collection and forms a

Debye sheath. However, high-energy primary electrons impacting the lunar surface can generate secondary electrons (Horányi et al., 1998). These secondary electrons may significantly contribute to the sheath formation around the Moon. Wang et al. (2016a) experimentally demonstrated that significant secondary electron emission can alter the potential structure from a typical Debye sheath. While the effect of secondary electron emission on lunar surface charging has been discussed in the literature (Vaverka et al., 2016), there is a notable lack of analytical investigation regarding secondary electron contributions to sheath formation around the Moon.

From the above discussion, it is evident that the simplified Maxwellian assumption may underestimate or overestimate several features of the lunar photoelectron sheath. It may lead to inconsistent predictions of electric potential and field structures within the photoelectron sheath, which limits their applicability to realistic situations. This concept needs to be refined to enrich the understanding of the photoelectron sheath formation and a more precise estimation of the sheath features. Thus, as the first objective, the thesis focuses on

★ *Improving the understanding of the near-surface plasma environment via*

- Refinement and development of a new sheath model.
- Applying the findings to the exploration schemes.

One direct implication of this sheath structure is the dust dynamics above the lunar surface. Dust particles are ejected in the region just above the lunar surface via various mechanisms, including micrometeorite bombardment and electrostatic ejections. These floating dust particles undergo electrostatic charging under local plasma and solar illumination. These charged particles dynamically evolve within the electrostatically active plasma environment due to the electric field within the sheath and gravity. The charging equation of a dust exposed to the plasma sheath under solar illumination can be written as (Bouchoule, 1999; Shukla and Mamun, 2002; Vladimirov et al., 2005; Tsytovich et al., 2008; Sodha, 2014)

$$\frac{dQ_d}{dt} = I_{\text{ph}} + I_{\text{pe}} + I_{\text{se}} + I_{\text{si}}\,, \tag{1.6}$$

where Q_d is the dust charge. I_{pe}, I_{se}, and I_{si} are the respective charge collection currents associated with sheath photoelectrons, solar wind electrons, and ions to the dust particle. I_{ph} refers to the photoemission current from the dust exposed to solar UV radiation - in dark regions, this term becomes 0. This equation illustrates the time evolution of charge on

the dust particle. As the dust particles migrate within the sheath, the equation of motion of the dust particle can be written as

$$m_d \frac{d^2x}{dt^2} = Q_d(t, x)E(x) - m_d g_m \,, \tag{1.7}$$

where m_d is the mass of the dust particle, g_m is the lunar gravity, $E(x)$ is electric field within the sheath at altitude x. One has to simultaneously solve Eqs. 1.6 and 1.7 to derive the dynamical evolution of the charged dust particles. These equations form a system of coupled differential equations that require three initial conditions for a solution. Since the particle is initially at the surface, one initial condition is at $t = 0$, $x_0 = 0$. Initial speed and initial dust charge, just after the detachment of the dust from the surface, are the other two important initial conditions, and their manifestation with the sheath features determines the dynamics of the detached dust particle over the lunar surface. Based on the initial conditions, the particles may exhibit three possible dynamical features: (i) the dust escapes from the Moon, (ii) the dust returns to the surface, and (iii) the dust floats within the sheath. The characteristics of the sheath, i.e., field strength $\big(E(x)\big)$ and dust charging currents, play a crucial role in determining these dynamical features. It is clear from the discussion that quantitative estimates of dust dynamics depend on sheath features. The consideration of a simplified Maxwellian distribution may overestimate or underestimate dust dynamical characteristics, which limit the applicability of the earlier studies carried out (Nitter et al., 1998; Colwell et al., 2005, 2007, 2009; Stubbs et al., 2007; Wang et al., 2008; Popel et al., 2013, 2014; Li et al., 2016; Zhao et al., 2021). However, the precise determination of the dynamical evolution of the electrostatically active dust is important in the context of the lunar complex dusty plasma environment. These moving charged dusts pose significant challenges to space missions due to their adhesive tendency, which contaminates the instrument and causes problems in their mechanical functions (Zakharov et al., 2020). Additionally, this electrostatic dust transport may contribute to local surface evolution around the Moon and other airless planetary bodies (Colwell et al., 2005, 2007, 2009). Precise estimates are needed in order to have a better understanding of surface-dust-plasma interaction, which is crucial for dust mitigation and conceptualization of space missions.

To quantitatively estimate dust dynamics, previous studies conducted a numerical investigation by varying the initial charge and velocity as independent variables (Nitter and Havnes, 1992; Nitter et al., 1998; Poppe and Horányi, 2010; Li et al., 2016). Currently,

there is no established theoretical basis or experimental measurement that can constrain the initial charge on the dust lying on the lunar surface. On the other hand, the initial velocity of the dust particle depends on the launching mechanism. The dust particles may be launched by several means, viz., micro-meteoroid impact, impact/ tidal shaking, (Richardson et al., 2004; Senshu et al., 2015), and large electrostatic repulsion (Wang et al., 2016b; Rosenfeld and Zakharov, 2020; Mishra, 2020a). The dust particle lying on the charged lunar surface is subjected to gravity, cohesion, and electrostatic forces. In order to detach the dust particles, an upward force is required, which should be greater than the combined forces of cohesion and gravity. Mechanical action created by fast meteoroid impacts can separate dust particles from the lunar surface in the form of impact ejecta (Popel et al., 2016). Meteoroid impact is considered an externally induced source of the dust detachment. Apart from this mechanical effect, the electrostatic effects could be a significant intrinsic source leading to the dust detachment from the lunar surface.

For this, the electrostatic force should exceed the combined forces of cohesion and gravity, so that the dust particle detaches from the surface and lifts above. If one considers the charge on the dusty surface to be uniformly distributed, based on Gauss's law, we may write the dust particle charge at the surface as

$$Q_{ds} = 4\pi\epsilon_0\, a^2\, E_s\,, \tag{1.8}$$

where E_s is the electric field of the lunar surface at the surrounding of the dust particle. Taking $E_s \approx 3.5$ V/m for the nominal photoelectron sheath, for $a < 20\,\mu$m, Eq. 1.8 gives that the charge on the dust particle is smaller than one electronic charge. It suggests that no dust particle could rise off the lunar surface for such a low charge density. Laboratory experiments (Wang et al., 2016b) and space observation (Zook and McCoy, 1991), however, have demonstrated that dust can be lofted under the action of electrostatic processes induced by surface interaction with ambient plasma and solar irradiation. Wang et al. (2016b) explains these observations with a patched-charged model. They suggested the presence of micro-cavities between the dust particles and adjacent surfaces, which could yield a large negative charge and intense particle-particle repulsive forces due to the emission/re-absorption of the photoelectrons and/or secondary electrons. In their experiments, the dust particles are observed to accumulate a significant net negative charge. Consequently, detached charged dust particles have less likelihood to sustain within the sheath with upward-directed near-surface electric field, which is widely pre-

dicted in various studies (Nitter et al., 1998; Wang et al., 2008; Poppe and Horányi, 2010; Li et al., 2016; Popel et al., 2022). The plasma conditions in the lunar environment are considerably tenuous compared to those in a typical laboratory framework. Therefore, accumulating enough charge to detach dust particles may require a prolonged duration in space conditions. Hence, the above discussion warrants a critical need for further investigation into dust dynamics and electrostatic dust detachment. So the next objective of the dissertation is to revise this concept with the modified understanding of the sheath formation and investigate,

★ *The dust dynamics in the near-surface plasma environment on the lunar dust particles via*

- Studying the dynamical evolution of dust particles within the sheath.
- Developing a new conceptual basis of electrostatic dust detachment to constrain the initial conditions.

The studies so far in this thesis provide significant insight into the plasma sheath on the Moon through analytical and numerical simulation tools. This comprehensive understanding encouraged us to investigate the significance of local surface reliefs/ topography, which might significantly affect the local plasma environment and dynamical processes, resulting in complex structures of electric potential and fields both on the surface and within the sheath (Poppe et al., 2012b). In view of the refined understanding of the sheath formation and plasma processes, the last objective of the thesis is to

★ *Study the influence of local reliefs in modifying the local plasma environment.*

In summary, this thesis presents a comprehensive investigation into the structure of the plasma sheath surrounding the Moon, highlighting its significant implications through applying fundamental physics principles and advanced analytical and numerical calculations. The findings are pivotal for enhancing our understanding of lunar environments and serve as a critical foundation for conceptualizing laboratory test experiments and designing innovative experiments with lunar modules for future missions to the Moon.

1.3 Thesis outline

In this thesis,

Chapter 1 introduces the subject and discusses the previous studies starting from 1955, highlighting the gaps and unresolved issues that are addressed in this thesis work.

Chapter 2 presented an analytical formulation of the photoelectron Velocity Distribution Function (VDF) above the sunlit lunar surface. This formulation includes the following particulars: (i) Flare Irradiance Spectral Model 2 (FISM2) data (Chamberlin et al., 2020): It provides high accuracy (0.1 nm) UV/EUV solar spectrum - this, in turn, gives a refined spectral behaviour of the photoelectrons, and that subsequently affects the final VDF. (ii) Photoelectron yield: The measured spectral data of the photoelectric yield of the lunar samples from Willis et al. (1973) is manifested with FISM2 spectral data to characterize the emitted photoelectrons. The spectral data suggests that the significant contribution to the VDF comes from two distinct wavelengths, i.e. from Lyman α (121.57 nm), and near 100 nm spectral spike. (iii) Latitude dependent solar spectrum and (iv) regolith temperature (Mishra and Bhardwaj, 2019): to include effective component of photon flux giving rise to photoemission and defines the number of electrons available for the emission inside the surface lattice (Fowler, 1967) and characterizing the photoelectron distribution. (iv) FD-statistics of the electrons within surface lattice: it is used to derive the photoelectron flux using Fowler's theory of photoelectron emission (Fowler, 1929). The photoelectron VDF has been characterized for both uncharged and charged surfaces in terms of population density - subsequently, the VDF corresponding to free and captured photoelectrons have been derived distinctly. Detailed characterization of allowed velocity regimes of "free" and "captured" photoelectron populations have been performed in terms of surface charge, and solar zenith angle. Photoelectron temperature and mean energies for different photoelectron (free and captured) populations have been derived. A comparison of analytically derived VDF with the experimentally measured distribution (Feuerbacher et al., 1972) has been made. Accounting for these facts, the numerical results demonstrate new findings and have been extensively discussed.

Chapter 3 presented the development of a comprehensive photoelectron sheath model, which includes the following novel aspects discussed in Chapter 2 related to lunar photoelectrons and considers solar wind comprising of cold ions (Nitter et al., 1998; Lisin et al., 2014; Dyadechkin et al., 2015), and Kappa distributed electrons (Pierrard and Lazar, 2010; Kureshi et al., 2020). This model describes the photoelectron sheath and plasma configuration over the sunlit locations on the Moon in terms of altitude and latitude profiles of the inherent electric potential, electric field, and plasma density. In the location with zero/insignificant photoemission close to the terminator or pole, this model shows the ex-

istence of a classical Type C Debye-type potential structure with a negative surface potential that monotonically goes to zero. This model quantifies a Type B sheath with a positive surface potential that monotonically decreases to zero in the photoemission-dominated region. Under certain boundary conditions, the model also gives another solution for the same locations, along with the Type B solution. Here, the surface potential (irrespective of positive or negative) decreases to a negative minimum at some altitude and then increases to zero, giving rise to a non-monotonic Type A potential structure (as shown in Figure 1.9). In this chapter, a comprehensive parametric study has been conducted to examine the dynamic changes in the lunar photoelectron sheath resulting from variations in solar irradiation and surrounding plasma conditions.

Chapter 4 highlights the capability of this model to predict the plasma environment around the Moon. As a case study, the investigation of the electric potential development over the Chandrayaan-3 landing site (Ch3 LS) under the influence of observed solar ultraviolet/extreme-ultraviolet radiation and real plasma parameters measured by THEMIS has been carried out. A dynamic variation of the potential structure around the sunlit landing site has been observed through the analysis. The non-monotonic features around Ch3 LS derived from Earth's Plasma Sheet plasma parameter are in good agreement with the Lunar Prospector measurements (Halekas et al., 2008).

Chapter 5 highlights the possibility of secondary electron-dominated inverse sheath formation in the nightside of the Moon. In the lunar nightside, with significant Secondary Electron Emission (SEE) yield, highly energetic primary plasma electrons can generate significant SEE, which can invert the surface potential from negative to positive and can create an inverse sheath in the vicinity of the nightside lunar surface. In this chapter, we assessed the plasma temperature regime for the feasibility of the inverse sheath.

Chapter 6 revisits the dust dynamics over lunar regolith using the model developed, which is extensively discussed in the previous chapters. The investigation reveals that the presumption of Maxwellian photoelectrons in previous analyses underestimates and overestimates various results. The estimates of dynamical evolution from this study suggest the existence of a narrow parametric regime corresponding to the periodic hopping trajectory of the dust particle over the lunar surface. In other cases, the dust particles are shown to re-impact the surface after a single ballistic hop. This study further identifies that the discrete charging of the dust could be crucial in determining the dust dynamics, particularly in the tenuous plasmas. The analysis of the discrete dust charging model reveals significant discrepancies with the continuous dust charging model and suggests a

lower likelihood of static dust levitation in the lunar environment. The present study is important for unraveling the fundamental processes governing surface evolution on the Moon and other airless bodies throughout the Solar System.

Chapter 7 addressed and proposed a solution to the fundamental problem and physical mechanism of dust detachment from the lunar surface. The electrostatic charge fluctuation at the microscopic scale has been conceptualized, which could create a sufficient electric field and Coulomb force to overcome the dust-surface adhesive force and detach the dust particles. A Markovian process is manifested with a Monte Carlo scheme to simulate the concept. The simulation establishes the random generation and annihilation of fluctuating charged microscopic spots. The results demonstrate the existence of microscopic charged spots, capable of inducing sufficient electric field and Coulomb force of the order of a few MV/m and 10s of pN, respectively, which creates favorable conditions for lunar dust detachment. This concept fits the gap and puts forward a consistent mechanism describing dust dynamics and the generation of a dusty plasma scenario over the Moon.

Chapter 8 briefly discusses the effect of surface topography on the plasma sheath around the Moon. The potential structure of a simple crater-like depression is derived by varying local illumination angles within the crater floor. The geometrical calculations suggest that the results should remain intact for any size of the simple crater with the same depth-to-diameter h/D ratio. The results are expected to be valid for surface features larger than the lunar photoelectron sheath thickness. For features equal to or larger than the local plasma Debye length, horizontal effects may arise, making it impossible to solve Poisson's equation in one dimension. For this case, further investigation was carried out using an open-source 3D modeling tool named Spacecraft Plasma Interaction Software (SPIS). Preliminary SPIS results highlighted the importance of the local illumination angle and derived various features of the non-monotonic sheath as predicted by the analytical results. Also, SPIS considers vertical and horizontal variations in the simulations and 3D variation of potential and density profiles of various sheath populations. Although SPIS presumes Maxwellian photoelectrons, the capability of SPIS to study the lunar plasma environment can be extensively explored and will be taken up in the future.

Finally, **Chapter 9** summarizes, concludes the thesis, and discusses the future scopes.

Chapter 2

Photoelectrons

2.1 Introduction

Photoelectrons are an integral part of the near-surface space charge region and play a significant role in determining the complex plasma environment around the sunlit Moon (Nitter et al., 1998; Stubbs et al., 2007; Poppe and Horányi, 2010; Popel et al., 2013, 2014; Sodha and Mishra, 2014; Mishra and Bhardwaj, 2019; Zhao et al., 2021). This region is called the Lunar photoelectron sheath, as it is dominated by photoelectrons. The photoelectron sheath exhibits an inherent electric field that can levitate electrically charged small dust particles (Nitter et al., 1998; Poppe and Horányi, 2010; Popel et al., 2013; Mishra and Bhardwaj, 2019). To realistically quantify the plasma environment, accurate estimation of photoelectron characteristics is essential. Hence, the determination of the velocity distribution function (VDF) of the lunar photoelectrons is most important.

The cloud formation and photoelectron distribution from the lunar fines returned during the Apollo missions have been experimentally studied by Feuerbacher et al. (1972); Willis et al. (1973). To explain the experimental results and gain physics insight, several theoretical investigations were performed. In this context, the majority of the previous analyses describing photoelectron cloud (sheath) assume a predefined velocity distribution of the constituent photoelectrons as of Maxwellian nature (Manka, 1973; Nitter et al., 1998; Stubbs et al., 2007; Sternovsky et al., 2008; Popel et al., 2013; Burinskaya, 2014, 2015; Dyadechkin et al., 2015; Li et al., 2016; Zhao et al., 2021). Moreover, while assuming the Maxwellian distribution, they also assumed photoelectron temperature without any judicious justification. Though Walbridge (1973) used different photoelectron distributions but did not give a mathematical derivation of the algebraic form of the distribution func-

tion - the same expression was later used by Popel et al. (2014) to derive the sheath features. Apart from that, Senshu et al. (2015) has developed an angle-resolved velocity distribution function of photoelectrons by scanning and digitizing the laboratory-measured VDF of Feuerbacher et al. (1972). However, in all the discussed cases, the self-consistent nature of the photoelectron generation from the lunar surface has been ignored.

To get an adequate estimate of photoelectrons, it is necessary to include all necessary parameters. First, the photoelectron population is sensitive to photon flux. Thus, the incoming Solar UV radiation spectrum must be effectively incorporated. This spectrum departs greatly from Planck's distribution, owing to strong emission lines such as H-Lyman alpha (Bauer, 1973). The emitted photoelectron contains information on strong emission lines that cannot be recognised in the Maxwellian distribution, which averages these effects. The regolith work function is another important factor in defining the effective solar spectra that produce photoemission. The photoelectric efficiency χ is also a key parameter in defining photoelectron properties. The χ significantly depends on the energy of the incident photons and the regolith work function as experimentally measured by Feuerbacher et al. (1972) from lunar samples. So, it is noticed that a set of simplifications is used in these earlier analyses, which not only limits their applicability to real scenarios but also constrains the physics insight of the problem.

Mishra and co-workers (Sodha and Mishra, 2014; Mishra and Misra, 2018; Mishra and Bhardwaj, 2019; Mishra, 2020b) attempted to overcome these simplifications by including Fowler's theory of photoemission. It is important to note that Feuerbacher et al. (1972) measured the work function of the lunar sample using the Fowler method (Fowler, 1931). Their study highlighted the applicability of Fowler's theory of photoemission for the Moon as early as the 1970s. Fowler's theory of photoemission gives a self-consistent generation of photoemission from the solid body exposed to photons, considering the FD-statistics of the lattice electrons. Mishra and co-workers adapted this approach to the lunar condition and incorporated adequate regolith temperature in their study. Adapting Fowler's theory, there is considerable scope to integrate all relevant parameters related to photoemission, which could significantly improve the characteristics and understanding of the photoelectron cloud compared to estimates derived from the earlier simplified approaches. This chapter discusses the new velocity distribution function of lunar photoelectrons.

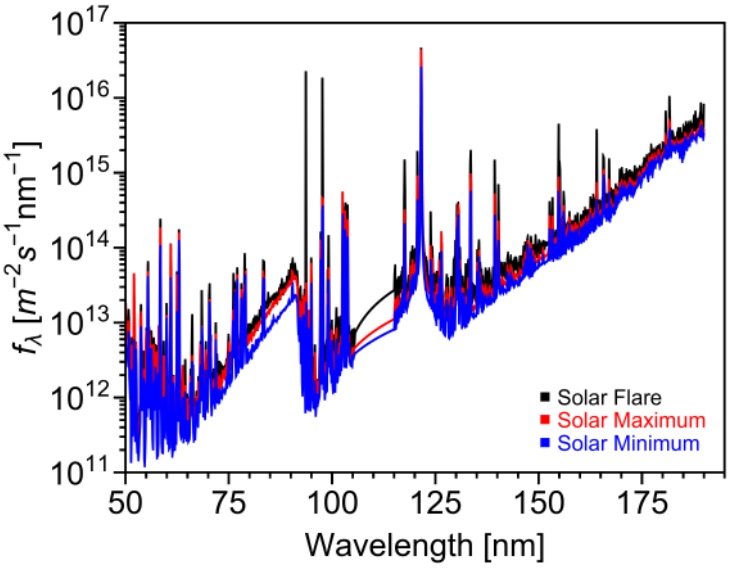

Figure 2.1: Typical EUV emission spectrum with at 1 AU from the Flare Irradiance Spectral Model 2 (FISM2) (Chamberlin et al., 2020).

2.2 Significant parameters characterizing photoelectrons

The photoemission occurs as the solar radiation interacts with the lunar surface - the high-energy photons overcoming the regolith work function generate photoelectrons. The photoemission flux depends on the radiation spectrum and material properties (photoelectric yield, work function), along with the surface temperature. This section discusses the required parameters for characterizing the lunar photoelectrons.

2.2.1 Work function

The work function (W_f) is the minimum energy photon required to remove an electron from the material. It is an important parameter that defines the energy range of photons capable of emitting photoelectrons. The work function of the regolith ranges from 4 to 6 eV. (Grobman and Blank, 1969). The lower values are considered for hydrogen-rich areas of the lunar surface, and the higher values are considered to be for lunar regolith areas (Popel et al., 2013). In this thesis, following the measurement of Feuerbacher et al. (1972), $W_f = 5$ eV is used throughout the calculations.

2.2.2 Solar spectrum

In order to address the photoelectron population, one needs to have information about solar radiation spectra falling on the given location. Theoretically, it can be estimated by

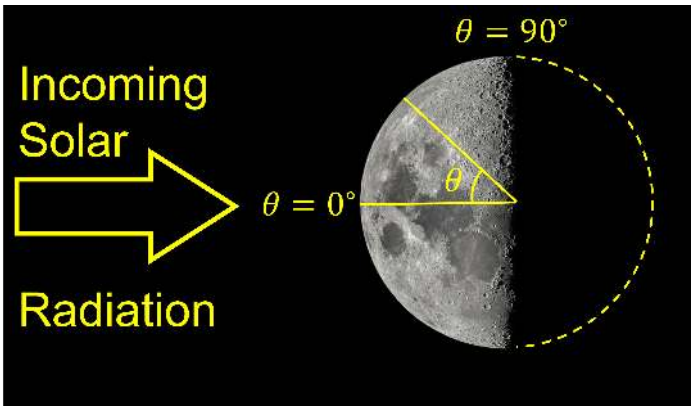

Figure 2.2: Schematic illustration showing lunar surface illuminated by solar radiation.

considering the sun as a black body, radiating at a temperature of 5800 K, and following Planck's law of electromagnetic radiation (Bauer, 1973). The observed solar spectra match quite well for the visible and infrared regions; however, they differ significantly from Planck's distribution in the UV/EUV region. This divergence arises primarily because of strong emission lines, such as H-Lyman alpha (Bauer, 1973). Note, due to high regolith work function (between 4 - 6 eV, (Grobman and Blank, 1969)), mainly high energy UV/EUV photons give rise to significant photoemission from the lunar surface. Hence, throughout this thesis, the solar radiation spectra obtained from the Flare Irradiance Spectral Model 2 (FISM2), i.e., illustrated in Fig. 2.1, are used. FISM2 is an empirical Solar Spectral Irradiance model that provides solar spectra from 0.01—190 nm at 0.1 nm spectral bins. It is based on the measurements of various space-based instrument datasets (e.g., SORCE XPS L4, SDO EVE, and SORCE SOLSTICE). Plenty of high-energy spikes with significant photon flux are noticed in the observed spectrum. Considering the high work function of regolith, these high-energy photons might significantly contribute to the photoelectron generation/ population over the lunar surface. As shown in Fig. 2.1, the fluxes of incoming high-energy photons undergo significant variation with solar activity, which might vary the near-surface lunar photoelectron population.

Due to the unidirectional (parallel beam) nature of the incoming solar photon flux, only one hemisphere is illuminated by the sunlight. Since the perpendicular component of the incoming photon flux is responsible for photoemission, the maximum effective photon flux causes a photoemission incident at the equator $(\theta = 0^\circ)$ (see Fig. 2.2). Due to the curvature of the Moon, the effective photon flux at any latitude θ is reduced by a factor of $\cos\theta$ from the same at the equator. At the terminator (the day-night boundary) where $\theta = 90^\circ$, the effective photon flux responsible for photoemission becomes zero.

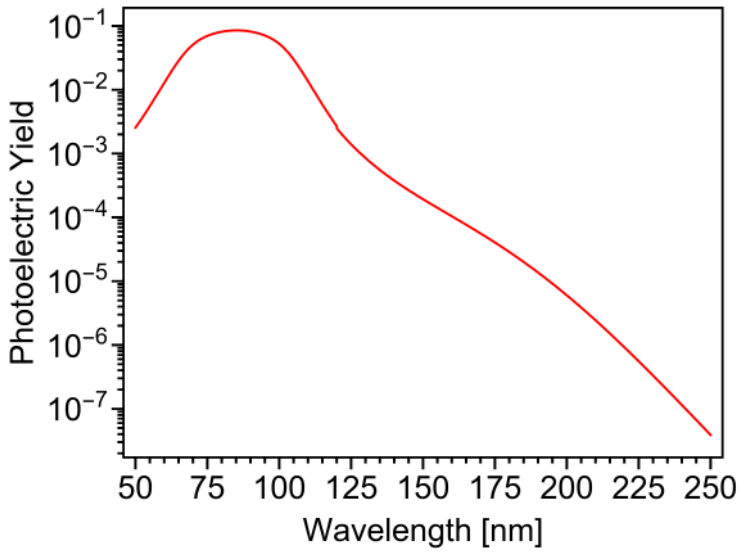

Figure 2.3: The photoelectric yield measured by Willis et al. (1973).

2.2.3 Photoelectric efficiency

The photoelectric efficiency or quantum yield χ is another important parameter in determining the photoelectron characteristics. It is the ratio of the number of emitted electrons to the number of incident photons. This χ for the lunar surface significantly depends on the energy of the incident photons and the regolith work function. χ may also vary over an order of magnitude at a given photon energy, depending on the surface material (Feuerbacher et al., 1972), the roughness of the surface (Feuerbacher et al., 1972; Grard, 1997; Dove et al., 2018), etc. Dove et al. (2018) experimentally show that photoemission current above the lunar surface may reduce as the surface becomes rougher, which is likely due to the re-absorption of emitted photoelectrons to the other locations on the surface. So, increasing surface roughness reduces the photoelectric efficiency of the material. However, the degree of reduction should be different for different photon energies. Therefore, the regional nature of the porosity/ roughness properties of the regolith layer is a significant factor affecting the photoelectron efficiency, and hence, the distribution of photoelectrons. The theoretical formulation of Sodha and Mishra (2014) suggests that χ might also depend on regolith temperature. There are two widely used spectral variations of $\chi(\lambda)$ available in the literature. One is reported by Walbridge (1973), which increases linearly with photon energy up to 9 eV and takes a constant value (0.2) for high-energy photon radiation. This has been used by Popel's group (Popel et al., 2013, 2014) in determining the lunar plasma environment. Another variant of $\chi(\lambda)$ is based on the spectral

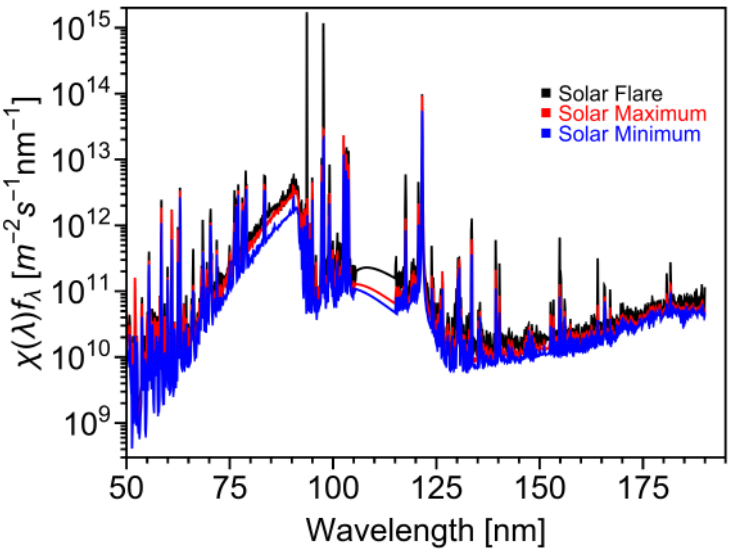

Figure 2.4: Spectral dependence of function (χf_λ) representing effective solar spectrum causing photoemission.

measurements from the lunar soil samples returned by the Apollo 14 and 15 missions (Feuerbacher et al., 1972; Willis et al., 1973). Here, they obtained the regolith work function to be 5 eV and χ takes an optimum value of around 14 eV (90 nm) photon radiation. So, the yield provided by Willis et al. (1973) carries information about the surface material properties, surface roughness properties, etc, of the lunar surface. Considering this experimental validation, we have based our calculation corresponding to the quantum yield given by Willis et al. (1973). This $\chi(\lambda)$ and corresponding photoemission current ($4.5\,\mu\mathrm{Am}^{-2}$) have been widely used in the earlier literature (Nitter et al., 1998; Sternovsky et al., 2008; Poppe and Horányi, 2010). Mishra (2020b) has given an approximated empirical fit of Willis et al. (1973)'s $\chi(\lambda)$ as

$$\begin{aligned}\chi(\lambda) = 10^{-7} \exp\big[&138.207 - 3.072\lambda + 2.906\times10^{-2}\lambda^2 \\ &- 1.361\times10^{-4}\lambda^3 + 3.092\times10^{-7}\lambda^4 - 2.751\times10^{-10}\lambda^5\big] \\ &\big(\text{for}\quad \lambda \geq 120\,\text{nm}\big)\,,\end{aligned} \tag{2.1}$$

$$\begin{aligned}\chi(\lambda) = 10^{-3}\left[0.202 + \left(\frac{85.114}{1 + 1.91\times10^{-3}l_m^2 + 5.93\times10^{-7}l_m^4 + 1.69\times10^{-8}l_m^6}\right)\right] \\ \big(\text{for}\quad 50\,\text{nm} < \lambda < 120\,\text{nm}\big)\end{aligned} \tag{2.2}$$

where $l_m = \lambda - 85.172$. These equations have been used throughout the thesis, which reproduces several features of the quantum yield measured by Willis et al. (1973) (see

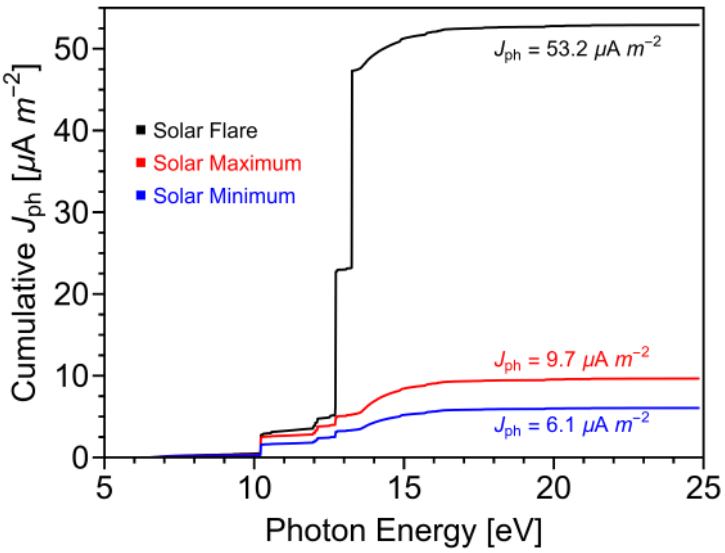

Figure 2.5: The cumulative photoelectron current from the lunar surface.

Fig. 2.3). The observed spectral dependence of χ (Willis et al., 1973) is coupled with the observed solar photon flux and graphically presented in Figure 2.4 - essentially, it depicts the spectral variation of the photoemission flux from the uncharged lunar surface. The figure indicates that not only Lyman - α, but also other high-energy photons might significantly contribute to the photoemission from the lunar surface.

The expression of photoemission current from the uncharged lunar surface is given by

$$J_{ph} = \cos\theta \int_{\lambda_{\min}}^{\lambda_{\max}} \chi(\lambda)\, f_\lambda\, d\lambda = \cos\theta \int_{E_{\lambda_{\max}}}^{E_{\lambda_{\min}}} \chi(E_\lambda)\, f_\lambda\, \frac{d\lambda}{dE_\lambda}\, dE_\lambda\,, \tag{2.3}$$

where E_λ is the energy of the photons with wavelength λ and f_λ is the photon flux associated with the observed solar spectrum. θ is the subsolar angle, $\theta = 0$ refers to the subsolar point while $\theta = \pi/2$ corresponds to the pole/terminator. $\lambda_{\min}$ is the minimum wavelength available in the FISM2 data and $\lambda_{\max}$ is the wavelength corresponding to the regolith work function. Any photon with energy less than the regolith work function is ineffective for photoemission.

Fig. 2.5 shows cumulative photoelectron flux from the uncharged lunar surface at $\theta = 0$ calculated using Eq. 2.3. The regolith work function is taken to be 5 eV, and $\chi(\lambda)$ reported by Willis et al. (1973) has been used for calculations. The total photoemission flux using FISM2 data is found to be 53.2 μAm^{-2}, 9.7 μAm^{-2}, and 6.1 μAm^{-2} for Solar flare, maxima and minima respectively which are different than 4.5 μAm^{-2} measured by

Willis et al. (1973). This signifies that the photoemission current significantly varies with the solar activity, as concluded by Sternovsky et al. (2008). From Fig. 2.5, it is observed that the significant photoemission comes from the photon energy ranges between 10—15 eV. Therefore, since the lunar surface is illuminated by photons spanning a broad spectral range, it is expected that the energy or velocity of the emitted photoelectrons should exhibit a distribution.

2.2.4 Regolith temperature

The temperature of the lunar surface is another important factor determining the electron population available for photoemission within the lattice (Fowler, 1967). This is primarily determined by a dynamic balance between the power loss from thermal radiation and emission cooling, as well as the absorbed solar radiation. Lunar Reconnaissance Orbiter based Diviner Lunar Radiometer Experiment lunar surface temperature varies within the range 400—150 K over the equator $(\theta = 0^\circ)$ to the terminator $(\theta = 90^\circ)$ (Williams et al., 2017). The surface temperature's latitude dependence has also been taken into account in this analysis - for simplicity, an empirical relation given by Mishra and Bhardwaj (2019) is used. Mathematically it may be expressed as $T_0(\theta) = T_0(\theta = 0)\left[1 - \left(\frac{5}{4\pi}\right)\theta\right]$. Here θ is in radian.

Coupling these parameters, the detailed characterization of lunar photoelectrons has been undertaken in further sections. Next, the photoelectron velocity distribution derivation over the sunlit lunar surface is discussed.

2.3 Photoelectron Distribution Function

2.3.1 Uncharged Lunar Surface

Following free electron theory, the number of electrons per unit volume having momenta between $\vec{p}$ and $\vec{p} + d\vec{p}$ within a solid is given by (Seitz (1940); Sodha and Mishra (2014))

$$d^3 n_e = \left(\frac{2}{h^3}\right) F_D \left[\frac{|\vec{p}|^2}{2m_e k T_0} - \frac{E_F}{kT_0}\right] dp_x\, dp_y\, dp_z\,, \tag{2.4}$$

where $F_D(\eta) = (1 + \exp\eta)^{-1}$ is the Fermi Dirac distribution function and E_F is the Fermi energy. h, k, and m_e are Planck's constant, Boltzmann's constant, and the electronic mass, respectively. The number of electrons per unit area, hitting the surface $(x = 0)$ from inside

per unit time

$$d^3n_1 = \left(\frac{2}{h^3}\right)\left(\frac{p_x}{m_e}\right) F_D\left[\frac{|\,\vec{p}\,|^2}{2m_e kT_0} - \frac{E_F}{kT_0}\right] dp_x\, dp_y\, dp_z\,. \tag{2.5}$$

Now Fowler's theory says that if $\Lambda(E_\lambda)$ photons with wavelength λ per unit area per unit time incident on the surface, the probability of absorbing the photon by the electron hitting the surface is $\psi(E_\lambda)\Lambda(E_\lambda)$. Here $\psi(E_\lambda)$ is the probability of absorbing a photon of energy E_λ by an electron. After that, crossing the surface barrier height, W_a, the momentum $\vec{p}\,'$ of the photoelectrons will be given by the relation

$$\frac{p_x'^2}{2m_e} = \frac{p_x^2}{2m_e} + \frac{hc}{\lambda} - W_a\,, \tag{2.6}$$

$$p_y' = p_y\,, \tag{2.7}$$

$$p_z' = p_z\,. \tag{2.8}$$

Substituting $\vec{p}$ by $\vec{p}\,'$ in Eq. (2.5) we get the number of photoelectrons emitted per unit area, per unit time, just outside the surface

$$d^3n_{ph} = \psi(E_\lambda)\Lambda(E_\lambda)\left(\frac{2}{h^3}\right)\left(\frac{p_x'}{m_e}\right) F_D\left[\frac{|\,\vec{p}\,'\,|^2}{2m_e kT_0} - \xi_\lambda\right] dp_x'\, dp_y'\, dp_z'\,, \tag{2.9}$$

where $\xi_\lambda = (hc/\lambda - W_f)/kT_0$, and $W_f = (W_a - E_F)$. Now, after the following substitutions $\varepsilon_x = \dfrac{p_x'^2}{2m_e kT_0}$, $\varepsilon_y = \dfrac{p_y'^2}{2m_e kT_0}$, $\varepsilon_z = \dfrac{p_z'^2}{2m_e kT_0}$, and $\varepsilon_t = \varepsilon_y + \varepsilon_z$, Eq. (2.9) will become

$$d^2n_{ph} = \left(\frac{4\pi m_e k^2 T_0^2}{h^3}\right)\psi(E_\lambda)\Lambda(E_\lambda) F_D\left[\varepsilon_x + \varepsilon_t - \xi_\lambda\right] d\varepsilon_x\, d\varepsilon_t\,. \tag{2.10}$$

Now integrating Eq. (2.10) over ε_t from 0 to ∞, we get

$$dn_{ph} = \left(\frac{4\pi m_e k^2 T_0^2}{h^3}\right)\psi(E_\lambda)\Lambda(E_\lambda)\ln\left[1 + \exp(\xi_\lambda - \varepsilon_x)\right] d\varepsilon_x\,. \tag{2.11}$$

Integrating Eq. (2.11) over ε_x from 0 to ∞, we get the outward flux of electrons from the particle surface ($x = 0$):

$$J_{ph} = \left(\frac{4\pi m_e k^2 T_0^2}{h^3}\right)\psi(E_\lambda)\Lambda(E_\lambda)\Phi(\xi_\lambda) = \chi(E_\lambda)\Lambda(E_\lambda)\,, \tag{2.12}$$

where $\chi(E_\lambda)$ is the photoelectric efficiency of the surface and $\Phi(\xi_\lambda) = \displaystyle\int_0^{\exp\xi_\lambda} \left[\ln(1+\eta)/\eta\right] d\eta$. Utilizing Eq. (2.12), Eq. (2.10) can be written as

$$d^2n_{ph} = \left(\frac{\chi(E_\lambda)\Lambda(E_\lambda)}{\Phi(\xi_\lambda)}\right) F_D\left[\varepsilon_x + \varepsilon_t - \xi_\lambda\right] d\varepsilon_x\, d\varepsilon_t\,. \tag{2.13}$$

From this, the photoelectron density above the lunar surface between ε_x and $\varepsilon_x + d\varepsilon_x$ and ε_t and $\varepsilon_t + d\varepsilon_t$ can be written as

$$d^2 n_{pe} = \left(\frac{m_e}{2kT_0}\right)^{1/2} \left(\frac{\chi(E_\lambda)\Lambda(E_\lambda)}{\Phi(\xi_\lambda)}\right) \varepsilon_x^{-1/2} F_D\left[\varepsilon_x + \varepsilon_t - \xi_\lambda\right] d\varepsilon_x \, d\varepsilon_t \,. \tag{2.14}$$

The following equations are derived for a material with work function W_f and temperature T_0, exposed to a monochromatic photon flux $\Lambda(E_\lambda)$. Extending it to the lunar surface exposed to solar radiation, the number density of the emitted photoelectrons within an elementary energy space lying between ε_x and $\varepsilon_x + d\varepsilon_x$, and ε_t and $\varepsilon_t + d\varepsilon_t$, respectively, near the surface at latitude θ, can be written as

$$d^2 n_{pe} = \left(\frac{m_e}{2kT_0}\right)^{1/2} \cos\theta \int_{\lambda_{\min}}^{\lambda_{\max}} \left[\frac{\chi(\lambda) f_\lambda \, d\lambda}{\Phi(\xi_\lambda)}\right] \varepsilon_x^{-1/2} F_D[\varepsilon_x + \varepsilon_t - \xi_\lambda] d\varepsilon_x \, d\varepsilon_t \,, \tag{2.15}$$

$\lambda_{\min}$ is the minimum wavelength available in the FISM2 data and $\lambda_{\max} = hc/W_f$. In cartesian coordinates Eq. 2.15 can be written as

$$d^3 n_{pe} = \frac{1}{2\pi} \left(\frac{m_e}{kT_0}\right)^2 \cos\theta \int_{\lambda_{\min}}^{\lambda_{\max}} \left[\frac{\chi(\lambda) f_\lambda \, d\lambda}{\Phi(\xi_\lambda)}\right] F_D \left[\frac{m_e \mathbf{u}^2}{2kT_0} - \xi_\lambda\right] d^3\mathbf{u} \,, \tag{2.16}$$

where $\mathbf{u}$ refers to the photoelectron velocity. The total number density of photoelectrons near the uncharged lunar surface can be written as

$$n_{p0} = \int_0^\infty \int_{-\infty}^\infty \int_{-\infty}^\infty d^3 n_{pe}. \tag{2.17}$$

In spherical polar coordinates with azimuthal symmetry,

$$d^3\mathbf{u} = 2\pi u^2 \sin\phi \, du \, d\phi \,, \tag{2.18}$$

where ϕ is the angle between the electron velocity vector and the x axis (axis perpendicular to the surface). Eq. 2.16 thus can be re-written as

$$d^2 n_{pe} = \left(\frac{m_e}{kT_0}\right)^2 \cos\theta \int_{\lambda_{\min}}^{\lambda_{\max}} \left[\frac{\chi(\lambda) f_\lambda \, d\lambda}{\Phi(\xi_\lambda)}\right] u^2 \, F_D \left[\frac{m_e u^2}{2kT_0} - \xi_\lambda\right] du \, \sin\phi \, d\phi \,. \tag{2.19}$$

Integrating Eq. 2.19 with ϕ from 0 to $\pi/2$, we get

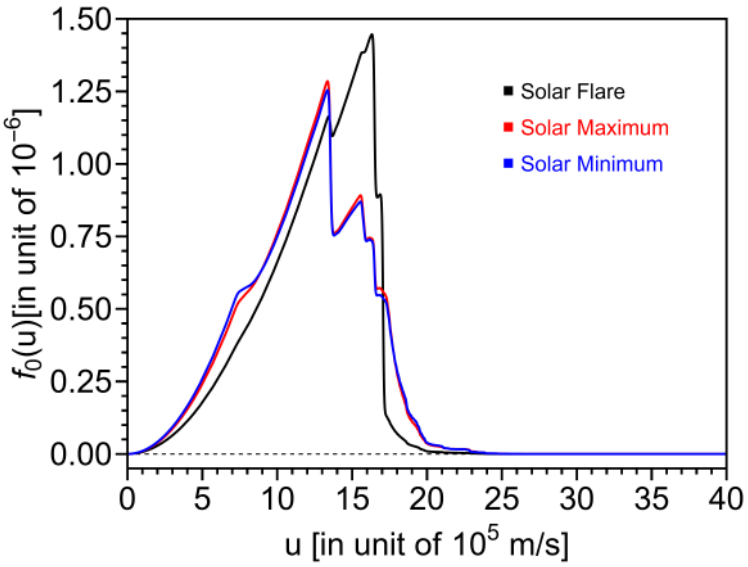

Figure 2.6: The variability of the photoelectron velocity distribution function (VDF) in the proximity of the lunar surface corresponds to the observed solar activity from FISM2.

$$dn_{pe} = \left(\frac{m_e}{kT_0}\right)^2 \cos\theta \int_{\lambda_{\min}}^{\lambda_{\max}} \left[\frac{\chi(\lambda) f_\lambda \, d\lambda}{\Phi(\xi_\lambda)}\right] u^2 \, F_D \left[\frac{m_e u^2}{2kT_0} - \xi_\lambda\right] du \,. \tag{2.20}$$

The photoelectron velocity distribution (VDF) function near the uncharged surface can be expressed as

$$f_0(u) = \frac{1}{n_{p0}} \frac{dn_{pe}}{du} \,. \tag{2.21}$$

The expression of photoelectron distribution near the uncharged surface is given in Eq. 2.21, which suggests its dependence on incident solar flux, quantum yield, regolith work function, and regolith temperature. Note, that this expression is normalized to unity. As a result, the distribution function doesn't depend explicitly on θ. However, based on LRO observation, Williams et al. (2017) reports, regolith temperature (T_0) varies between 400 — 150 K from subsolar point to the terminator, which makes f_0 implicitly depend on θ.

The black, red, and blue curves in Fig. 2.6 show the photoelectron distribution for the uncharged surface for solar flare, maxima, and minima, respectively. For solar maxima and minima, the distributions show two distinct peaks around 1.33×10^6 m/s and 1.56×10^6 m/s with corresponding energy around 5 eV and 7 eV, respectively. These are the excess energy of the photoelectron after overcoming the barrier height, i.e., $(E_\lambda - W_f)$, which suggests the dominant contribution comes from Lyman α (121.57 nm), and

	n_{p0} [cm^{-3}]	$< E_m >$ [eV]
Solar Flare	533.66	4.75
Solar Maxima	101.28	4.46
Solar Minima	63.86	4.42

Table 2.1: Number densities and mean energy of photoemitted electrons for solar flare, maxima, and minima.

then from the photons near 100 nm spectral spikes. But for solar flares, the contribution from Lyman α (121.57 nm) is relatively small compared to other peaks near 7 and 7.6 eV. This is due to the significantly increased photon flux observed in the 90 — 100 nm range (refer to Figs. 2.1 and 2.4), which results in a enhance contribution of photoemission flux at the point where the quantum yield of Willis et al. (1973) (shown in Fig. 2.3) attains its peak.

The mean energy associated with the photoemitted electron can be calculated using the derived VDF (Eq. 2.21). Mathematically, it can be expressed as

$$< E_m >= \frac{1}{2} m_e < u^2 > \ . \tag{2.22}$$

Manifesting this expression with Eqs. 2.21, the expressions of $< u^2 >$ of various population can be expressed as

$$< u^2 >= \frac{\int_0^\infty u^2 f_0(u) du}{\int_0^\infty f_0(u) du} \, . \tag{2.23}$$

Table 2.1 shows that the number of photoemitted electrons increases with an increase in photon flux in solar spectra. The mean energy of emitted photoelectrons is slightly higher ($E_{max} - E_{min} = 0.04$ eV) for solar maxima compared to solar minima. But for flare, the mean energy increases ($E_{flare} - E_{max} = 0.29$ eV) toward higher energy due to larger photon fluxes in the higher energies (> 7 eV).

2.3.2 Charged Lunar Surface

In the photoelectron-dominated region of the Moon, the surface acquires a finite electric potential and creates a photoelectron sheath in its vicinity. In the photoemission-dominated region, the literature suggests two types of sheath structures characterized by monotonic (Type B) and non-monotonic (Type A) electric potentials (Nitter et al., 1998; Zhao et al., 2021). In the case of a monotonic sheath structure, the surface acquires a finite positive potential $V_{0,M}$ and monotonically decreases to zero with altitude. For non-

monotonic sheath structures, the surface potential $V_{0,N}$ decreases to negative potential minimum $V_m < 0$ at an altitude x_m and then increases to zero with $V_{0,N} - V_m \geq 0$. In both cases, an upward-directed electric field exists near the surface, which acts as a potential well with altitude and captures the emitted photoelectrons. Hence, the emitted photoelectrons have to overcome a potential barrier V_s to escape to infinity. Here, $V_s = V_{0,M}$ for monotonic and $V_{0,N} - V_m$ for non-monotic potential structure. These sheath structures suggest two kinds of electron populations within the sheath, viz., (i) the emitted photoelectrons that escape to infinity, those are referred to as "free photoelectrons," (n_{pef}), and (ii) the photoelectrons which do not have sufficient energy to overcome the Coulomb potential well and hence captured within the sheath, are referred as "captured photoelectrons" (n_{pec}). From Nitter et al. (1998) their population density can be written as

$$n_{\text{pef}} = \int_{u_m}^{\infty} \int_{-\infty}^{\infty} \int_{-\infty}^{\infty} d^3 n_{pe} \,, \tag{2.24}$$

and

$$n_{\text{pec}} = 2 \int_{0}^{u_m} \int_{-\infty}^{\infty} \int_{-\infty}^{\infty} d^3 n_{pe} \,, \tag{2.25}$$

where $u_m = \left[2eV_s/m_e\right]^{1/2}$ i.e. $u_m = \left[2eV_{0,M}/m_e\right]^{1/2}$ for monotonic (Type B) and $\left[2e(V_{0,N} - V_m)/m_e\right]^{1/2}$ for non-monotonic (Type A) case. u_m is minimum speed in the x direction to overcome the potential barrier V_s and escape to infinity. Factor 2 in Eq. 2.25 appears because the incoming and outgoing photoelectrons contribute to the captured term at any layer. This is discussed in detail in Chapter 3. So we can write,

$$n_{p0} = n_{\text{pef}} + n_{\text{pec}}/2 \,. \tag{2.26}$$

The expressions for $d^3 n_{pe}$ in Eqs. 2.24 and 2.25 can easily be transformed into spherical polar coordinate by applying appropriate limits over u and ϕ. For instance, *free photoelectrons* have velocities between u_m and ∞. However, the photoelectrons with $u_x = u\cos\phi < u_m$ do not contribute to the free photoelectron term. Hence, the limit of ϕ can be given by from 0 to $\phi_m = \cos^{-1}(u_m/u)$. Integrating Eq. 2.19 with ϕ from 0 to $\phi_m = \cos^{-1}(u_m/u)$, one gets

$$dn_{pef} = \left(\frac{m_e}{kT_0}\right)^2 \cos\theta \int_{\lambda_{\min}}^{\lambda_{\max}} \left[\frac{\chi(\lambda) f_\lambda \, d\lambda}{\Phi(\xi_\lambda)}\right] \times u^2 \left(1 - \frac{u_m}{u}\right) F_D \left[\frac{m_e u^2}{2kT_0} - \xi_\lambda\right] du \,. \tag{2.27}$$

After overcoming the potential barrier, these free electrons escape from the system. For *captured photoelectrons*, two electron populations contribute. The electrons with $u < u_m$ has the effective velocity range $(0, u_m)$ and $(0, \pi/2)$. Another population with $u\cos\phi < u_m$ has the effective velocity range (u_m, ∞) and $(\phi_m, \pi/2)$. Hence, in case of captured photoelectron, we have

$$dn_{pec1} = \left(\frac{m_e}{kT_0}\right)^2 \cos\theta \int_{\lambda_{\min}}^{\lambda_{\max}} \left[\frac{\chi(\lambda) f_\lambda \, d\lambda}{\Phi(\xi_\lambda)}\right] \times u^2 F_D \left[\frac{m_e u^2}{2kT_0} - \xi_\lambda\right] du \quad \text{for} \quad u \le u_m \,, \tag{2.28}$$

and

$$dn_{pec2} = \left(\frac{m_e}{kT_0}\right)^2 \cos\theta \int_{\lambda_{\min}}^{\lambda_{\max}} \left[\frac{\chi(\lambda) f_\lambda \, d\lambda}{\Phi(\xi_\lambda)}\right] \times u^2 \left(\frac{u_m}{u}\right) F_D \left[\frac{m_e u^2}{2kT_0} - \xi_\lambda\right] du \quad \text{for} \quad u \ge u_m \,. \tag{2.29}$$

Therefore, the VDFs for free and captured photoelectrons can be expressed as

$$f_{pef}(u) = \frac{1}{n_{p0}} \frac{dn_{pef}}{du} \,, \tag{2.30}$$

$$f_{pec1}(u) = \frac{1}{n_{p0}} \frac{dn_{pec1}}{du} \,, \tag{2.31}$$

$$f_{pec2}(u) = \frac{1}{n_{p0}} \frac{dn_{pec2}}{du} \,, \tag{2.32}$$

Note that we have normalized the distribution with n_{p0}. Therefore, the distributions presented above indicate the fraction of photoelectrons contributing to different populations. The mean energy associated with the photoemitted electron from the charged surface can be found from Eq. 2.22 using the expressions of $< u^2 >$ of various populations, which can be expressed as

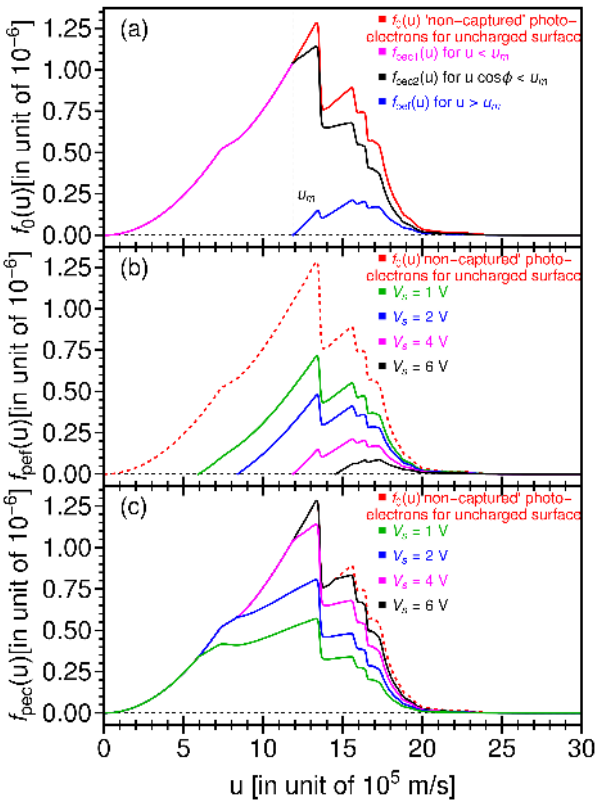

Figure 2.7: (a) The photoelectron velocity distribution function in the proximity of the lunar surface corresponds to the observed solar spectra. Red line: $f_0(u)$ for 'non-captured' photoelectrons from the uncharged surface, Magenta line: $f_{pec1}(u)$ for captured photoelectrons with $u < u_m$, Black line: $f_{pec2}(u)$ for captured photoelectrons with $u > u_m$ and $u\cos\phi < u_m$, Blue line: For free photoelectrons with $u > u_m$ and $u\cos\phi > u_m$. Here $V_s = 4$ V. (b) Velocity distribution of function 'free' photoelectrons. (c) Velocity distribution function of 'captured' photoelectrons. The different colour curves in (b) and (c) correspond to the photoelectron distribution at different values of V_s. The red dashed lines in (b) and (c) are the 'non-captured' photoelectron distributions $\left(f_0(u)\right)$ from uncharged surfaces. This is given to illustrate how much fraction of photoelectrons becomes 'free' and 'captured' when the surface acquires a finite potential V_s. Parameter used: $W_f = 5$ eV, $\theta = 0^\circ$.

$$< u^2 >_{pef} = \frac{\int_{u_m}^{\infty} u^2 f_{pef}(u)du}{\int_{u_m}^{\infty} f_{pef}(u)du}, \tag{2.33}$$

$$< u^2 >_{pec1} = \frac{\int_{0}^{u_m} u^2 f_{pec1}(u)du}{\int_{0}^{u_m} f_{pec1}(u)du}, \tag{2.34}$$

$$< u^2 >_{pec2} = \frac{\int_{u_m}^{\infty} u^2 f_{pec2}(u)du}{\int_{u_m}^{\infty} f_{pec2}(u)du}. \tag{2.35}$$

To numerically visualize the VDFs for the charged lunar surface, let us first briefly discuss the charging of the lunar surface. Initially, the surface starts with zero electric po-

θ	V_s [V]
0°	6.6
60°	5.5
80°	3.3

Table 2.2: Surface potential and dip potential for Type A and Type B sheath for different locations of Moon. Other parameters used: $W_f = 5$ eV, $n_{se} = 5$ cm^{-3}, $T_e = 15$ eV.

tential (uncharged). As solar radiation incident on the lunar surface, photoelectron emission might take place and charge the surface positively. Additionally, the solar wind/ ambient plasma electrons and ions collection also contribute to the negative and positive surface charging, respectively. In the photoemission-dominated region, initially, the photoemission flux dominates over the solar wind/ ambient plasma electron collection flux, and the surface starts acquiring a positive charge, which increases with time. Subsequently, the photoemission current reduces with time and balances incoming plasma collection current in the steady state - here, the surface acquires a steady-state electric potential $V_s > 0$. The Red curve in Fig. 2.7a shows the photoelectron VDF for the uncharged surface. As the surface acquires finite potential, a finite proportion of the photoelectrons get trapped by this potential well ($V_s > 0$). This results in a different photoelectron distribution in the steady state compared to the uncharged lunar surface. The blue line in Fig. 2.7a refers to the free photoelectron distribution with $u > u_m$. For $V_s = 4$ V, only 10% emitted photoelectrons near the surface escape to infinity. The potential barrier (well) captures the rest. As discussed in the section 2.3.2, there are two populations corresponding to captured photoelectrons. The magenta line in Fig. 2.7a, refers to the captured photoelectrons with $u \leq u_m$ it shares 46% of emitted photoelectrons for $V_s = 4$ V. Remaining 44% of emitted photoelectrons with $u \cos\theta \leq u_m$ is illustrated as the black line in Fig. 2.7a. As V_s increases, the photoelectrons have to overcome a higher potential barrier, and u_m shifts towards higher values. As a result, photoemission due to low-energy photons becomes less significant in the free photoelectron population. Since, Eqs. 2.30, 2.31, and 2.32 have been normalized with n_{p0}, Fig. 2.7b shows that the area under the curve decreases with increasing V_s, while opposite has been observed for Fig. 2.7c. This can be attributed to the fact that the free photoelectrons population decreases with increasing V_s, which results in increasing captured photoelectron population and indicates that the majority of the photoelectrons ($\approx 90\%$ for $V_s = 4$ V) gets trapped if the lunar surface acquires a finite electric potential with $V_s > 0$.

Since the lunar surface potential V_s varies with θ (Stubbs et al., 2007), it is important

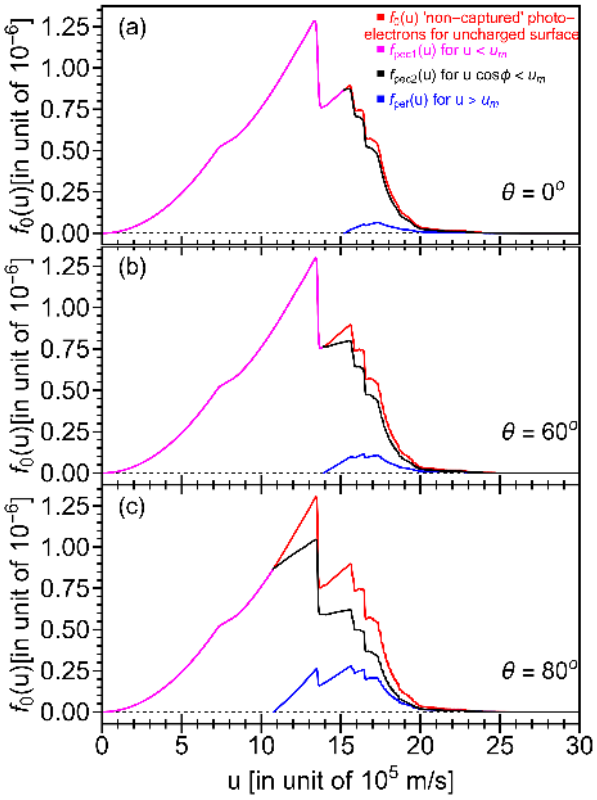

Figure 2.8: The photoelectron velocity distribution function in the proximity of the lunar surface corresponds to the observed solar spectra. Red line: $f_0(u)$ for 'non-captured' photoelectrons from the uncharged surface, Magenta line: $f_{pec1}(u)$ for captured photoelectrons with $u < u_m$, Black line: $f_{pec2}(u)$ for captured photoelectrons with $u > u_m$ and $u\cos\phi < u_m$, Blue line: For free photoelectrons with $u > u_m$ and $u\cos\phi > u_m$. Solid line: Type B monotonic solution, Dashed line: Type A non-monotonic solution. (a) $\theta = 0°$, (b) $\theta = 60°$, (c) $\theta = 80°$. Here, the V_s values are taken from Table 2.2. Parameter used: $W_f = 5$ eV.

θ	n_{p0} [cm^{-3}]	n_{pef} [cm^{-3}]	$n_{pec}/2$ [cm^{-3}]
0°	101.28	1.91	99.37
60°	50.64	2.04	48.60
80°	17.58	2.52	15.06

Table 2.3: Number densities corresponding to "uncharged surface", "free", and "captured" photoemitted electrons for different values of θ.

to discuss the latitudinal variation of photoelectron distribution near the lunar surface. For simplicity, the lunar surface potential V_s can be found balancing photoemission flux and incoming solar wind flux, which is

$$J_{ph} = J_{se}\,, \tag{2.36}$$

where the flux of incoming electrons

$$J_{se} = n_{se}\left(\frac{kT_e}{2\pi m_e}\right)^{1/2}\,, \tag{2.37}$$

and the photoemission flux

$$J_{ph} = \int_{u_m}^{\infty} u_x\, d^3 n_{pe}\,, \tag{2.38}$$

where the expression $d^3 n_{pe}$ is taken from Eq. 2.16. For typical solar wind plasma with density $n_{se} = 5\ \mathrm{cm}^{-3}$ and electron temperature $T_e = 15\,\mathrm{eV}$, steady state potential V_s for different values of θ have been tabulated in Table 2.2. Fig. 2.8 illustrates the latitudinal variation of photoelectron distribution near the lunar surface. The red curves in Fig. 2.8 show that the distribution for uncharged lunar surface changes marginally with varying θ. However, as indicated in Table 2.2, V_s decreases with increasing θ, and a latitudinal variation in distribution function has been observed in the case of charged lunar surface. Due to decreased effective photon flux and surface temperature for higher θ values, the number density near the uncharged surface decreases (see Table 2.3). As the surface acquires finite steady-state potential with $V_s > 0$, some emitted photoelectrons get trapped within the sheath. Table 2.3 shows that nearly 98.1% photoelectrons are captured by the potential barrier at $\theta = 0^\circ$. While for $\theta = 80^\circ$, the fraction of captured photoelectrons reduces to 85.7%. It is also observed that n_{pef} slightly increases with θ. These can be attributed to the fact that increasing θ gives rise to the reduction of V_s, which results in relatively weaker trapping of the emitted photoelectrons. Fig. 2.8a shows that $u_m > 1.52 \times 10^6$ m/s or $E_m > 6.6$ eV - note, E_m is the minimum energy required to escape to infinity from the surface after overcoming the lunar surface work function $W_f = 5$ eV. That means near the equator, a significant contribution of photoemission comes from the high-energy spikes with $\lambda < 100$ nm or $E_\lambda > 12$ eV in the observed solar spectrum (see Fig. 2.1). Whereas Fig. 2.8b, c shows from the mid-latitude to the terminator, other photon spikes also start to contribute to the n_{pef}. This fact illustrates that the Lyman α spike becomes ineffective in determining the "free photoelectron" contribution near the equator. Since in determin-

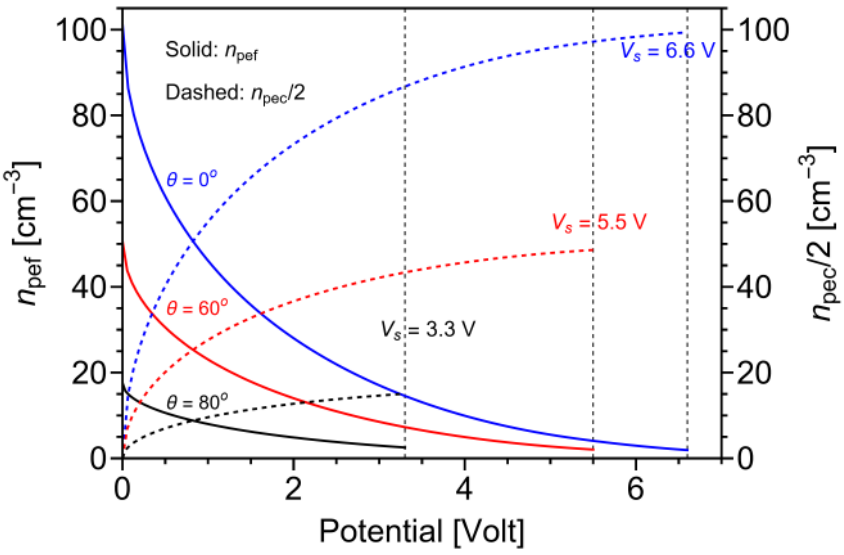

Figure 2.9: Variation of free (solid line) and captured (dashed line) photoelectron density in the proximity of lunar surface with V_s for different values of θ. Blue line: $\theta = 0°$, Red line: $\theta = 60°$, Black line: $\theta = 80°$.

ing V_s, the Eq. 2.36 is used requires only "free photoelectrons", along with the Lyman α, other low energy spike becomes ineffective in defining steady state V_s. Nonetheless, the photoelectrons emitted due to these low-energy photons contribute to the screening of surface potential via trapping within the sheath. However, as θ increases, V_s reduces, and as a result, low-energy spikes start contributing to the "free photoelectrons" and surface charging as one goes towards the terminator. Hence, the results suggest, most of the emitted photoelectrons get trapped within a photoelectron sheath, and a small number of photoelectrons can escape to infinity.

The variation of various photoelectron population densities with V_s has been illustrated in Fig. 2.9. For uncharged surfaces, all the photoelectrons escape to infinity, so $n_{pef} = n_{p0}$ and $n_{pec} = 0$ for $V_s = 0$. As the surface acquires finite potential with $V_s > 0$, low-energy photoelectrons, which cannot overcome the potential barrier, get trapped. Hence, n_{pef} reduces and n_{pec} increases with increasing V_s. Due to higher photoemission near $\theta = 0°$, n_{p0} is high (see Table 2.3). As a result, a higher potential barrier is required to trap most of the photoelectrons compared to higher values of θ. In earlier literature by Mishra (2020b), it has been quantitatively shown that under nominal solar wind conditions, approximately 0.1 s is required to achieve a steady-state photoelectron sheath. Initially, the surface remains uncharged ($V_s = 0\,\mathrm{V}, t = 0\,\mathrm{s}$), then the surface gradually acquires finite potential and achieves the steady state. So, Figs. 2.7 and 2.9 may also be regarded as a temporal variation of photoelectron distribution and densities.

θ	$< E_m >_0$	$< E_m >_{pef}$	$< E_m >_{pec1}$	$< E_m >_{pec2}$
0°	4.46	9.17	3.50	8.04
60°	4.46	8.34	3.09	7.29
80°	4.45	6.83	1.89	5.59

Table 2.4: Mean energies of photoelectrons in eV of various populations for different values of θ.

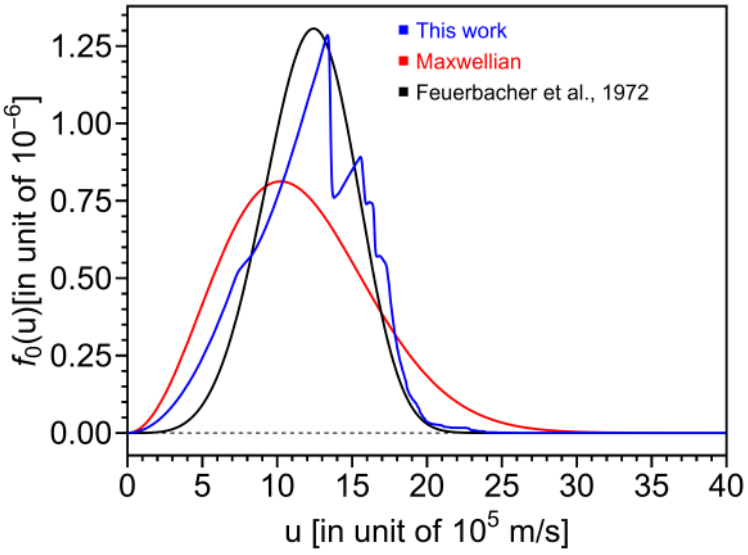

Figure 2.10: The photoelectron velocity distribution function in the proximity of the lunar surface corresponds to the observed solar spectra. Red line: Distribution from current formulation, Blue line: Maxwellian distribution, Black line: Distribution measured by Feuerbacher et al. (1972).

The mean energies of photoelectrons of various populations for different values of θ are given in Table 2.4. No significant variation of mean energy is observed for uncharged surfaces with θ variation. Near the equator, photoelectrons have to overcome higher potential barriers to escape to infinity. As a result, at $\theta = 0°$, the mean energy of "free photoelectrons" is maximum, and it decreases with increasing θ. Similarly, a higher potential barrier traps more energetic photoemitted electrons, which results in higher mean energy of captured photoelectrons near the equator and decreases towards the terminator. Table 2.4 shows that, within a steady-state photoelectron sheath, three different photoelectron populations have different mean energies. The overall mean energy of the photoemitted electrons is the weighted sum of the average energies in each population i.e., $< E_m >= p_f < E_m >_{pef} + p_{c1} < E_m >_{pec1} + p_{c2} < E_m >_{pec2}$, where p's are the fraction of number density with respect to n_{p0} for different populations. The mean energy of photoelectrons from the uncharged surface ($< E_m >_0$) is the same as the overall mean energy of the photoelectron sheath with finite V_s.

Earlier investigations have demonstrated the significance of photoelectron distribution in determining the photoelectron sheath characteristics (Walbridge, 1973). However, previous studies have assumed simplified Maxwellian distribution ($\propto u^2\, e^{-u^2/u_{th}^2}$) for photoemitted electrons (Nitter et al., 1998; Burinskaya, 2014; Zhao et al., 2021). The photoelectron energy distribution was experimentally measured from lunar fines returned during the Apollo missions by Feuerbacher et al. (1972). Poppe and Horányi (2010) fitted the distribution in the functional form $\propto u^4\, e^{-u^4/u_{pe}^4}$ which replicates several characteristics of the measured distribution with a peak at u_{pe} and rapid decrease thereafter. To compare these distributions with the present estimates, we consider the same $< E_m >$, i.e. same $< u^2 >$ for all the cases. This gives $u_{th} = 1.02 \times 10^6$ m/s and $u_{pe} = 1.05 \times 10^6$ m/s. Fig. 2.10 shows these distributions along with present estimates. The distribution of Feuerbacher et al. (1972) closely matches the derived distribution. The presence of more high-energy photoelectrons in the Maxwellian distribution causes a significant departure from the measured and calculated distribution. Since the photoemission current from the uncharged surface is $\cos\theta \int_{\lambda_{min}}^{\lambda_{max}} \chi(\lambda)\, f_\lambda\, d\lambda$, the n_{p0} for the case of Maxwellian and Feuerbacher's distribution are found to 104.9 cm^{-3} and 99.6 cm^{-3} respectively at $\theta = 0^\circ$. This indicates that the consideration of simplified Maxwellian distribution results in slightly different n_{p0} and significantly different velocity distribution.

Note that the present study aims at the photoelectron VDF in the proximity of the lunar surface, and the discussion on altitudinal variation has not been emphasized. However, it would be interesting to comment on the nature of the altitudinal dependence of VDF as follows: We know that a photoelectron sheath is created in the vicinity of the lunar surface. The sheath is characterized by electric potential and electric field, which varies with altitude. So, at a finite altitude x with potential $V(x)$, if the photoelectron has velocity $\mathbf{u}'$ then from the energy conservation, we can write

$$\frac{1}{2} m_e\, \mathbf{u}^2 - eV_0 = \frac{1}{2} m_e\, \mathbf{u}'^2(x) - eV(x)\,, \tag{2.39}$$

where V_0 is the lunar surface potential. From Eq. 2.39 replacing $\mathbf{u}$ in Eq. 2.16, one gets the following equation

$$d^3n_{pe} = \frac{1}{2\pi}\left(\frac{m_e}{kT_0}\right)^2 \cos\theta \int_{\lambda_{\min}}^{\lambda_{\max}} \left[\frac{\chi(\lambda) f_\lambda \, d\lambda}{\Phi(\xi_\lambda)}\right] \times F_D\left[\frac{m_e \mathbf{u}'^2}{2kT_0} - \xi_\lambda + \frac{e(V_0 - V(x))}{kT_0}\right] d^3\mathbf{u}' \,, \tag{2.40}$$

that represents VDF at a particular altitude. And in the expression of u_m, V_0 will be replaced by $V(x)$. This expression is extensively used in the upcoming chapters.

This chapter highlights physics phenomena concerning photoemission from the lunar surface, showcasing various effects connected to solar radiation and lunar surface parameters. However, surface irregularity, like craters and other topographic features, is not addressed in the analysis. These features locally change the angle of sunlight, i.e. θ changes locally within the crater floor. We have shown the $f_0(u)$ for uncharged surface marginally varies with θ. But, for the charged lunar surface, V_s changes with θ, and the "free" and "captured" velocity distribution function will change according to the change in V_s. Due to the variation of θ, we see a spatial change of V_s which creates a horizontal electric field. For large spatial scales, this horizontal electric field is so small in comparison to the vertical field the velocity distribution function is only defined by V_s and θ. However, for small spatial scales, topographic features may create a significant horizontal electric field, which can influence the velocity distribution function, and the effect of this horizontal electric field should be included in the analysis.

2.4 Summary

This chapter presents a formulation describing the velocity distribution function (VDF) of photoelectrons over the sunlit Moon. In this course, this study includes the following aspects, (i) observed EUV/UV spectrum of the solar radiation (Chamberlin et al., 2020), (ii) measured photoelectric efficiency of the lunar regolith (Willis et al., 1973), (iii) latitude-dependent solar spectrum and regolith temperature (Mishra and Bhardwaj, 2019), (iv) realistic regolith temperature regimes from LRO-based Diviner instrument (Williams et al., 2017), (v) FD-statistics of the electrons within surface lattice – these are used to derive the photoelectron flux using Fowler's approach of photoemission (Fowler, 1929). Individually, these aspects have been undertaken in earlier literature, but combining them together features a more realistic scenario and puts forward a rather comprehensive approach in deriving the photoelectron distribution over the Moon. A significant difference in the

derived photoelectron distribution function is noticed for the uncharged and charged lunar surface. The charged surface with an upward-directed electric field traps some of the emitted photoelectrons and characterize various charge population and their distributions.

The photoelectron distribution is found to be a significant function of lunar surface potential. The results suggest that the photoelectron sheath in the steady-state traps nearly 90% of the emitted photoelectrons under the surface charge-induced Coulomb potential barrier. The calculations also suggest that different populations of photoelectrons within the photoelectron sheath are characterized by different mean energies. However, the overall weighted sum of the mean energy of various populations matches the mean energy of the photoelectrons from the uncharged surface. Moreover, the calculated photoelectron distribution is found in reasonable agreement with Feuerbacher's measurements (Feuerbacher et al., 1972) while it widely differs from the Maxwellian nature.

The derived photoelectron VDF is used in the next chapter, where in detail sheath formation of various types above the sunlit lunar surface will be discussed. Further, this analysis is essential for understanding the electrostatic charging lunar dust and subsequent dynamics. The calculation presented here may have practical implications in designing test experiments for future lunar investigations. Although these calculations are based on the typical lunar parameters, the underlying physics, and formulation are well applicable for the other airless bodies with the resembling physical conditions and parameters.

Chapter 3

Photoelectron sheath model

3.1 Introduction

The lunar photoelectron sheath is a non-neutral space charge region above the charged sunlit lunar surface dominated by photoelectrons. This sheath possesses inherent electric potential and field structures that are physically characterized by Poisson's equation. The degree of surface charging varies across different locations on the Moon, leading to the formation of different potential/field structures within the sheath. As discussed in section 1.2, the Poisson's equation can be written as

$$\frac{d^2V}{dx^2} = -\frac{e}{\epsilon_0}\left[n_{\mathrm{si}} - n_{\mathrm{se}} - n_{\mathrm{pe}}\right], \tag{3.1}$$

where e is the electronic charge, ϵ_0 is the permittivity in free space, V is the electric potential at altitude x. n_{si}, n_{se}, and n_{pe} are the population densities of solar wind ions, solar wind electrons, and photoelectrons within the sheath, respectively. Poisson's equations connect the electric potential with the charge density. One needs to solve this equation with the boundary conditions $V(x = 0) = V_0$ and $V'(x \to \infty) = 0$ to quantitatively estimate the characteristics of the plasma sheath. Starting from the first conceptualization by Gold (1955), many attempts have been carried out in the literature to estimate the characteristics of the lunar photoelectron sheath, which have been discussed in detail in Chapter 1. Based on the works of Guernsey and Fu (1970); Fu (1971), Nitter et al. (1998) came up with the most elegant model of photoelectron sheath, which suggests the possibility of three kinds of potential structures within the sheath — a schematic is illustrated in Figure 3.1. On the locations with negligible photoemission, the surface has a negative surface potential due to dominant plasma electron collection that altitudinally increases to zero,

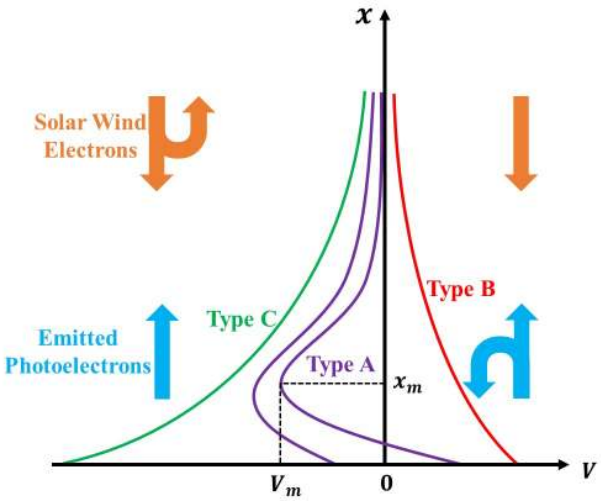

Figure 3.1: Different types of sheaths on the Lunar surface. Here, x refers the altitude and V is the electric potential.

forming a Type C sheath. This is a normal Debye-type potential structure. For significant photoemission, the potential is positive and monotonically decreases to zero to form a Type B sheath. The boundary conditions lead to another sheath solution where the surface potential will decrease to a negative minimum and then increase to zero, giving rise to a non-monotonic potential structure (Type A sheath). These potential structures are the solutions of Poisson's equation that can be written as

$$\frac{d^2V}{dx^2} = -\frac{e}{\epsilon_0}(n_{\rm si} - n_{\rm sef} - n_{\rm sec} - n_{\rm pef} - n_{\rm pec})\,. \tag{3.2}$$

Eq. 3.2 establishes the relationship between the electric potential and the charge population within the photoelectron sheath. Depending on the type of plasma sheath (as shown in Figure 3.1), there can be up to four different populations of electrons within the sheath. The first two populations are the plasma electrons that interact with the lunar surface and the photoelectrons that escape to infinity. These are referred to as "free plasma electrons" $(n_{\rm sef})$ and "free photoelectrons," $(n_{\rm pef})$ respectively. The other two populations are the plasma electrons and photoelectrons, which are reflected by a potential barrier within the sheath. These are known as "captured plasma electrons" $(n_{\rm sec})$ and "captured photoelectrons" $(n_{\rm pec})$, respectively. Other than electrons, positively charged plasma ions $(n_{\rm si})$ also contribute to the photoelectron sheath. The surface and dip potential (potential minima) are used as boundary conditions to solve Poisson's equation (Eq. 3.2). Note that the surface and dip potential depend on the charging currents connected with the lunar surface, which depends on the characteristics of the charge populations. Also, realistic es-

timates of number densities are essential. This requires the inclusion of several lunar and solar parameters in their mathematical expression. That means one has to incorporate accurate solar spectra and relevant lunar parameters like work function and photoelectric efficiency. For solar wind, it's necessary to include plasma parameters and velocity distribution functions that are consistent with the lunar plasma scenario.

From the discussion given in Chapter 1, we noticed certain simplifications in the previous analyses related to the lunar photoelectron sheath, which limits their applicability to the realistic scenario. Because most of the studies assumed a preexisting photoelectron cloud above the charged sunlit lunar surface, and assumed these photoelectrons follow a Maxwellian distribution, and assigned a photoelectron temperature without any proper justification. However, experimental measurements from the lunar samples highlighted that the velocity distribution of photoelectrons is significantly different from the simplified Maxwellian nature (Feuerbacher et al., 1972; Willis et al., 1973). This suggests previous studies ignored the self-consistent mechanism of photoelectron generation and subsequent sheath formation. In Chapter 2, highlighting these limitations, a realistic velocity distribution function (VDF) of photoelectrons has been derived which includes the following novel aspects in the analysis of lunar photoelectrons, i.e., (i) observed EUV/UV spectrum of the solar radiation (Chamberlin et al., 2020), (ii) measured photoelectric efficiency of the lunar regolith (Willis et al., 1973), (iii) latitude dependent solar spectrum and regolith temperature (Mishra and Bhardwaj, 2019), (iv) FD-statistics of the electrons within surface lattice - it is used to derive the photoelectron flux using Fowler's theory of photoelectron emission (Fowler, 1929). This VDF is going to be used in this chapter to estimate the photoelectron contribution in the lunar photoelectron sheath.

Apart from photoelectrons, solar wind (SW)/ambient plasma electrons significantly contribute to the sheath formation. For simplicity in calculations, many studies assumed these electrons to follow a simplified Maxwellian distribution. However, there exist good space observations which suggest these electrons are consistent with a non-Maxwellian kappa distribution (Halekas et al., 2008, 2009b; Pierrard and Lazar, 2010). Hence, the non-Maxwellian kappa distribution for solar wind/ambient plasma electrons is going to be used in this chapter to estimate the solar wind/ambient plasma electrons contribution in the lunar photoelectron sheath. On the other hand, ions, due to their higher mass, have a thermal speed that is much less than the drift speed. As a result, ions can be considered cold and enter the sheath with a drift speed at the same angle as the photons, which vary temporally with the orbital motion of the Moon, i.e., θ (Nitter

et al., 1998; Lisin et al., 2014; Dyadechkin et al., 2015). θ is the angle of incidence of photons with the normal to the surface. This can also be regarded as the sub-solar angle/ latitude. Inclusion of these aspects significantly improves the inherent physics understanding of photoelectron generation and subsequent sheath formation, with more accurate quantitative estimation.

For the analysis simplification, Eq. 3.2 can be normalized by the following replacements: $v = -eV/kT_0$ and $x = z\lambda_d$. The equation Eq. 3.2 can be rewritten as

$$\frac{d^2v}{dz^2} = \frac{1}{n_0}\left[n_{\rm si} - n_{\rm sef} - n_{\rm sec} - n_{\rm pef} - n_{\rm pec}\right], \tag{3.3}$$

where $\lambda_d = \left(\epsilon_0 kT_0/n_0e^2\right)^{1/2}$, and $n_0 = n_{\rm pe}(v_0) + n_{e\infty}/\alpha$. For Type A sheath $n_{\rm sec} = 0$ for $z < z_m$ and $n_{\rm pec} = 0$ for $z > z_m$. For Type B, $v_m = 0$, $n_{\rm sec} = 0$ and for Type C, $v_0 = v_m$ and $n_{\rm pec} = 0$. Here $v_0 = -eV_0/kT_0$ is the normalized surface potential and $v_m = -eV_m/kT_0$ is the normalized dip potential. Next, the mathematical expressions of different charge densities are derived, and computational schemes are discussed.

3.2 Photoelectron population

The emitted photoelectrons traverse normal to the surface and distribute themselves according to the potential structure over the space in the vicinity of the lunar surface and form a photoelectron sheath. Accounting the large curvature of the Moon, for all practical purposes, we consider the planar geometry of the surface at a given location. To evaluate the potential structure, consider a virtual plane parallel to the horizontal lunar surface (at finite x) at potential V. Following Eq. 2.40 and integrating Eq. 2.15 from $\varepsilon_t = 0$ to ∞, the number density of photoelectrons between normalized energy ε_x and $\varepsilon_x + d\varepsilon_x$ at distance x can be written as

$$\begin{aligned} dn_{pe}(v) &= \left(\frac{m_e}{2kT_0}\right)^{1/2} \cos\theta \\ &\times \int_{\lambda_{\rm min}}^{\lambda_{\rm max}} \left[\frac{\chi(\lambda) f_\lambda \, d\lambda}{\Phi(\xi_\lambda)}\right] \varepsilon_x^{-1/2} \ln\left[1 + \exp\left\{\xi_\lambda - \varepsilon_x + v_0 - v\right\}\right] d\varepsilon_x \,, \end{aligned} \tag{3.4}$$

The description of each term is given in section 2.3. The photoelectron sheath may be characterized by two kinds of photoelectron populations, viz., (i) the photoelectrons that escape to infinity, i.e., "free photoelectrons" and are denoted as "$n_{\rm pef}$", (ii) those photoelectrons which are reflected by the potential barrier, i.e., "captured photoelectrons" and is

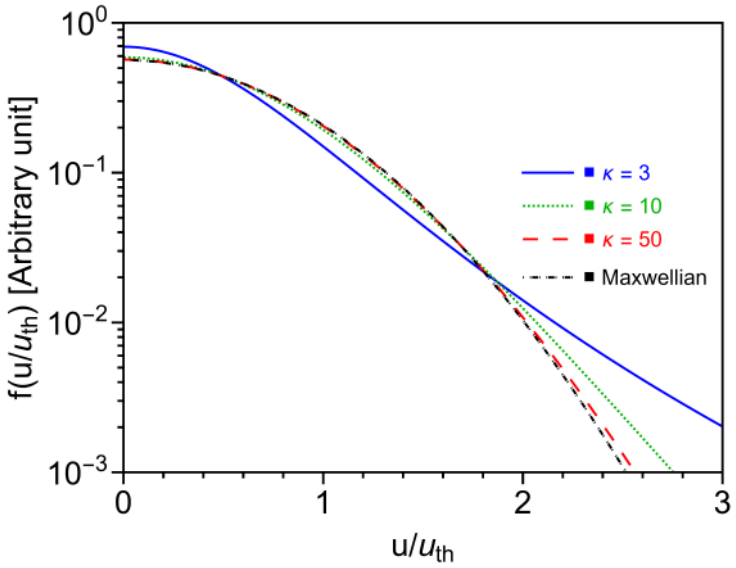

Figure 3.2: Comparison between Maxweillan and κ-distribution for various values of κ.

presented as "n_{pec}". Using Eq. 3.4, these density populations can be expressed as

$$n_{\text{pef}}(x) = \int_{\varepsilon_{xm}(x)}^{\infty} dn_{pe}(x)\,, \tag{3.5}$$

and

$$n_{\text{pec}}(x) = 2\int_{0}^{\varepsilon_{xm}(x)} dn_{pe}(x)\,. \tag{3.6}$$

Factor 2 in Eq. 3.6 appears due to the fact that the incoming and outgoing photoelectrons at any layer contribute to the captured term. Here $\varepsilon_{xm}(x) = v_m - v(x)$ is the minimum energy of the photoelectron at x to overcome the potential confinement $v_m = -eV_m/kT_0$ at x_m.

3.3 Contribution from solar wind/ambient plasma

Solar wind is another integral part of the lunar plasma environment and plays a significant role in establishing the lunar surface charge and sheath. The constituent charging current depends on the energy distribution of the solar wind plasma particles (i.e., electrons/ ions). In a typical geophysical scenario, solar wind/ambient plasma electrons are assumed to follow Maxwellian distribution, which can be expressed as

$$f_m(\mathbf{u})\, d^3\mathbf{u} = n_{e\infty}\left(\frac{m_e}{2\pi\, kT_e}\right)^{3/2} \exp\left(-\frac{m_e\mathbf{u}^2}{2kT_e}\right) d^3\mathbf{u}\,. \tag{3.7}$$

However, according to Lunar Prospector and other in-situ measurements of a variety of space plasmas observations, the energy distribution of the electrons accreting on the lunar regolith is characterized by a non-Maxwellian Kappa distribution (Halekas et al., 2008, 2009b; Pierrard and Lazar, 2010). The distribution of the solar wind electrons can be expressed as

$$f_\kappa(\mathbf{u})\, d^3\mathbf{u} = n_{e\infty}\beta\left(\pi\gamma u_{\text{th}}^2\right)^{-3/2}\left[1+\left(\frac{\mathbf{u}^2}{\gamma u_{\text{th}}^2}\right)\right]^{-\kappa-1} d^3\mathbf{u}\,, \tag{3.8}$$

where $n_{e\infty}/2$ is the density of the plasma electrons at infinity approaching to the surface, $\mathbf{u}$ refers to the electron velocity, $u_{\text{th}} = (2kT_e/m_e)^{1/2}$ corresponds to the thermal speed of the electrons, m_e and T_e are electron mass and temperature, $\gamma = \kappa - 3/2$, $\beta = \Gamma(\kappa+1)/\Gamma(\kappa-1/2)$ and κ is the spectral index of distribution. Figure 3.2 shows the increased tail and decreased core population in κ-distribution with respect to the Maxwellian distribution. κ-distribution more effectively mimics the observed high-energy electron populations, offering a more accurate framework for understanding solar wind/ ambient plasma electron dynamics in the lunar plasma environment. So, in this chapter, the solar wind/ ambient plasma electrons follow κ-distribution. Note that Eqs. 3.7 and 3.8 are the distributions for the electrons far away from the sheath. As the electrons enter the sheath at x with sheath potential $V(x)$, the velocity component within the sheath can be written as

$$\frac{1}{2}m_e\mathbf{u}_\infty^2 = \frac{1}{2}m_e\mathbf{u}^2(x) - eV(x)\,, \tag{3.9}$$

or

$$\mathbf{u}_\infty^2 = \mathbf{u}^2(x) + \left(\frac{v(x)}{\alpha}\right)u_{\text{th}}^2\,, \tag{3.10}$$

where $\mathbf{u}_\infty$ is the total electron velocity at infinity (outside the sheath), and $\alpha = T_e/T_0$. Then, the velocity distribution function of the solar wind/plasma electrons within the sheath can be written as

$$f_\kappa(x,\mathbf{u})\, d^3\mathbf{u} = n_{e\infty}\beta\left(\pi\gamma u_{\text{th}}^2\right)^{-3/2}\left[1+\left(\frac{\mathbf{u}^2}{\gamma u_{\text{th}}^2}+\frac{v(x)}{\gamma\alpha}\right)\right]^{-\kappa-1} d^3\mathbf{u}\,. \tag{3.11}$$

Depending on the sheath profile, the population density corresponding to "free" and "captured" solar wind electrons within the sheath can be given by

$$n_{\text{sef}}(x) = \int_{u_m(x)}^{\infty}\int_{-\infty}^{\infty}\int_{-\infty}^{\infty} f_\kappa(x,\mathbf{u})\, d^3\mathbf{u}\,, \tag{3.12}$$

and

$$n_{\rm sec}(x) = 2\int_0^{u_m(x)}\int_{-\infty}^{\infty}\int_{-\infty}^{\infty} f_\kappa(x,\mathbf{u})\, d^3\mathbf{u}\,, \tag{3.13}$$

where $u_m(x) = \left(2e\left(V(x)-V_m\right)/m_e\right)^{1/2} = u_{\rm th}\left(\left(v_m - v(x)\right)/\alpha\right)^{1/2}$ is the minimum speed of the solar wind electron at x to overcome the potential minimum v_m at x_m.

In a typical solar wind/ambient space plasma condition, ions (primarily protons) have a high drift velocity (around 400 km s^{-1} near the Moon), which greatly exceeds their thermal velocity. As a result, their thermal motion is negligible in comparison. In this thesis, the ions are considered cold and are characterized by a drift velocity $\mathbf{u}_{i\infty}$ and density $n_{i\infty}$. The ion energy conservation and continuity yield the ion density as (Nitter and Havnes, 1992; Nitter et al., 1998)

$$n_{\rm si}(v) = n_{i\infty}\left[1+\frac{2v}{\alpha M_x^2}\right]^{-1/2}, \tag{3.14}$$

where $M_x = M\cos\theta$, $M = u_{i\infty}/u_B$ is the Mach number, $u_B = (kT_e/m_i)^{1/2}$ is the Bohm speed, θ is the angle of incidence of ions with normal (similar to photon incidence) and m_i is the ion mass.

3.4 Numerical Result and Discussions

3.4.1 Boundary conditions

The plausible solution of the Poisson equation should be aided with suitable boundary conditions. At least two boundary conditions are required to solve the Poisson equation. These are: i) at the surface $V(x=0) = V_0$ and ii) at infinity, the sheath electric field is zero $-V'(x\to\infty)\to 0$. To determine these:

1. We consider that charge neutrality is maintained at the sheath edge. i.e., at $x\to\infty$, $v\to 0$, the quasi-neutrality is maintained by the solar wind electrons/ions and photoelectrons, i.e.,
$$n_{\rm pe}(\infty) + n_{\rm se}(\infty) - n_{\rm si}(\infty) = 0\,. \tag{3.15}$$

2. We consider the sheath to be in a steady state with zero net current. The photoemission and solar wind ion collection charge surface positively while the solar wind electrons result in negative charging. In the steady state, these charging currents

should be balanced within the sheath. Mathematically, it can be presented as

$$I_{\rm ph} - I_{\rm se} + I_{\rm si} = 0\,. \tag{3.16}$$

At the sheath edge

$$\begin{aligned}\int_{\varepsilon_{xm}(0)}^{\infty} \left(\frac{2kT_0}{m_e}\right)^{1/2} \varepsilon_x^{1/2}\, dn_{pe}(0) \\ + \int_{-\infty}^{-u_m(\infty)} \int_{-\infty}^{\infty}\int_{-\infty}^{\infty} u_x f_\kappa(\infty, \mathbf{u})\, d^3\mathbf{u} \\ + n_{i\infty}\left(\frac{kT_e}{m_i}\right)^{1/2} M_x = 0\,.\end{aligned} \tag{3.17}$$

3. For Type A sheath, as depicted, a potential minimum exists at $x = x_m$. At this point, $dv/dz = 0$. Multiplying both sides of Eq. 3.3 by $2dv/dz$ and using $dv/dz = 0$ and $v = 0$ as $z \to \infty$, one obtains another boundary condition specifically for Type A sheath as

$$\left(\frac{dv}{dz}\right)^2 = 2\int_0^{v_m} \frac{1}{n_0}\left[n_{\rm si} - n_{\rm sef} - n_{\rm sec} - n_{\rm pef}\right] dv = 0\,. \tag{3.18}$$

So, for Type A sheaths, additional conditions will be at $x = x_m$: $V(x_m) = V_m$ and $-V'(x_m) = 0$.

The simultaneous solution of these equations provides the necessary boundary conditions for Poission's equation.

3.4.2 Computations scheme and data

At any given location on Moon, the necessary input parameters are T_0, W_f, $\chi(\lambda)$, f_λ, θ, $n_{i\infty}$, T_e, and M. For solar wind ions $M_x = \max\left[1, M\cos\theta\right]$ is assumed (Nitter et al., 1998). Following Nitter et al. (1998), $M = 10$ is taken in this study. The minimum value of unity is taken to satisfy the Bohm sheath criterion (Bohm, 1949; Nitter et al., 1998), that is applicable for Type C sheath. The unknown parameters are v_0 and $n_{e\infty}$. One additional unknown parameter is v_m, i.e., applicable for Type A sheath. To determine these unknowns for Type B and Type C sheaths, one has to solve Eqs. 3.15 and 3.17 simultaneously. For Type A, Eqs. 3.15, 3.17 and 3.18 simultaneously describe the desired unknowns, i.e. surface potential, minimum potential, and $n_{e\infty}$. After getting these sheath features, v_0, v_m and $n_{e\infty}$ are used to solve the Poisson's equation (Eq. 3.3).

The attitudinal variation of normalized electric potential $v(z)$ within the sheath can

be obtained by solving Eq. 3.3 numerically with given boundary conditions. For Type A and B sheath, there exist zero fields at the potential minimum. Integrating Eq. 3.3 from $v = v_m$ to an arbitrary v, using the condition $(dv/dz) = 0$ at $z = z_m = x_m/\lambda_d$, we get

$$\left(\frac{dv}{dz}\right)^2 = 2\int_{v_m}^{v} \frac{1}{n_0}\left[n_{\rm si} - n_{\rm sef} - n_{\rm sec} - n_{\rm pef} - n_{\rm pec}\right] dv = F(v)\,. \tag{3.19}$$

For Type B sheath, $n_{\rm sec} = 0$ and the positive square root of Eq. 3.19 is physically tenable. The above equation reduces to

$$\left(\frac{dv}{dz}\right) = \left[F_B(v)\right]^{1/2}. \tag{3.20}$$

For Type A sheath, $n_{\rm sec} = 0$ for $z \le z_m$, the positive square root is physically acceptable and for $z > z_m$, $n_{\rm pec} = 0$ negative square root is considered. In this case, one has

$$\begin{aligned}\left(\frac{dv}{dz}\right) &= \left[F_L(v)\right]^{1/2} \quad z \le z_m\,,\\ &= -\left[F_R(v)\right]^{1/2} \quad z > z_m\,.\end{aligned} \tag{3.21}$$

The distance z_m can be determined by

$$z_m = \int_{v_0}^{v_m} \frac{dv}{\left[F_L(v)\right]^{1/2}}\,. \tag{3.22}$$

For Type C, at the potential minimum $v_m = v_0$, but the field is not zero. So, integrating Eq. 3.3 from $v = 0$ to an arbitrary v, using the condition $(dv/dz) = 0$ at $z \to \infty$, one gets

$$\left(\frac{dv}{dz}\right)^2 = 2\int_{0}^{v} \frac{1}{n_0}\left[n_{\rm si} - n_{\rm sef} - n_{\rm sec} - n_{\rm pef}\right] dv = F_C(v)\,. \tag{3.23}$$

The negative square root gives the physically tenable solution. So,

$$\left(\frac{dv}{dz}\right) = -\left[F_C(v)\right]^{1/2}. \tag{3.24}$$

Depending on the different plasma populations, Poisson's equation gives two possible solutions (i.e, Type A and Type B sheath) for a given value of $\theta < \theta_{A\to C}$. The system tends to seek a stable solution for the state with the lower potential energy (Guernsey and Fu, 1969, 1970); Following Guernsey and Fu (1969), the total potential energy can be

expressed as

$$U = -\frac{\epsilon_0}{2}\int_0^\infty \left(\frac{dV}{dx}\right)^2 dx\,. \tag{3.25}$$

Replacing $v = -eV/kT_0$, and $z = x/\lambda_d$, Eq. 3.25 becomes

$$U = -\frac{\epsilon_0}{2\lambda_d}\left(\frac{kT_0}{e}\right)^2 \int_0^\infty \left(\frac{dv}{dz}\right)^2 dz\,. \tag{3.26}$$

For sheath A, dv/dz is a double-valued function of v, this can be written as

$$U_A = -\frac{\epsilon_0}{2\lambda_d}\left(\frac{kT_0}{e}\right)^2 \left[\int_{v_0}^{v_m} \left[F_L(v)\right]^{1/2} dv - \int_{v_m}^{0} \left[F_R(v)\right]^{1/2} dv\right]. \tag{3.27}$$

For sheath B

$$U_B = -\frac{\epsilon_0}{2\lambda_d}\left(\frac{kT_0}{e}\right)^2 \int_{v_0}^{0} \left[F_B(v)\right]^{1/2} dv\,. \tag{3.28}$$

For calculations, a typical solar spectrum (the red curve of Figure 2.1), estimated from FISM2 (Chamberlin et al., 2020), is used. Grobman and Blank (1969) reported the regolith work function to vary in the range $W_f \sim 4-6$ eV for the region across the sub-solar point and limb. For this analysis, $W_f = 5$ eV is taken. As discussed in Section 2.2.3, the spectral dependence of the photoelectric yield of the lunar surface reported in Willis et al. (1973) is used in the calculation. The temperature of the lunar surface is another important factor determining the electron population available for photoemission within the lattice. This is primarily determined by a dynamic balance between the power loss from thermal radiation and emission cooling, as well as the absorbed solar radiation. Lunar Reconnaissance Orbiter based Diviner Lunar Radiometer Experiment lunar surface temperature varies within the range 400–150 K over the equator $(\theta = 0^\circ)$ to the terminator $(\theta = 90^\circ)$ (Williams et al., 2017). The surface temperature's latitude dependence has also been taken into account in this analysis - for simplicity, an empirical relation given by Mishra and Bhardwaj (2019) is used. Mathematically it may be expressed as $T_0(\theta) = T_0(\theta = 0)\left[1 - \left(\frac{5}{4\pi}\right)\theta\right]$. Here θ is in radian.

Depending on the position of the Moon in its orbit, the ambient plasma parameter varies. Based on the LP measurements, Halekas et al. (2008) report the plasma parameters in terms of number density $n_{i\infty}$, mean thermal temperature T_e as follows: Solar wind $(0.5-10\,\mathrm{cm}^{-3}, 5-30\,\mathrm{eV})$; Plasma Wake $(0.001-0.1\,\mathrm{cm}^{-3}, 50-150\,\mathrm{eV})$; SEP event $(0.001-0.1\,\mathrm{cm}^{-3}, 1\,\mathrm{keV})$; for Terrestrial magnetosphere: Tail lobe $(0.001-0.5\,\mathrm{cm}^{-3}, 0.1 <$

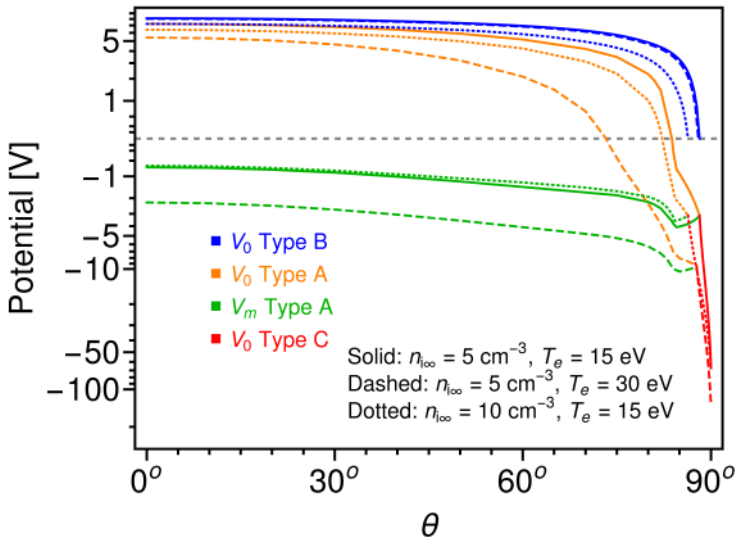

Figure 3.3: Surface (V_0) and dip (V_m) potential variation with subsolar angle θ. For three different photoelectron sheaths.

keV); Plasma sheet $(0.01 - 1\,\mathrm{cm}^{-3},\ 0.1 - 2\,\mathrm{keV})$. The range of plasma density that covers all solar activities lies in the range $1 - 100\,\mathrm{cm}^{-3}$ (Gosling et al., 1977; Shodhan et al., 1999) is used for the present calculations. For solar wind electrons, terrestrial magnetosphere, the terrestrial plasma sheet, Pierrard and Lazar (2010) report $2 < \kappa < 6$. $\kappa = 3$ is considered for the present set of calculations study. Next, we illustrate the numerical results.

3.4.3 Surface and dip potential

The latitude (θ) dependence of the surface (V_0) and dip (V_m) potential is illustrated in Figure 3.3 - all the three possible sheath profiles (i.e., Type A, B, and C) are discussed for different values of $n_{i\infty}$ and T_e. The blue line illustrates the surface potential (V_0) variation for Type B sheath. Due to the significant photoemission current, it attains maximum positive value at the subsolar point $(\theta = 0^\circ$, equator$)$. The reduction in effective photoemission flux with increasing θ, results in decrease in the positive value of the surface potential. A marginal decrease in (V_0) is observed for small θ values, however, a sharp drop is noticed for large $\theta\,(> 80^\circ)$. At a particular angle θ, i.e., Zero Potential Angle $(\theta_{ZPA,B})$, the surface potential becomes zero, and Type B sheath diminishes beyond the value of $(\theta_{ZPA,B})$.

The red curve represents the θ variation in the surface potential (negative) for the Type C sheath that exists close to the terminator. Due to dominant solar wind electron collection and reduced contribution of photoemission, the surface acquires a negative po-

tential. At the terminator ($\theta = 90^\circ$), the photoemission flux becomes zero, and the surface attains maximum negative potential. For smaller latitudes, the increase in photoemission reduces the negative surface potential, and at latitude $\theta_{A\to C}$, the sheath changes from Type C to Type A - here, the red curve joins orange and the green lines of Figure 3.3. For lower values of θ than $\theta_{A\to C}$ surface (V_0) and dip (V_m) potential exists due to the presence of a significant number of electron population near the surface. At $\theta_{A\to C}$, $V_0 = V_m$. As θ decreases from $\theta_{A\to C}$, the values of V_0 and V_m increases. The V_m always remains negative. At a particular latitude, where the orange curve touches zero potential in Figure 3.3, V_0 becomes zero and can be denoted as $(\theta_{ZPA,A})$. For $\theta_{ZPA,A} < \theta < \theta_{A\to C}$, V_0 takes negative values while for $\theta < \theta_{ZPA,A}$, V_0 is positive. The difference between the surface and the dip potentials $V_0 - V_m$ approximately matches with the surface potential of Type B monotonic sheath, and $V_0 - V_m$ decreases with θ. These potential structures are sensitive to solar wind/ ambient plasma density $(n_{i\infty})$ and plasma temperature (T_e). Due to increasing accretion current, the lunar surface potential decreases with increasing $n_{i\infty}$ and T_e. For Type A, V_m develops to trap photoelectrons between the $x = 0$ and $x = x_m$, and for $x > x_m$, it reflects incoming plasma electrons from infinity. So, the magnitude of V_m increases with increases T_e to reflect plasma electrons with larger energy. But increasing $n_{i\infty}$, results in increasing positive ion flux along with electron flux. As a result, for the same T_e, the magnitude of V_m slightly decreases. For Type C sheaths, the surface might acquire a more negative potential within increasing $n_{i\infty}$ and T_e. However, for $\theta = 90^\circ$, photoemission is zero, and the surface potential becomes independent of $n_{i\infty}$ and becomes more negative for larger T_e.

The potential structure (latitude profile) suggests the existence of an electric field parallel to the surface directed toward the terminator. The electric field magnitude is weak near the equator because of a small decrease in surface potential. However, in the Type B potential structure, the field intensity increases near $\theta \sim 80^\circ$ due to a sharp decrease in surface potential. A similar effect might be observed at lower θ for Type A potential structure. The field intensity increases up to the terminator due to the presence of sharp potential structures of Type A and Type C sheaths. The strong horizontal field structure may force the positively charged dust particles near the surface to go toward the terminator.

The variation of $\theta_{A\to C}$, $\theta_{ZPA,A}$, and $\theta_{ZPA,B}$ with plasma density and electron temperature are shown in Figures 3.4 and 3.5, respectively. The results can be understood in terms of the increasing influence of solar wind electron collection current. It is also

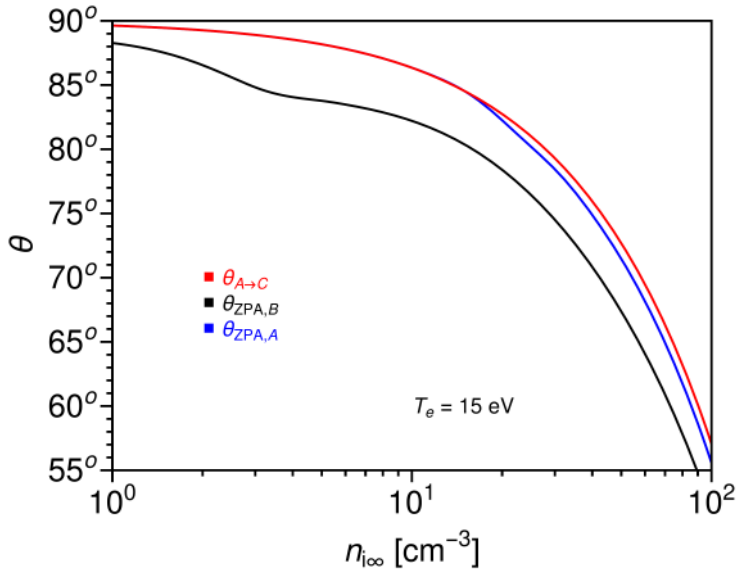

Figure 3.4: The variation of $\theta_{A\rightarrow C}$, $\theta_{ZPA,A}$, & $\theta_{ZPA,B}$ with plasma density. SW parameter used: $T_e = 15$ eV.

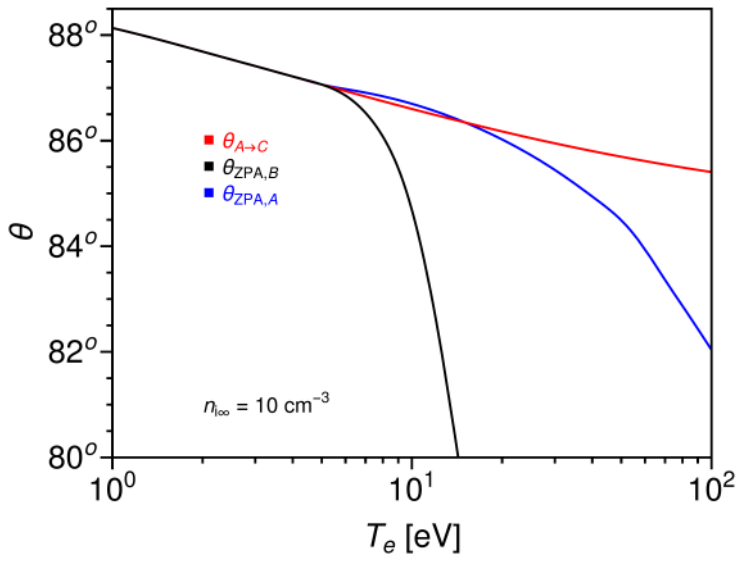

Figure 3.5: The variation of $\theta_{A\rightarrow C}$, $\theta_{ZPA,A}$, & $\theta_{ZPA,B}$ with electron temperature. SW parameter used: $n_{i\infty} = 10\ \text{cm}^{-3}$.

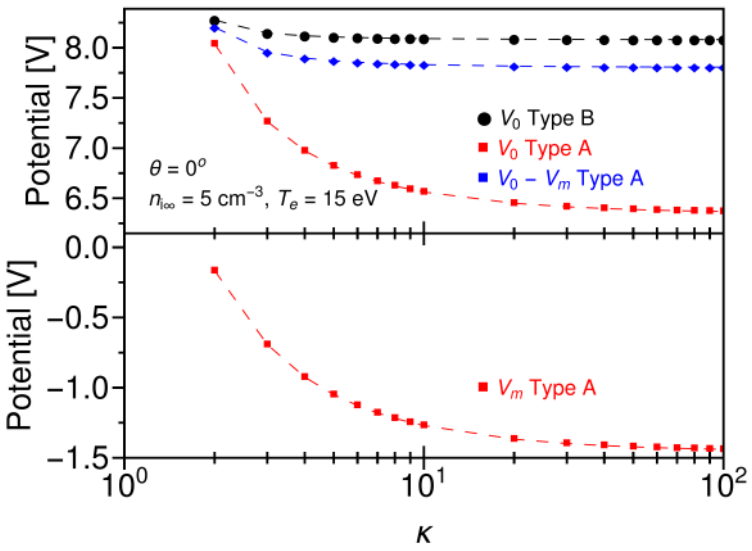

Figure 3.6: The variation of V_0, V_m with κ. Other parameter used: $n_{i\infty} = 5$ cm^{-3}, $T_e = 15$ eV, $M = 10$, $\theta = 0^\circ$.

noticed that all the characteristic angles decrease with increasing plasma density Figure 3.4. The difference between $\theta_{ZPA,A}$ and $\theta_{ZPA,B}$ arises due to the presence of V_m for Type A sheath which increases the effective barrier height for the photoemission. It lowers photoelectron population density for a smaller value of θ for Type A sheath whereas, at $\theta_{ZPA,B}$, Type B sheath diminishes. As the plasma density increases, a sharp decrease in these three angles are noticed. A slight difference between $\theta_{A\to C}$ and $\theta_{ZPA,B}$ have been noticed for higher values of $n_{i\infty}$ ($>\sim 20\,\mathrm{cm}^{-3}$). This finite difference may be attributed to the fact that in this regime, the ions enter into the sheath with a drift speed of $u_B \cos\theta$, i.e., greater than the Bohm speed and M_x takes values > 1. As a result, Eqs.(3.15), (3.17), and (3.18) derives slightly different $\theta_{A\to C}$ than $\theta_{ZPA,B}$. The effect of $M_x > 1$ on $\theta_{ZPA,A}$ can also be seen by the black curve in Figure 3.4.

Figure 3.5 shows that due to the higher electron temperature and subsequent electron collection flux decreases the values of $\theta_{A\to C}$, $\theta_{ZPA,A}$, and $\theta_{ZPA,B}$. For the smaller value of T_e it is noticed that the three angle matches corresponding to $V_m = 0$ - it indicates Type A and Type B sheaths coincide and only Type B and C sheaths exist for smaller values of T_e. The angle $\theta_{ZPA,A}$ sharply falls with increasing T_e. The black curve in Figure 3.5 also indicates that for some value of T_e, $\theta_{ZPA,A}$ may reach to zero and the entire surface of the Moon may acquire negative potential. This scenario may exist during the Moon's surface interaction with CMEs, or Earth's magnetospheric plasma.

Figure 3.6 illustrates the surface (V_0) and minimum (V_m) potentials, respectively

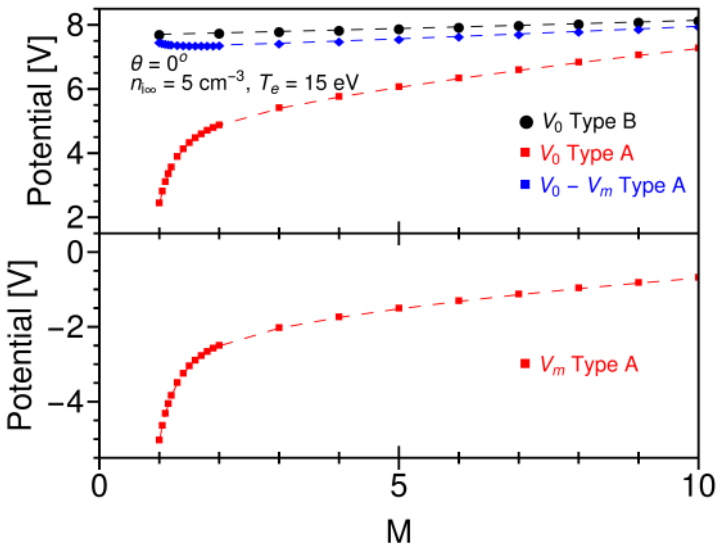

Figure 3.7: The variation of V_0, V_m with M. Other parameter used: $n_{i\infty} = 5$ cm^{-3}, $T_e = 15$ eV, $\kappa = 3$, $\theta = 0^\circ$.

for Type A & B, as a function of κ. V_0 and V_m noticed to be decreases with increasing κ. Because as κ increases, the contribution of the thermal electrons in the incoming solar wind flux increases, which makes V_m more negative and reduces V_0. As κ reaches higher values, the solutions reach the Maxwellian solar wind derivation.

Figure 3.7 shows the surface (V_0) and minimum (V_m) potentials, respectively for Type A & B, as a function of M. Since ions are massive, increasing M slightly increases positive ion flux; as a result, V_0 for Type B slightly increases. For Type A, V_0 and V_m were noticed to increase with increasing M. The increase was rapid between the M values of 1 to 2.

3.4.4 Sheath structure

The sheath features in terms of altitudinal/latitudinal dependence of the electric potential and electric field within the lunar sheath are explored - these parameters are effectively considered responsible for the plasma and dust transport over the lunar surface.

3.4.4.1 Type C sheath

Figure 3.8 illustrates the Type C sheath. The black line represents the altitude profiles of the electric potential and field corresponding to $\theta = 90^\circ$, i.e., at the terminator, where the photoemission from the surface is absent and solar wind plasma solely dominates the charging. For a typical solar wind plasma, viz., $n_{i\infty} = 5$ cm^{-3}, $T_e = 15$ eV, the surface

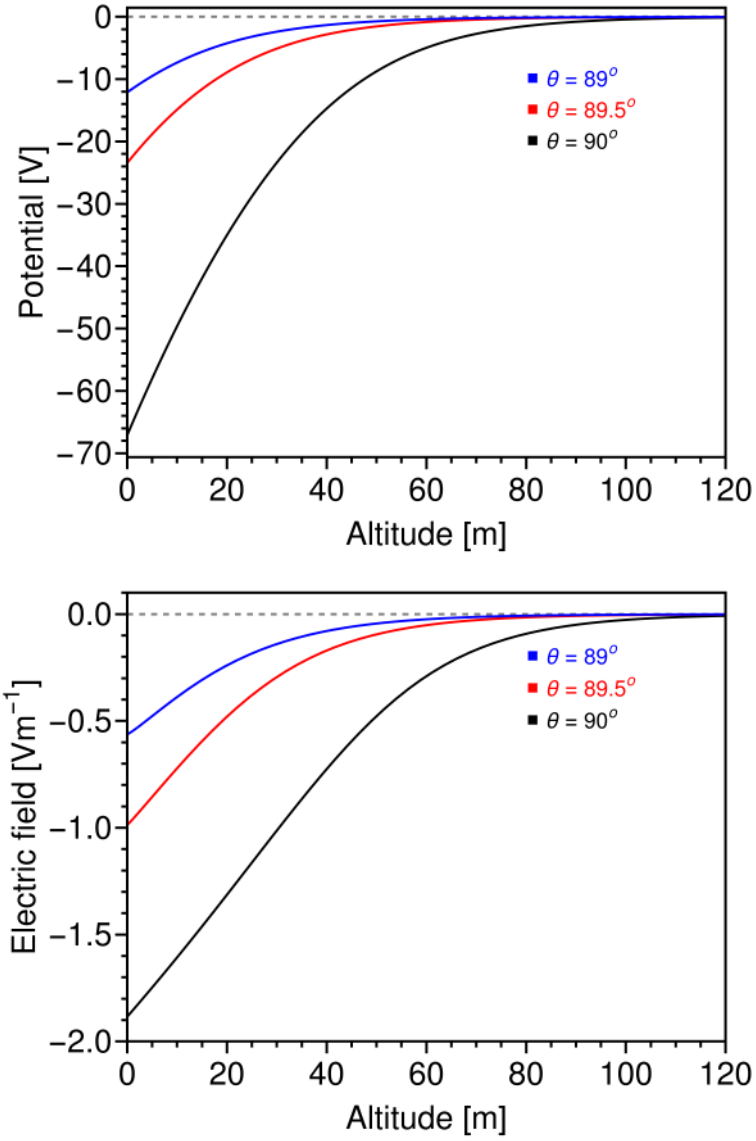

Figure 3.8: Altitude profiles of the (top) electric potential and (bottom) field intensity within Type C sheath over the lunar surface for different values of solar latitude θ near the terminator. SW parameter used: $n_{i\infty} = 5$ cm^{-3}, $T_e = 15$ eV.

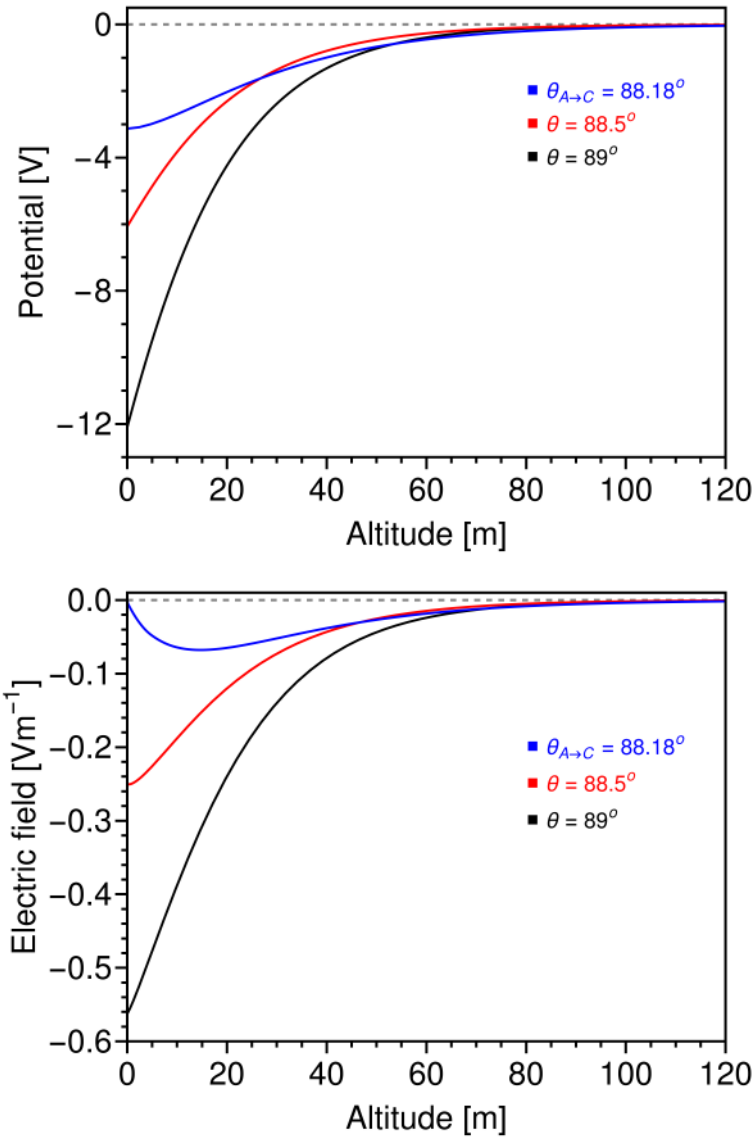

Figure 3.9: Altitude profiles of the (top) electric potential and (bottom) field intensity within Type C sheath over the lunar surface for different values of solar latitude θ near the C to A transition region. SW parameter used: $n_{i\infty} = 5$ cm^{-3}, $T_e = 15$ eV.

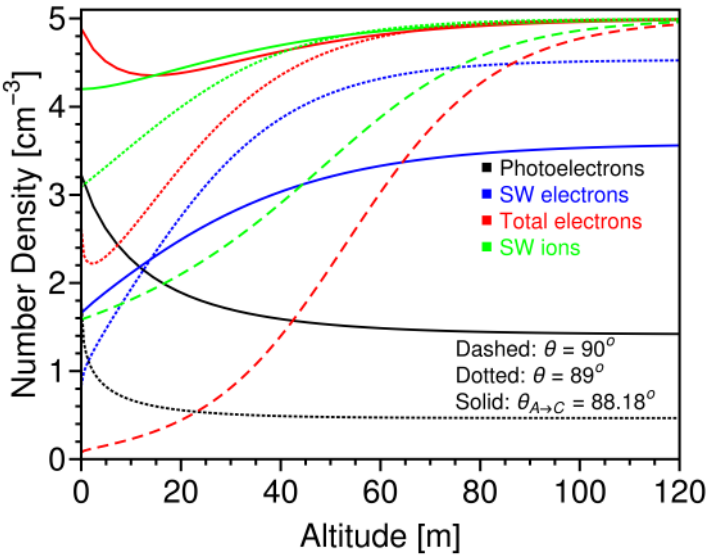

Figure 3.10: Altitude profiles of ion density (Green), plasma electron density (Blue), photoelectron density (Black), and total electron density (Red) within Type C sheath. SW parameter used: $n_{i\infty} = 5$ cm^{-3}, $T_e = 15$ eV.

acquires ~ -67 V. This negative potential is screened out by the solar wind positive ions and a usual Debye sheath forms in the vicinity of the terminator. The sheath terminates (i.e. surface potential becomes zero) at an altitude around $\sim$ 100 m. As θ decreases below 90°, due to an increase in surface temperature and effective photon flux, the positive nature of the surface potential increases. Figure 3.8 shows that the screening length decreases with decreasing θ. A monotonically decreasing electric field (in magnitude) profile is also noticed in the bottom panel of the Figure 3.8 near the terminator. Qualitatively, the top panel of Figure 3.8 suggests the horizontal electric field is directed towards the terminator when θ approaches to 90°. The transition of Type C to Type A sheath is illustrated in Figure 3.9. The top panel of Figure 3.9 shows the screening length increases as θ approaches $\sim$ 88.18°, i.e., $(\theta_{A\to C})$. The bottom panel of Figure 3.9 illustrates the altitude profile of the electric field near the C to A transition. At $\theta \sim 88.18°$, the surface electric field becomes zero. This is the point where Type C sheath transforms into a Type A sheath, and non-monotonic electric field structures are noticed to form near this transition angle. The top panel of Figure 3.9 suggests as θ approaches near C to A transition, the horizontal electric field remains directed towards the terminator nearby surface. But after, at an altitude (where the blue line intersects the red line, and the red line intersects the black line in the top panel of Figure 3.9), the field direction switches towards the equator. These oppositely directed field structures may give rise to complex dust/ plasma dynamics.

The nature of electric potential and field structure of Type C sheath can be under-

stood from the altitude profiles of space charge densities given in Figure 3.10. The green and red dashed lines represent the altitudinal variation of ion and electron densities for $\theta = 90^\circ$. The ion density decreases towards the surface because of constant ion flux (see Eq. 3.14). The electron density also decreases near the surface because of larger repulsion due to higher negative potential. For the Debye sheath, the ion density remains greater than the electron density throughout the sheath. For $\theta = 89^\circ$ (dotted line in Figure 3.10), photoelectrons also contribute to the space charge density within the sheath. Since the photoelectron flux is constant throughout the sheath, the photoelectron density is higher near the surface and decreases with increasing height. Despite the presence of photoelectrons within the sheath, the total electrons within the sheath remain smaller than ion density for $\theta = 89^\circ$. As a result, the electric potential and field structures follow the Debye trend. But for $\theta = 88.18^\circ$, photoelectron density increases, which leads to a negative net space charge close to the surface (see the red and green solid line in Figure 3.10). Due to this double-layer structure, the electric field first decreases in the net negative space charge region. Thereafter, ion density dominates, and the electric potential and field increase and screen out to zero. As a result, the screening length increases as one approaches towards $\theta_{A\to C}$.

3.4.4.2 Type A and B sheath

For the typical solar wind parameters $n_{i\infty} = 5\,\mathrm{cm}^{-3}$, $T_e = 15\,\mathrm{eV}$, Figure 3.11 shows that for $\theta < 88.18^\circ$, the sheath structure depicts Type A sheath. A potential minimum develops within the sheath (top panel of Figure 3.11). At the location of the potential minimum, the electric field becomes zero (middle panel). This can be understood from the electron and ion population within the sheath, which has been illustrated in the bottom panel of Figure 3.11. In the region between the surface and the location of the dip potential x_m, a negative space charge region exists. This results in decreasing trend of electric potential from V_0 at the surface to V_m at x_m. Thereafter in the positive space charge region $x > x_m$, ions screens out the negative potential and the Type A sheath terminates. It suggests a double-layer structure within the Type A photoelectron sheath. Near $\theta \sim 88.18^\circ$ the surface potential remains negative. However, for $\theta < 83.77^\circ$, the surface becomes positively charged. The location of the x_m differs slightly for different values of θ. The screening length is noticed to be higher near $\theta_{A\to C}$, and decreases while decreasing θ. This can be attributed to the lower ion density available for the screening V_m for higher values of θ, which suggests sheath termination at larger altitudes. Overall, we note that Type A sheath is extended

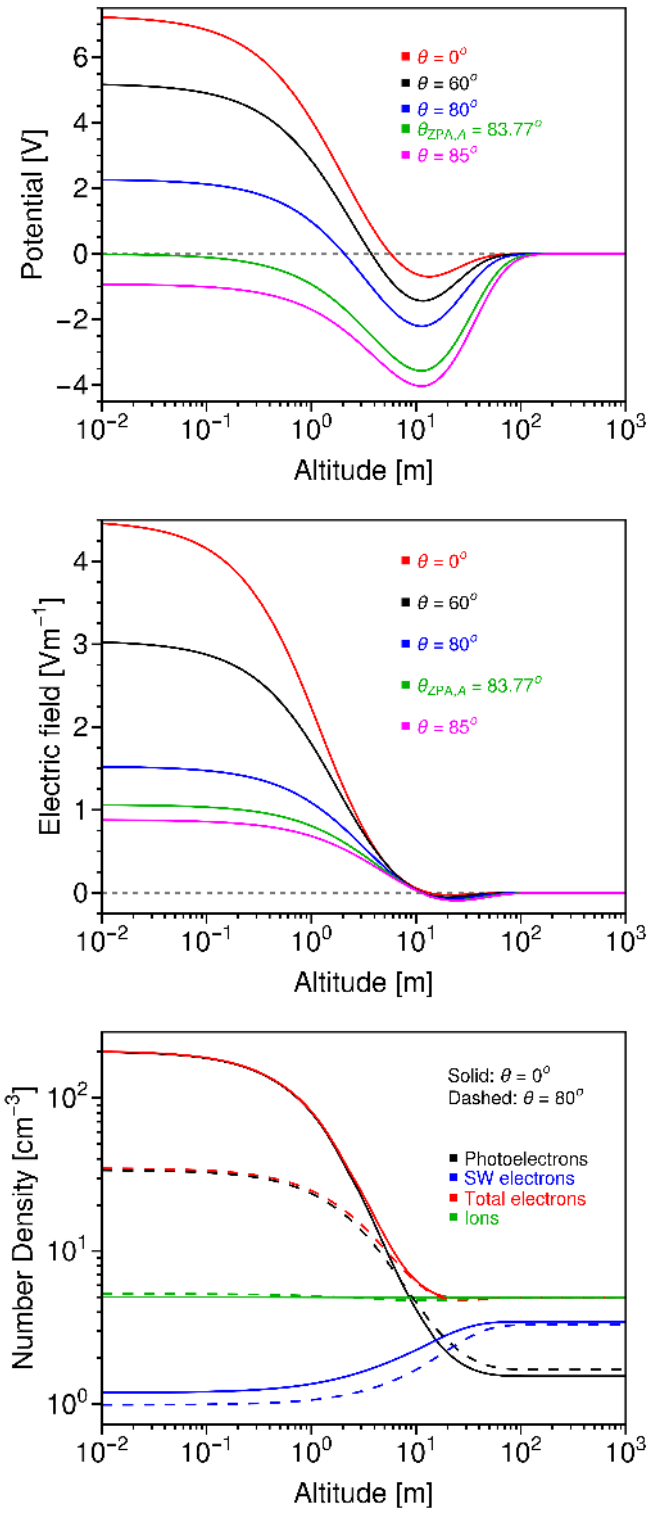

Figure 3.11: Altitude profiles of the (top) electric potential, (middle) field intensity, and (bottom) number density (Solid line: $\theta = 0°$, Dashed line: $\theta = 80°$) within Type A sheath over the lunar surface for different values of solar latitude θ. SW parameter used: $n_{i\infty} = 5$ cm^{-3}, $T_e = 15$ eV.

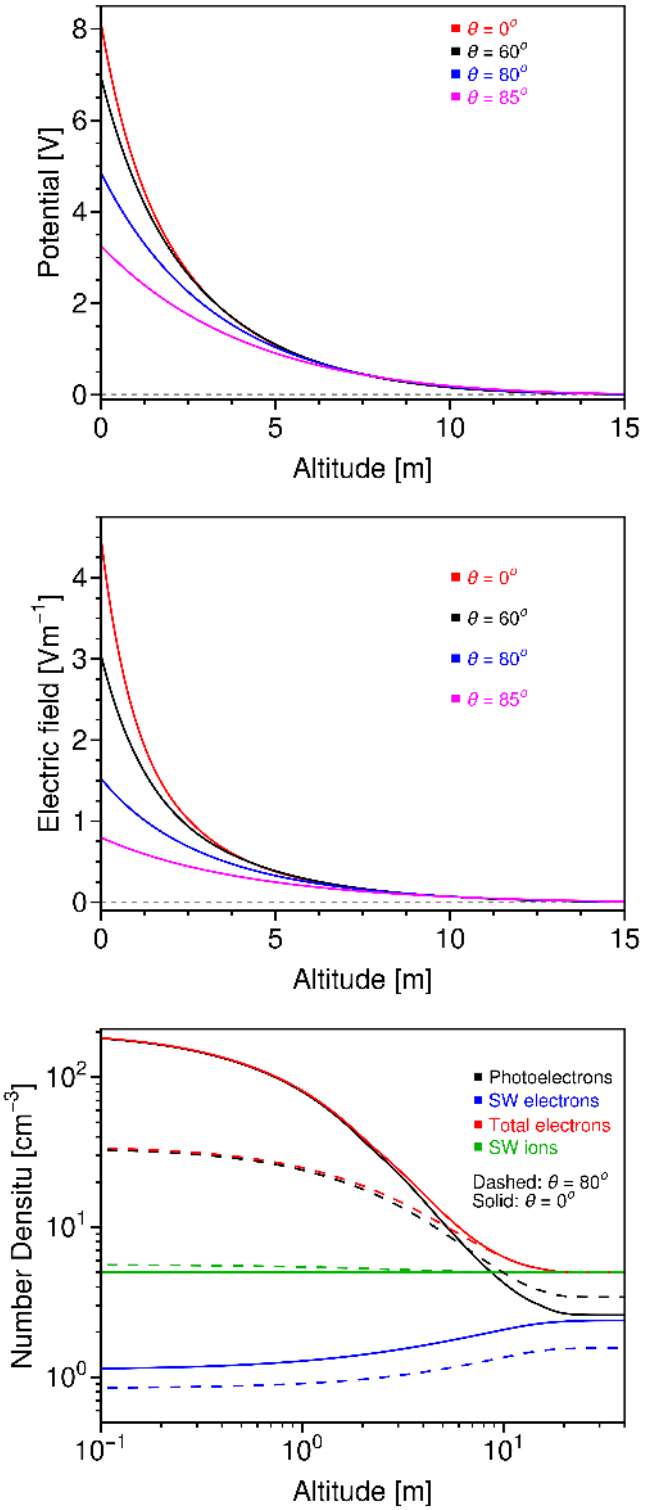

Figure 3.12: Altitude profiles of the (top) electric potential, (middle) field intensity, and (bottom) number density (Solid line: $\theta = 0°$, Dashed line: $\theta = 80°$) within Type B sheath over the lunar surface for different values of solar latitude θ. SW parameter used: $n_{i\infty} = 5$ cm^{-3}, $T_e = 15$ eV.

up to $\sim 80 - 100$ m. The ion density is noticed unchanged from $n_{i\infty}$ for lower values of θ, whereas a marginal variation is noticed near the surface for higher θ values.

Figure 3.12 represents Type B sheath solution for different θ values, i.e., monotonically decreasing sheath for the positively charged lunar surface. Type B sheath is observed to sustain within 12 m altitude from the surface - note, it is significantly smaller than Type A sheath. This can be understood from the space charge density within the sheath. The bottom panel of Figure 3.12 depicts that the photoelectron density is higher than solar wind electron density contribution throughout the sheath. Moreover, the net electron density is larger than the solar wind ion density throughout the sheath and satisfies the boundary condition, i.e., it matches the ion density at the sheath edge. Hence, the photoelectron-dominated negative space charge region exists for the Type B sheath, which screens out the positive electric potential at a much faster rate than that in the case of Type A. The corresponding latitudinal/ altitudinal variation of Type B sheath's electric potential and field structures have been shown in the top and middle panels of Figure 3.12, respectively. The screening length is noticed to slightly varies with increasing θ from the subsolar point ($\theta = 0^\circ$). The value of the positive surface potential is observed maximum at the subsolar point - it corresponds to the maximum photoemission flux at ($\theta = 0^\circ$). As the analysis suggests, the effective barrier height (i.e., $W_f + eV_0$) describes (corresponds to free photoemission flux) the relevant photon spectrum for surface charging. For instance, for typical solar wind plasma and observed photon distribution, the surface at $\theta = 0^\circ$ acquires $V_0 \sim 8.1$ V in the steady state, and hence the photons with energy $E_\lambda > W_f + eV_0 \sim 13.1$ eV i.e. $\lambda < 95$ nm contributes to the free photoemission flux and are effective radiation for the surface charging. This indicates that high energy spikes of the solar spectrum are eventually responsible for developing a steady-state electrostatic environment over the lunar surface. This potential screens out over an altitude of 12 m.

For higher values of θ, the effective photoemission flux and population density decreases as the photon flux available for electron emission decreases by a factor of $\cos\theta$. Additionally, the decrease in the regolith temperature with θ determines the electron population available for emission within the lattice, which also assists this effect. As a result, the surface potential decreases with increasing θ. Lower surface potential introduces a smaller potential barrier for photoemission. For instance, for $\theta = 80^\circ$, $V_0 \sim 4.6$ V and photons with energy $E_\lambda > 9.6$ eV (i.e., $\lambda < 129$ nm) contributes for free photoemission flux. The bottom panel of the Figure 3.12 represents that the photoelectron population

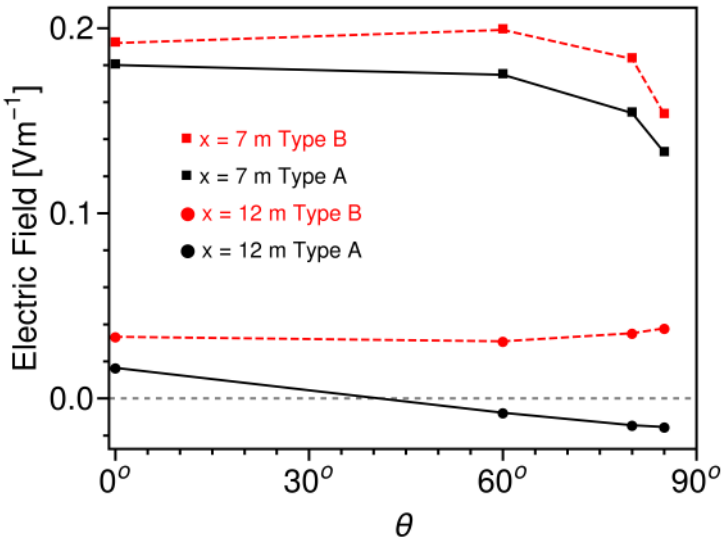

Figure 3.13: Latitudinal variation of the vertical electric field at different altitudes.

density is distributed to a larger altitudinal extent at higher θ values which corresponds to lower surface potential. For instance, the photoelectron density at the sheath edge is higher for $\theta = 80^\circ$ (dashed line) with respect to $\theta = 0^\circ$ (solid line). The net electron density (photoelectron plus solar wind plasma contribution), which causes the surface potential screening, however, shows the monotonic altitudinal/ latitudinal decrease and suggests the reduced screening length with θ for Type B sheath. The sharper decay in the potential in the vicinity of the surface (lower altitudes) can majorly be attributed to the photoelectron population. The middle panel of Figure 3.12 suggests that positively charged particles/ ions always exhibit a vertical push due to decaying positive field structures in Type B sheath. On the contrary, this push might differ for Type A sheath around $x > x_m$ due to field reversal (see Figure 3.11). Considering the field structures, a significant difference in the particle/ plasma transport is anticipated for the two kinds of sheaths (i.e., Type A and Type B).

Figure 3.13 shows the latitudinal variation of the electric field at different altitudes for Type A and Type B sheaths - this information is extracted from the Figures 3.11 and 3.12. For $n_{i\infty} = 5\ \text{cm}^{-3}$, $T_e = 15$ eV the field is noticed to vary with a slower rate between the subsolar point and mid-latitudes, while as it approaches $\theta_{A\to C}$ observable variations have been noted. We see, the field remains positive for the Type B sheath - it suggests that a positively charged particle/ plasma population is always pushed latitudinally towards the terminator (upward) for all θ values up to $\theta_{ZPA,B}$. Due to varying decay rates, the bunch is pushed with a higher force near the equator, and its magnitude decreases

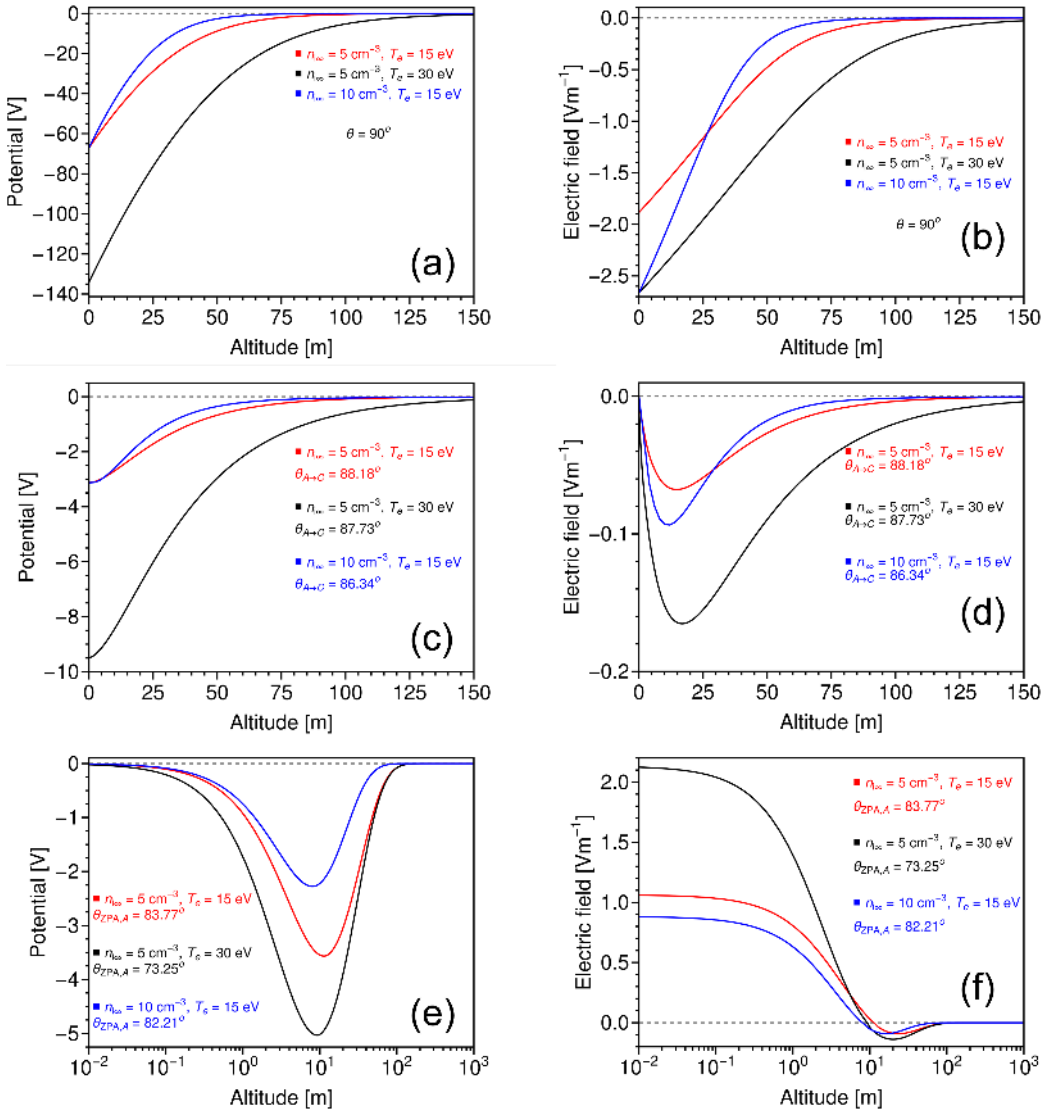

Figure 3.14: Altitude profiles of electric potential and field at different values of θ. For different sets of plasma parameters.

as one moves toward the terminator. We realized the field intensity takes negative values at higher latitudes and altitudes (i.e., near $\theta_{ZPA,A}$) - it suggests that the electrostatic push reverses its direction on these locations and decelerates the particle/ plasma movement latitudinally. This push might reverse the direction of the plasma/ particle transport (towards the equator) if this effectively neutralizes the forward movement through a positive electric field. This latitudinal field reversal in the case of a stable Type A sheath might again be a source of complex dust/plasma dynamics within the sheath on the lunar surface.

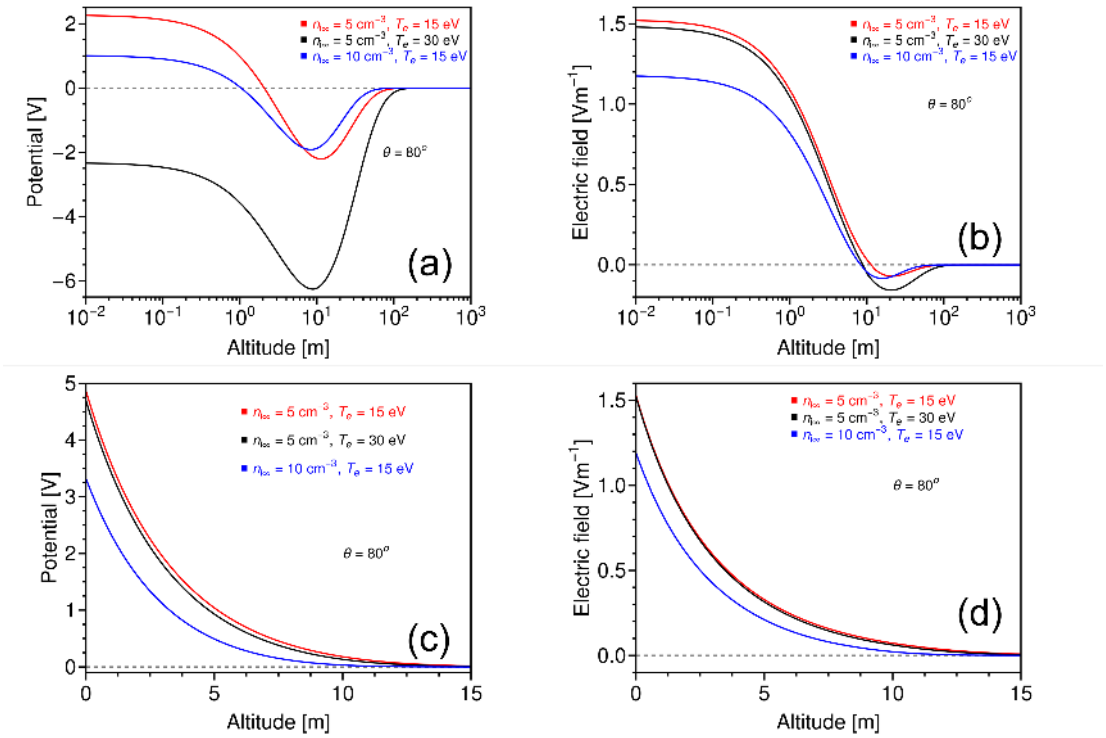

Figure 3.15: Altitude profiles of electric potential and field at $\theta = 80°$. For different sets of plasma parameters.

3.4.4.3 Effect of plasma density and temperature variation

The effect of varying solar wind plasma parameters is shown in Figures 3.14 and 3.15. The blue and red lines refer to variations in solar wind ion density, while the red and black lines highlight the effect of solar wind electron temperature variation on the sheath structures. A usual Debye sheath forms at the terminator, i.e., $\theta = 90°$. At $\theta = 90°$, the quasineutrality condition (Eq. 3.15) at infinity gives $n_{se}(\infty) = n_{si}(\infty)$. With this, the current balance equation (Eq. 3.17) becomes independent of the plasma density, and hence, the surface potential becomes independent of the plasma density (Red and Blue lines in Figure 3.14a). With the increase in the electron temperature, higher electron accretion flux leads to a more negative surface potential - it is illustrated by the black and red lines in Figure 3.14a. Moreover, since the screening length of the Debye sheath is proportional to the square root of electron temperature and inversely proportional to the square root of plasma density. Hence, for high temperatures, the screening length increases (red and black lines in Figure 3.14a) while the same negative potential is screened out at lower altitudes for higher plasma density (red and blue lines in Figure 3.14a). Due to this sharp change in sheath electric potential, the electric field profile is shown in Figure 3.14b - it becomes more negative with increasing plasma density. The variation of $\theta_{A\to C}$, $\theta_{ZPA,A}$

on plasma parameter has illustrated in Figures 3.4 and 3.5. Figures 3.14c and 3.14d show the electric potential and field structures of the sheath at $\theta_{A\to C}$. The trend for the surface potential variation remains approximately the same for the varying plasma density. The electric potential, however, is noticed to screen out at a lower altitude for the higher plasma density - it may be attributed to the higher contribution from the solar wind ions within the sheath, which screens the potential faster. An increase in electron temperature makes the surface potential more negative and requires a higher altitude to screen out the potential effect. Figure 3.14d shows that due to higher plasma density, the electric field (blue line) falls sharply and then rapidly increases to zero (at the sheath edge). It implies the negative space charge region decreases with increasing ion density. On the contrary, increasing the electron temperature increases the thickness of the negative space charge region due to the large repulsion by the negatively charged surface. The magnitude of the negative optimum electric field depends on the net electron (photoelectron and solar wind electron) density and its latitude dependence (i.e., $\cos\theta_{A\to C}$). Figures 3.14e and 3.14f illustrates the sheath characteristics corresponding to zero surface potential. The sheath features for $x > x_m$ are similar to the sheath formed at the transition angle $\theta_{A\to C}$. For $x < x_m$, the presence of a negative space charge decreases the potential as the altitude increases. It is noticed that V_m becomes more negative while decreasing the number density or increasing electron temperature. This can be understood from the location of $\theta_{ZPA,\,A}$ for a particular set of parameters. Since $\theta_{ZPA,\,A}$ decreases with increasing plasma density, the increasing photoemission flux results in a less negative value of V_m at lower $\theta_{ZPA,\,A}$. Moreover, the increasing electron temperature increases the electron accretion flux; this results in a more negative V_m in order to balance the flux by repelling the incoming electrons.

Figure 3.15 represents the Type A, and Type B sheath features at $\theta = 80^\circ$. An increase in the plasma density and temperature increases the electron accretion flux, which results in a decrease in surface potential for both the Type A and B sheaths. For Type A sheath, the parametric dependence of V_m and other features can be understood as follows: For Type A, V_m develops to trap photoelectrons between the $x = 0$ and $x = x_m$ creating a potential well of $V_0 - V_m > 0$, and for $x > x_m$, V_m reflects incoming plasma electrons from infinity. So, the magnitude of V_m increases with increases T_e to reflect plasma electrons with larger energy (see the black curve in Figure 3.15a). But increasing $n_{i\infty}$, results in increasing positive ion flux and density along with electron flux within the sheath. As a result, for the same T_e, the magnitude of V_m slightly decreases to accommodate additional electrons within the sheath and to maintain the quasi-neutrality at the sheath edge.

Due to higher ion density, V_m is screened out to a relatively lower altitude (see the blue curve in Figure 3.15a). The dependence of the screening length of the Type B sheath and length x_m of the Type A sheath on plasma parameters can be understood as follows: higher plasma density refers to the availability of a larger electron population near the surface, which reduces the potential faster with the altitude. The higher temperature of electrons decreases the positive surface potential with higher electron accretion, and the smaller positive surface potential screens out at a relatively lower altitude.

3.4.4.4 Electrostatic Energy for Sheaths A and B

We note from the analysis that for certain θ values, solutions for both Type A and Type B sheath exist - it is essential to comment on the stability of the sheath. Note that, having net negative potential energy, both the solutions of Poisson's equation are valid. However, the solution with higher potential energy is a short-lived metastable solution which ultimately transforms into the low energy stable state (Guernsey and Fu, 1970). Table 3.1 gives the parametric variation of the ratio of the total potential energy of Type B and Type A sheath (U_B/U_A) at different latitudes derived using Eqs. 3.27 and 3.28. Note, both U_A and U_B have negative values and refer to stable solutions. The condition $U_B/U_A < 1$ suggests a more stable Type A sheath, whereas $U_B/U_A > 1$ suggests that Type B sheath is more stable. Our calculations suggest that for nominal solar wind, the potential energy of non-monotonic sheath (Type A) near $\theta_{A\to C}$ is less than the monotonic (Type B) solution - it suggests, Type A sheath is more probable over these locations. However, the numerical results show for smaller values of the plasma parameter (e.g., 1st column, Table 3.1), both Type A & Type B solutions are equally probable near the equator. For higher values of plasma density and temperature (i.e., typical solar wind plasma), the ratio becomes slightly less than unity near the equator (e.g., 2nd column, Table 3.1), which illustrates that Type A sheath becomes more stable while a more stable Type B sheath is noticed over mid-latitudes. The possibility of Type B sheath decreases further with increasing plasma density and temperature (3rd column, Table 3.1).

3.4.4.5 Comparison with Maxwellian photoelectrons

In Chapter 2, the importance of photoelectron VDF has been highlighted. Figure 3.16 illustrates the comparison between the Type A sheath characteristics considering Maxwellian and Fermionic photoelectrons. Following Nitter et al. (1998), the Maxwellian VDF for

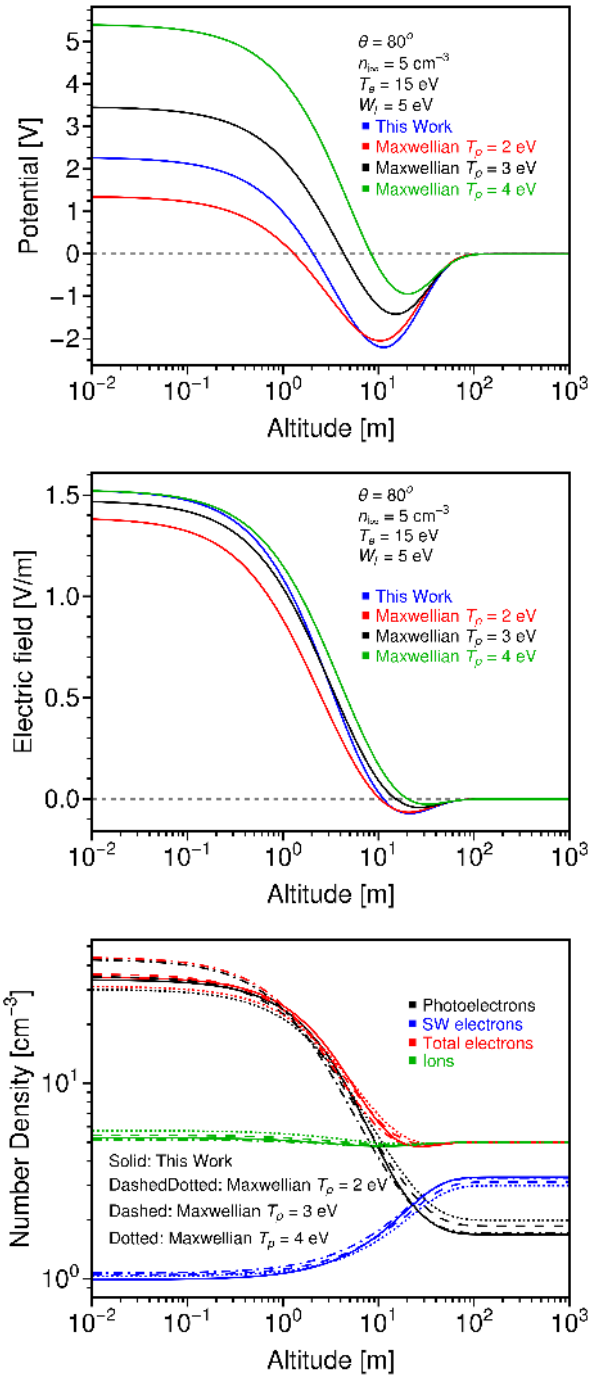

Figure 3.16: Comparison of the altitude profiles of the (top) electric potential, (middle) field intensity, and (bottom) number density within Type A sheath for Fermionic and Maxwellian photoelectrons.

Angle (θ) (degree)	$n_{i\infty} = 5\,\mathrm{cm}^{-3}$ $T_e = 15\,\mathrm{eV}$	$n_{i\infty} = 10\,\mathrm{cm}^{-3}$ $T_e = 15\,\mathrm{eV}$	$n_{i\infty} = 5\,\mathrm{cm}^{-3}$ $T_e = 30\,\mathrm{eV}$
0°	1.00	0.97	0.92
20°	1.00	0.94	0.92
40°	1.00	1.01	0.97
60°	1.01	1.02	1.01
80°	1.01	1.02	0.94
82.5°	0.96	0.92	0.82
85°	0.77	0.43	0.51

Table 3.1: Ratio of the total potential energy of Type B and Type A sheath (U_B/U_A) for different values of θ.

photoelectrons can be written as

$$f_p(x,\,\mathbf{u})\,d^3\mathbf{u} = n_{\mathrm{p0}}\left[\frac{m_e}{2\pi kT_p}\right]^{3/2}\exp\left[-\frac{m_e\mathbf{u}^2}{2kT_p}+\frac{e\big(V(x)-V_0\big)}{kT_p}\right]d^3\mathbf{u}\,, \tag{3.29}$$

where T_p is the photoelectron temperature, and $n_{\mathrm{p0}}/2$ is the photoelectron density escaping from the surface at $x = 0$. Using the above distribution, the potential structure corresponding to Maxwellian photoelectrons can be derived for a certain set of input parameters. However, since there is no constraint on the choice of photoelectron temperature, different choices of T_p give rise to different numerical estimates of the sheath structure as shown in Figure 3.16. The assumption of a higher photoelectron temperature leads to overestimation of the lunar surface potential and underestimation of the photoelectron density in the vicinity of the lunar surface. In contrast, the present study does not assume any photoelectron temperature. Rather, it derives the mean energies of emitted lunar photoelectrons using the self-consistent mechanism of photoelectron generation and subsequent sheath formation. Hence, this model provides a more accurate prediction of the potential structure around the Moon. The comparison shows a significant difference in potential structure, but the field strength within the sheath varies slightly around 0.1 V/m. However, this value is important as it significantly affects the behavior of charged dust dynamics within the sheath. Furthermore, the range of the upward-directed electric field and the altitude where the field reverses differ by several meters, which results in significant variations regarding the lofting and subsequent levitation of lunar dust. The dust charging and dynamics are discussed in detail in Chapter 6.

	Lyman α	FISM2
Type B		
$\theta = 0^\circ$	$V_0 = 2.3$ V	$V_0 = 7.3$ V
$\theta_{ZPA,B}$	60.7°	86.3°
Type A		
$\theta = 0^\circ$	$V_0 = 1.47$ V	$V_0 = 6.42$ V
	$V_m = -0.59$ V	$V_m = -0.64$ V
$\theta_{ZPA,A}$	48.6°	82.2°
	$V_m = -0.77$ V	$V_m = -2.27$ V
$\theta_{A\to C}$	58°	86.3°
	$V_0 = -0.81$ V	$V_0 = -3.13$ V

Table 3.2: Comparision between the photoelectron sheaths derived using only Lyman α radiation and FISM2 spectra. SW parameter used: $n_{i\infty} = 10$ cm^{-3}, $T_e = 15$ eV.

3.4.4.6 Lyman α vs other EUV photons

It is interesting to point out that though Lyman α radiation (121.57 nm) dominates the EUV photons in the typical solar spectrum ($\sim$ 80%, Bauer (1973)), the other high energy spikes (other than Lyman α) also significantly contribute to the lunar surface charging (Figure 2.1). To illustrate this fact, we compare the sheath parameters derived using only Lyman α radiation and the complete EUV spectrum from FISM2 spectra in Table 3.2 - a significant difference in the two cases due to varying photoemission flux is observed. For instance, the Lyman α photoemission flux is one order of magnitude smaller than the total FISM2 photoemission flux. As depicted in the analysis, for the positively charged surfaces, the effective potential barrier for the free photoemission flux is $W_f + eV_0$. In the case of full FISM2 spectra (for $\theta = 0^\circ$), the steady-state surface potential is larger, and due to a larger potential barrier, the particular Lyman α spike becomes ineffective, and contribution primarily comes from high energy photons for the photoemission. Due to the small photoemission flux for Lyman α radiation, the critical θ values shift towards the equator (i.e., lower θ values). The smaller magnitude of V_m can be attributed to less number of photoelectrons available near the surface for only Lyman α consideration. Table 3.2 summarize the sheath parameters and demonstrate the effect.

3.4.4.7 Some exotic cases

In each lunar orbit, the Moon passes through the Earth's magnetosphere tail lobe and plasma sheet for a short duration. Following Halekas et al. (2008) for ambient plasma parameters, the sheath features have been derived and are shown in Table 3.3. Due to high electron temperature, a sufficiently high negative charge ($\sim$ kV) development is noticed at

	Tail lobe $n_{i\infty} = 0.5$ cm^{-3} $T_e = 100$ eV	Plasma sheet $n_{i\infty} = 1$ cm^{-3} $T_e = 1$ keV
Type B		
$\theta = 0^\circ$	$V_0 = 10.9$ V	$V_0 = 9.8$ V
$\theta_{ZPA,B}$	89.8°	89.5°
Type A		
$\theta = 0^\circ$	$V_0 = -0.65$ V	$V_0 = -147.2$ V
	$V_m = -10.64$ V	$V_m = -154.9$ V
$\theta_{ZPA,A}$	-	-
$\theta_{A\to C}$	89.6°	87.9°
	$V_0 = -43.9$ V	$V_0 = -570.9$ V
Type C		
$\theta = 90^\circ$	$V_0 = -446.8$ V	$V_0 = -4468.2$ V

Table 3.3: Typical Lunar photoelectron sheath properties for Earth's magnetospheric tail lobe and plasma sheet parameters.

the terminator ($\theta = 90^\circ$). This negative nature of the surface potential decreases sharply by one order magnitude at Type C to Type A sheath transition angle. Moreover, $\theta_{A\to C}$ is very close to the terminator, which illustrates the existence of a large electric field parallel to the surface. This large horizontal electric field may lead to complex dust/plasma dynamics near the terminator. Intuitively, this strong electric field may drive positively charged dust particles towards the terminator. In a recent article, Popel et al. (2022) have suggested the Lorentz force connected with the magnetic field of the Earth's magnetotail can drive the charged (positive) dust towards the equator. We suggest that this motion may be affected by such a high electrostatic Coulomb repulsion. In certain conditions, it might overcome the $\mathbf{u} \times \mathbf{B}$ effect of the Earth's magnetotail and may divert the motion towards the terminator. As the Moon passes through the magnetotail, the surface potential at the equator for the Type A sheath becomes negative. Note that though the photoelectron-dominated Type B sheath solution also exists with positive surface potential over the sunlit locations for this plasma conditions, Type A sheath (negative surface potential) is found to be a more stable solution at the equator and double layer solution exists throughout the region. It suggests that under certain conditions, the entire surface of the Moon acquires negative potential. Under highly exotic plasma environments with high negative surface potential (especially when the Moon passes through the plasma sheet), in situ instrument operation and roving activities become challenging even over the sunlit Moon.

The present study brings out some intriguing physics effects on the photoelectron sheath structure over Moon under different plasma conditions. The analysis, however, is based on certain simplified assumptions, and here we brief these limitations and discuss their possible effects. The surface irregularity is neglected in the analysis, which might lead an inhomogeneous photoelectron sheath over the lunar surface. Moreover, the effect of levitated dust particles has been ignored in the lunar photoelectron sheath formation - it is justified by considering very low dust density within the lunar sheath ($\sim 10^{-3}\,\mathrm{cm}^{-3}$, Popel et al. (2013)). However, the levitated dust may marginally affect the electron density population within sheath due to photoemission from dust. Intuitively, in turn, it may decrease the sheath expansion of the monotonic Type B sheath and reduce the value of x_m for the Type A sheath. On the contrary, the Type C sheath thickness may increase due to the increase in photoemitted electrons. The role of magnetic anomalies and Earth's magnetic field is not considered in this formulation. The presence of a magnetic field may affect the charging currents and limits the applicability of the present theory in the magnetic anomaly region. Despite these limitations, this analysis gives a rational solution and enriches the understanding of sheath physics.

3.5 Summary

A theoretical model describing the photoelectron sheath structure on the Moon's sunlit regolith has been developed. The formulation includes observed solar EUV/UV spectrum (FISM2), solar wind plasma, measured photoelectric yield, and Fermionic nature of the photoelectrons as novel features which are consistently accounted for solving the Poisson's equation to determine the photoelectron sheath properties. The quasineutrality and flux balance at the sheath edge are used as boundary conditions to derive the intermediate parameters, viz., surface potential and optimum (minimum) potential, which are further integrated as a basis to derive altitudinal and latitudinal profile of the sheath electric potential/ field by solving Poisson's equation. The analysis brings out the possibility of monotonic (Type B & C) and non-monotonic (Type A) sheaths (shown in Figure 3.1) over the sunlit Moon - their occurrence is found sensitive to the solar radiation (spectrum), solar wind (ambient plasma density) and surface (photo-efficiency) parameters.

A finite region near the terminator where the photoemission contribution is marginal, the surface acquires a negative charge due to dominant solar wind/ ambient plasma interaction. In this condition, a typical Debye sheath (Type C) forms that can

stretch up to $\sim$ 100 m vertical altitude depending on ambient plasma conditions. As one moves away from the terminator latitudinally, the contribution from photoemission increases, transforming the sheath structure to a non-monotonic type (Type A) where potential minima exist close to the surface. The potential minimum always takes negative values, and it forms just on the surface ($x_m = 0$) when the sheath transits from Type A to Type C. In the case of Type A sheath, the surface potential takes positive magnitude near the equator and negative values near the terminator, whereas a $\sim$ 60 m and $\sim$ 120 m vertical extension of the sheath, respectively, are observed for nominal solar wind plasma condition. Along with Type A sheath, Poisson's equation also gives a monotonically decreasing sheath (Type B) solution. Type B sheath solution predicts a photoelectron sheath with smaller thickness, for instance, $\sim$ 12 m, compared to Type A sheath. For normal solar wind conditions, the non-monotonic (Type A) sheath is noticed to be stable near the terminator region, while both types of the sheath are equally probable near the equator region. We also noticed that under exotic plasma conditions, for instance, when the Moon passes through Earth's magnetotail/ magneto sheet, Type A sheath becomes more stable, and under certain conditions entire sunlit Moon be at negative potential. Moreover, in contrary to the preconceived notion, we also conclude that the high energy photons of the solar spectra other than the Lyman- α spike also contribute significantly in determining the surface charge and subsequent sheath structure.

A few specific physical scenarios are considered for the illustrations of the concept presented herein; however, the analysis is self-consistent and is very well applicable for resembling physical conditions. The passage of the Moon through different plasma conditions (like solar wind, Earth's tail lobe, Earth's plasma sheath, and SEP/CME event) yields exotic electrostatic configuration on Moon - a specific case of the Moon transit through Earth's magnetosphere is undertaken in this analysis. It suggests complex surface charging and sheath structure over the sunlit lunar globe, and its understanding could be helpful for the mitigation of electrostatic challenges for efficient instrument operation on lunar modules under such conditions. The landing sites candidates of the ARTEMIS are clustered near the Moon's south pole. According to this analysis, the surface of these locations acquires around negative $50 - 60$ V for the nominal solar wind conditions. However, as the Moon passes through Earth's magnetosphere, the negative potential may reach to a few hundred to thousand volts at these locations - the subsequent plasma behaviour and charging effects could be detrimental for the instrument/electronics operation, and it needs to be equipped with essential rectification scheme for such campaigns. The in-

vestigation carried out herein is of practical implications in conceptualizing the test experiments in labs and designing the possible experiments with lunar modules for future lunar missions.

Chapter 4

Sheath structure around Chandrayaan 3 landing site: A case study

4.1 Introduction

The successful landing of Chandrayaan-3 (Ch3) showcased India's end-to-end capabilities of safe lunar landing and rover exploration. This mission intends to advance our understanding of the Moon and nourish the path for future interplanetary missions. With many advanced scientific payloads, Ch3 contributed to lunar exploration by (i) demonstrating a safe and soft landing on the lunar surface, (ii) demonstrating the rover's mobility and capability for in-situ exploration, and (iii) conducting in-situ science experiments. This mission's success is a significant step forward in India's lunar exploration program. Being an airless body, Moon is exposed to the harsh space plasma conditions, which generates a complex plasma/ electrical environment in the vicinity of the lunar surface locally — depending on plasma conditions and solar activities, this electrical environment could be intense and deleterious to the onboard instrument operation and electronics (Farrell et al., 2008; Halekas et al., 2011c; Jackson et al., 2011, 2015; Zakharov et al., 2020). During the expedition, Ch3 resides within this complex plasma environment on the lunar surface. The knowledge of the environment might be helpful for the risk assessment, rectification, test-bed experiments, and interpretation of upcoming Ch3 data connected with the plasma environment.

As discussed in previous chapters, the Moon passes through various plasma pop-

ulations. In Chapter 3, it was established that for nominal solar irradiation conditions, the photoelectron sheath could stretch up to 10 to 100 m from the equator to the terminator, respectively. Any object residing within this non-neutral space region interacts with the local plasma environment and charged particles within the sheath, which eventually results in a charge development on the object (Farrell et al., 2008). Moreover, the objects roaming on the charged lunar dusty surface (regolith-wheel interaction) might acquire huge charge acquisition due to frictional (triboelectric) charging — due to the lack of a significant dissipation mechanism, particularly around terminator where photoemission is marginal/ absent, it may be as large as millions of volts (Rhodes et al., 2020; Mishra and Sana, 2022). It could be disastrous for instrument operations (Jackson et al., 2011, 2015; Rhodes et al., 2020; Mishra and Sana, 2022). In fact, the local plasma environment has a major impact on excessive charge dissipation, and its understanding is warranted to optimize the rover movement and onboard experiments. (Farrell et al., 2008; Jackson et al., 2011, 2015).

Ch3 launched on 14th July 2023 and successfully landed on 23rd August 2023 with a mission life of 14 Earth days. The landing site (LS) is located at the nearside, close to the south pole (69.367621° S, 32.348126° E (Indian Space Research Organisation (ISRO), 2023a)). This chapter aims to investigate the plasma environment over the lunar surface around the Ch3 LS. Note, during the operation time of two weeks, the solar illumination and plasma parameters change at the Ch3 LS, which leads to a temporal variation of the surface potential and subsequent altitudinal profile of the plasma environment (i.e., characterized by the electric field and potential). This dynamic temporal variation could be crucial in shaping the outcomes of the measurements of onboard scientific experiments (for instance, Langmuir probe), which are the key to providing valuable insights into the lunar plasma environment. This analysis brings out an assessment of the local plasma environment over LS, which will be faced during Lander/rover operations, and it could be utilized further in interpreting the Ch3 measurements.

4.2 Illumination condition on the Ch3 LS

The Ch3 LS is located at 69.367621° S, 32.348126° E (Indian Space Research Organisation (ISRO), 2023a). As discussed, the charging and electrostatic environment critically depend on the degree of photoemission, which varies with the solar zenith angle (sza) (Mishra and Bhardwaj, 2019) and the local plasma conditions, the time variation of the sza is one

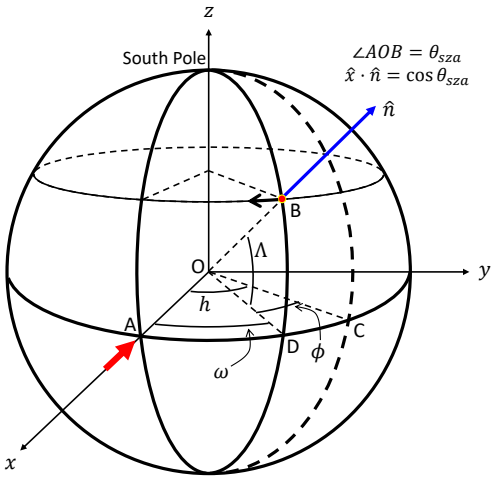

Figure 4.1: Geometrical representation of Solar Zenith Angle ($\theta_{sza} = \angle AOB$). A: Subsolar Point, B: Landing Site (LS, red dot), C: (Latitude, Longitude) = $(0°, 0°)$, D: Intersecting point of the LS's meridian with the equator. The angles, $h = \angle AOC$: hour angle, $\Lambda = \angle DOB$: latitude, $\phi = \angle DOC$: longitude, and $\omega = \angle AOD$: the angle between the meridians of subsolar point and LS. The black arrow near point B represents the direction of LS shift over time due to the Moon's rotation about its axis in due course of its orbital motion around Earth.

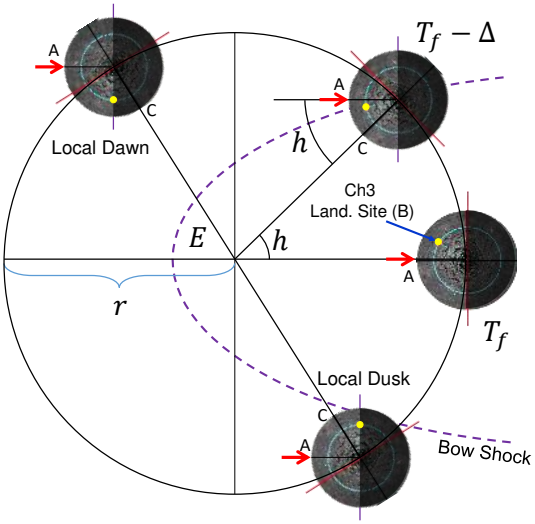

Figure 4.2: South polar orthographic projection of orbital motion of Moon around Earth (point E). T_f: Time of the full Moon. At $t = T_f$, point C reaches A. The yellow bullet point is the location of the Ch3 LS. The hour angle $h = \pi\frac{\Delta[\text{Days}]}{14}$. The LS remains under solar illumination for approximately half-day before $(T_f - 9)$ Days (local dawn) to half-day after $(T_f + 4)$ Days (local dusk). (Not to scale)

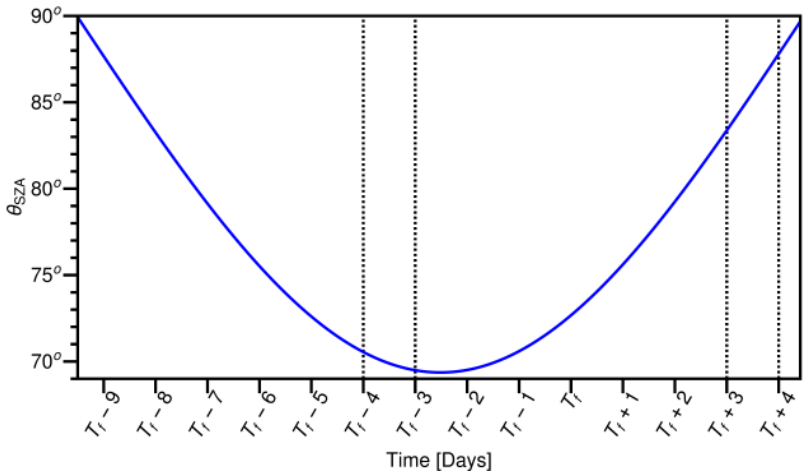

Figure 4.3: Variation of θ_{sza} of Ch3 LS with time. Sunshine will be available for this duration only to operate the solar panels. T_f is the time of the Full Moon. The vertical lines separate different regions, SW: Solar Wind, MSH: Magnetosheath, MS: Inner magnetosphere.

of the key parameters defining the plasma environment over Ch3 LS. We first discuss and derive the solar zenith angle at Ch3 LS using the lunar orbital parameters. The Moon possesses an elliptical (nearly circular) orbit around the Earth with a revolution period of 27.3 days and a synodic period of 29.5 days. The orbital plane of the Earth-Moon system is slightly different from the Sun-Earth plane and has a small axial tilt. For simplicity in the calculation, we neglect the axial tilt and axial shift, and assume the circular orbit is of the Moon with the revolution and synodic period of mean 28 days. Based on these presumptions, Figure 4.1 illustrates the solar zenith angle θ_{sza} of a given location on the Moon that is described by latitude (Λ) of the site and the angle ω. Following geometry in Figure 4.1, the unit vector along $\overrightarrow{OB}$ can be written as

$$\hat{n} = \cos\Lambda\cos\omega\,\hat{x} + \cos\Lambda\sin\omega\,\hat{y} + \sin\Lambda\,\hat{z}\,. \tag{4.1}$$

The direction of unidirectional solar illumination is along $\overrightarrow{AO}$ in the x axis, thus one has

$$\hat{x}\cdot\hat{n} = \cos\theta_{sza}\,, \tag{4.2}$$

or,

$$\cos\theta_{sza} = \cos\Lambda\cos\omega\,, \tag{4.3}$$

where ω depends on the hour angle h and longitude ϕ of the given LS; h is the angle between the meridian (point A) and the prime meridian (longitude 0°, point C). Note, h

depends on time, e.g., 0° for full Moon, and from Figure 4.2, $h = \pm 90°$ are the locations of the first and last quarters. Based on Figure 4.2, we set reference time T_f for a full Moon, and thus one has

$$\omega = h - \phi \quad \text{for} \quad T < T_f\,, \tag{4.4}$$

$$\omega = \phi \quad \text{for} \quad T = T_f\,, \tag{4.5}$$

$$\omega = h + \phi \quad \text{for} \quad T > T_f\,. \tag{4.6}$$

Figure 4.2 suggests that the Ch3 LS will be illuminated by solar radiation from the half day before $T_f - 9$ to half day after $T_f + 4$. The variation of θ_{sza} in this due course is shown in Figure 4.3 for different time frames with respect the full moon. As evident from Figure 4.3 that when Moon enters the tail lobe, θ_{sza} is nearly 70°, within the plasma sheet, the θ_{sza} varies approximately between 70° and 80° and when Moon leaves the tail lobe θ_{sza} varies approximately between 80° and 85°.

4.3 Plasma parameters around Ch3 LS

As the Moon orbits around the Earth, it passes through various plasma populations. In the operation time of Ch3, the LS passes through solar wind plasma as well as through the Earth's magnetospheric plasma. The plasma conditions at the Ch3 LS is highly dynamic and subject to significant variability. As a result, it is expected that a complex electric potential structure develops in the vicinity of the LS. Understanding the nature and characteristics of this plasma population and potential structure is important for interpreting Ch3 data connected with the plasma environment, as the potential structure determines how does the plasma and the charged dust particles interact with the rover/lander surfaces and onboard instruments.

To simulate the realistic scenario, data from the *ARTEMIS P2* spacecraft (former *THEMIS-C* probe) is used as an input plasma parameter (Angelopoulos, 2011). The data of the THEMIS mission is available on `http://cdaweb.gsfc.nasa.gov/cdaweb/istp_public/`. We choose a long time pass between 17th January 2013 and 31st January 2013, covering typical plasma parameters near the Ch3 LS based on (Vaverka et al., 2016). The data have been resampled to 1-hour equidistant intervals with a reference time $T_f =$ 27th January 2013 04:30UTC (date and time of full Moon). Figures 4.4 and 4.5 illustrate a typical plasma density and temperature variation near the illuminated Ch3 LS. Due to the

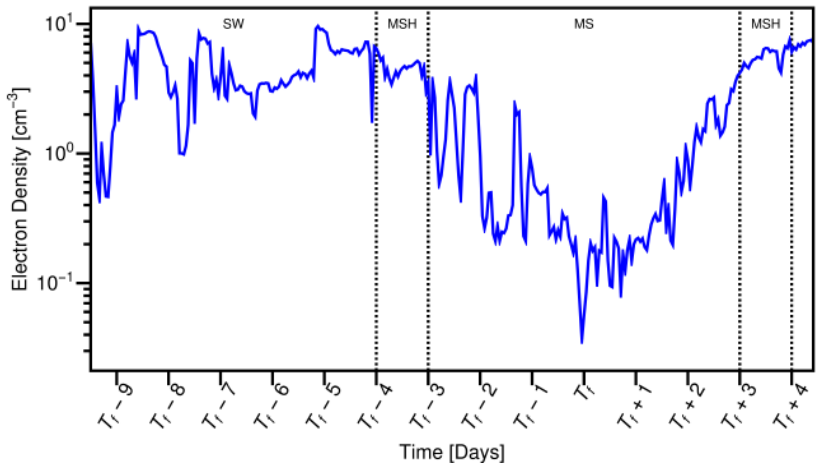

Figure 4.4: Sample electron density around Ch3 LS during the passage measured by THEMIS-C probe (Angelopoulos, 2011). T_f is the time of the Full Moon. The vertical lines separate different regions, SW: Solar Wind, MSH: Magnetosheath, MS: Inner magnetosphere.

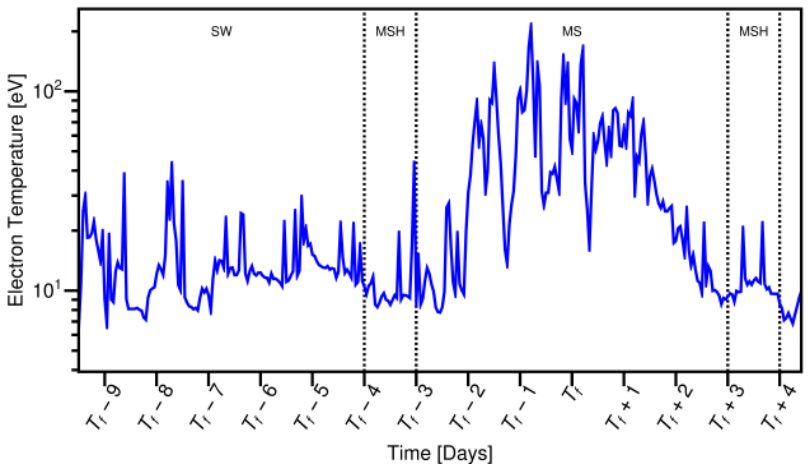

Figure 4.5: Sample electron temperature around Ch3 LS during the passage measured by THEMIS-C probe (Angelopoulos, 2011). T_f refers to the time of the Full Moon. The vertical lines separate different regions, SW: Solar Wind, MSH: Magnetosheath, MS: Inner magnetosphere.

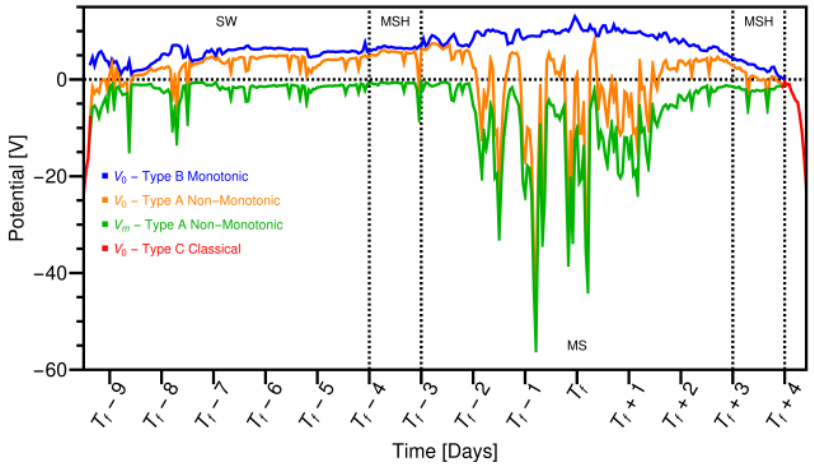

Figure 4.6: Temporal variation of the lunar surface (V_0) and dip (V_m) potential around Ch3 LS during the passage. T_f is the time of the Full Moon. The vertical lines separate different regions, SW: Solar Wind, MSH: Magnetosheath, MS: Inner magnetosphere.

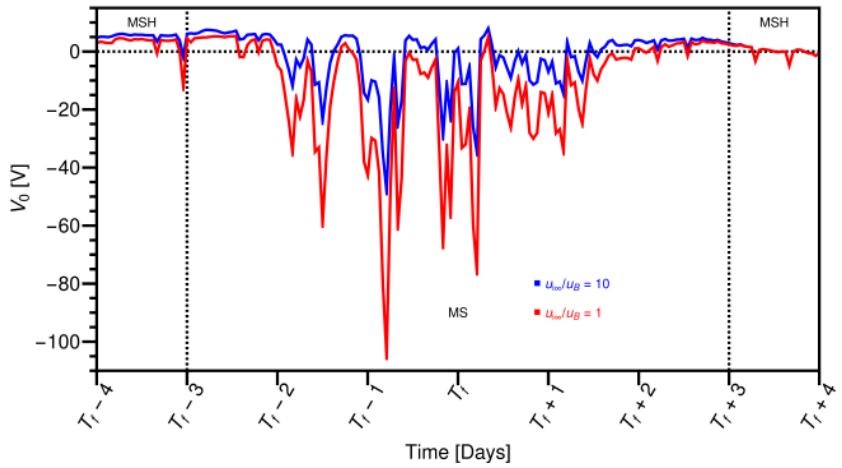

Figure 4.7: Temporal variation of the lunar surface (V_0) potential around Ch3 LS during the passage through Earth's magnetosphere for different $u_{i\infty}/u_B$.

large computation time, we use 1-hour averaged data. This, however, results in missing significant high energy spikes (> 100 eV) in the THEMIS-C data.

4.4 Numerical results and discussions

4.4.1 Surface and dip potential

In order to describe the plasma environment nearby LS, we need to identify the following input parameters: T_0, W_f, $\chi(\lambda)$, f_λ, θ_{sza}, n, T_e, κ and $u_{i\infty}$. Here we use $W_f = 5$ eV throughout our calculation. Following Nitter et al. (1998), $u_{i\infty}/u_B = 10$ is taken for the calculations in analysis — it is also considered as a variant to illustrate its significance

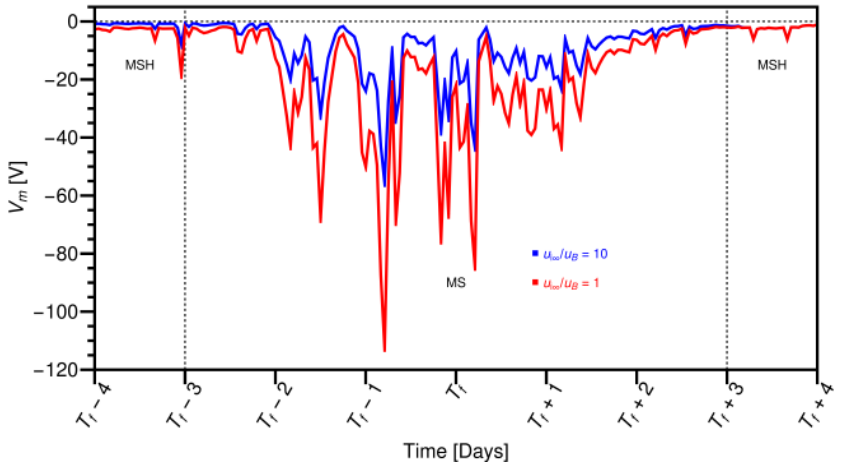

Figure 4.8: Temporal variation of the dip (V_m) potential around Ch3 LS during the passage through Earth's magnetosphere for different $u_{i\infty}/u_B$.

on local plasma environment and surface charging. $\kappa = 3$ is considered for the present calculation (Pierrard and Lazar, 2010). We use an empirical relation of surface temperature's θ_{sza} dependence given by Mishra and Bhardwaj (2019); it may be approximated as $T_0(\theta_{sza}) = T_0(\theta_{sza} = 0)\left[1 - \left(\frac{5}{4\pi}\right)\theta_{sza}\right]$. Here θ_{sza} is in radian. The temporal variation of θ_{sza} illustrated in Figure 4.3 in due course of 14 days of LS illumination. Other significant parameters, viz., the photon flux, and ambient plasma density/ temperature have been taken from FISM2 (Figures 2.1 and 2.4) and THEMIS-C (Figures 4.4 and 4.5) descriptions as discussed in the earlier sections.

Figure 4.6 illustrates the temporal variation of the surface and dip potential around Ch3 LS during the passage. A very dynamic variation in the potential values has been observed throughout the passage. Near the local dawn (half day before $T_f - 9$) and local dusk (half day past $T_f + 4$), due to marginal photoemission, the surface acquires a negative potential which might result in a classical Type C sheath structure. Here we expect the formation of an ion-dominated positive space charge region within the sheath. Within $(T_f - 9\,, T_f + 4)$ the photoemission from the surface becomes significant and the model predicts the possible existence of two types of potential structures, viz., Type A and B sheaths. When Moon passes through solar wind, the surface primarily acquires a finite positive surface potential and a small negative dip potential corresponding to Type A sheath. In addition to that Type B sheath also predicts a finite but slightly higher positive surface potential. As the Moon enters the Earth's magnetosphere, the surface majorly acquires a negative surface potential corresponding to Type A sheath which represents a more stable solution. Based on the THEMIS-C 1-hour average data, it is observed that the

surface potential corresponding to Type A sheath may reach around -48 V and dip potential around -55 V near $(T_f - 1)$. A rapid variation of Type A surface and dip potential have been observed during the magnetosphere passage due to rapid variation of interacting plasma parameters. This change of plasma parameters and potential structures may cause complex charging of the object operating at the Ch3 LS. Our analysis suggests that during the Ch3 LS passage, i.e., $(T_f - 9,\ T_f + 4)$, both Type A and Type B potential structures can exist for each θ_{sza} values, and thus it is essential to comment on the stability of these solutions. In the case of a plasma sheath around a photoemitting object, the total potential energy of the system for a particular solution decides whether the solution is stable or not. According to Guernsey and Fu (1970), the total potential energy can be expressed as

$$U = -\frac{\varepsilon_0}{2} \int_0^\infty \left(\frac{dV}{dx}\right)^2 dx\,. \tag{4.7}$$

From this equation, we can see that the total potential energy is negative for both Type A and B. So both solutions are stable. However, the solution with higher potential energy is a short-lived metastable solution that ultimately transforms into a low-energy, more stable state. For typical solar wind conditions, in Chapter 3, we quantitatively show that for higher values of θ_{sza}, non-monotonic Type A potential structure is a more stable solution. This is in good agreement with the measurements of Halekas et al. (2008) (see Figure 7 and paragraphs [46] and [49] in Halekas et al. (2008)), which favors the existence of stable non-monotonic potential structure with a large negative surface and dip potential. Hence, in this case study, the focus is on Type A sheath which represents a more stable sheath configuration.

For calculations, we have considered $u_{i\infty}/u_B = 10$ for the solar wind/ ambient plasma. However, the solar wind plasma's bulk speed significantly lowers near the bow shock (Ma et al., 2020). Moreover, $u_{i\infty}$ for Earth's magnetosphere plasma may differ due to different originating sources. Figures 4.7 and 4.8 illustrates the variation of V_0 and V_m for different $u_{i\infty}/u_B$. We notice that the surface and dip potential values decrease with decreasing $u_{i\infty}/u_B$. It may be understood in terms of decreasing ion current available for the charging. The figures also illustrate that for the plasma ions with a smaller $u_{i\infty}$ the LS surface potential might reach around -100 V and dip potential around -115 V near $(T_f - 1)$. Hence, the variation in $u_{i\infty}$ may also be significant in determining the altitudinal potential/ field profile within the photoelectron sheath.

4.4.2 Sheath structure

After acquiring a notion of the lunar surface potential, we next illustrate the sheath structure using these known V_0 and V_m values as boundary conditions. Note, determining the sheath structures for the entire THEMIS-C data requires a large computation time and hence we chose the typical θ_{sza} values which cover the solar illuminated span of Ch3 LS (i.e., from dawn to dusk) while its passage through Earth's magnetospheric plasma (see Figure 4.3). We illustrate the altitudinal sheath potential profile for $\theta_{sza} = 70^\circ$, 75°, 80°, and 85° using THEMIS-C plasma parameters at given θ_{sza}.

Figure 4.9 illustrates typical sheath structures during the LS passage through the Earth's magnetosphere. The surface acquires negative potential for $\theta_{sza} = 70^\circ$, 75°, due to the accretion of high-temperature plasma electrons. This surface potential decrease to a more negative potential value, i.e., a minimum, altitudinally above the surface. A negative space-charge region develops between the surface and the location of V_m. The effect of V_m screens out within the positively charged region spanning up to 600 m. For $\theta_{sza} = 80^\circ$, 85° the surface acquires small positive potential due to a competing effect in charging currents connected with increasing ion number density and decreasing electron temperature. The sheath span in this case is screened out within 100 m altitude. This variation in the polarity of the surface potential might cause large differential charging of the object altitudinally operating at Ch3 LS — it may drive local electric fields on the operating surface and might alter any plasma measurements.

In dealing with computational constraints, we have taken 1-hour averaged THEMIS-C data. However, in this approach, transient high-temperature spikes are missed from the data that may hold significance locally. These high-temperature spikes result in more negative surface charge due to the enhanced plasma electron collection current. In order to illustrate its significance, we use Lunar Prospector-based Electron Reflectometer data reported by Halekas et al. (2008). They report terrestrial magnetosphere plasma parameter as follows: n ranges from 0.001 to 0.5 cm^{-3}, $T_e < 0.1$ keV for tail lobe and n ranges from 0.01 to 1 cm^{-3}, T_e from 0.1 to 2 keV for plasma sheet. These parameters are exotic in terms of plasma density and temperature, which can be used to visualize the effect of the high-temperature spikes. We use $n_{i\infty} = 0.25\,\mathrm{cm}^{-3}$, $T_e = 100$ eV to derive a typical sheath structure for the tail lobe with $\theta_{sza} = 70^\circ, 80^\circ, 85^\circ$ based on Figure 4.3. Moreover, for the plasma sheet, we use $n_{i\infty} = 0.5\,\mathrm{cm}^{-3}$, $T_e = 1$ keV and $\theta_{sza} = 70^\circ, 75^\circ, 80^\circ$ in calculations.

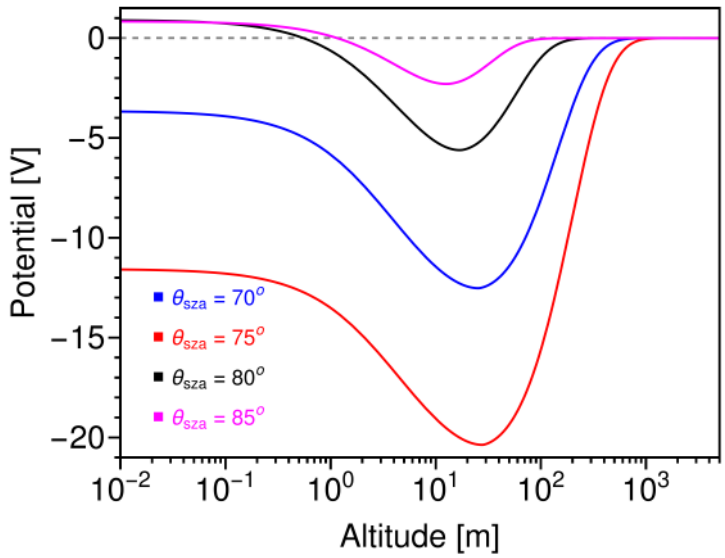

Figure 4.9: Non-monotonic (Type A) potential structure for different values of θ_{sza} using THEMIS-C data. Parameter Used: For $\theta = 70°$: $n_{i\infty} = 0.3\,\mathrm{cm}^{-3}$, $T_e = 60.6$ eV. For $\theta = 75°$: $n_{i\infty} = 0.2\,\mathrm{cm}^{-3}$, $T_e = 82.4$ eV. For $\theta = 80°$: $n_{i\infty} = 1.3\,\mathrm{cm}^{-3}$, $T_e = 25.3$ eV. For $\theta = 85°$: $n_{i\infty} = 5.5\,\mathrm{cm}^{-3}$, $T_e = 10.7$ eV.

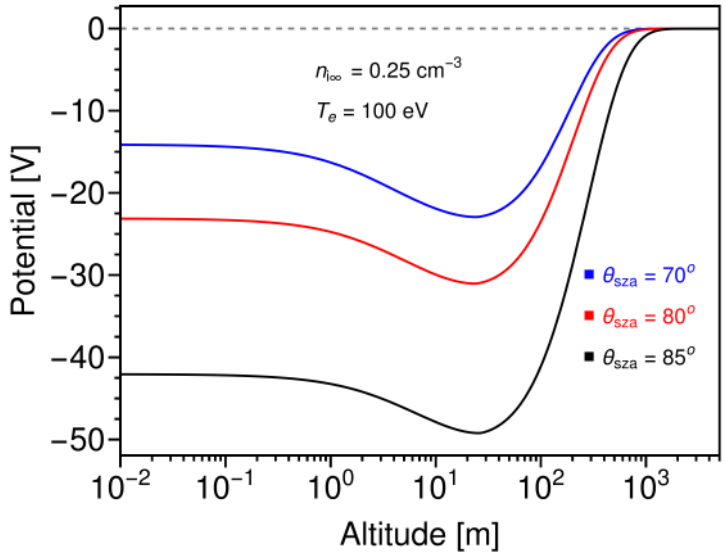

Figure 4.10: Non-monotonic potential structure for different values of θ_{sza} using the typical tail lobe parameter $n_{i\infty} = 0.25\,\mathrm{cm}^{-3}$, $T_e = 100$ eV (Halekas et al., 2008).

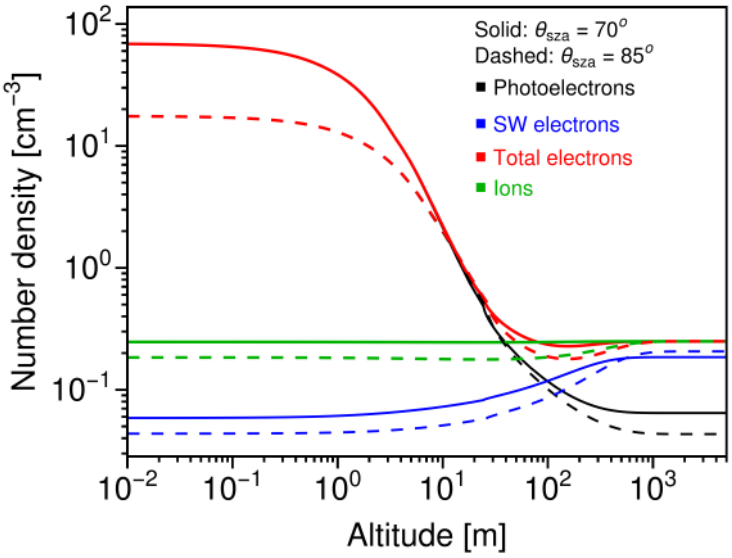

Figure 4.11: Altitude profiles of ion density n_{si} (Green), plasma electron density n_{se} (Blue), photoelectron density n_{pe} (Black), and total electron density n_{te} (Red) within Non-monotonic potential structure using the typical tail lobe parameter $n_{i\infty} = 0.25\,\mathrm{cm}^{-3}$, $T_e = 100$ eV (Halekas et al., 2008). Solid Line: $\theta_{sza} = 70°$, Dashed Line: $\theta_{sza} = 85°$.

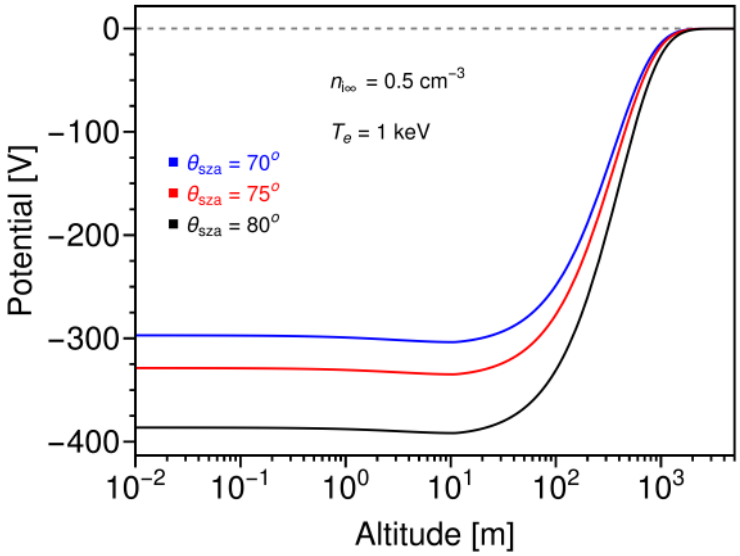

Figure 4.12: Non-monotonic potential structure for different values of θ_{sza} using the typical plasma sheet parameter $n_{i\infty} = 0.5\,\mathrm{cm}^{-3}$, $T_e = 1$ keV (Halekas et al., 2008).

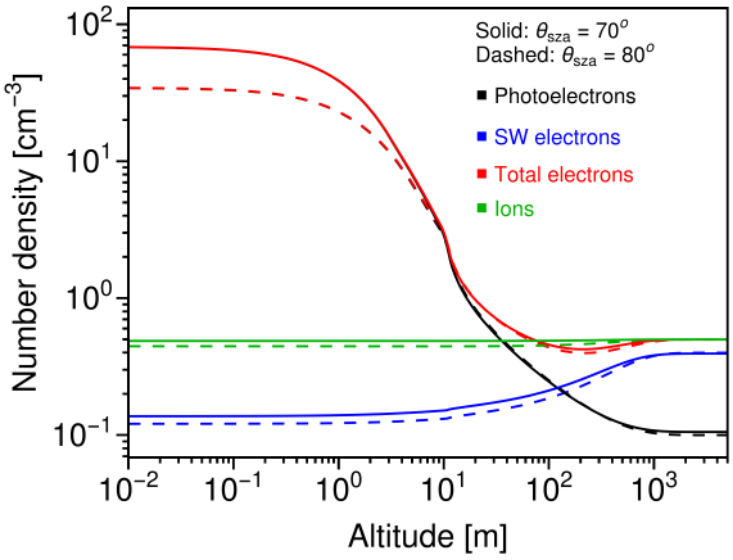

Figure 4.13: Altitude profiles of ion density $n_{\rm si}$ (Green), plasma electron density $n_{\rm se}$ (Blue), photoelectron density $n_{\rm pe}$ (Black), and total electron density $n_{\rm te}$ (Red) within Non-monotonic potential structure using the typical plasma sheet parameter $n_{i\infty} = 0.5\,{\rm cm}^{-3}$, $T_e = 1$ keV (Halekas et al., 2008). Solid Line: $\theta_{sza} = 70^{\circ}$, Dashed Line: $\theta_{sza} = 80^{\circ}$.

Figure 4.10 illustrates the sheath (electric potential) profile for the LS passage through the tail lobe. The surface acquires negative potential ranges from -15 to -42 V and a potential minimum ranges -23 to -49 V from $\theta_{sza} = 70^{\circ}$ to 85° respectively. The sheath spans altitudinally up to 800 m. Figure 4.11 shows the density profiles within the sheath. Within this double-layer structure, a photoelectron-dominated dense negative space charge region exists near the surface for $x < x_m$. For $x > x_m$, a low-density plasma ion-dominated space charge region exists. For the tail lobe parameter, electron density at the surface is around 20 cm^{-3}. A significantly high negative potential and extended sheath have been observed for the LS passage through the plasma sheet — this is illustrated in Figure 4.12. For different values of θ_{sza}, the surface potential varies from -297 to -386 V and a potential minimum ranges from -304 to -392 V from $\theta_{sza} = 70^{\circ}$ to 80° respectively, and the sheath extends up to 2 km. The density profile for the plasma sheet parameters has been shown in Figure 4.13. For the plasma sheet parameter, the electron density at the surface is around 40 cm^{-3}. The simplest means of measuring the local plasma parameters is by the Langmuir probe (LP) (Hartzell et al., 2023). The key plasma parameters are the electron (ion) density and their temperature. The LP might detect these parameters nearby the surface — the photo-illuminated regions are dominated by the photoelectrons. As discussed in Chapter 2.3.2, there exist three distinct populations of photoelectrons; their mean energies in the vicinity of the surface are given in Table 4.1.

θ_{sza}	$V_0 - V_m$	$< E_m >_0$	$< E_m >_{pef}$	$< E_m >_{pec1}$	$< E_m >_{pec2}$
70°	8.9	4.46	11.71	4.19	10.15
75°	8.8	4.45	11.62	4.18	10.07
80°	6.5	4.45	9.10	3.46	7.97
85°	3.1	4.46	6.72	1.80	5.48

Table 4.1: Mean energies of photoelectrons in eV of various populations for different values of θ_{sza}. The other parameters used are the same as in Figure 4.9.

This suggests that LP will encounter different photoelectron populations however, as discussed in Chapter 2.3.2, the weighted sum of the average energies in each population equals with the mean energy of photoelectrons from the uncharged surface $< E_m >_0$, the photoelectron temperature for the above-discussed cases has been found to be $T_{pe} = (2/3) < E_m >_0 \approx 3$ eV.

The results illustrated in this study correspond to the most stable Type A non-monotonic sheath solution with a surface potential $V_{0,N}$ and a negative minimum $(V_m < 0)$ such that $(V_{0,N} - V_m) \geq 0$. These solutions are prominent at higher lunar latitudes, where the local plasma flux contribution becomes significant compared to the photoemission current. The local minima might trap the low-energy photoemitted electrons and reflect incoming plasma electrons of insufficient energy $(< |V_m|)$. V_m takes the magnitude equivalent to the energy of the incoming plasma electron temperature, and the difference $(V_{0,N} - V_m)$ takes a positive value of a magnitude comparable to the trapped photoelectron temperature (i.e., of a few volts) (Guernsey and Fu, 1970; Fu, 1971; Halekas et al., 2008). The significant negative magnitude of V_m yields a negative surface potential as an acceptable solution. For instance, in the case of Earth's magnetospheric tail lobe/ plasma sheet, though the plasma density is very low, the electron temperature is quite large (around 100's V). It results in a large negative value of V_m, i.e., significantly higher than the trapped photoelectron temperature (few V), and the surface acquires a large negative potential — this is shown in Figures 4.10 and 4.12. At this point, it would be appropriate to comment on the monotonic sheath solutions of Poisson's equation. These solutions represent the most stable structures at lower latitudes (nearby the subsolar point, θ_{sza} near 0°) under normal solar wind conditions where photoemission significantly dominates over local plasma currents — this leads to stable Type B (monotonically decreasing sheath) with a positive surface potential $(V_{0,M})$ of a few volts (Guernsey and Fu, 1970; Fu, 1971; Nitter et al., 1998).

From these results illustrated in Figures 4.10, and 4.12, we note that the potential structures can significantly differ under real conditions from the average value-based re-

sults obtained using THEMIS-C data. As discussed, this variability is attributed to the complex and dynamic plasma environment surrounding the Moon. The variation of the plasma density and temperature significantly affects the charging currents and, therefore, the sheath structure in the vicinity of the lunar surface. It suggests the necessity of accurate determination of the local plasma conditions, i.e., one of the major contributions from LP measurements during Ch3 campaign.

In this study, we examine the effects of various plasma conditions (Solar wind and Earth's magnetospheric plasma) on the potential structure over Ch3 LS, predicting a dynamic variation of the plasma environment properties. In the low photoemission region near the local dawn (half day before $T_f - 9$) and local dusk (half day past $T_f + 4$), our model predicts a typical Type C classical sheath with a negative surface potential and positive space charge region with low electron density. Between $(T_f - 9\,, T_f + 4)$ Type A non-monotonic potential structures exists with surface potential ranges from 8 to -48 V and potential minimum ranges from -0.5 to -55 V (at an altitude of 15 to 20 m). In addition, the existence of Type B monotonic sheaths with surface potential ranges from 1 to 12 V is also predicted. Since θ_{sza} varies between 69.36° and 90°, as discussed in Chapter 3, Type A sheath is likely to be more stable. However, in both cases, a photoelectron-dominated negative space charge region is created near the vicinity of the surface with a typical photoelectron density ranging from 10 to 40 cm^{-3} around 1 m above the surface. The plasma (solar wind) electron density decreases by 20 to 30% near the surface within Type A and B sheaths. The Langmuir probe (LP) (RAMBHA payload) on board Ch3 lander may have encountered these estimated sheath populations.

In a press release, plots of several LP voltage sweeps were shared in a single image, along with a comment suggesting that these LP IV curves indicates an electron density of approximately 5 to 30 cm^{-3} in the early morning hours of the lunar day (Indian Space Research Organisation (ISRO), 2023b). As of now, detailed results from the RAMBHA Langmuir probe measurements taken on the Moon are still awaited. Since the sheath population density varies with altitude, measurements of Ch3 are very local at a single altitude. In contrast, the Rashid-1 rover of the Emirates Lunar Mission (ELM) carried four Langmuir Probes mounted at different vertical locations on the rover, to measure the altitudinal variation of plasma parameters (Clausen et al., 2025). Unfortunately, the landing of ELM in the Atlas crater was unsuccessful, and no measurements were conducted.

Although the Langmuir probe is one of the simplest instruments to measure plasma parameters (Hartzell et al., 2023), in a rarefied lunar plasma medium, measure-

ments of photoelectron-dominated electron cloud may be challenging. In this case, the illuminated part of the probe and the spacecraft emit a significant amount of photoelectrons, which may dominate the actual constituents of the plasma environment. This will give a significantly different IV curve (Eriksson et al., 2007) and plasma estimates. In such cases, it is necessary to extract the photocurrent from the probe and develop a photoemission removal protocol to obtain an accurate measurement of the unperturbed plasma environment (Johansson et al., 2017).

Any stationary object (lander) within the sheath also undergoes electrostatic effects due to the presence of ambient plasma electrons/ ions and photoelectrons within the non-neutral space charge region and subsequent photoemission from the operating surface. Since a negative space charge region exists near the surface for a Type A potential structure which typically extends nearly up to 20 m, the lander/ rover is supposed to reside in the negative space charge region (Figure 4.13). Within this negatively charged region sheath, the ambient electrons might act as a source of negative charging of the object — in the absence of any electron emitting mechanism, the object might acquire a negative potential. However, as the object is also exposed to the energetic UV radiation in illuminated regions, the photoemission from the object might counter the electron collection as a source of positive charging current, and the competing effect of the two currents with dominant photoemission might yield the surface at a finite positive potential (Jackson et al., 2015). Physically, the effective charge/potential on the object is determined by the flux balance on the surface. Hence, the environment developed around the spacecraft may significantly influence the surrounding sheath by creating its own potential structure around the object. In that aspect, comprehensive numerical modeling of the interaction between the rover and plasma in a lunar environment should be conducted (Clausen et al., 2025).

Another significant mechanism leading to electrostatic charging of the operating surfaces is frictional charging, particularly applicable to the movement on the charged lunar surface. For instance, due to triboelectrification, the objects roving over lunar regolith may accumulate the charge of the order of $\sim$ MV, and the dissipation of these charges becomes crucial for the long-term operation of instruments (Rhodes et al., 2020; Mishra and Sana, 2022). Dissipation of charges highly depends on the local plasma environment (Farrell et al., 2008; Jackson et al., 2011, 2015). Although, Jackson et al. (2015) suggests within the photoelectron sheath any objects reach equilibrium with small electric potential very quickly, however, objects within a high negative surface potential acquire a similar amount of initial charges, which may take longer dissipation time and may affect any

measurements of the instrument near the wheel. Considering this, the rover/ instrument operation may be challenging on the locations exhibiting insufficient photoemission, for instance, LS passage near dawn/ dusk.

Our results indicate that the plasma environment obtained from THEMIS data, which represents a moderate sheath profile (i.e., electric potential/ field), is anticipated not to pose any significant threat to the instrument's operation during the Ch3 campaign — the possible implications due to this could easily be maneuvered with established rectification techniques. However, it is essential to note that a significant concern could be high negative potential development within the sheath on Ch3 LS, which is caused by intense transient high energy spikes in the plasma electron population connected with various solar activities and Earth's magnetospheric effects. In this case, the sheath may comprise the electrical environment at a few 100's volts. In such a scenario, the efficient operation of the instruments could be challenging as it could obstruct precise measurements and be detrimental to operating electronics. So, precautionary measures to deal with these conditions should be taken care of during the campaign.

The present study brings out some intriguing physics effects on the photoelectron sheath structure around Ch3 LS under different plasma conditions (solar wind and Earth's magnetospheric plasma). However, the analysis is based on certain simplified assumptions. The analysis ignores the effect of the magnetic field considering its nominal magnitude and marginal effects on the charging currents. For instance, note that Ch3 LS is not near the magnetic anomaly region, but the Moon encounters the Earth's magnetic field of the order of 10^{-9} to 10^{-8} T as it passes through the magnetotail (Hones, 1985; Harada, 2015; Popel et al., 2022). However, due to the large gyro-radius around 1.5 and hundreds of km of the plasma electrons and ions, respectively, and the significantly smaller region of our interest, the effect of the magnetic field on charging currents and hence on the surface charge may safely be ignored (Mishra and Bhardwaj, 2020). To avoid the complexity in the analysis and numerical computations, the contribution of secondary electron emission (SEE) from the lunar surface, which is marginal compared to the photoemission in the present context, is also ignored. The effect of levitated dust particles on the sheath formation has also been ignored in this analysis considering very low dust density within the lunar sheath ($\approx 10^{-3}\text{cm}^{-3}$; (Popel et al., 2013)). However, photoemission from levitated dust may slightly increase the electron population density within the sheath. Intuitively, it may result in decreasing the sheath expansion of the monotonic Type B sheath and reducing the value of x_m for the Type A sheath. On the other hand, the increase in photoemitted

electrons may increase the Type C sheath thickness. As noted, for the parameter space of our interest in the present context, these simplifications contribute insignificantly, and the analysis is very well applicable for this case study, i.e., in accessing the plasma environment at the LS of Ch3.

4.5 Summary

As a case study, the plasma environment around Ch3 LS has been studied utilizing the analytical photoelectron sheath model discussed in Chapter 3. Numerical simulations of sheath formation near the lunar surface have been carried out during the passage of sunlit Ch3 LS through the solar wind and Earth's magnetospheric plasma. Our study suggests all three kinds of potential structures (Type A, B, & C) exist at the Ch3 LS at different times of its exposure to solar illumination. When Ch3 LS passes through solar wind plasma, θ_{sza} varies approximately between 70° and 90°. For θ_{sza} close to 90°, due to marginal photoemission, the surface acquires a finite negative potential, and a classical Type C sheath exists around Ch3 LS. The temporal existence of Type C sheath is noticed to be small only for approximately one day (half day each during local dusk and dawn). Between $T_f - 9$ to $T_f + 4$, based on θ_{sza} and the plasma parameters, we have shown that both Type A and Type B potential structure exists over sunlit Ch3 LS. Between Type A & B, the solution with higher potential energy represents a short-lived metastable solution that ultimately transforms into a low-energy, more stable state. Our calculations suggest the non-monotonic Type A sheath represents a more stable potential structure around Ch3 LS. Halekas et al. (2008) measurements also favors the possibility of stable non-monotonic structures in such physical conditions. The electric potential variation is very dynamic throughout the passage of Ch3 LS, and the surface potential varies between 8 to -48 V and the potential minimum between -0.5 to -55 V (at an altitude of 15 to 20 m). For exotic conditions, for instance, within Earth's magnetospheric plasma sheet, the surface potential varies from -297 to -386 V and a potential minimum ranges from -304 to -392 V from $\theta_{sza} = 70°$ to 80° respectively. This study predicts the photoelectron density ranges from 10 to 40 cm^{-3} and the temperature of photoelectrons around 3 eV near the surface of Ch3 LS, which could be verified by the in situ measurements.

The implications of these results have been discussed in the analysis that may be useful in interpreting the data connected with the plasma environment obtained through the Chandrayaan 3 campaign.

Chapter 5

Plasma sheath around lunar nightside

5.1 Introduction

The characteristics of the plasma sheath around the Moon significantly differ from dayside to nightside. As discussed in previous chapters, on the dayside, the primary mechanism driving surface charging is UV-induced photoelectrons, resulting in the acquisition of a finite surface potential. The surface potential is screened by the emitted photoelectrons and the surrounding plasma constituents, giving rise to a lunar photoelectron sheath (Nitter et al., 1998; Poppe and Horányi, 2010; Sodha and Mishra, 2014; Mishra and Bhardwaj, 2019). However, the surface charging on the lunar night side is dominantly created by ambient plasma electrons. Surface acquires a finite negative potential, and classical Debye sheath forms around the nightside lunar surface (Nitter and Havnes, 1992; Nitter et al., 1998; Halekas et al., 2002, 2005; Colwell et al., 2007). Typically, the lunar surface potential spans from $+10$ V to -4 kV in relation to the surrounding plasma from dayside to nightside (Halekas et al., 2008; Saito et al., 2014). While numerous studies have extensively investigated surface charging of the lunar nightside, there has been a notable lack of attention directed towards understanding the formation of the plasma sheath in the lunar nightside (Halekas et al., 2002, 2005; Stubbs et al., 2007; Halekas et al., 2008, 2009a; Chandran et al., 2013; Saito et al., 2014; Kureshi et al., 2020). The work by Nitter and Havnes (1992) provided a theoretical analysis of the formation of a plasma sheath above the surfaces of solid bodies exposed to space plasma, specifically the electron and ion currents are considered in their analysis. Their formulation, however, might not apply to the

realistic nightside scenario as the Moon faces various plasma populations in its orbit.

Based on Lunar Prospector measurements of electrons in the ambient plasma population, Halekas et al. (2008) has reported the various plasma parameters around the Moon as follows: Terrestrial magnetosphere: Tail lobe $(0.001 — 0.5\,\mathrm{cm}^{-3}, < \ 0.1\,\mathrm{keV})$; Plasma sheet $(0.01 — 1.0\,\mathrm{cm}^{-3}, 0.1 — 2\,\mathrm{keV})$; Solar wind $(0.5 — 10\,\mathrm{cm}^{-3}, 5 — 30\,\mathrm{eV})$; Plasma wake $(0.001 — 0.1\,\mathrm{cm}^{-3}, 50 — 150\,\mathrm{eV})$; SEP event $(0.001 — 0.1\,\mathrm{cm}^{-3}, 0.05 — 1\,\mathrm{keV})$. These hot electrons within the Earth's magnetospheric plasma may give rise to Secondary Electron Emission (SEE) from the lunar surface. This may alter the potential structure of the nightside lunar surface, and the plasma sheath structure may differ from the Classical Debye sheath. The importance of SEE on dust and surface charging in space has been highlighted in the early literature (Chow et al., 1993; Horányi, 1996; Horányi et al., 1998; Abbas et al., 2010; Richterová et al., 2012; Dukes and Baragiola, 2013; Vaverka et al., 2013, 2016; Němeček et al., 2018). However, none of these studies have explored the SEE effect on the sheath formation. The study of Wang et al. (2016a) experimentally demonstrated the sheath formation in the presence of SEE. Experimentally, they have shown the possibility of three kinds of sheaths, viz., (i) Classical Debye type sheath with negative surface potential, (ii) Inverse sheath with positive surface potential, and (iii) Non-monotonic sheath with potential minima away from the solid surface. The study of sheath formation due to SEE around the lunar surface holds significant importance from both a scientific and a mission perspective. Due to SEE, the potential and field structure differ from the Debye sheath, which could lead to different dust charging and dynamics around the dark side of the Moon. Understanding the characteristics of the near-surface space charge region is essential for the design of instruments intended for in situ plasma measurement. SEE in the nightside could add significant spatial and temporal variability to the near-surface plasma environment. Inspired by the work of Wang et al. (2016a), we have assessed the possibility of these three types of sheath formation considering Maxwellian primary and secondary electrons and cold ions. Our analysis didn't find a non-monotonic sheath in the presence of SEE, but it shows the possibility of the inverse sheath in the high plasma electron temperature regimes. This chapter presented an analytical formulation of the inverse sheath in the lunar nightside (without photoemission) and the possible lunar and plasma parameter regimes. For simplicity in calculation and to establish the conceptual basis, both primary and secondary electrons are assumed to follow a simplified Maxwellian distribution.

5.2 Debye sheath

In the absence of photoemission and SEE, a classical Debye sheath is anticipated when the lunar surface is exposed to ambient plasma Nitter and Havnes (1992); Nitter et al. (1998). Due to dominant electron accretion, the surface acquires a finite negative potential $(V_0 < 0)$, which has been screened by positively charged ions. So, a positive space charge region is created between the negatively charged surface and quasineutral plasma, and this region is called the Debye sheath. In the context of the Moon, the potential profile of the Debye sheath can mathematically be derived by considering the incoming Maxwellian plasma electrons and cold ions that enter the sheath with a Bohm speed (Bohm, 1949). The potential structure can be found by solving the following Poisson's equation

$$\frac{d^2V}{dx^2} = -\frac{e}{\epsilon_0}\left(n_i - n_{e,free} - n_{e,capt}\right), \tag{5.1}$$

where $n_{i(e)}$ is the ion (electron) density. V is the potential at altitude x. e and ϵ_0 are the electronic charge and permittivity in free space. Since the surface acquires a finite negative potential, which monotonically increases to zero, there will be two populations of electrons within the Debye sheath: (i) Plasma electrons that hit the surface are "free plasma electrons $(n_{e,free})$", and (ii) Plasma electrons that have been reflected by negative potential barrier in the sheath are called "captured plasma electrons $(n_{e,capt})$".

At the sheath edge $(x \to \infty)$, the distribution function of plasma electrons is given by

$$f_e(\infty, E) = n_{e\infty}\sqrt{\frac{1}{4\pi kT_eE}}\exp\left[-\frac{E}{kT_e}\right], \tag{5.2}$$

where $n_{e\infty}/2$ is the density of the plasma electrons that travel toward the uncharged surface at infinity. E and T_e are the energy and temperature. k is the Boltzmann constant. From the conservation of energy, at an altitude x we can write

$$E(x) - eV(x) = E_\infty. \tag{5.3}$$

So, the distribution function of plasma electrons at an altitude x

$$f_e(x, E) = n_{e\infty}\sqrt{\frac{1}{4\pi kT_eE}}\exp\left[-\frac{E}{kT_e} + \frac{eV(x)}{kT_e}\right]. \tag{5.4}$$

Using Eq. 5.4, we can write the plasma electron densities as

$$n_{e,free}(x) = \int_{E_m}^{\infty} f_e(x,\, E)\, dE = \frac{n_{e\infty}}{2} \exp\left[\frac{eV(x)}{kT_e}\right] \left[1 - \mathrm{erf}\left[\sqrt{\frac{e\big(V(x) - V_0\big)}{kT_e}}\right]\right], \quad (5.5)$$

and

$$n_{e,capt}(x) = 2\int_{0}^{E_m} f_e(x,\, E)\, dE = n_{e\infty} \exp\left[\frac{eV(x)}{kT_e}\right] \mathrm{erf}\left[\sqrt{\frac{e\big(V(x) - V_0\big)}{kT_e}}\right], \quad (5.6)$$

where $\mathrm{erf}(u) = 2/\sqrt{\pi}\int_0^u \exp\left(-t^2\right) dt$, V_0 is the lunar surface potential. $E_m = e\big(V(x) - V_0\big)$ is the minimum energy in the x direction at x to overcome V_0. Factor 2 in Eq. 5.6 comes from the fact that captured electrons consist of two equal parts, moving in opposite directions. From the ion energy conservation and continuity, we can write (Nitter et al., 1998)

$$n_i(x) = \frac{n_{i\infty}}{\sqrt{1 - \frac{2eV(x)}{kT_e}}}, \quad (5.7)$$

where $n_{i\infty}$ is ion density at infinity.

5.2.1 Lunar surface potential

To determine the lunar surface potential, following Nitter et al. (1998), we assume the charge neutrality and flux balance at the sheath edge. So, quasineutrality gives

$$n_e(\infty) = n_i(\infty), \quad (5.8)$$

or

$$n_{e\infty}\left[1 + \mathrm{erf}\left[\sqrt{-\frac{eV_0}{kT_e}}\right]\right] = 2n_{i\infty}. \quad (5.9)$$

In steady state, balancing plasma electron and ion current gives

$$\int_{E_m}^{\infty} \sqrt{\frac{2E}{m_e}}\, f_e(\infty,\, E)\, dE = n_{i\infty}\sqrt{\frac{kT_e}{m_i}}, \quad (5.10)$$

or

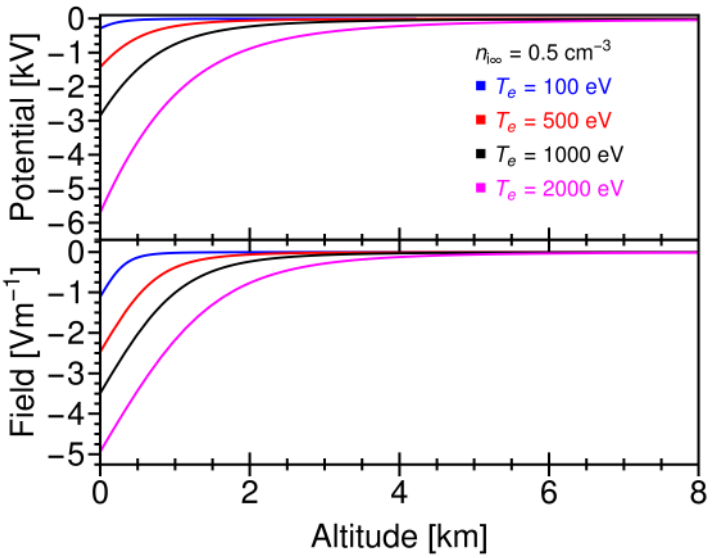

Figure 5.1: Potential and electric field structure within Debye sheath. Other parameter used $n_{i\infty} = 0.5$ cm^{-3}.

$$n_{e\infty}\sqrt{\frac{kT_e}{2\pi m_e}}\exp\left[\frac{eV_0}{kT_e}\right] = n_{i\infty}\sqrt{\frac{kT_e}{m_i}}\,. \tag{5.11}$$

Here, $m_{i(e)}$ is the ion (electron) mass. Simultaneous solution of Eqs. 5.9 and 5.11 gives $n_{e\infty}$ and V_0. Solving Eq. 5.1 with the boundary conditions: $V(x=0) = V_0$ and $V(x \to \infty) = 0$ gives the potential structure of the Debye sheath.

Based on the Lunar Prospector measurements reported by Halekas et al. (2008), we choose the plasma electron temperature to vary between 100 to 2000 eV, and the density between 0.25 to 0.5 cm^{-3}. The plasma parameter regimes cover the extreme scenarios of Earth's magnetospheric plasma. Figure 5.1 illustrates the potential and electric field structure within Debye sheath. Due to high-temperature plasma electrons, the surface may acquire very high negative potential (in the order of kVs). However, the magnitude of the downward-directed surface electric field within this low-density plasma may reach up to a few volts per meter. The magnitude of the negative potential increases with an increase in T_e because electron flux for higher T_e requires a large negative potential to balance with the ion flux. As the Debye length is proportional to the square root of T_e, the sheath edge increases with increasing T_e. The bottom panel of Figure 5.2 shows the density profiles within the sheath. A positive space charge region is created to screen out the high negative potential. From Eq. 5.9, we can see that $n_{e\infty} \propto n_{i\infty}$, the magnitude of V_0 for Debye sheath does not depend on the plasma density. The plasma density becomes important in determining screening length because the Debye length is inversely proportional to the

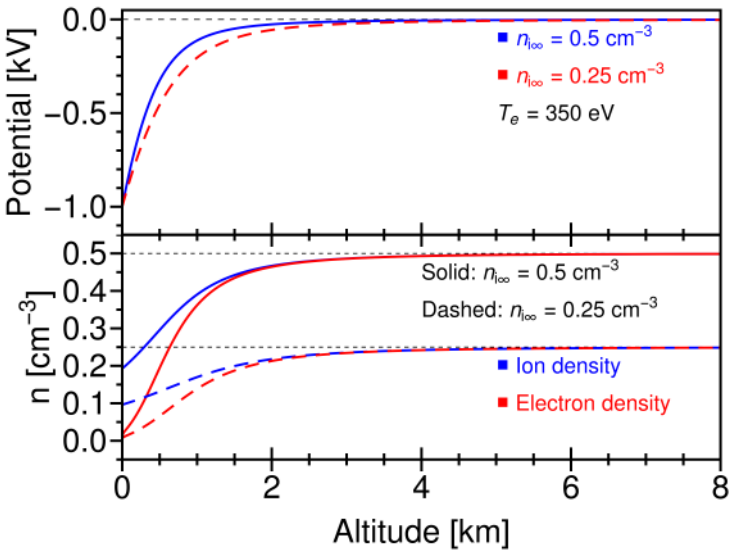

Figure 5.2: Potential (top) and density (bottom) profiles within Debye sheath for different $n_{i\infty}$.

square root of the plasma density. Figure 5.2 shows that variation of $n_{i\infty}$ does not affect the surface potential, but the screening length decreases as $n_{i\infty}$ increases.

The Debye sheath solution is an ideal scenario where the lunar surface is exposed to plasma and electron emission is insignificant. However, these high-temperature plasmas can result in the emission of secondary electrons and might alter the sheath structure. Next, we will address the sheath formation in the presence of significant Secondary Electron Emission (SEE).

5.3 Inverse sheath in presence of SEE

As the surface is bombarded by high-energy plasma electrons (e.g. Earth's magnetospheric plasma), it knocks out the low-energy electrons from the surface in the form of Secondary Electron Emission (SEE). Due to significant SEE, the lunar surface may acquire positive potential $(V_0 > 0)$ (Wang et al., 2016a). Here, we assess the possibility of inverse sheath formation in the presence of SEE. Assuming the emitted secondary electrons follow Maxwellian distribution, the secondary electron flux from the lunar surface can be written as (Prokopenko and Laframboise, 1980; Wang et al., 2016a)

$$J_{se} = J_{se0} \exp\left[-\frac{eV_0}{kT_{se}}\right], \tag{5.12}$$

where T_{se} is the temperature of the emitted secondary electrons. Goertz (1989) reported that the mean energy of emitted secondary electron lies in the range from 1 to 5 eV. We

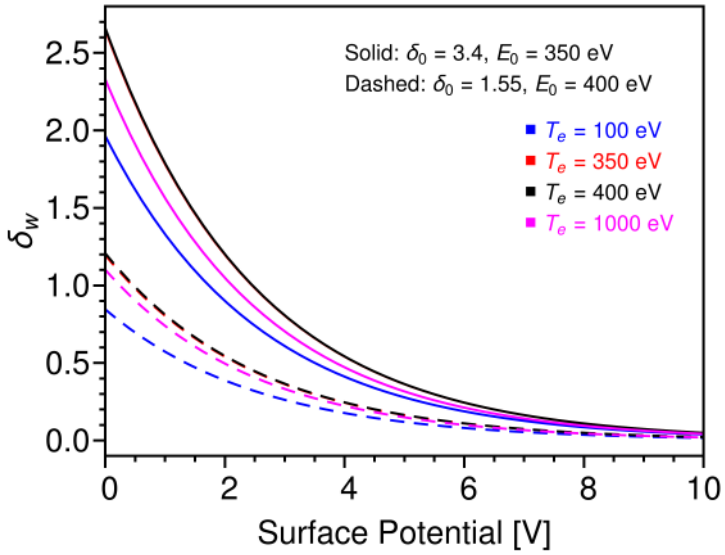

Figure 5.3: Depandance of δ_w with V_0 and T_e. Other parameter used: $T_{se} = 2.5$ eV.

will use $T_{se} = 2.5$ eV in our further calculation. From Prokopenko and Laframboise (1980); Wang et al. (2016a) we can write

$$J_{se0} = \int_0^\infty \delta(E + eV_0) \sqrt{\frac{2E}{m_e}} f_e(\infty, E)\, dE\,, \tag{5.13}$$

or,

$$J_{se0} = \delta_{eff}\, n_{e\infty} \sqrt{\frac{kT_e}{2\pi m_e}}\,, \tag{5.14}$$

where

$$\delta_{eff} = \left[\frac{1}{kT_e} \exp\left[\frac{eV_0}{kT_e}\right] \int_{eV_0}^\infty \delta(E) \exp\left[-\frac{E}{kT_e}\right] dE\right]\,. \tag{5.15}$$

And

$$J_{se} = \delta_{eff} \exp\left[-\frac{eV_0}{kT_{se}}\right] n_{e\infty} \sqrt{\frac{kT_e}{2\pi m_e}} = \delta_w\, n_{e\infty} \sqrt{\frac{kT_e}{2\pi m_e}}\,. \tag{5.16}$$

Here, $\delta(E)$ is the SEE yield. From Sternglass (1954) we can write

$$\delta(E) = 7.4\delta_0 \left(\frac{E}{E_0}\right) \exp\left[-2\sqrt{\frac{E}{E_0}}\right]\,, \tag{5.17}$$

where δ_0 is the optimum value of the SEE yield peaking at the primary electron energy E_0. We will use $\delta_0 = 3.4$ at $E_0 = 350$ eV and $\delta_0 = 1.55$ at $E_0 = 400$ eV. The first

one is derived from the laboratory measurements of the Apollo 17 lunar samples, and the second one is the best value for the lunar samples returned by the Apollo 14 and 15 astronauts (Horányi et al., 1998; Poppe, 2011). We can see from Eqs. 5.15 and 5.16 that δ_w is a significant function of T_e and $V_0 > 0$. Figure 5.3 illustrates the variation of δ_w with V_0 varying T_e as a parameter. We can see that at $V_0 = 0$, δ_w is higher near E_0 and decreases as T_e increases or decreases from E_0. Since the positive surface potential will act as a barrier to the emitted secondary electrons, δ_w decreases with increasing V_0.

Considering Maxwellian secondary electrons, we can write the distribution function of secondary electrons at finite x as

$$f_{se}(x,\, E) = n_{se0}\sqrt{\frac{1}{4\pi k T_{se} E}}\exp\left[-\frac{E}{kT_{se}} + \frac{e\big(V(x) - V_0\big)}{kT_{se}}\right]. \tag{5.18}$$

From this, we can easily show that

$$J_{se0} = n_{se0}\sqrt{\frac{kT_{se}}{2\pi m_e}}, \tag{5.19}$$

where $n_{se0}/2$ is the density of secondary electrons travel away from the uncharged surface at $x = 0$. Equating this equation with Eq. 5.14 we get

$$n_{se0} = n_{e\infty}\,\delta_{eff}\sqrt{\frac{T_e}{T_{se}}}. \tag{5.20}$$

For inverse sheath, the Poisson equation becomes

$$\frac{d^2V}{dx^2} = -\frac{e}{\epsilon_0}\big(n_i - n_{se,free} - n_{se,capt} - n_{e,free}\big). \tag{5.21}$$

Here, we only have "free plasma electrons". But two secondary electron populations: (i) secondary electrons that escape to infinity are "free secondary electrons $(n_{se,free})$", and (ii) secondary electrons that have been reflected by the positive potential barrier in the sheath are called "captured secondary electrons $(n_{se,capt})$". Here, free electrons (both plasma and secondary electrons) at x have available energy range $(E_m,\, \infty)$ where $E_m = eV(x)$. However, secondary electrons within $(0,\, E_m)$ contributes to $n_{se,capt}$. Following a similar operation as in Eqs. 5.5 and 5.6 we get

$$n_{e,free}(x) = \frac{n_{e\infty}}{2}\exp\left[\frac{eV(x)}{kT_e}\right]\left[1 - \mathrm{erf}\left[\sqrt{\frac{eV(x)}{kT_e}}\right]\right], \tag{5.22}$$

and

$$n_{se,free}(x) = \frac{n_{se0}}{2} \exp\left[\frac{e\big(V(x) - V_0\big)}{kT_{se}}\right]\left[1 - \text{erf}\left[\sqrt{\frac{eV(x)}{kT_{se}}}\right]\right], \tag{5.23}$$

and

$$n_{se,capt}(x) = n_{se0} \exp\left[\frac{e\big(V(x) - V_0\big)}{kT_{se}}\right] \text{erf}\left[\sqrt{\frac{eV(x)}{kT_{se}}}\right], \tag{5.24}$$

Therefore, from quasi-neutrality at the sheath edge we can write

$$n_{se}(\infty) + n_e(\infty) = n_i(\infty)\,, \tag{5.25}$$

or,

$$n_{se0} \exp\left[-\frac{eV_0}{kT_{se}}\right] + n_{e\infty} = 2n_{i\infty}\,. \tag{5.26}$$

And the flux balance equation becomes

$$n_{e\infty}\sqrt{\frac{kT_e}{2\pi m_e}} - n_{se0}\sqrt{\frac{kT_{se}}{2\pi m_e}} \exp\left[-\frac{eV_0}{kT_{se}}\right] = n_{i\infty}\sqrt{\frac{kT_e}{m_i}}\,. \tag{5.27}$$

From Eq. 5.20 we can see that n_{se0} depends on $n_{e\infty}$, so replacing n_{se0} in Eqs. 5.26 and 5.27 and solving simultaneously we can determine $n_{e\infty}$ and V_0. Thereafter, we can solve Eq. 5.21 with the boundary conditions: $V\big(x = 0\big) = V_0$ and $V\big(x \to \infty\big) = 0$ to get the potential structure of the inverse sheath.

Figure 5.4 shows the dependence of surface potential (V_0) on T_e, δ_0, and E_0. For a particular set of δ_0, and E_0, there is a temperature regime of T_e where inverse sheath can sustain. Our calculation shows that for $(\delta_0,\, E_0) = (1.55,\, 400\,\text{eV})$ within $T_e \approx (94\,\text{eV},\, 7.1\,\text{keV})$ and for $(\delta_0,\, E_0) = (3.4,\, 350\,\text{eV})$ within $T_e \approx (24\,\text{eV},\, 25\,\text{keV})$ inverse sheath is possible with maximum surface potential at $T_e \approx 775$ and 653 eV respectively. The peak surface potential and the corresponding value of T_e are noticed to increase with increasing δ_0 and E_0 due to an increase in effective SEE current. Figure 5.5 shows the potential and electric field profiles of inverse sheath created due to significant SEE from the lunar surface. For the nominal SEE yield parameter, the surface acquires a few volts of positive potential. An upward-directed electric field exists within the inverse sheath. However, the magnitude of the field is found to be less than 1 V m^{-1}, an order of magnitude smaller compared to Debye sheath (Figure 5.1). This field could be a significant

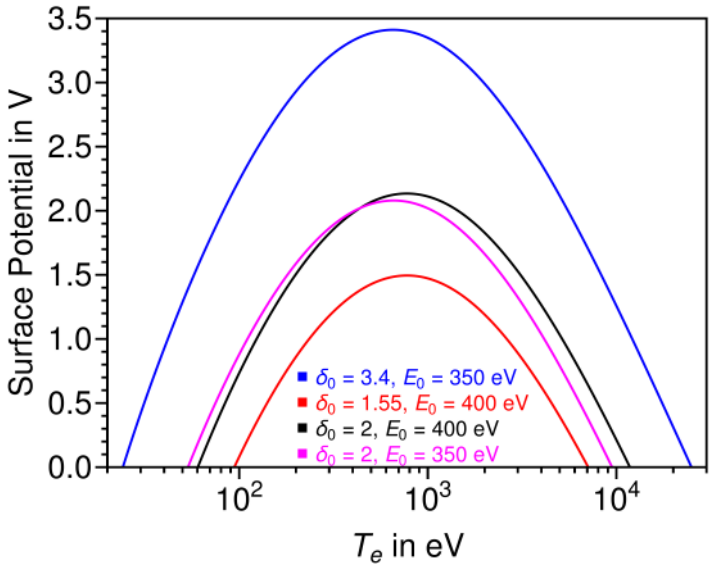

Figure 5.4: Surface potential variation with T_e. Other parameter used $n_{i\infty} = 0.5\,\mathrm{cm}^{-3}$, $T_{se} = 2.5$ eV.

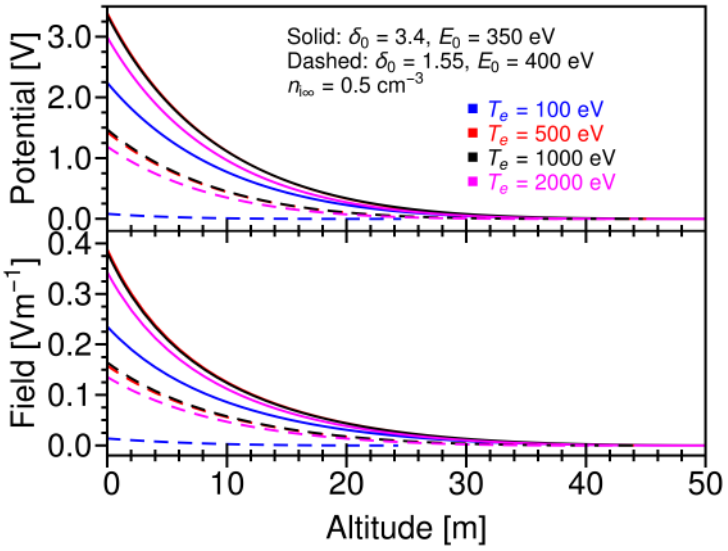

Figure 5.5: Potential and electric field structure within inverse sheath due to SEE. Other parameter used $n_{i\infty} = 0.5\,\mathrm{cm}^{-3}$, $T_{se} = 2.5$ eV.

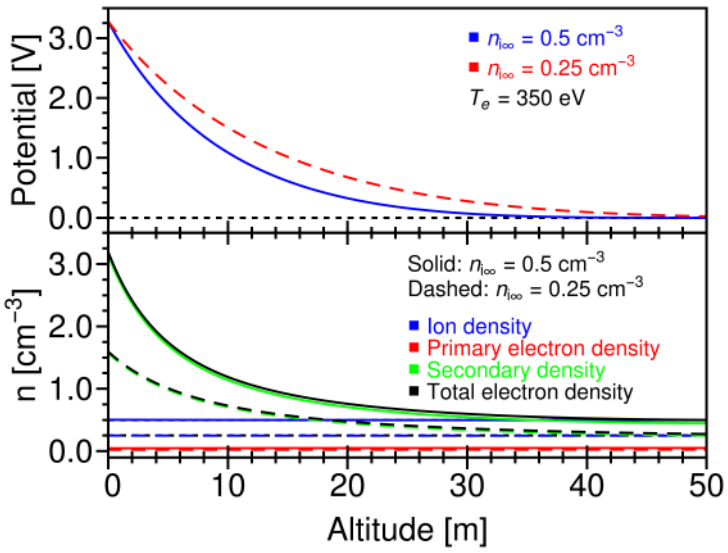

Figure 5.6: Potential (top) and density (bottom) profiles within inverse sheath due to SEE for different $n_{i\infty}$. Other parameter used: $\delta_0 = 3.4$, $E_0 = 350$ eV, $T_{se} = 2.5$ eV.

source of local plasma and dust dynamics and transport. The sheath thickness varies between 10 to 40 m. Since the larger surface potential requires a higher altitude to screen out, sheath thickness increases with increasing V_0. However, the sheath thickness also depends on the density of the space charge region. The $n_{i\infty}$ is an important parameter in determining the sheath thickness as the degree of screening increases with increasing $n_{i\infty}$; this results in a decrease in sheath thickness. This has been illustrated in Figure 5.6. It also depicts that the inverse sheath is a negative space charge region that is dominated by secondary electrons. Plasma electron density is noticed to be one order of magnitude smaller. The total electron density equals the ion density at the sheath edge to maintain the quasineutrality.

In case where SEE is absent or negligible, the nightside surface acquires a negative potential and forms a Debye sheath (Halekas et al., 2002, 2005; Colwell et al., 2007). In the present study, we found that under extreme plasma conditions, due to significant SEE yield, an inverse sheath develops around the positively charged surface. The dust particles within the sheath also undergo electrostatic charging. The charge on the dust particles depends on the charging currents. One expects the dust grains to have the same material properties as the surface and are similarly exposed to the energetic primary plasma electrons - it could lead to significant SEE flux from the dust, and the dominant SEE effect could charge dust positively. Note that the degree of SEE flux may differ from that of planar surfaces as SEE yield differs slightly for spherical dust particles (Prokopenko and Laframboise, 1980). Vaverka et al. (2016), theoretically, have demonstrated that SEE leads

to a positive charging of the dust grains to the plasma scenarios where a high negative potential was expected. Depending on the degree of charging, the existence of positively charged dust particles is possible within the inverse sheath created due to SEE. Since we have presented the case of high SEE yields, the upward-directed electric field within the inverse sheath can support such positively charged dust particles above the lunar surface. It may create a dusty plasma scenario at high latitudes (polar regions) and the nightside of the Moon.

From previous laboratory analysis and satellite measurements, it is evident that the SEE yield varies in a wide range (Willis et al., 1973; Horányi et al., 1998; Halekas et al., 2009a). Various satellite observations also have shown that the spatiotemporal variation of plasma conditions around the Moon is very dynamic (Halekas et al., 2008; Angelopoulos, 2011). So, depending on these parameters, locally on the lunar nightside, there might be a possibility that the Debye sheath and inverse sheath may exist in very close proximity. Therefore, the surface may experience a significant shift in the potential (charge) and may create a sufficiently large horizontal electric field. Due to significant temporal variability of plasma parameters, frequent alteration of local electric potential and field structure is possible. Overall, these variations may render the nightside of the Moon an electrically complex region.

5.4 Summary and future work

The possibility of inverse sheath formation on the night side of the lunar surface has been analytically assessed when the Moon is exposed to highly energetic ambient plasma. Calculation shows that the dominant SEE-induced positively charged lunar surface forms an inverse sheath, where a Debye sheath is expected to have a high negative potential. For a particular SEE yield, a temperature regime exists where the inverse sheath is possible. Secondary electrons dominate the sheath with a number density one order of magnitude greater than that of primary plasma electrons. Like the Debye sheath, the surface potential is found to be independent of the density of the quasi-neutral plasma. It only determines the degree of screening. For nominal SEE yield and ambient plasma parameter, the inverse sheath is found to be extended in the range of 10 to 40 m.

In the present study, a simplified model with Maxwellian plasma assumption is presented to illustrate the conceptual basis, which simplifies the solution of the Poisson equation. However, the observations of various space plasma environments suggest κ-

distribution as a more accurate fit to describe the velocity distribution of the plasma particles instead of the usual Maxwellian nature. This κ-distribution exhibits a higher proportion of the particles in its tail region and a lower population in its core compared to a Maxwellian distribution. Mishra et al. (2013) have shown higher secondary electron emission (SEE) yield and SEE flux for the κ-distributed electrons compared to the Maxwellian case. Intuitively, higher SEE flux corresponding to the κ-distributed plasma might yield a higher surface charge (positive) compared to the Maxwellian case, and larger screening might lead to a shorter sheath. The consideration of realistic plasma distributions is the next step to the problem and will be taken up in the near future.

Chapter 6

Dust dynamics

6.1 Introduction

Previous chapters presented the analytical formulation of plasma sheath formation around the Moon and quantitatively estimated several features of the sheath in terms of electric potential, field, and density profiles of various sheath populations. One of the direct implications of this structure is that dust particles can be mobilized in this electrostatically active medium. From the dusty regolith, the dust particles get detached through various mechanisms. These floating micron- and sub-micron-sized particles within the sheath acquire a finite amount of charge via collecting sheath constituents and photoemission (if the dust is illuminated with photons). These detached particles may then undergo dynamic evolution within the sheath, influenced by electrostatic and gravitational forces. Lunar horizontal glow is one of the evidence of these lunar dust dynamics (Rennilson and Criswell, 1974; Zook and McCoy, 1991; Wilcox, 2025). Laboratory studies also demonstrated the mobilization of micron-sized dust under exposure to the plasma environment (Wang et al., 2009, 2016b) - it suggests that electrostatic effects could be significant in dust lifting and transporting the dust locally. These experiments also demonstrated the variation in reflectance spectra as a result of local surface evolution via electrostatic transport (Opp et al., 2024). Although these observational and experimental studies efficiently highlighted the importance of electrostatic dust mobilization in terms of local space weathering, the complete insight into this phenomenon can be extracted through the theoretical formulation. As discussed in Chapter 1, many studies have analytically addressed the dust charging and subsequent dynamics around the Moon. However, their study over-/under-estimated several features of electric potential and field structures due

to some simplified assumptions in the analysis. As a result, subsequent dust dynamics are anticipated to be less likely applicable in the realistic scenario. Overcoming these simplifications, previous chapters derived more realistic estimates of sheath characteristics. Using these estimates, the dust charging and subsequent dynamics can be revisited. To consolidate it, in this chapter, a test dust particle is introduced within the sheath, and its charging, dynamics, and possibility of levitation have been examined.

6.2 Dust in the sheath

The floating dust particle undergoes electrostatic charging while traversing through the sheath. As it passes through different sheath layers, it collects constituent sheath populations. Since the dust is also exposed to solar radiation, it also emits photoelectrons. Accounting for the inherent charging effects, the equation representing the particle motion and dust charging can be written as (Bouchoule, 1999; Shukla and Mamun, 2002; Vladimirov et al., 2005; Tsytovich et al., 2008; Sodha, 2014)

$$m_d \frac{d^2x}{dt^2} = -Q_d \frac{dV}{dx} - m_d g\,, \tag{6.1}$$

and

$$\frac{dQ_d}{dt} = I_{p,dust} + I_i + I_{e,free} + I_{e,capt} + I_{p,free} + I_{p,capt} = I_{tot}\,. \tag{6.2}$$

where m_d is the dust particle mass and g is the acceleration due to lunar gravity. V is the sheath potential at the altitude x. $I_{p,dust}$ is the photoemission current from the dust particle. Other charging currents correspond to the sheath constituent discussed in section 3.1. Q_d is the dust particle charge and I_{tot} is dust charging current. In the next section, the mathematical expressions of the charging currents used in Eq. 6.2 are derived.

6.3 Charging currents

Here we derive the mathematical expressions of the charging currents used in Eq. 6.2.

6.3.1 Electron collection currents within the sheath

The sheath primarily comprises the photoelectrons (those are released from the lunar surface) and the solar wind plasma (electrons/ ions). The general expression of electron col-

lection current is (Nitter et al., 1998)

$$I_j(x) = -e \iiint_{u_j} u\, \sigma_j(u)\, f_j(x, \mathbf{u})\, d^3\mathbf{u}\,, \tag{6.3}$$

where u_j is the three-dimensions velocity space to be integrated over and f_j is the three dimensional velocity distribution function, and $\sigma_j(u)$ is the cross-section

$$\sigma_j(u) = \pi a^2 \left(1 + \frac{2eV_d}{m_e u^2}\right), \tag{6.4}$$

where a is the particle radius, V_d is the dust potential with respect to the local sheath potential, V is the local sheath potential, e and m_e are electric charges and mass respectively. The relation between Q_d and V_d can be written as $Q_d = 4\pi\epsilon_0 a\, V_d$, where ϵ_0 is the permittivity in free space. $j = e\,(p)$ means solar wind (photo-) electrons.

Following Eq. 2.40 for photoelectrons we can write

$$\begin{aligned} f_p(x, \mathbf{u}) d^3\mathbf{u} = \frac{1}{2\pi}\left(\frac{m_e}{kT_0}\right)^2 \cos\theta \int_{\lambda_{\min}}^{\lambda_{\max}} \left[\frac{\chi(\lambda) f_\lambda\, d\lambda}{\Phi(\xi_\lambda)}\right] \\ \times F_D\left[\frac{m_e \mathbf{u}^2}{2kT_0} - \xi_\lambda - v_0 + v(x)\right] d^3\mathbf{u}\,. \end{aligned} \tag{6.5}$$

The description of each term is given in section 2.3. $v_0 = -eV_0/kT_0$ and $v(x) = -eV(x)/kT_0$ are normalized lunar surface potential and normalized sheath potential at x respectively. V_0 is the lunar surface potential.

The non-Maxwellian κ distribution of solar wind electrons can be written as,

$$\begin{aligned} f_e(x, \mathbf{u}) d^3\mathbf{u} = n_{e\infty}\beta\left(\pi\gamma u_{\text{th}}^2\right)^{-3/2} \\ \times \left[1 + \left(\frac{\mathbf{u}^2}{\gamma u_{\text{th}}^2} + \frac{v(x)}{\gamma\alpha}\right)\right]^{-\kappa-1} d^3\mathbf{u}\,. \end{aligned} \tag{6.6}$$

The description of each term is given in section 3.3.

Now, in spherical polar coordinates with azimuthal symmetry,

$$d^3\mathbf{u} = 2\pi u^2 \sin\phi\, du\, d\phi\,, \tag{6.7}$$

where ϕ is the angle between the electron velocity vector and the x axis (axis perpendicular to the surface). Now, one needs the available velocity space to integrate (Eq. 6.5 and 6.6) and evaluate currents (Eq. 6.3). Consider two cases,

1. When $V_d > 0$

   Free electrons at a layer with potential V within the sheath have velocities between $u_m = \left[2e\big(V(x) - V_m\big)/m_e\right]^{1/2}$ (minimum speed in the x direction at x to overcome the potential minimum V_m at x_m) and ∞. Any electron with $u_x = u\cos\phi < u_m$ is not contribute to the free electron collection current. So the free electron collection current is given by

$$I_{j,free} = -e\int_{u_m}^{\infty}\int_{0}^{\phi_m}\sigma_j(u)\,A_j\,du\;d\phi\,, \tag{6.8}$$

   where $A_j = 2\pi\,u^3\,f_j(x,\,u)\,\sin\phi$ and $\phi_m = \cos^{-1}(u_m/u)$.

   For *captured electrons*, we have two populations. In one population with $u < u_m$ has the effective velocity range $(0, u_m)$ and $(0, \pi/2)$. Another with $u\cos\phi < u_m$ has the effective velocity range (u_m, ∞) and $(\phi_m, \pi/2)$. So the captured electron collection current is given by

$$\begin{aligned} I_{j,capt} = -2e\Bigg[&\int_{u_m}^{\infty}\int_{\phi_m}^{\pi/2}\sigma_j(u)\,A_j\,du\,d\phi \\ &+\int_{0}^{u_m}\int_{0}^{\pi/2}\sigma_j(u)\,A_j\,du\,d\phi\Bigg]\,, \end{aligned} \tag{6.9}$$

   where factor two comes from the outgoing and incoming electrons within the sheath.

2. When $V_d < 0$

   Electrons with velocities with $u < u_s = \left[-2eV_d/m_e\right]^{1/2}$ are excluded. So for *Free electrons*, the velocity range becomes $(u_1 = \max[u_m, u_s], \infty)$. Hence, the free electron collection current is given by

$$I_{j,free} = -e\int_{u_1}^{\infty}\int_{0}^{\phi_m}\sigma_j(u)\,A_j\,du\,d\phi\,. \tag{6.10}$$

   And the *captured electrons* have the velocity ranges $(u_2 = \min[u_m, u_s], u_m)$. So, the captured electron collection current is given by

$$\begin{aligned} I_{j,capt} = -2e\Bigg[&\int_{u_1}^{\infty}\int_{\phi_m}^{\pi/2}\sigma_j(u)\,A_j\,du\,d\phi \\ &+\int_{u_2}^{u_m}\int_{0}^{\pi/2}\sigma_j(u)\,A_j\,du\,d\phi\Bigg]\,. \end{aligned} \tag{6.11}$$

Expressions of σ_j, u_m, u_s, A_j

For photoelectrons

$$\begin{aligned} \sigma_p(u) &= \pi a^2 \left(1 - v_d \cdot \frac{u_{\mathrm{p}}^2}{u^2}\right), && (6.12)\\ u_m &= u_{\mathrm{p}} \left[v_m - v(x)\right]^{1/2}, && (6.13)\\ u_s &= u_{\mathrm{p}} \left[v_d\right]^{1/2}, && (6.14) \end{aligned}$$

$$\begin{aligned} A_p = \left(\frac{m_e}{kT_0}\right)^2 \cos\theta \int_{\lambda_{\min}}^{\lambda_{\max}} \left[\frac{\chi(\lambda) f_\lambda \, d\lambda}{\Phi(\xi_\lambda)}\right] \\ \times \left[1 + \exp\left(\frac{u^2}{u_{\mathrm{p}}^2} - \xi_\lambda - v_0 + v(x)\right)\right]^{-1} u^3 \sin\phi \,, \end{aligned} \tag{6.15}$$

where $u_{\mathrm{p}} = \left(2kT_0/m_e\right)^{1/2}$, and $v_d = -eV_d/kT_0$ refers the normalized dust potential.

For solar wind electrons

$$\begin{aligned} \sigma_e(u) &= \pi a^2 \left(1 - \frac{v_d}{\alpha} \cdot \frac{u_{\mathrm{th}}^2}{u^2}\right), && (6.16)\\ u_m &= u_{\mathrm{th}} \left[\left(v_m - v(x)\right)/\alpha\right]^{1/2}, && (6.17)\\ u_s &= u_{\mathrm{th}} \left[v_d/\alpha\right]^{1/2}, && (6.18) \end{aligned}$$

$$\begin{aligned} A_e = 2\pi \, n_{e\infty} \beta \left(\pi\gamma u_{\mathrm{th}}^2\right)^{-3/2} \\ \times \left[1 + \left(\frac{u^2}{\gamma u_{\mathrm{th}}^2} + \frac{v(x)}{\gamma\alpha}\right)\right]^{-\kappa-1} u^3 \sin\phi \,, \end{aligned} \tag{6.19}$$

where $u_{\mathrm{th}} = \left(2kT_e/m_e\right)^{1/2}$ is the solar wind electron thermal speed and $\alpha = T_e/T_0$.

6.3.2 Photoemission current from the dust particle

1. When $V_d > 0$ or $v_d < 0$

$$\begin{aligned} I_{p,dust} = e\pi a^2 \int_{\lambda_{\min}}^{\lambda_{\max}} \left[\frac{\chi(\lambda) f_\lambda \, d\lambda}{\Phi(\xi_\lambda)}\right] \\ \times \left[-v_d \ln\left\{1 + \exp\left(\xi_\lambda + v_d\right)\right\} + \Phi\left(\xi_\lambda + v_d\right)\right]. \end{aligned} \tag{6.20}$$

2. When $V_d < 0$ or $v_d > 0$

$$I_{p,dust} = e\pi a^2 \int_{\lambda_{\min}}^{\lambda_{\max}} \chi(\lambda) f_\lambda \, d\lambda \,. \tag{6.21}$$

6.3.3 Ion current

The ion current is given by

$$I_i = e n_{i\infty} u_{i\infty} \sigma_i \,, \tag{6.22}$$

where

$$\sigma_i = \pi a^2 \left[1 + \frac{2v_d}{\alpha M^2 + 2v} \right] . \tag{6.23}$$

Here, $M = u_{i\infty}/u_B$ is the Mach number. $u_B = (kT_e/m_i)^{1/2}$ is Bohm speed.

6.4 Sheath structures used for calculations

The motion of dust particles is influenced by the sheath electric field (as shown in Eq. 6.1). Additionally, the previous section demonstrated that dust charging currents significantly depend on the local potential structure within the sheath. In Chapter 3, the possibility of three types of potential structures within the lunar photoelectron sheath was quantitatively demonstrated. In the region where photoemission is insignificant, the surface exhibits a negative surface potential due to the collection of electrons from the plasma. This negative potential increases (decreases in magnitude) with altitude until reaching zero, forming a Type C sheath, which follows a typical Debye-type potential structure. Conversely, in regions with significant photoemission, the surface potential is positive and gradually decreases to zero, creating a monotonically decreasing Type B sheath. However, under certain specific physical conditions, the formation of a non-monotonic potential structure (Type A sheath) is demonstrated, where the surface potential initially decreases to a negative minimum before rising back to zero. In this chapter, the dust dynamics will be investigated within all three types of sheath structures illustrated in Figures 6.1, 6.2, and 6.3. The set of input parameters used are discussed in Section 3.4.2. And a detailed discussions of these potential and field structures are given in Chapter 3.

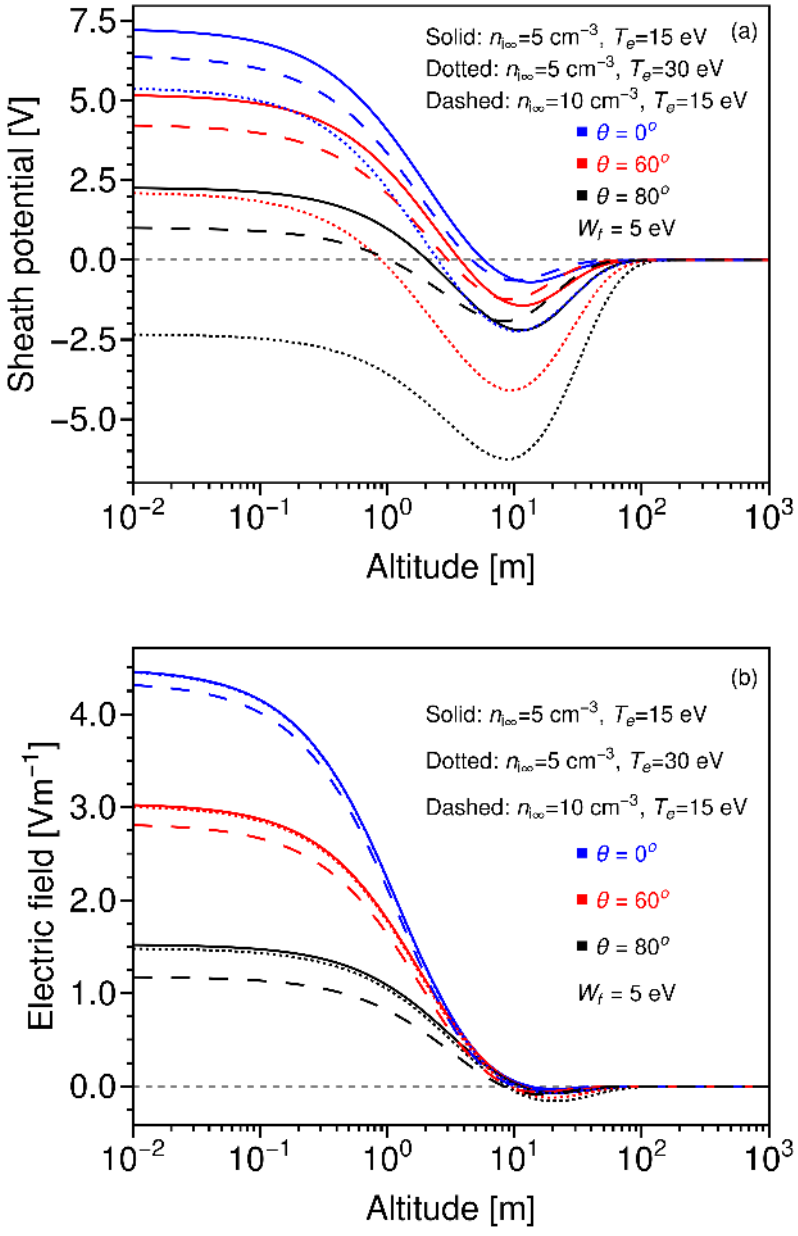

Figure 6.1: Altitude profiles of the (a) electric potential, (b) field intensity within Type A sheath over the lunar surface for different values of solar latitude θ for different solar wind plasma parameters.

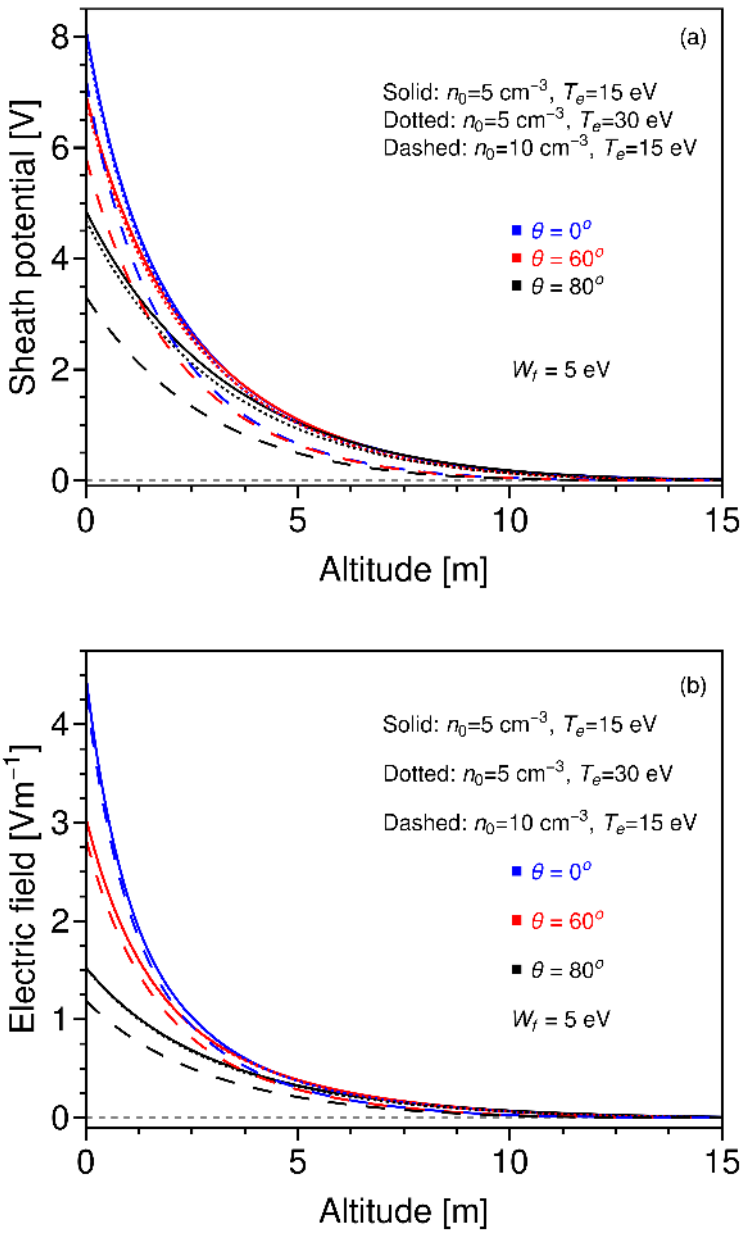

Figure 6.2: Altitude profiles of the (a) electric potential, (b) field intensity within Type B sheath over the lunar surface for different values of solar latitude θ for different solar wind plasma parameters.

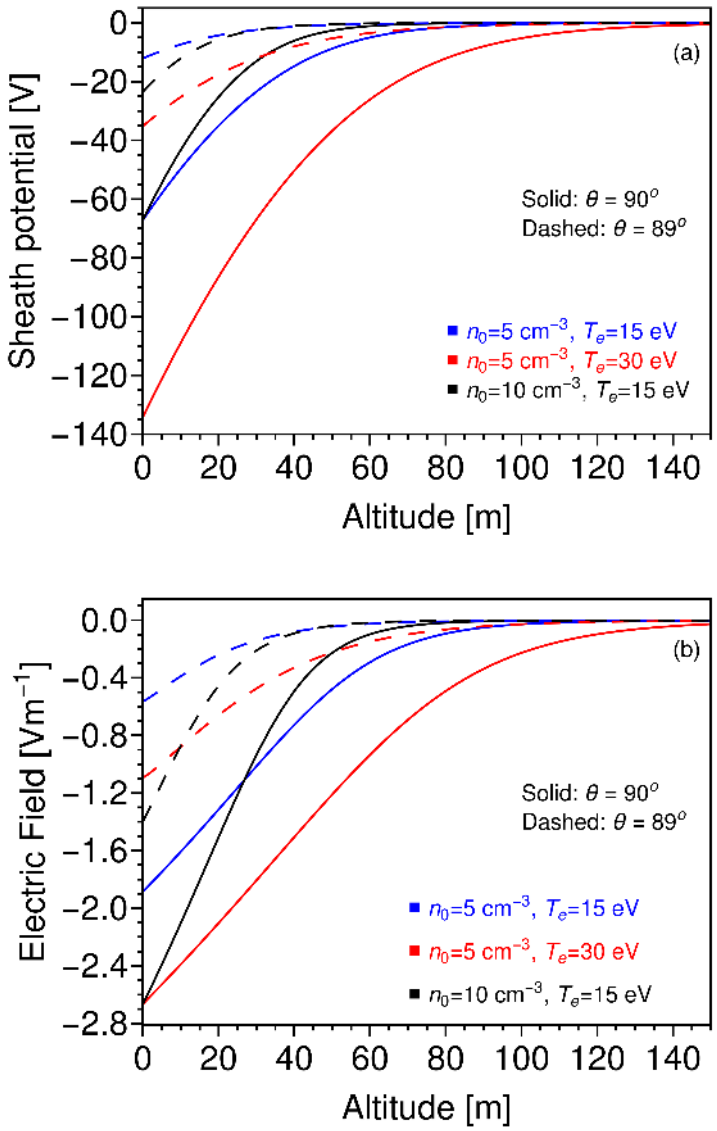

Figure 6.3: Altitude profiles of the (a) electric potential, (b) field intensity within Type C sheath over the lunar surface for different values of solar latitude θ for different solar wind plasma parameters.

6.5 Static equilibrium

In the steady state within the sheath, an isolated dust particle acquires a finite amount of charge or electric potential with respect to the ambient plasma. The steady-state dust charge (and potential) may be evaluated by balancing the charging current on the dust particle. In this case, setting $dQ_d/dt = 0$ in Eq. 6.2 one gets

$$I_{tot} = 0\,. \tag{6.24}$$

Using the expressions of the charging currents discussed in the Section 6.3, Eq. 6.24 has been numerically solved to derive $V_{d,\mathrm{eq}}$. We can see that the charging current depends on the local sheath potential V, which itself is a function of altitude. We know V as a function of altitude from the sheath profile (illustrated in Figures 6.1, 6.2, and 6.3). Using this information $V_{d,\mathrm{eq}}$ has been calculated at each altitude within the sheath. Note that $V_{d,\mathrm{eq}}$ doesn't depend on the particle size, while the particle charge varies linearly with the particle radius.

From Eq. 6.1, the net force on a dust particle can be written as

$$F_{\mathrm{net}} = F_e - F_g = -4\pi\epsilon_0 a\, V_d \frac{dV}{dx} - m_d g\,, \tag{6.25}$$

where F_e is electrostatic force and F_g is gravitational force. The mass of the spherical dust particle can be written as $m_d = \frac{4}{3}\pi\rho_d a^3$, where ρ_d is the material density of the dust particle. Here, we have used $\rho_d = 3$ g cm^{-3}. In the steady state, at a finite x, if the electrostatic force F_e equals with F_g and hence $F_{\mathrm{net}} = 0$. We can write

$$a_{\mathrm{bal}} = \left[-\frac{3\epsilon_0\, V_{d,\mathrm{eq}}\,(dV/dx)}{g\rho_d}\right]^{1/2}. \tag{6.26}$$

6.5.1 For Type A & B sheath

Figure 6.4 illustrates the altitude profiles of the steady-state dust potential $V_{d,\mathrm{eq}}$ for different solar illumination and solar wind plasma conditions within Type A and B sheath structures. In both cases, the dust acquires a finite negative potential (charge) near the lunar surface for lower values of θ. This can be attributed to the fact that for low θ values near the subsolar point and mid-latitude (see the blue and red lines in Figure 6.4), the photoelectron density is higher near the surface, leading to the negative charging of

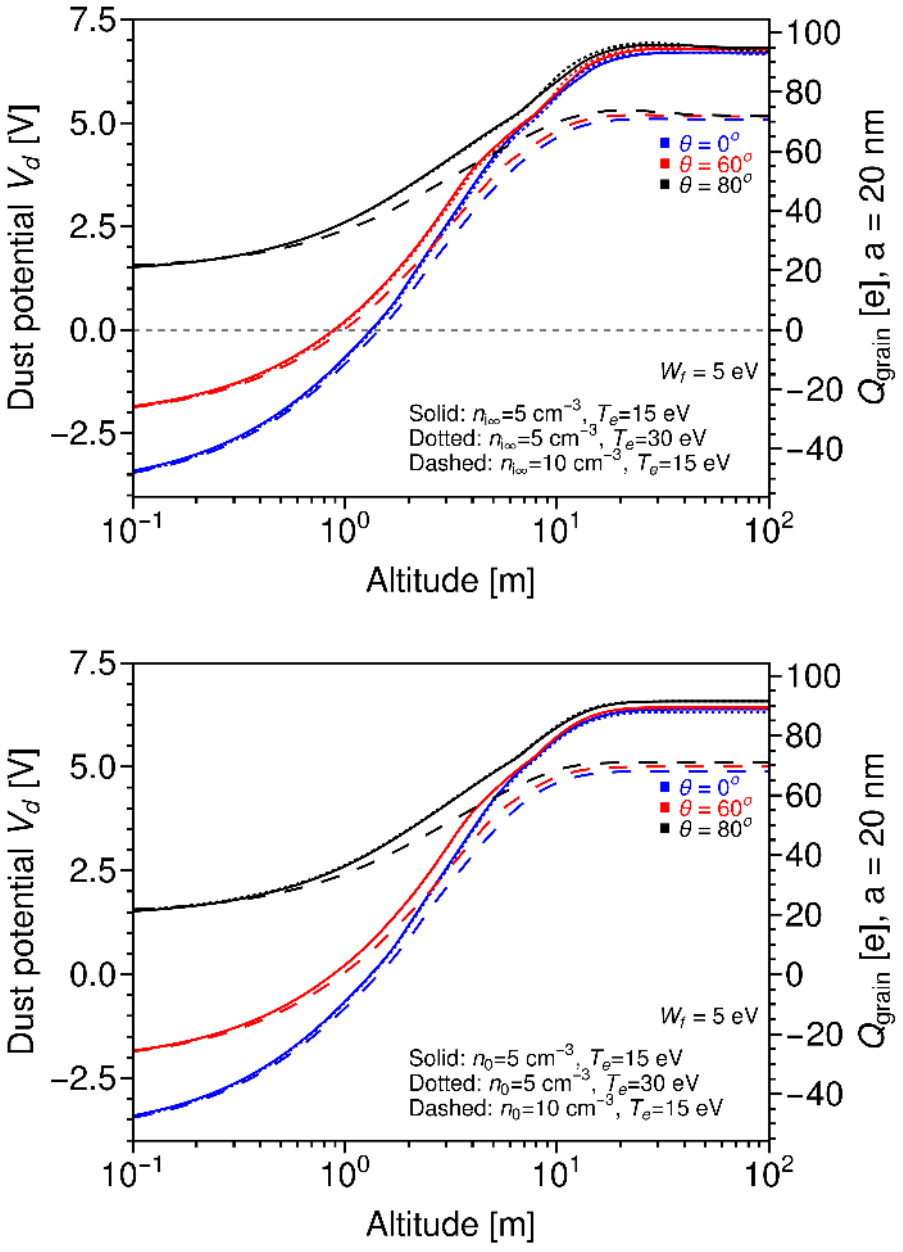

Figure 6.4: The equilibrium dust potential as a function of altitude within Type A (top panel) and Type B (bottom panel) potential structure. The right axis shows the corresponding steady-state charge on 20 nm dust particle.

the dust particle. As the altitude increases, the population density of the sheath photoelectrons decreases, and the charging is dominated by the photoemission from the dust particle, which results in positive charging. However, for higher values of θ, (the black line in Figure 6.4), the photoemission from the dust becomes dominant, and the dust acquires a positive potential everywhere within the less dense photoelectron sheath. The effect of solar wind plasma parameters, i.e., $n_{i\infty}$ and T_e can be explained as follows. The solar wind electron and ion accretion flux increases with increasing plasma density and temperature. However, near the surface, due to the presence of the dominant photoelectron population, no significant deviation in $V_{d,\mathrm{eq}}$ is noticed. As altitude increases, the solar wind electron density increases, giving rise to more negative charging, which reduces the positive dust potential. However, a significant reduction is observed in increasing $n_{i\infty}$ than T_e. We notice a slight increase in $V_{d,\mathrm{eq}}$ within the range 12 to 40 m while increasing T_e for Type A solutions. Within a non-monotonic sheath, this region is dominated by positively charged ions, which gives rise to a slightly higher ion accretion current, resulting in higher positive charging. But as we reach the sheath edge, due to quasineutrality, a significant number of electrons give rise to further negative charging, slightly reducing the positive potential. These kinds of features within altitudes 12 to 40 m have not been observed for Type B. Because Type B sheaths terminate within around 12 m, and above this region, the dust is exposed to UV radiation and quasi-neutral solar wind plasma. As a result, the dust charge attains a constant positive value above the sheath edge of the Type B potential structure due to dominant UV-induced photoemission. However, the values and trends of $V_{d,\mathrm{eq}}$ for Types A and B are noticed to vary only slightly for various plasma parameters. The figure suggests that a 20 nm dust particle may acquire $-47e$ to $95e$ charges within the steady-state Type A sheath configuration, whereas for Type B, charges are found to vary from $-47e$ to $91e$ for the same set of input parameters.

Figure 6.5 shows the electric and gravitational force ratio for 20 nm dust particle - the results of Figure 6.1 (for Type A) and Figure 6.2 (for Type B) are combined with Figure 6.4 to derive the electrostatic force on the dust particle within the Type A and B sheaths. We see that for lower values of θ, there exist two balancing points or static levitation points (the blue and red curves), while for higher values of θ (the black curves), there exists only one static levitation point. The lower balancing point is unstable because dF_{net}/dx is positive (Nitter and Havnes, 1992). The height of the balancing point decreases with increasing θ. Because of higher electric field strength at the low θ values results in a higher static levitation point. The height of the lower balancing/levitation point increases, and

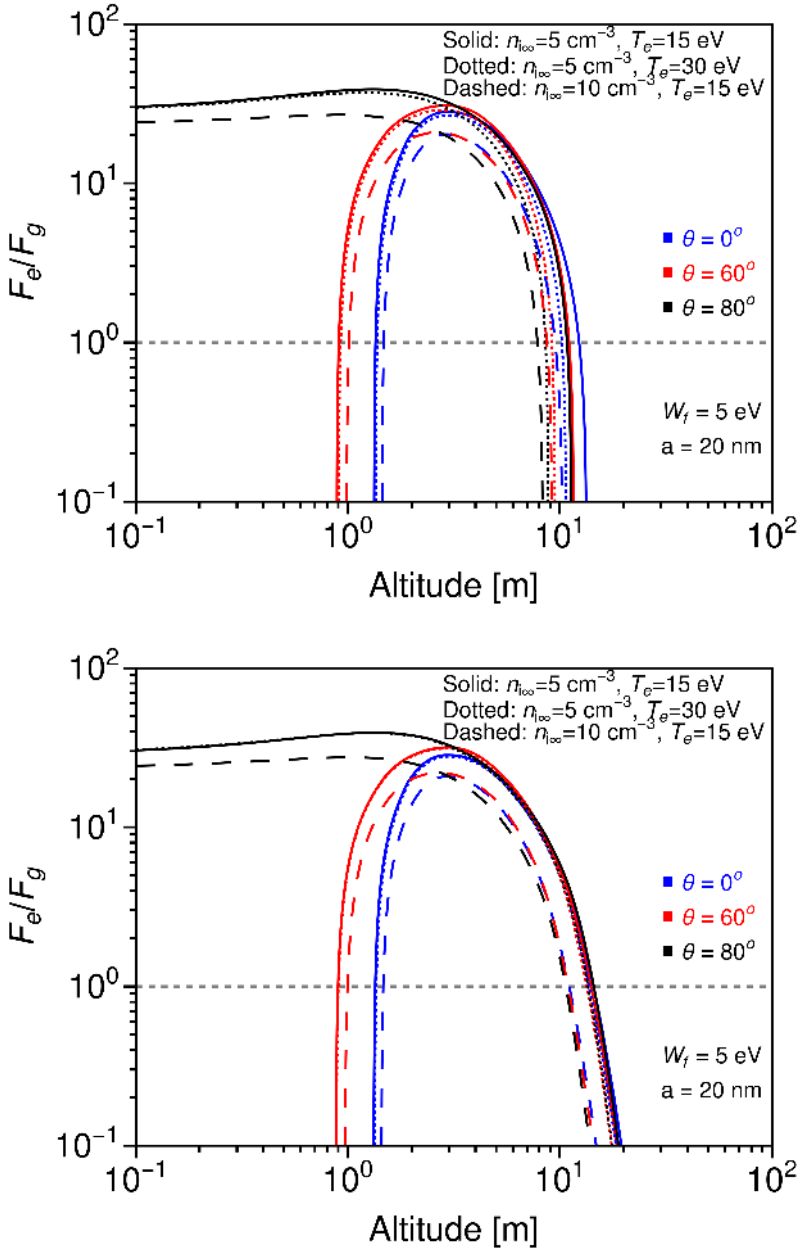

Figure 6.5: The ratio of the electric to gravitational force for 20 nm dust particle within Type A (top panel) and Type B (bottom panel) potential structure.

the upper balancing point decreases with increasing plasma density and temperature. From Figure 6.4, it is noticed that the equilibrium dust charge reversal from near-surface negative to positive happens at relatively higher altitudes with increasing $n_{i\infty}$ and T_e. With increasing $n_{i\infty}$ and T_e, the sheath electric field reaches zero at lower altitudes (field reversal from positive to negative occurs for Type A, see Figure 6.1b). Hence, the lower altitude for $Q_dE > 0$ increases, and the upper altitude for $Q_dE > 0$ decreases and reduces the altitudinal span where Q_dE remains positive, which results in a rise in altitude of the lower levitation point and a fall in the upper levitation point. The F_e/F_g ratio for Type A falls sharply with altitude above the upper levitation point due to the field reversal from positive to negative near potential minima. And the F_e/F_g becomes negative due to the downward-directed sheath electric field. On the other hand, for Type B, F_e/F_g remains positive above the upper levitation point and its magnitude gradually decreases with altitude due to a decrease in the upward-directed sheath electric field.

Figure 6.6 shows the static levitation height as a function of dust particle radius. Due to the increase in dust potential near the static levitation point with θ, larger dust particles may levitate at higher latitudes. The maximum particle radius exhibiting levitation decreases with increasing plasma density and temperature as the sheath electric field and dust charge near the levitation point decrease. It is also noticed that very small-sized dust particles ($\sim$ 125 nm) can be stably levitated above the lunar surface in nominal solar wind conditions. For the Type A sheath, the maximum levitation height for the smaller dust particles is noticed to be smaller than Type B sheath. This can be attributed to the existence of negative minima and downward-directed electric fields above the minima, which obscure the possibility of stable levitation beyond the field reversal point. This can not be observed in the Type B sheath, where the upward-directed electric field monotonically decreases to zero with altitude. The static equilibrium behavior of a dust particle with Type A and Type B sheaths exhibits nearly similar trends. Additionally, the presence of a double-layer space-charge region within the Type A sheath gives rise to some extra features which can not be observed in the photoelectron-dominated monotonic Type B sheath. Further analysis of dust dynamics in the photoelectron-dominated region is carried out only for Type A sheath, and it is anticipated that a nearly similar trend will be observed for the case of Type B potential structure.

The present study uses a self-consistently derived Velocity Distribution Function (VDF) of lunar photoelectrons rather than simplified Maxwellian statistics discussed in Chapter 2. As a result, this study yields results that, while supporting some of the gen-

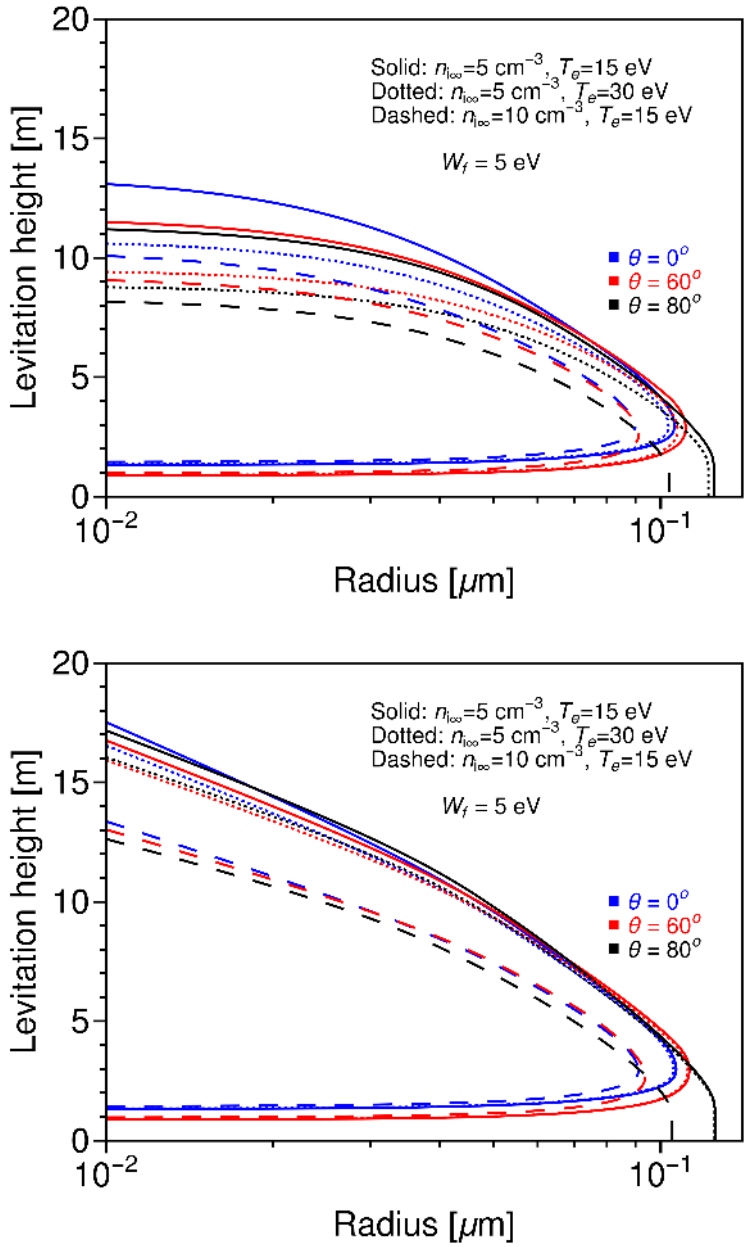

Figure 6.6: The levitation height as a function of dust particle radius within Type A (top panel) and Type B (bottom panel) potential structure.

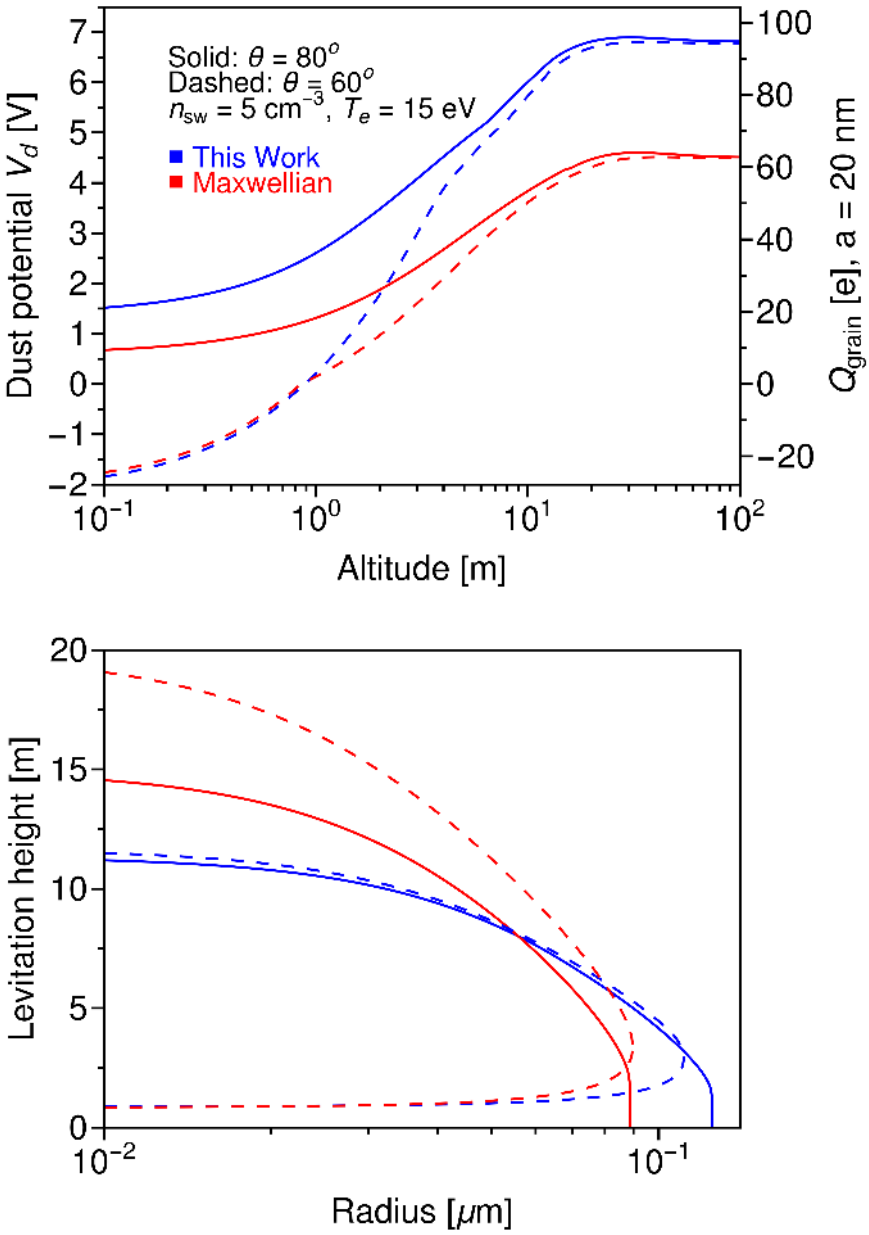

Figure 6.7: Top Panel: The equilibrium dust potential (charge) as a function of altitude. Bottom Panel: The levitation height as a function of dust particle radius. The Blue and Red curves correspond to the Fermi–Dirac and Maxwellian distribution of the photoelectrons, respectively.

eral trends reported in the literature, show significant numerical differences, corroborating with more realistic scenarios in the context of lunar dust dynamics. From Figure 6.7 we note the significant departure in the results at higher latitudes - the Maxwellian assumption overestimates the static levitation height for smaller dust particles and underestimates the maximum size of the dust particle that can achieve static levitation.

6.5.2 For Type C sheath

Near the terminator region with higher values of θ, photoemission is marginal due to the grazing incidence of the incoming photon flux. Here, the surface acquires a finite negative potential due to dominant solar wind/ plasma electron collection and forms an ion-dominated Type C Debye-type sheath in the vicinity. Figure 6.3 illustrates the potential and field structures within the Type C sheath near the terminator. The electric field is directed downward within the sheath. Although the surface is not receiving significant illumination, the dust particle above the surface can receive full illumination. Figure 6.8 illustrates for $\theta = 89^{\circ}$, the dust acquires a finite positive potential within the entire Type C sheath region. The trend can be explained using Figure 3.10 shown in Chapter 3. Near the surface, photoelectrons (although a small amount) are collected on the dust along with solar wind/plasma ions and electrons collection. As the dust is also illuminated, additional positive charging occurs due to photoemission. Near the surface, ion collection dominates, and positive dust charge increases up to a certain altitude due to a decrease in photoelectrons with increasing altitude. As electron density increases with altitude, after a certain height, the negative charging due to higher electron flux increases, but overall positive charging due to the cumulative effect of ion collection and photoemission dominates. As a result, the positive magnitude of the dust charge/potential decreases. Near the sheath edge, the electron flux dominates over the ion flux, but due to higher values of UV-induced photoemission, the dust achieves a constant surface potential near the sheath edge.

For $\theta = 90^{\circ}$, Figure 6.3 illustrates exotic results here, the dust charge near the surface acquires a significantly high positive value due to significant ion collection. Whereas, near the sheath edge, the dust acquires a negative charge/potential due to dominant electron collection. For $\theta = 90^{\circ}$, there is no photoemission from the surface. The lofted dust will be illuminated by photons and develop a positive charge near the edge of the sheath due to the dominant photoemission occurring in that region. However, near the surface, photoemission from the dust becomes negligible. This is because the higher positive po-

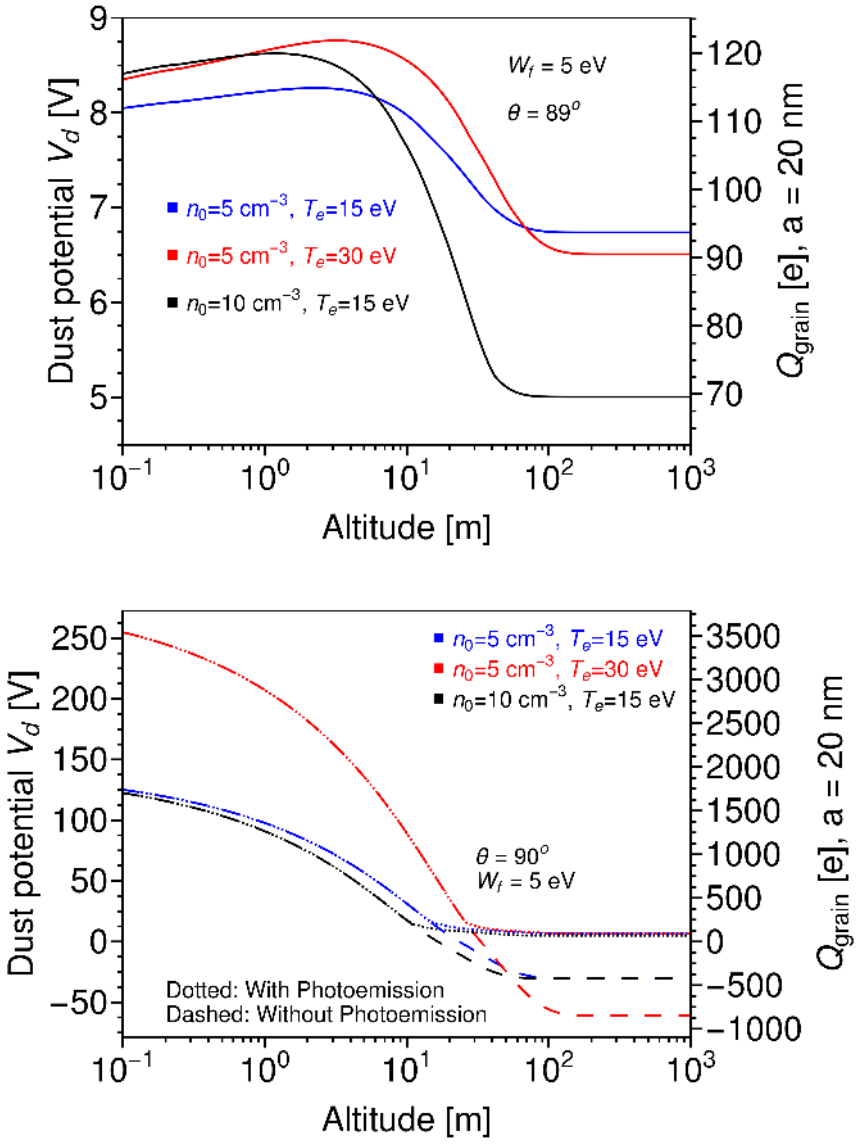

Figure 6.8: The equilibrium dust potential as a function of altitude within Type C potential structure for different values of θ near the terminator. The right axis shows the corresponding steady-state charge on 20 nm dust particle.

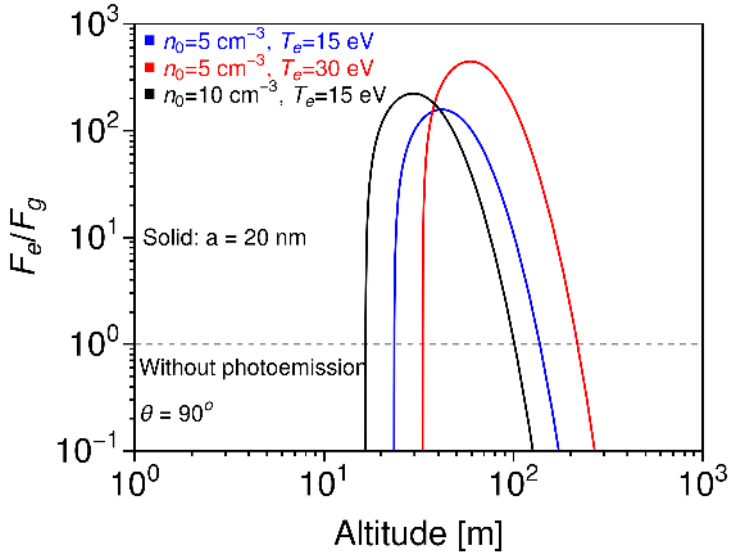

Figure 6.9: The ratio of the electric to gravitational force for 20 nm dust particle within Type C potential structure.

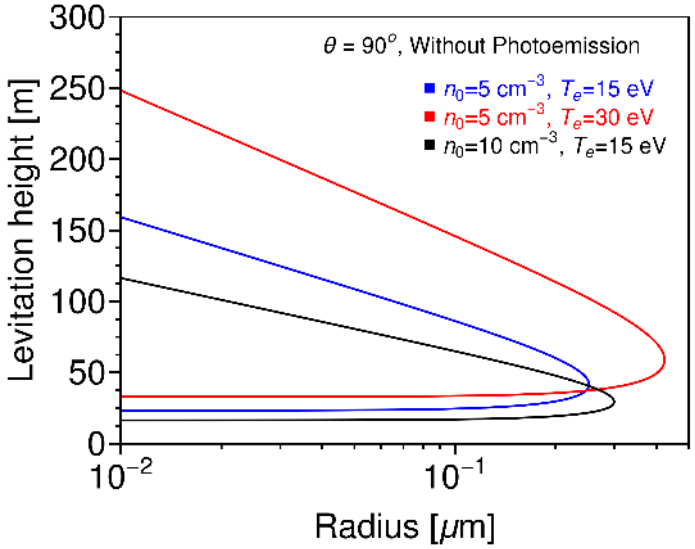

Figure 6.10: The levitation height as a function of dust particle radius within Type C potential structure.

tential due to dominant ion collection creates a larger potential barrier, which traps nearly all of the emitted photoelectrons, resulting in an insignificant contribution from photoemission close to the surface. Stable levitation of lunar dust within the Type C sheath is not feasible near $\theta = 90^{\circ}$ because positively charged dust does not experience an upward vertical force due to the downward-directed electric field. For $\theta = 90^{\circ}$, neglecting photoemission from the dust particle, the analysis of the static levitation points and levitation heights for different dust particle sizes has been illustrated in Figures 6.9 and 6.10. These results illustrate similar trends as predicted by Nitter et al. (1998) for $\theta = 90^{\circ}$. In the present analysis, the non-Maxwellian kappa distribution of electrons has been used instead of the Maxwellian, which has been used by Nitter et al. (1998). Similar to Type A and B sheaths, for Type C, there exist two stable levitation points. Here, the downward-directed electric field creates an upward-directed electric force on the negatively charged dust particle. As a result, the levitation point increases with increasing electron temperature, which gives rise to larger negative dust charge and larger field strength. In contrast, increasing density screens the effect of the potential structure to a lower altitude and increases ion density and flux, which results in lower values of static levitation points as shown in Figure 6.9. Due to similar reasons, Figure 6.10 illustrates an increase in levitation height and maximum dust size for levitation with an increase in plasma temperature and with a decrease in plasma density. These results, however, are not applicable for $\theta = 90^{\circ}$. Because at the terminator, any lofted dust we get full illumination within the sheath and acquires a positive charge. So, this result can only be regarded as valid for locations with zero photoemission, which means for the case of the lunar nightside. Li et al. (2016), adapting the model of Nitter et al. (1998), predicted the dust levitation height and the maximum size of the levitated dust over the entire lunar surface. However, considering the spherical Moon, the concept of the shadow line has not been included in their analysis. In the lunar nightside ($\theta > 90^{\circ}$), if the dust is lifted beyond a certain height H_s, the dust will be illuminated by sunlight. The H_s can be given for the spherical Moon as

$$H_s = R_m \left(\frac{1 - \sin\theta}{\sin\theta} \right) , \tag{6.27}$$

where R_m is the radius of the Moon, and θ should be greater than or equal to $\pi/2$ in radian. Hence, to determine the dust dynamics in night side near the terminator, the concept of the shadow line should be incorporated in the analysis.

It should be noted that the particles undergo dynamical evolution and require a

finite time to reach the aforementioned static levitation. When a dust particle (of any size) is ejected from the surface, its charge undergoes dynamic variation due to various charging effects. The trajectory of the dust particle thus is shaped by electrostatic and gravity forces. Although larger dust particles do not achieve static levitation within the sheath, they can remain suspended and float within the sheath for a finite time during dust dynamics and create an observable dust cloud. The particle dynamics is a significant function of the initial conditions, and the larger size particles can lift to a meter-scale altitude for the appropriate set of parameters.

6.6 Dust levitation dynamics

In the last section, we discussed the static levitation conditions, which primarily refer to the steady-state configuration of the dust dynamics. In this section, we derive and feature the motion of dust particles detached from the surface with a finite speed into the sheath. The detailed dynamical evolution of the dust particle is presented only for the Type A sheath structure. The dynamics for Type B are expected to be similar to those of Type A and will not be addressed separately. For Type C, the static equilibrium analysis indicates that dust particles cannot stably levitate within the Type C sheath structure; therefore, the dynamics of Type C are not considered in this study. Note, the fate of the injected dust particle strongly depends on the initial conditions, that is discussed next.

6.6.1 Initial conditions

Initial speed and initial dust charge, just after the detachment of the dust from the surface, are two important parameters and their manifestation with the sheath features determine the dynamics of the detached dust particle over the lunar surface. Based on the initial conditions, the particles intuitively may exhibit three possible dynamical features: (i) The dust escapes from the Moon, (ii) the dust returns back to the surface, and (iii) the dust floats within the sheath.

The initial charge on the detached dust particle is quite crucial in deriving dust dynamics. In the absence of any established theoretical basis or experimental measurement, intuitively, one may consider the following feasible estimates for the initial dust charge to utilize them as simulation input. Note that the aim of this chapter is to discuss the dust dynamics after lifting, and the in-depth analysis of the electrostatic dust detachment is discussed in the next chapter.

(i) If one considers the charge on the dusty surface to be uniformly distributed, based on Gauss's law, we may write the dust particle charge at the surface as (Wang et al., 2016b)

$$Q_{ds} = 4\pi\epsilon_0\, a^2\, E_s\,, \tag{6.28}$$

where E_s is the electric field of the lunar surface at the surrounding of the dust particle. Taking $E_s \approx 3.5$ V/m for the nominal photoelectron sheath, for $a < 20\,\mu$m, Eq. 6.28 gives that the charge on the dust particle is smaller than one electronic charge. This estimate suggests that the net electrostatic repulsive force is too small to overcome the gravity force in this case.

Due to the dielectric nature of the lunar surface and dust particles (that exhibit extremely poor electrical conductivity), charge patches are created on a dusty surface due to its exposure to UV radiation and/or plasma (Wang et al., 2016b). Moreover, due to the random nature of charging currents, charges on the lunar surface and dust particles fluctuate and vary significantly from those derived from the Gauss law (Rosenfeld and Zakharov, 2020; Mishra, 2020a).

(ii) In this view, following Farrell et al. (2007), we have taken a possibility that the dust potential possesses an identical potential to that of the lunar surface. Based on this assumption, one can write

$$Q_{ds} = 4\pi\epsilon_0\, a\, V_s\,, \tag{6.29}$$

where V_s is the local lunar surface potential surrounding the dust particle.

(iii) Following the work of Wang et al. (2008), the dust particle should acquire sufficient charge to overcome the lunar gravity during its flight through the sheath. In this case, an estimate for the initial charge can be represented as

$$Q_{ds} = \big(1+\delta\big)\frac{m_d g}{E_s}\,. \tag{6.30}$$

Here, $\delta < 1$ is taken such that Q_{ds} takes an integral value and gives initial acceleration.

The initial velocity of the dust particle, i.e., another significant parameter, depends on the launching mechanism. The dust particles may be launched by several means, viz., micro-meteoroid impact, impact/ tidal shaking, (Richardson et al., 2004; Senshu et al., 2015) and large electrostatic repulsion (Wang et al., 2016b; Mishra, 2020a). Wang et al. (2016b) experimentally showed that within micro-cavities between adjacent dust particles below the surface, the emission and subsequent re-absorption of photoelectron and/or

secondary electrons can generate significantly large negative charges and intense particle-particle repulsive forces that can launch the dust particles from the surface. Mishra (2020a) proposed that sufficient electric field and Coulomb repulsion can be created between the dust and surface due to random charge fluctuations at the microscopic scale, which could detach the dust particle from the lunar surface, overcoming dust-surface adhesive force and gravity. Using this model, Mishra and Bhatt (2023) derived the optimum launch velocity of the electrostatically detached dust particle. They show that the smaller particles are estimated to obtain larger velocity ($i.e.$, $\sim 30\,\mathrm{m/s}$ for $20\,\mathrm{nm}$) after detachment, and its magnitude decreases with increasing particle size ($\sim 5\,\mathrm{m/s}$ for $100\,\mathrm{nm}$).

We have carried out the simulation by varying the initial velocity, considering it as a free parameter from 0 to 10 m/s, and using all three types of initial charge estimates discussed above. Note, after launch, i.e., described in terms of initial charge and initial velocity, from the surface, the dust particle undergoes electrostatic charging via photoemission and collection of the sheath constituents - the continued charging effects complicate the dynamic evolution of the dust particles. The expressions/ estimates of the charging currents are presented in the section 6.3.

6.6.2 Solution of the equation of motion

For Moon, $g = 1.63\ \mathrm{m/s^2}$, the escape velocity is 2.38 km/s. For nominal solar radiation and wind plasma conditions, the net repulsive force acting on the dust is not strong enough to allow it to escape from the lunar gravity. Based on initial conditions, the dust particle majorly returned to the surface after a single ballistic trajectory. In our simulation, only a few cases are found where the dust particle remained suspended within the sheath for a longer duration.

The left panel of Figure 6.11 shows the position, velocity, and charge of the dust particles as a function of time for the particles of different sizes launched (detached) from the surface with an initial velocity $u_0 = 0$ and initial charge $Q_0 = (1+\delta)\frac{m_d g}{E_s}$ within the sheath at $\theta = 80^\circ$. For $a = 20$ nm, $Q_0 = 1e$ (Red); $a = 50$ nm, $Q_0 = 11e$ (Green); $a = 100$ nm, $Q_0 = 85e$ (Blue). As the dust particle leaves the surface and travels within the sheath, the particle accelerates upward if the electric force exceeds gravity. At higher altitudes, it decelerates when the sheath electric field decreases, and the subsequent charge variation results in a rise to a periodic hopping trajectory. Small dust particles with lower masses get larger upward acceleration and reach higher altitudes (see the top panel of Figure 6.11, 20 nm dust particle has a higher altitudinal span than 100 nm). It is noticed that a

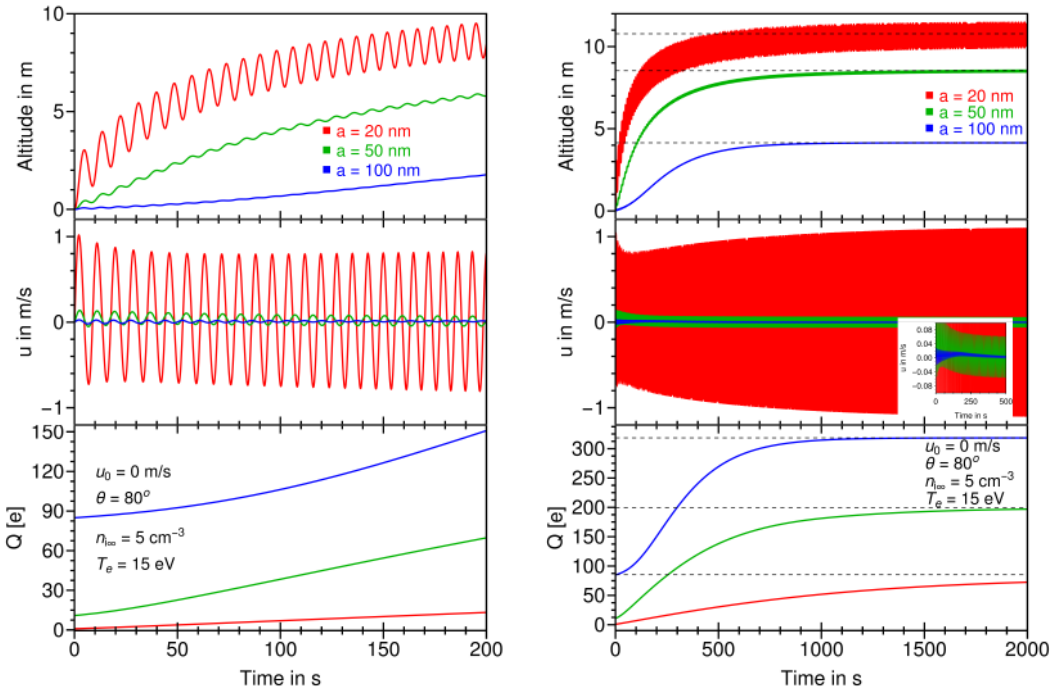

Figure 6.11: Time evolution of position, velocity, and charge of dust particles of different sizes launched from the surface with initial velocity $u_0 = 0$ and initial charge $Q_0 = (1 + \delta)\frac{m_d g}{E_s}$ within the sheath at $\theta = 80°$. For $a = 20$ nm, $Q_0 = 1e$ (Red); $a = 50$ nm, $Q_0 = 11e$ (Green); $a = 100$ nm, $Q_0 = 85e$ (Blue). The left panel shows the trajectories up to 200 seconds, and the right panel shows the same for 2000 seconds to show the steady state feature. The dashed lines correspond to the static levitation altitude (top panel) and corresponding equilibrium charge (bottom panel) of the dust particles of a particular size.

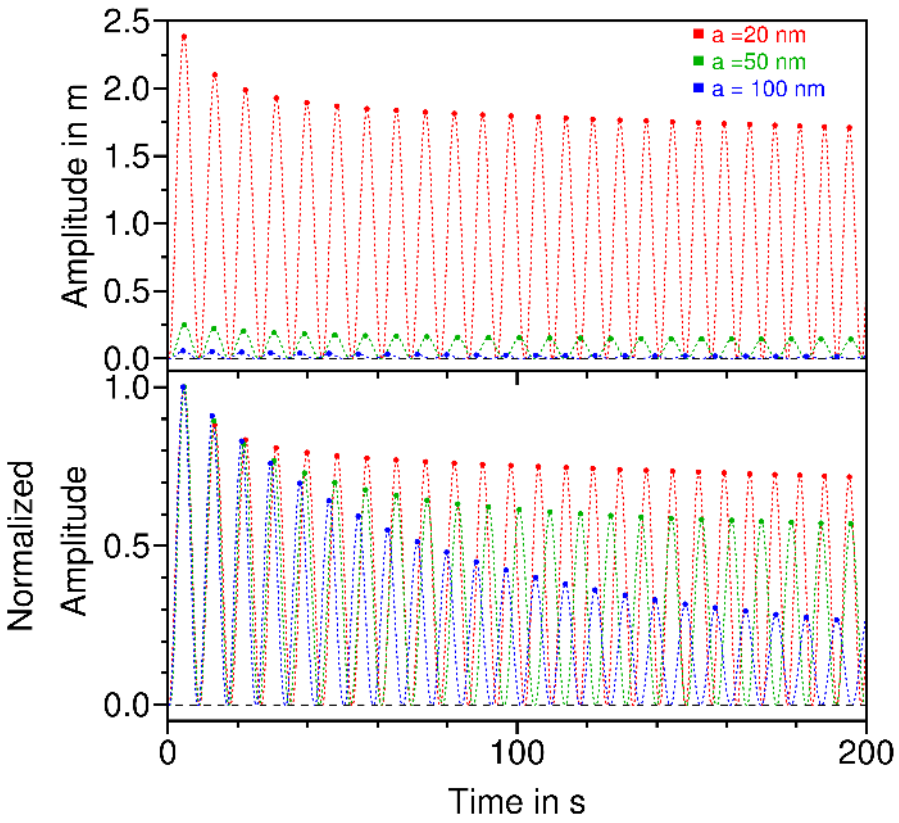

Figure 6.12: Time evolution of amplitude and normalized amplitude of periodic hopping trajectory of the dust particles. The normalized amplitude is defined as the ratio between the amplitude at a particular time and the amplitude of the first period. The same parameters are used, as in Figure 6.11.

20 nm (Red) dust particle has a higher hopping amplitude than that of 50 nm (Green), followed by a 100 nm (Blue) dust particle. Due to the higher acceleration, the velocity of the smaller particle increases, giving rise to a rapid increase in altitude and a rapid decrease in the corresponding electric field at that altitude. Due to the decreasing sheath field, it faces a larger deceleration at the point of maximum altitude, resulting in higher altitudinal coverage during a hop. For instance, a 20 nm dust particle shows an altitudinal coverage of $\sim$ 7.5—9.5 m after two hundred seconds, while it is literally constant for a 100 nm particle. Since the altitudinal coverage decreases with increasing particle size, the variation in electric force and velocity within this altitudinal range is small, leading to a longer hopping period for larger particles.

While travelling within the sheath, the dust charge varies due to photoemission and collection of sheath constituents. We notice that the positive dust charge increases over time due to dominant photoemission from the dust surface. As a result, the electric force on the dust particle increases, increasing upward acceleration, which increases the dust particle's altitude over time. As the positive dust charge increases, it will decrease the photoemission current by creating a positive potential barrier toward the emitted photoelectrons. So, the degree of increase in electric force gets reduced, and the particle hopping starts to saturate about a finite altitude. The left panel of Figure 6.11 shows the variation up to 200s. From this, we can see that the dust particle is approaching the static levitation altitude. The equilibrium dust charge $Q_{d,\mathrm{eq}}$ and corresponding static levitation height l_s have been illustrated in Figures 6.4 and 6.6. For $a = 20$ nm, $(l_s,\, Q_{d,\mathrm{eq}}) = (10.8\,\mathrm{m},\, 85.4e)$, for $a = 50$ nm, $(l_s,\, Q_{d,\mathrm{eq}}) = (8.5\,\mathrm{m},\, 199.4e)$ and for $a = 100$ nm, $(l_s,\, Q_{d,\mathrm{eq}}) = (4.1\,\mathrm{m},\, 318.6e)$.

The right panel of Figure 6.11 illustrates the trajectory of the dust particles up to two thousand seconds. We notice that 100 nm dust (blue) achieves the steady state within the 1250s, while the 50 nm (green) converges to $l_s = 8.5\,\mathrm{m}$ and its charge reaches very close to $Q_{d,\mathrm{eq}} = 199.4e$ at 2000s. However, we see that the 20 nm dust (red) hops around $l_s = 10.8\,\mathrm{m}$, and its charge is yet to reach $Q_{d,\mathrm{eq}} = 85.4e$. Larger particles take less time to reach the steady state as the photoemission and plasma collection current is higher, which results in a shorter charging time. On the other hand, the charging is slower for smaller grains, and it takes longer to achieve a steady state. In simulations, the trajectory of 20 nm has been computed for 6000s; the particle could not attain the steady state even in this time scale and hops around $l_s = 10.8\,\mathrm{m}$. Although the altitudinal coverage of the periodic hopping trajectory increases, Figure 6.12 shows that the amplitude (the difference between the maximum and minimum altitude attained by the dust particle in

a given period) decreases with time. This is consistent with the general entropy principles as dusty plasma mimics a dissipative system - the dissipation in this present scenario is associated with the dust charge variations during its dynamics (trajectory). The nonlinear variation of the amplitude of the periodic hopping trajectory can be explained as follows: Integrating Eq. 6.1 with $u = dx/dt$, we get the energy equation as

$$\frac{u_2^2}{2} + \frac{Q_{d2}V_2}{m_d} + gx_2 = \frac{u_1^2}{2} + \frac{Q_{d1}V_1}{m_d} + gx_1 + \int_{t_1}^{t_2} \frac{I_{tot}\,V}{m_d}\,dt\,. \tag{6.31}$$

In this equation, the energy created by the charging currents is represented by the fourth term on the right side (Li et al., 2016). This term gives rise to this nonlinear effect in the system. For 100 nm dust, I_{tot} takes a large value, and their dynamics are restricted within very small altitudes where sheath potential strength V is large. In this case, the fourth term introduces significant nonlinearity into the system. In the case of 20 nm dust particles, which lift at higher altitudes within the sheath, show a weaker nonlinear effect due to small I_{tot} and small V at higher altitudes. As shown in the bottom panel of Figure 6.12, the variation in normalized amplitude changes at a higher rate for larger-size particles. It means that the charge on the larger grains varies faster rate during its dynamics, which leads to rapid energy dissipation. This variation is due to the fourth term on the right side of Eq. 6.31. Should be noted that the previous results of Wang et al. (2008) and Zhao et al. (2022) do not show these nonlinear behaviors because they use a constant dust charge while addressing the dust dynamics. With the inclusion of varying dust charge during its dynamics (trajectory), this study points out the significance of the dissipation mechanism in the realistic dusty plasma scenario over the Moon.

As noticed in Figure 6.1, the photoelectron sheath's potential and electric field structure significantly vary with θ. Figure 6.13 shows the dynamics of a 20 nm dust at three different latitudes (i.e., θ). From the vertical profiles of electric potential and field (shown in Figure 6.1), we see that their strength decreases with increasing θ. Therefore, the electrostatic repulsion force on a positively charged dust is higher at the equator $(\theta = 0^\circ)$ and reduces towards the higher latitudes (e.g., $\theta = 80^\circ$). As a result, the dust particle reaches a higher altitude near the equator due to a higher upward electrostatic push, and the upward push and altitude decrease towards higher θ (see the top panel of Figure 6.13). The bottom panel of Figure 6.13 shows that initially, the dust charge shows a pattern of reduction and enhancement for a finite time duration - this is more visible in the in-set picture. This pattern is a consequence of charging fluxes on dust during the hops

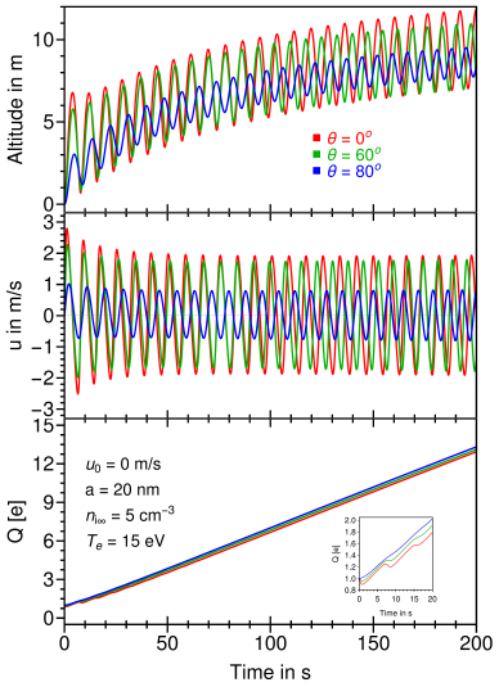

Figure 6.13: Time evolution of position, velocity and charge of 20 nm dust particle for different θ values launched from the surface with initial velocity $u_0 = 0$ and initial charge $Q_0 = (1+\delta)\frac{m_d g}{E_s} \approx 1e$ within the sheath.

(altitudinal oscillations). As the dust passes through a dense photoelectron cloud near the surface where the photoelectron collection dominates, making the particle negatively charged, whereas the photoemission dominates at higher altitudes and makes dust positively charged. Note that due to photoemission, overall positive charging is effectively higher, and the dust charge increases over time. Moreover, as the photoelectron density reduces with altitude and increasing θ, the degree of charge variation reduces (the red and green curves in the bottom panel of Figure 6.13). For higher θ values, e.g., 80°, the sheath's photoelectron density becomes smaller, and the photoemission from the dust dominates as the particle traversing the sheath (the blue curve in the bottom panel of Figure 6.13). For the same reasons, the degree of positive charging is slightly faster for higher values of θ.

At any given latitude θ, the variation of u_0 exhibits variation in the hopping trajectory of the ejected particle; that is quite self-explanatory. Figure 6.14 illustrates the dynamical evolution of a dust particle launched from the surface with different velocities. In the case of a higher initial velocity, the altitudinal coverage (amplitude of the hopping) is larger. Higher u_0 also increases the magnitude of the maximum and minimum velocity. Due to higher u_0, the dust quickly passes through the near-surface photoelectron layers.

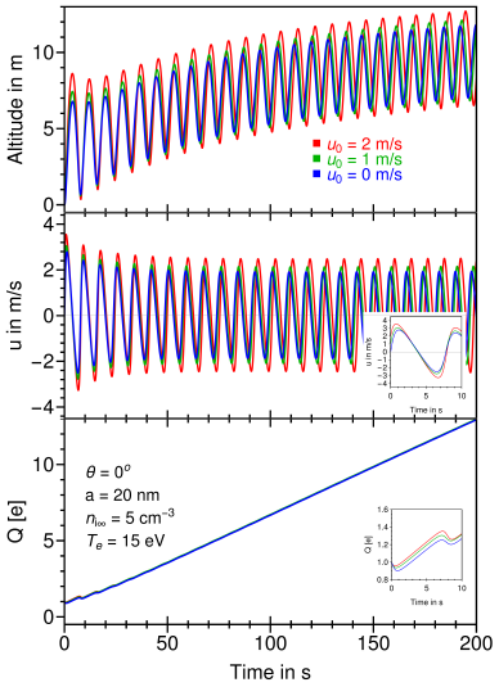

Figure 6.14: Time evolution of position, velocity and charge of 20 nm dust particle for different values of u_0, launched from the surface at $\theta = 0^\circ$ and initial charge $Q_0 = \left(1 + \delta\right)\frac{m_d g}{E_s} \approx 1e$ within the sheath.

As a result, photoelectron collection from the sheath reduces, which causes less reduction of dust charge in the beginning phase (in time) when the dust is near the surface (see the inset of the bottom panel of Figure 6.14). However, as the dust reaches a higher altitude due to dominant photoemission, the dust charge shows marginal variation for all the three values of u_0 at a larger time scale.

As discussed earlier (in section 6.6.1), the initial charge of a dust particle can substantially alter its dynamical evolution. This effect has been illustrated in Figure 6.15. It shows the dynamics of the dust particles with $x_0 = 0$, $u_0 = 0\,\mathrm{m/s}$ and $Q_0 = 4\pi\epsilon_0\, a\, V_s$. The following dynamical evolution significantly differs from the dynamics discussed earlier considering Q_0 corresponding to Eq. 6.30. In case when the dust charge is taken equivalent to the lunar surface potential (Eq. 6.29), the electrostatic force on the dust becomes very high compared to earlier cases. For example, a 20 nm dust feels 32 times higher electrostatic force than $Q_0 = \left(1 + \delta\right)\frac{m_d g}{E_s} \approx 1e$. For 50 and 100 nm dust, the force increases by a factor of 7.3 and 1.9, respectively. Due to this, smaller dust particles experience significant vertical push, which significantly increases its velocity. This quick increase in velocity might lead the dust particle to cross the potential minima at x_m within the sheath. Above the potential minima, the electric field is directed downward - this will attract the dust

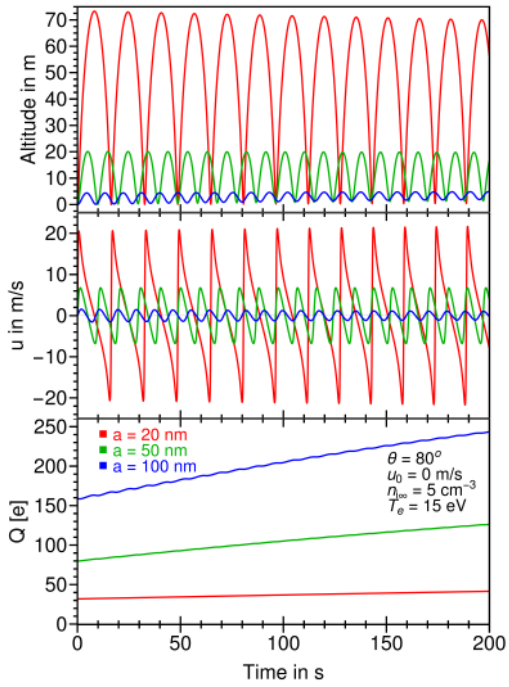

Figure 6.15: Time evolution of position, velocity and charge of dust particles of different sizes, launched from the surface at $\theta = 80^\circ$ with $u_0 = 0$ m/s and initial charge $Q_0 = 4\pi\varepsilon_0\, a\, V_s$ within the sheath. For $a = 20$ nm, $Q_0 = 32e$ (Red); $a = 50$ nm, $Q_0 = 80e$ (Green); $a = 100$ nm, $Q_0 = 159e$ (Blue).

particle towards the surface and a rapid decrease in velocity takes place. As soon the dust reaches below the x_m, the field again apply as an upward force, reducing the degree of deceleration. In this course the dust might reach very close to the surface. However, in this traverse, the dust becomes more positively charged due to significant photoemission - this leads to a relatively higher electrostatic push in the upward direction, and give rise to a periodic hopping trajectory over time. The dynamical evolution (Figure 6.15), however, does not show significant non-linear effects. This can be understood using Eq. 6.31. In the region of significant V (low altitude), along with kinetic energy, the electrostatic potential energy is higher than the non-linear fourth term in the right-hand side of Eq. 6.31. At higher altitudes, the term again becomes small due to lower V and overall reduces the non-linear effects.

The calculations, results, and discussions made so far have focused solely on the cases resulting in periodic hopping trajectories. In the following section, we will quantitatively discuss the fate of the injected dust particle from the surface with a set of initial conditions, i.e., in terms of initial velocity, and initial charge at different latitudes.

		$Q_0 = (1+\delta)\frac{m_d g}{E_s}$					$Q_0 = 4\pi\varepsilon_0 a V_s$				
		u_0 in m/s									
		0	1	2	5	10	0	1	2	5	10
20nm	80°	Y	Y	-	-	-	Y	Y	Y	-	-
	60°	Y	Y	Y	-	-	Y	Y	Y	-	-
	0°	Y	Y	Y	-	-	-	-	-	-	-
50nm	80°	Y	-	-	-	-	Y	Y	-	-	-
	60°	-	-	-	-	-	Y	Y	-	-	-
	0°	-	-	-	-	-	-	-	-	-	-
100nm	80°	Y	-	-	-	-	Y	-	-	-	-
	60°	-	-	-	-	-	-	-	-	-	-
	0°	-	-	-	-	-	-	-	-	-	-

Table 6.1: Fate of a test dust particle injected from the surface with various initial charges and velocities. "Y" indicates the possibility of periodic hopping dynamics, and "-" indicates a single ballistic trajectory.

a in nm	$\theta = 0°$	60°	80°
20	1	1	1
50	4	6	11
100	29	43	85

Table 6.2: Dust charge at the lunar surface to overcome lunar gravity at different θ calculated from Eq. 6.30. The charges are in terms of e.

6.6.3 Fate of an injected dust particle

Here, we consider the dust particle is launched from the surface with a given initial charge and vertical velocity and analyze the motion of the dust particles to constrain the set of initial conditions that lead to a single ballistic hop or periodic hopping trajectory of the particles. Following Eq. 6.28, first, we assigned zero initial charges for 20, 50, and 100 nm dust and launched them with initial velocities of 1, 2, 5, and 10 m/s from the three locations at 0°, 60°, 80° latitudes over the Moon. Calculations suggest that in every possible combination, the dust particle returns to the surface after a single hop and does not undergo periodic hopping. This happens because the dust particle cannot accumulate the required charge to overcome gravity during its flight. There may be many reasons why the dust particles could not acquire sufficient charge: (i) If the dust is launched with a

a in nm	$\theta = 0°$	60°	80°
20	102	73	32
50	253	181	80
100	506	362	159

Table 6.3: Dust charge equivalent of lunar surface potential at different θ calculated from Eq. 6.29. The charges are in terms of e.

relatively small velocity, its motion should be confined very close to the surface. For instance, with $u_0 = 1$ m/s and $Q_0 = 0$, its traverse remains within 30 cm above the surface. Here, the neutral dust primarily accumulates negative charges due to the higher number density of the photoelectrons (particularly for the lower values of θ). The electrostatic force due to the upward-directed electric field added to the gravity pulls the dust toward the surface. (ii) For lower θ, at higher altitudes, the photoelectron density reduces. Due to dominant photoemission, in this case, the dust might acquire, though not sufficient enough to counter gravity against the electrostatic force and the particle falls on the surface at the end of its return flight. For example, consider a neutral dust particle is launched with $u_0 = 10$ m/s. Under gravity, the particle takes a single ballistic hop for about 12.3 seconds. From Table 6.2, to overcome downward deceleration and rise again above the surface, a 20 nm dust particle needs to accumulate at least $1e$ positive charge within this timescale. The photoemission current on the 20 nm neutral dust is around $0.08e$/s, and thus, it should acquire one positive electronic charge in 12.5 seconds. The dust also accumulates negative charges from the sheath's plasma and photoelectrons, which results in an increase in the positive charging time (> 12.5 s). In this case, the dust fails to achieve sufficient charge to overcome the downward deceleration and falls on the surface after the ballistic hop.

Based on simulation carried out, Table 6.1 shows the possibility of periodic hopping trajectory with initial charges $Q_0 = \left(1+\delta\right)\frac{m_d g}{E_s}$ and $Q_0 = 4\pi\epsilon_0\, a\, V_s$. The conditions where the periodic hopping (oscillation) is possible are marked with "Y," and the trajectories that end with a single hop are represented by an empty cell. We see that the dust does not undergo any periodic hopping trajectory for major choices of initial conditions. In the case of $Q_0 = \left(1+\delta\right)\frac{m_d g}{E_s}$, with lower velocity, where we get only a single hop, the reasons are in line with the first explanation in the last paragraph. In this scenario, because of higher photoelectron accretion, the positive charge on the dust decreases below the charge required to counter gravity force, and the electrostatic force becomes insufficient to lift the dust again. For higher values of u_0, the dust reaches higher altitudes, and a larger time of flight might give it an ample chance to accumulate sufficient positive charge such that it counters gravity but also pushes its motion to a periodic hop trajectory. However, in most cases, the dust is unable to gather sufficient charge to overcome downward deceleration during its motion and return back to the surface after a single hop, as discussed (explanation ii) in the last paragraph. For $Q_0 = 4\pi\epsilon_0\, a\, V_s$, from Table 6.3, we see that dust acquires a significantly large initial charge, which makes the dust particle

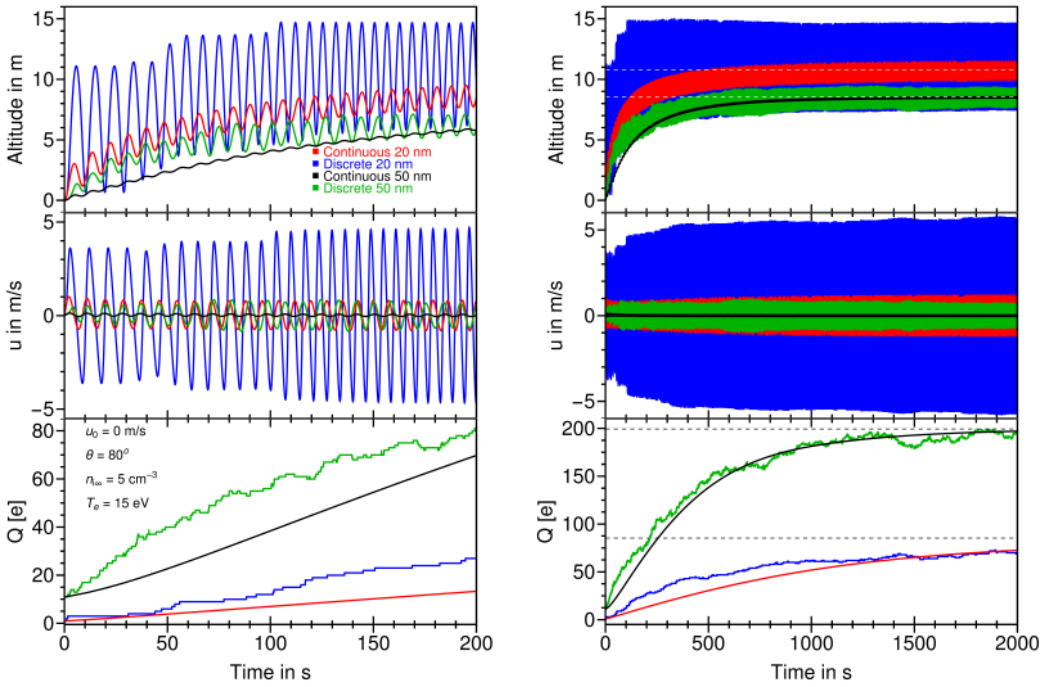

Figure 6.16: Comparison of discrete and continuous charging model in the time evolution of position, velocity and charge of 50 nm dust particle, launched from the surface at $\theta = 80^\circ$ with $u_0 = 0$ m/s and $Q_0 = 1e$ (for 20 nm) and $Q_0 = 11e$ (for 50 nm) within the sheath. The left panel shows the trajectories up to 200 seconds, and the right panel shows the same for 2000 seconds to show the steady state feature. The dashed lines correspond to the static levitation altitude (top panel) and corresponding equilibrium charge (bottom panel) of the dust particles of a particular size.

reach a higher altitude. Thereafter, while returning back, the downward velocity becomes very high, and for the same reason as discussed, it cannot flip the direction of the velocity. Therefore, in the case of the Moon, under nominal solar irradiation parameters, there are only a few initial conditions that induce the periodic hopping of the dust particle. This set of calculations gives the impression that periodic hopping is more probable for smaller grains, higher latitudes and lower velocity of dust injection.

6.7 Discrete charging

In the discussion so far, mean charge theory has been applied to describe dust dynamics, which is based on the continuous nature of the charging currents - it reciprocates in the dust charging and yields continuous variation of the dust charge with time. The approach is well applicable to physical systems comprised of dense plasma and a large number density of dust particles. However, in dealing with low particle densities, the discrete nature of the charge carriers may be important. For example, take a 20 nm dust in a

nominal solar wind plasma with $n_{i\infty} = 5\ \mathrm{cm}^{-3}$ and $T_e = 15$ eV. Considering Maxwellian electrons and protons, their accretion rates are $I_e \approx -0.02e/\mathrm{s}$ and $I_i \approx 0.0003e/\mathrm{s}$. Based on the "continuous charging model", the charge on the dust particle after one second is $Q \approx -0.0197e$. But if we consider the discreteness, the dust charge can be anything after one second. It can be 0 (if neither electron nor proton gets collected or dust collects both of them), $1e$ (proton collection), or $-1e$ (electron collection) etc. However, the possibility for different discrete charges is different, and it depends on the charging currents. In this case, the possibility of dust charge to be $-1e$ is higher because $I_e > I_i$. However, since both I_e and I_i are much less than one, there is a much higher possibility that the dust may not collect any charge. Therefore, the discrete nature of the dust charge is crucial because it might influence the trajectories of particles, especially for smaller dust particles. We apply a Monte Carlo approach to address the discreteness and quantized charge capture/emission. The probability per unit of time for absorbing a (photo)electron or ion and emitting a photoelectron can be expressed as (Cui and Goree, 1994)

$$\omega_j = I_j / Q_j \,, \tag{6.32}$$

where j denotes a particular charge species. $j = (p)e$, $Q_{(p)e} = -e$ for (photo)electron, $j = i$, $Q_i = e$ for ion, and $j = ph$, $Q_{ph} = e$ for single photoemission. Since I_j depends on sheath potential V, the probabilities also are the function of V. To implement this in the numerical simulation, we start solving Eq. 6.1, with an initial condition (Q_0, u_0) at $t_0 = 0$. We define a small time step Δt. In this time step, the particle moves to a different position. At this position, we define the probability of collection sheath constituent or emitting photoelectron as (Cui and Goree, 1994)

$$P_j = 1 + \exp\left(-\Delta t \omega_j\right). \tag{6.33}$$

To address the randomness of the charging currents, we generate random numbers $0 \leq R_j \leq 1$. If $P_j \geq R_j$, dust collects particular plasma species or emits a single photoelectron, and the dust charge changes discretely. Next, the same process is performed with updated dust, plasma, and dynamical parameters - the multiple cycles of this algorithm yield the time evolution of the dust particle trajectory.

Figure 6.16 illustrates the comparison of discrete and continuous charging on the dynamical evolution of the dust. The altitudinal variation is significantly different and

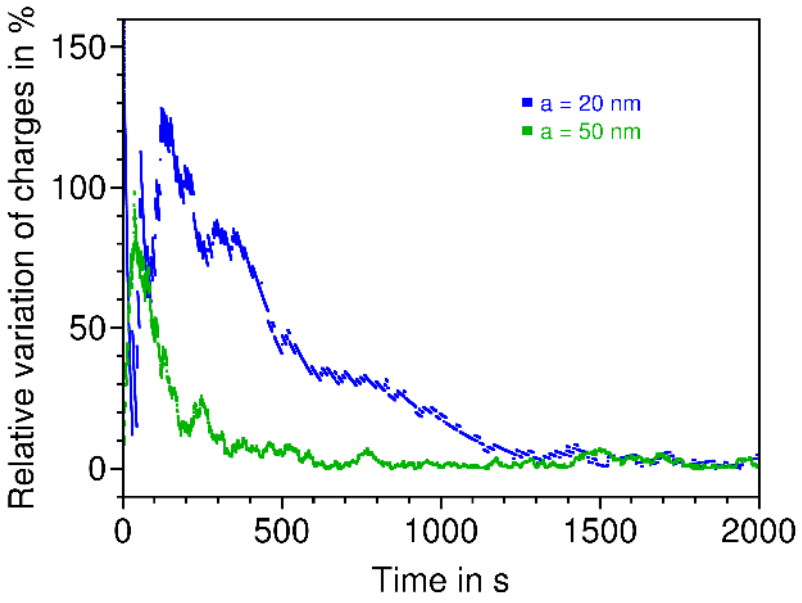

Figure 6.17: The time evolution of relative variation of charges in % between discrete and continuous charging model for 20 (Blue) 50 (Green) nm dust particle, launched from the surface with same initial conditions as in Figure 6.16.

random for the case of discrete charging. For smaller dust, the altitudinal coverage is noticed to be larger. This can be explained as follows: for 20 nm dust at the surface, $1e$ dust charge is sufficient to overcome the gravity. Now, near the surface, due to photoemission, if it emits a photoelectron, its charge becomes $2e$, which doubles the electrostatic repulsive force. As a result, the dust experiences a significantly large vertical push and covers a larger altitude. On the other hand, 50 nm dust, with an initial charge of $11e$, will feel a nearly 1.1 times larger electrostatic force upon emitting a single photoelectron. Figure 6.17 illustrates the relative variation of charges $\left(|Q_d - Q_C|/|Q_c|\right)$ in % between the discrete and continuous charging models. This shows that during the transient evolution within the sheath, smaller dust particles experience a higher variation of relative charges, which increases the variation in electrostatic force compared to larger particles. However, upon reaching close to the steady state, the relative variation of charges for both 20 nm and 50 nm particles reaches below 10 %. Hence, for smaller dust particles, the discrete charging may give significantly different dynamical evolution. It is noticed that the smaller dust particles take longer time to collect electrons/ions and emit photoelectrons than larger particles. This can be attributed to the fact that due to the larger area, the charging current and charging probability are higher for larger particles, giving rise to rapid variation of charge. The dust particles start with a small positive charge at $t = 0$. Due to the dominant photoemission current at $\theta = 80^\circ$, the positive dust charge rapidly increases, and

the charge variation significantly diverges from continuous charging. After some time, as the dust collects sufficient positive charge, photoemission current and probability of photoemission decreases, and electron collection increases. The dust charge after a sufficient time is noticed to fluctuate around the charge value that is derived from the continuous charging (see the right bottom panel of Figure 6.16).

Note that due to the probabilistic nature of the approach, the repetitive simulations with the same initial condition for a particular dust size provide different outcomes in each run. For instance, in the case of 20 nm dust (shown on Figure 6.16) calculations, the "oscillating" and "falling down" ratio is 0.61 if we run the simulation 50 times while 0.59 for 100 runs (keeping the initial condition the same). Here, we have shown the simulation results representing the periodic hopping nature of the dust dynamics. However, we have also analyzed the motion with various initial conditions, as discussed in section 6.6.3. The simulation suggests that if the dust particles do not gain enough charge during the first pass through the photoelectron sheath, they can not overcome gravity and re-impact to the surface. If they gain sufficient charge, there is also a possibility of charge reduction due to the collection of opposite charges during subsequent passages, which again results in re-impact to the surface. From the discussion of 6.6.3, we get the periodic hopping motion of the dust particles using continuous charging that is limited by a parameter space in initial charge and velocity. The discrete charging model reduces the likelihood of periodic hopping motion and subsequent levitation, even further.

6.8 Summary and future work

A numerical simulation of dust charging and dynamics within the lunar photoelectron sheath has been carried out using the comprehensive sheath model discussed in Chapter 3. A test dust particle has been introduced within the sheath, and using the sheath electric potential and field profiles, the equation of motion and the equation of dust charging have been solved. The static levitation conditions have been derived for various solar wind plasma parameters at various locations of the Moon and discussed for all Type A, B, and C sheaths. Thereafter, the dynamical evolution of dust particle charge and trajectory within Type A sheath have been derived under various initial conditions in different locations on the Moon. A self-consistent and more realistic approach to photoemission and sheath formation is adopted in this work - while supporting some of the general trends reported in the literature, the results illustrate a significant difference in their numerical estimates

which effectively reflects in the dust dynamics.

The results of static equilibrium suggest: (i) The equilibrium dust potential (or charge) $V_{d,\mathrm{eq}}(Q_{d,\mathrm{eq}})$ varies altitudinally and latitudinally within the lunar photoelectron sheath. At lower θ, the dust particles acquire negative charge near the surface, whereas at higher latitudes, the dust charge remains positive within the entire sheath region. For instance, for 20 nm particle, the charge varies between $-47e$ to $95e$ within the non-monotonic Type A sheath and between $-47e$ to $91e$ within the monotonic Type B sheath over the sunlit Moon. (ii) The equilibrium dust potential within the Type C sheath near the terminator is found to be positive throughout the sheath region, which hinders the possibility of stable levitation within a downward-directed electric field structure. (iii) For Type A and B sheaths, static levitation point(s) exist for certain-sized dust particles, where electrostatic force balances gravity. For lower θ, two such points exist - the point corresponding to the higher altitude is considered stable. For higher θ values, only one (stable) static levitation point exists. At each θ, a cutoff radius exists beyond which static levitation could not be obtained. For instance, for $\theta = 80^{\circ}$, static levitation of dust particles larger than $\sim$ 125 nm is not possible. The results of static equilibrium suggest the possibility of a dust layer stably suspended above the sunlit Moon within Type A and Type B sheaths. However, it has been found that the dynamic condition does not always favor the formation of a stable dust layer. To form a dust layer, the particles must be lifted from the surface and reach the balancing point to get settled. However, depending on the launching mechanisms, the dust particles detach from the surface with a finite initial velocity and charge and get settled with time. The results for the dynamic evolution of the dust particle based on the continuous charge model show : (i) A small regime of initial conditions exists where the dust particle undergoes a periodic hopping trajectory and proceeds towards the static levitation point. In other cases, the dust particles re-impact the surface after a single ballistic hop. (ii) Larger dust particles take less time to reach the static levitation point. (iii) The altitudinal variation of the dust charge during its dynamics yields nonlinear variation of the hopping amplitude - the effect is more pronounced for the larger size particles.

The inclusion of the discrete nature of dust charging, however, illustrates a significant difference compared to continuous charging. The discrete charging model shows: (i) The randomness of charging currents induces discreteness of the dust charging, and dust particle exhibits significantly different dynamical evolution compared to that obtained from continuous charging. (ii) The effect of discreteness is noticed to be significant for

smaller dust particles. (iii) In most cases, the dust particles are not able to accumulate sufficient charges. Thus cannot sustain themselves within the sheath and re-impact the surface, which reduces the likelihood of stable dust levitation. A detailed demonstration and comparison of the discrete and traditional continuous dust charging models reveal new findings and advance the understanding of dust behavior in the lunar plasma environment. We anticipate that detecting this kind of motion of very fine dust particles on the Moon would be very challenging. However, a lab experiment similar to Wang et al. (2016b) can be proposed where this situation can be mimicked, and the trajectory of the particles can be tracked. Moreover, the conceptual basis of the charge discreteness can also be tested using the dust sample of uniform-size grains, which, as per notion, will perform different dynamical evolution for each particle due to randomization of the charging flux and discrete charging effects.

Although the possibility of stable levitation is very small, transient events of dust layer formation are possible due to electrostatically detached dust particles with a single ballistic hop. Since the electric potential profiles within the sheath vary from the equator to the terminator, the horizontal electric field is created, which can give rise to the horizontal transport of the electrostatically lofted dust particles. Though the horizontal field is six orders of magnitude weaker than the vertical field near the mid-latitude, significant dust transport is possible in this region. To qualitatively assess this, we may consider a lofted dust particle with zero horizontal speed under a horizontal electronic field $E_h \approx 10^{-6}$ V/m. The horizontal displacement can be written as

$$h = \frac{Q_d E_h}{2m_d} t^2 . \tag{6.34}$$

For a 20 nm dust with $Q_d = 1e$, sustaining within the sheath over $t = 2000$ s can be horizontally transported up to 3.2 m - a considerable amount of dust might be transported considering the geological time scale.

This chapter did not analyze the detailed dust dynamics near the terminator region and on the nightside of the Moon. Near the terminator region, due to the grazing angle, and on the nightside, the surface doesn't get full illumination, which results in insignificant/zero photoemission; the surface acquires a negative potential and forms a Type C Debye-type sheath. Here, the electric field is directed towards the surface. However, a lofted dust particle might get full solar illumination (if the dust is above the shadow line on the nightside), and due to significant photoemission, the equilibrium dust charge be-

comes positive. As a result, static levitation is not expected in the terminator region. The sheath structure near the terminator is dominantly characterized by plasma ions and electrons; the plasma parameters (e.g., $n_{i\infty}$ and T_e) are important in determining the potential and field structure. In the dayside of the terminator, the horizontal electric field is created due to decreasing effective solar radiation with increasing θ, whereas, on the other hand, the difference in plasma populations on the nightside creates a horizontal electric field. Since near the terminator, the potential profiles undergo rapid horizontal variation, which creates a relatively strong horizontal field, giving rise to large transient horizontal transport. In the nightside, away from the terminator region, a Type C Debye-type sheath forms. Results from static equilibrium indicate the possibility of stable dust levitation in this area. Mathematical analyses similar to those used for Type A can be applied to study dust dynamics. However, Chapter 5 demonstrated that secondary electron emission upon the bombardment of highly energetic primary electrons on the lunar nightside can significantly alter the structure of the local plasma sheath. Dust particles may also emit significant secondary electrons and may be levitated in the secondary electron-dominated inverse sheath discussed in Chapter 5. The detailed formulation using the accurate velocity distribution function of the primary and secondary electrons could be taken up in the near future. Additionally, the presence of surface topography further complicates the picture of the plasma environment around the terminator or polar region of the Moon. Any positive topography can obstruct the incoming solar wind plasma upstream and create a wake-like structure on the leeward side - a better understanding of the plasma population is required to describe the field structure and subsequent dust transport in such regions. The present study has discussed the particular cases of dust charging and dynamics over the Moon and is the basis for future studies that could be undertaken by including the aforementioned aspects. Moreover, though the theory and analysis have been applied to the lunar perspective, they are equally applicable to any situation resembling similar physical systems.

Chapter 7

Electrostatic dust detachment

7.1 Introduction

Previous chapters demonstrated that solar irradiation (i.e., radiation and wind plasma) electrostatically alters the lunar surface and overlying dust particles that undergo electrostatic charging, and a near-surface space charge region, i.e., photoelectron sheath Manka (1973), is created in the vicinity of the sunlit surface. The sheath is characterized by inherent electric potential/ field structure, with a typical electric field $\sim$ 5 to 10 V m^{-1} at the surface as estimated in the earlier chapters and previous studies (Nitter et al., 1998; Stubbs et al., 2006, 2007; Farrell et al., 2007; Poppe and Horányi, 2010; Sodha and Mishra, 2014; Mishra and Bhardwaj, 2019; Zhao et al., 2021). This field is anticipated to levitate submicrometer- and micrometer-sized dust particles above the lunar surface, allowing them to evolve dynamically with space and time as shown in Chapter 6. This complex dust dynamics is believed to be the main cause of the Lunar Horizontal Glow that is proposed by light scattering through floating charged dust particles (Rennilson and Criswell, 1974; Zook and McCoy, 1991). Early studies and Chapter 6 in this thesis investigated dust dynamics and subsequent levitation to a significant extent; however, the dust detachment from the lunar surface is one of the crucial aspects of understanding the electrostatic processes governing the lunar dusty plasma environment (Hartzell and Scheeres, 2011; Wang et al., 2016b; Zakharov et al., 2020; Mishra, 2020a; Mishra and Bhatt, 2023). The dust particles may be launched by several means. Mechanical action created by fast meteoroid impacts can separate dust particles from the lunar surface in the form of impact ejecta (Popel et al., 2016). Apart from this, the electrostatic effects could be a significant intrinsic source leading to the dust detachment from the lunar surface (Sheridan and Hayes, 2011;

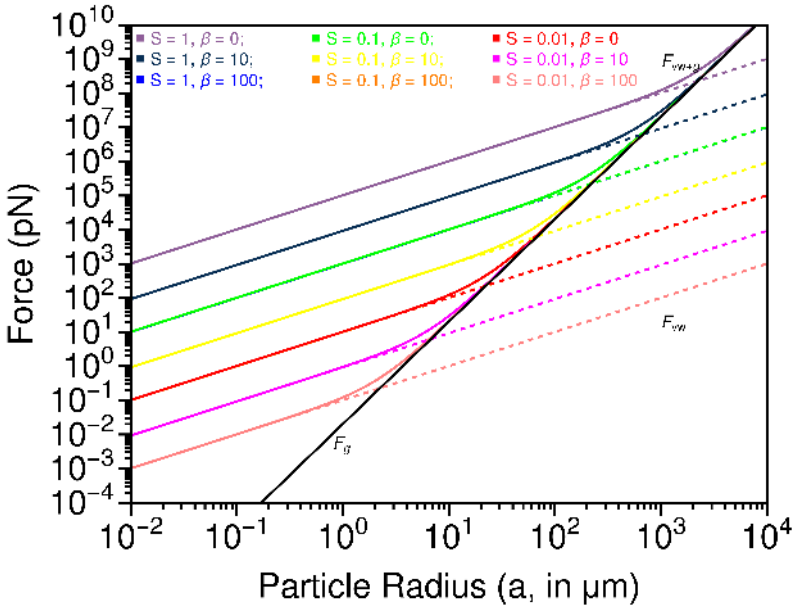

Figure 7.1: The constituent forces corresponding to the dust particle.

Wang et al., 2016b; Rosenfeld and Zakharov, 2020; Mishra, 2020a).

The dust particle lying on the charged lunar surface is subjected to gravity, cohesion, and electrostatic forces. If the electrostatic force exceeds the combined forces of cohesion and gravity, the dust particle detaches from the surface and lifts above. The gravitational and cohesive forces operating on spherical grains can be written as

$$F_g = \frac{4\pi}{3} a^3 \rho g \,, \tag{7.1}$$

$$F_{vw} = k_s S^2 a \left[\frac{b}{b+a}\right] = \frac{k_s S^2 a}{1+\beta} \,, \tag{7.2}$$

where a and b are the radius of the dust particle and roughness, respectively, $\beta = a/b$ (Mishra, 2020a), $k_s = H/24\Omega^2$, H is the Hamakar constant ($\approx 4.3 \times 10^{-20}$ J), $\Omega = 0.132$ nm characterizes the diameter of an oxygen ion, S is the cleanliness parameter (Popel et al., 2016), $\rho = 3\,\mathrm{g\ cm^{-3}}$ is the mass density of lunar dust and $g = 1.63\,\mathrm{m\ s^{-2}}$ is the lunar gravity.

Figure 7.1 illustrates the magnitude of the cohesive and gravitational forces that bind dust particles with the lunar surface - note that the electrostatic repulsion should prevail over this cumulative effect to detach particles from the surface. For instance, a dust of 20 nm requires ~ 0.1 pN force to detach it from the lunar surface (for given S and β). Applying Gauss law of electrostatics (Nitter et al., 1998; Stubbs et al., 2006, 2007; Farrell

et al., 2007; Poppe and Horányi, 2010; Sodha and Mishra, 2014; Mishra and Bhardwaj, 2019; Zhao et al., 2021) to the sunlit lunar conditions, the surface electric field (~ 5 V m^{-1}) yields the mean surface charge density $\sim 5 \times 10^8\, e$ m^{-2}. Presuming the overlying dust particles acquire the same charge density, a 20 nm dust barely acquires a single electronic charge. It suggests that no dust particle could rise off the lunar surface for such a low charge density. In fact, the electrostatic lifting requires ~ 5 orders of magnitude higher charge density and/ or dust charge.

Laboratory experiments (Flanagan and Goree, 2006; Wang et al., 2009, 2016b) and space observation (Zook and McCoy, 1991), however, have demonstrated dust flights under the action of electrostatic processes induced by surface interaction with ambient plasma and solar irradiation. Wang et al. (2016b) explain these observations with a patched-charged model. They suggested the presence of micro-cavities between the dust particles and adjacent surfaces, which could yield a large negative charge and intense particle-particle repulsive forces due to the emission/re-absorption of the photoelectrons and/or secondary electrons. In their experiments, the dust particles are observed to accumulate a significant net negative charge. Consequently, detached charged dust particles have less likelihood of undergoing periodic hopping trajectories within the photoelectron sheath, which is widely predicted in Chapter 6 and in various studies (Nitter et al., 1998; Wang et al., 2008; Poppe and Horányi, 2010; Li et al., 2016; Popel et al., 2022). The plasma conditions in the lunar environment are considerably tenuous compared to those in typical laboratory framework. Therefore, accumulating enough charge to detach dust particles may require a prolonged duration in space conditions. Moreover, Wang et al. (2016b) discussed the requirement of significantly high-energy photoelectrons to accumulate enough charge for the detachment of $\sim 10\,\mu$m diameter dust inferred for the lunar horizon glow (Rennilson and Criswell, 1974). Although solar soft X-ray radiation may create such photoelectrons under lunar conditions (Rennilson and Criswell, 1974), significant photon flux and quantum yield in the UV region yield UV-induced photoemission as the dominant source for the lunar surface charging over sunlit locations. These facts emphasize a critical need for further investigation into electrostatic dust detachment.

Charge fluctuation is another significant mechanism that could provide an additional explanation for dust release (Cui and Goree, 1994; Sheridan and Hayes, 2011; Sheridan, 2013; Rosenfeld and Zakharov, 2020; Mishra, 2020a). Sheridan and Hayes (2011) highlighted that the charge fluctuation on a dust particle resting on a surface exposed to a bulk plasma could lead to dust detachment. Considering Maxwellian plasma electrons

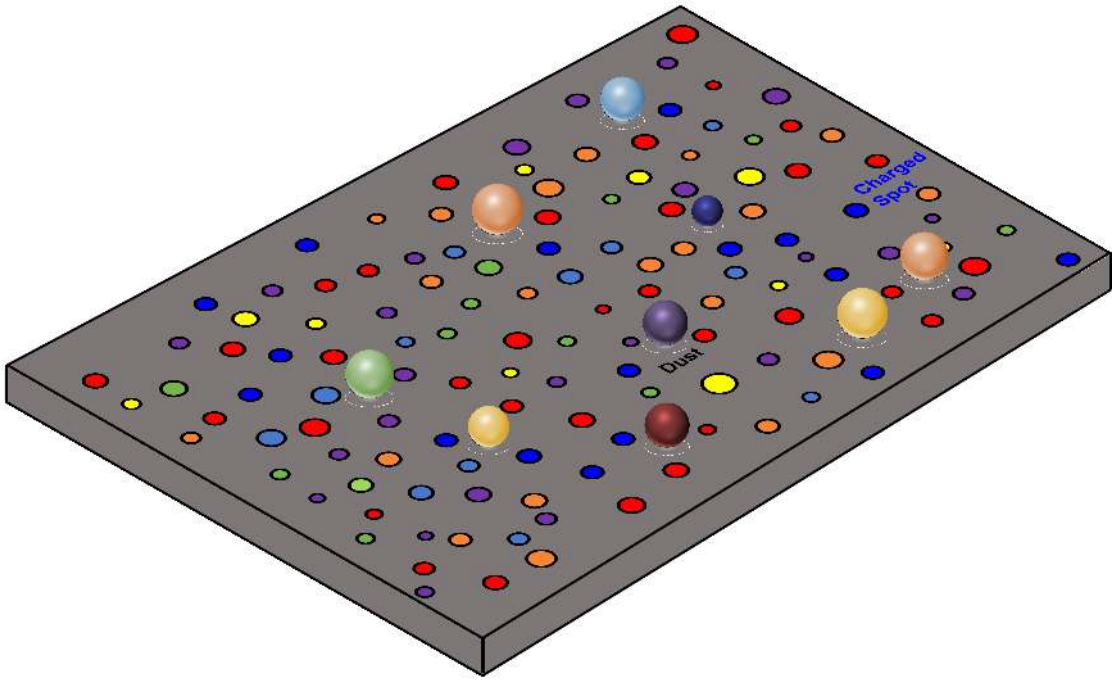

Figure 7.2: Physical scenario of the dust particles and charged microscopic spots.

and cold ions, they derive a simple empirical relation determining fluctuating charge magnitude, showing a dependence as square root of T_e (electron temperature). Later, this model was further developed to depict the charge fluctuation on dust particles in terms of physical quantities, viz., mean charge and charge variance (Sheridan, 2013). These models however consider bulk plasma, and accounts for electron and ion collection as dominant charging processes, while the electron emission from dust/ surface has not been emphasized. Rosenfeld and Zakharov (2020) used the concept of charge fluctuation in the context of a sunlit lunar plasma scenario. They suggested that the charge fluctuations at localized microscopic areas can generate a charge, on average, an order of magnitude higher than the mean charge. Natural randomization associated with incident solar/plasma irradiation is the key to inducing this mechanism, and sufficient charge development could lead to dust detachment from the lunar surface. Taking up this concept, Mishra (2020a) developed an analytical model in the context of the dusty lunar surface utilizing the theory of statistical variables. This model suggests that sufficient charge development at microscopic spots enables Coulomb ejection of dust particles from the surface. The given understanding of the spot generation and charging mechanisms is, however, quite qualitative and warrants a rigorous investigation.

To consolidate the concept, a Monte Carlo approach has been applied to the problem in refining the physics insight of the mechanisms and temporal behavior of the spots

and charges on the dusty lunar surface. The sunlit location persists the mean surface charge density of $\sigma_m \sim 5 \times 10^8\, e\ \mathrm{m}^{-2}$ in the nominal solar irradiation condition (Poppe and Horányi, 2010), i.e., 2000 $\mu\mathrm{m}^2$ area possesses one unit of electronic charge, and thus a microscopically small region ($< 1\ \mu\mathrm{m}^2$) can be considered uncharged for all practical purposes. Under dynamic equilibrium, the regolith surface beneath the photoelectron cloud is exposed to randomized fluxes of emitted photoelectrons, solar wind plasma, and sheath photoelectrons, which eventually are random charging events causing charge development on the surface. Due to the dielectric nature of the lunar surface (with extremely low conductivity), any incident charge spreads to a very small region around the point of incidence and creates a charged spot (Rosenfeld and Zakharov, 2020). Such charged spots remain intact until a charge of the opposite nature develops to delineate it. Due to random charging events, the charges fluctuate throughout the surface instead of uniform charging, creating randomly charged microscopic spots over the dusty regolith. A physical picture of this is shown in Figure 7.2. Manifesting the Markovian process with the Monte Carlo treatment, this work addresses the random nature of the spot charging and their dynamic (temporal) variation within microscopic regions.

Results show that submicroscopic non-overlapping circular charged spots are randomly created/annihilated over time in a given microscopic region of the lunar surface. Consequently, a finite number of charge spots are always present. These randomly charged spots can provide significant repulsive vertical electrostatic force and create favorable conditions for dust detachment from the lunar surface, overcoming the gravity and cohesive force.

7.2 Microscopic charge fluctuation

In demonstrating the charge fluctuation on a microscopic scale, we consider a steady-state photoelectron sheath superimposing the dusty regolith beneath it. The photoelectron sheath is created due to the cumulative effect of UV-induced photoemission and subsequent collection of the cloud photoelectrons and solar wind plasma. The macroscopic characteristics of the sheath are considered as input to simulate microscopic processes in the vicinity of the lunar surface. Any microscopic surface region can only see an electron-dominated cloud just above it. In the close vicinity of the microscopic region, the electron cloud is dominated by photoelectrons (more than 90%) (e.g. as shown in Figure 3 in Lisin et al. (2014), and in the bottom panel of Figure 3.11 in Chapter 3). The solar wind electron

flux from the electron cloud in the vicinity is approximately two orders of magnitude smaller than the photoelectron collection flux. Whereas, due to the higher mass of the proton, the solar wind ion flux is three orders of magnitude smaller. So, for simplicity in calculation and following the works of Rosenfeld and Zakharov (2020); Mishra (2020a), the effect of solar wind fluxes in the present analysis is ignored.

The works carried out in Chapters 2 and 3 are followed to derive the photoelectron sheath accounting for observed solar and regolith parameters. Based on the estimates, the photoelectron density just above the surface is taken 202 cm^{-3} and of Maxwellian nature with temperature 3 eV, and considered as input to the simulation. The cloud photoelectrons randomly collect in the microscopic region along with random photoemission. These charging events randomly generate/annihilate non-overlapping sub-microscopic circular charged spots within the microscopic region.

7.2.1 Monte Carlo protocol

The simulation setup starts with an uncharged microscopic region (for all practical purposes), which is superimposed by a nearby steady-state photoelectron cloud with density 202 cm^{-3} and mean temperature 3 eV. The cloud photoelectrons randomly collect in the microscopic region along with random photoemission. These charging events randomly generate/annihilate non-overlapping sub-microscopic circular charged spots within the microscopic region.

Charging currents: Due to random charging events, the charges fluctuate throughout the surface instead of uniform charging, creating randomly charged microscopic spots over the dusty regolith. In analysis, the random nature of the surface charging can be addressed using a Monte Carlo-type approach by assigning a finite probability of photoemission and electron collection. The probabilities depend on the expressions for the currents associated with the photoemission, and electron accretion can be represented as

$$J_{ph}(q) = \cos\theta \int_{\lambda_{\min}}^{\lambda_{\max}} \chi(\lambda) f_\lambda \, d\lambda \left[\frac{\Phi(\xi_\lambda + q\, c_1)}{\Phi(\xi_\lambda)}\right] \quad \text{for} \quad q > 0\,, \tag{7.3}$$

$$= \cos\theta \int_{\lambda_{\min}}^{\lambda_{\max}} \chi(\lambda) f_\lambda \, d\lambda \quad \text{for} \quad q < 0\,, \tag{7.4}$$

where, q is the charge on the surface, θ is the latitude, i.e., $\theta = 0^\circ$ is the equator, and $\theta = 90^\circ$ is the terminator. $\chi(\lambda)$ is the photoelectric yield of the lunar surface, f_λ is the photon flux

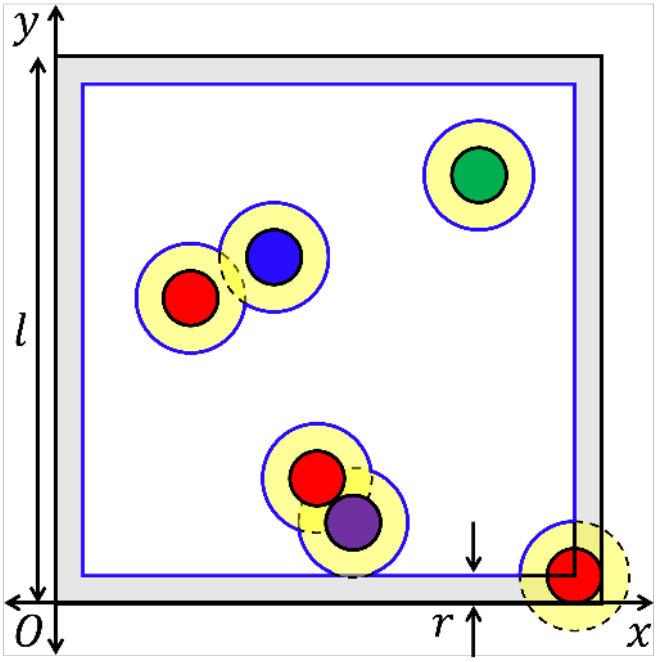

Figure 7.3: Schematic for illustrating charge spot (of radius r) generation in a square region of length l.

associated with observed solar spectra, $\xi_\lambda = (E_\lambda - W_f)/kT_0$, $\Phi(\xi_\lambda) = \int_0^{\exp \xi_\lambda} \Omega^{-1} \ln(1+\Omega) d\Omega$, and E_λ is the photon energy in eV for wavelength λ. k is the Boltzmann constant. W_f and T_0 are the regolith work function and temperature. Here

$$c_1 = -\frac{e^2}{2\pi\,\varepsilon_0\, r\, kT_0}\,. \tag{7.5}$$

e is the electronic charge. Considering the Maxwellian electron cloud in the vicinity of the lunar surface, the electron collection flux can be written as

$$J_{ec}(q) = n_0 \left(\frac{kT_e}{2\pi\, m_e}\right)^{1/2} \quad \text{for} \quad q > 0\,, \tag{7.6}$$

$$= n_0 \left(\frac{kT_e}{2\pi\, m_e}\right)^{1/2} \exp\left(-\frac{q\, c_1}{\alpha_e}\right) \quad \text{for} \quad q < 0\,, \tag{7.7}$$

where n_0 and T_e are the electron density and temperature, respectively and $\alpha_e = T_e/T_0$. m_e is the electronic mass.

Computational Space and Scheme: Consider a square region of length l (as shown in Figure 7.3). If $l \leq 1\,\mu$m, initially, this area is uncharged. As the photoemission and electron collection event occurs, circular microscopic spots start to develop. It is assumed that charged spots can not be generated outside the region and do not overlap. So, charging

events can occur either in the old charged spots or in the Valid Uncharged Region (VUR). Hence, spot centers must lie within the region $r \leq x \leq l - r$, $r \leq y \leq l - r$. Initially, the area of the valid uncharged region is $A_{\text{valid}} = (l - r)^2$. As time progresses, spots of different charges are randomly generated and annihilated. For every existing circular spot, the distance between its center and the newly generated spot center should be greater than $2r$ to avoid overlapping. So, each spot of radius r creates a circular region of radius $2r$, where no spot center can exist. Then the area of the valid uncharged region becomes $A_{\text{valid}} = (l - r)^2 - A_{\text{inf}}$. Here, A_{inf} is the area of the influence zone occupied by the spots. Figure 7.3 shows the uncharged valid region as the region bounded within the blue lines. At a certain time t_j, N number of charged spots are created. After a random time interval Δt, the charging event can randomly occur either on the valid uncharged region or on the old charged spot, depending on the probability connected with them. The total rate of charging events on VUR can be written as

$$p_{\text{VUR}} = A_{\text{valid}} \left[J_{ph}(q = 0) + J_{ec}(q = 0) \right] . \tag{7.8}$$

For charged spots, the rate can be written as

$$p_c = \pi r^2 \sum_{k=1}^{n} N_k \left[J_{ph}(q_k) + J_{ec}(q_k) \right] , \tag{7.9}$$

where N_k is the number of spots with charge q_k. And $N = \sum_{k=1}^{n} N_k$. The total rate of charging events in the entire region is

$$p_{\text{tot}} = p_{\text{VUR}} + p_c . \tag{7.10}$$

By generating random number R_t with $0 \leq R_t \leq 1$, the random time interval can be determined by(Cui and Goree, 1994)

$$\Delta t = -\frac{\ln\left(1 - R_t\right)}{p_{\text{tot}}} . \tag{7.11}$$

And

$$t_{j+1} = t_j + \Delta t . \tag{7.12}$$

Another random number R_v with $0 \leq R_v \leq 1$ is generated and compared with the probabilities of choosing the valid or charged region. If

$$P_{\mathrm{VUR}} = \frac{p_{\mathrm{VUR}}}{p_{\mathrm{VUR}} + p_c} > R_v\,, \tag{7.13}$$

the charging event will occur in the VUR, and a spot center will be randomly chosen. Otherwise, it will occur on the old charge spots. Since there are multiple charge spots with different charges, the probability of choosing a spot with a particular charge type is required, which is given by

$$P_{q_k} = \frac{N_k\left[J_{ph}(q_k) + J_{ec}(q_k)\right]}{\sum_{k=1}^{n} N_k\left[J_{ph}(q_k) + J_{ec}(q_k)\right]}\,. \tag{7.14}$$

A particular charged type is randomly selected using the probability P_{q_k}. After selecting charge type q_k, an old spot center can be randomly chosen out of N_k spots, each of equal probability $1/N_k$. Thereafter, the type of charging event that occurred needs to be derived. For that, a random number R_c with $0 \leq R_c \leq 1$ is generated and compared with the probability P_{ph} of a single photoemission or electron collection.

$$\begin{aligned} \text{If}\quad & P_{ph} = \frac{J_{ph}(q_k)}{J_{ph}(q_k) + J_{ec}(q_k)} > R_c\,, \\ & N_{q_{k+1}}(t_{j+1}) = N_{q_{k+1}}(t_j) + 1\,, \\ & N_{q_k}(t_{j+1}) = N_{q_k}(t_j) - 1\,, \\ & \text{photoemission occurred}\,. \end{aligned} \tag{7.15}$$

$$\begin{aligned} \text{If}\quad & P_{ph} = \frac{J_{ph}(q_k)}{J_{ph}(q_k) + J_{ec}(q_k)} < R_c\,, \\ & N_{q_{k-1}}(t_{j+1}) = N_{q_{k-1}}(t_j) + 1\,, \\ & N_{q_k}(t_{j+1}) = N_{q_k}(t_j) - 1\,, \\ & \text{electron collection occurred}\,. \end{aligned} \tag{7.16}$$

$q_k = 0$ should be used to determine charging events on the uncharged surface. Repeating the same for subsequent times gives a physical picture of the generation and annihilation of spots in a microscopic area.

The computations presented herein are carried out using several packages of MATHEMATICA, a product of Wolfram Research, Inc. For example, **RandomReal** is used to generate random numbers between 0 to 1 (Wolfram Research, 2007b). **RegionUnion** is used to find the union of the influence zone occupied by the spots (Wolfram Research,

2014b). **RegionDifference** is used to find the uncharged valid region after subtracting the influence zone from the square region (Wolfram Research, 2017). **RegionMeasure** is used to find the area of the VUR (A_{valid}) (Wolfram Research, 2014a). **RandomPoint** is used to randomly choose a new spot center within the VUR (Wolfram Research, 2015). **RandomChoice** is used to choose the existing charged spots randomly (Wolfram Research, 2007a). We have presented the result only for $l^2 = 0.01\ \mu\text{m}^2$ with r values are taken to be 10 and 20 nm. The computation schemes are valid for other l and r values but are limited to the computation capability of the computer. For example, if we take $l^2 = 1\ \mu\text{m}^2$ and $r = 10$ nm, approximately $l^2/4r^2 = 2500$ spots are possible. But **RegionMeasure** takes a long computation time while deriving A_{valid}, and when the number of spots exceeds around 50 in our current computation facility, the Karnel is noticed to stop. So, we have limited our computation only to $l^2 = 0.01\ \mu\text{m}^2$.

7.2.2 Microscopic charge fluctuation

For simulation, let's consider the microscopic region of area $l^2 = 0.01\ \mu\text{m}^2$. The random charging events create random non-overlapping circular charged spots of radius r. Following Rosenfeld and Zakharov (2020); Mishra (2020a), we have taken $r = 10$ nm. Applying the computational algorithm discussed in the previous section (Section 7.2.1), Figure 7.4 illustrates the temporal evolution of randomly generated charged spots - the snapshots at four different times are shown. The generation of ten randomly charged spots at different locations is observed at 500 s - these spots are characterized by a maximum and minimum charge of $3e$ and $-4e$, respectively, while the microscopic region attains $1e$ charge. At 1000 s, the simulation shows the annihilation of some existing spots and the creation of a few new random spots. The process continues to evolve with time.

A similar snapshots for $r = 20$ nm spot radius are shown in Figure 7.5. With the increase in charging currents for a larger spot, they can accumulate higher charges but exhibit lower surface charge density. Apart from the charge accumulation, the timescale of fluctuation (τ), which refers to the first change in spot charge by one unit electronic charge, is another significant parameter. Figure 7.6 shows the fluctuation time corresponding to ten thousand different runs for two different size spots. Figure 7.6 demonstrates that τ for $r = 20$ nm is smaller than the same for $r = 10$ nm for larger numbers of random runs.

Moreover, it shows a typical time scale of ~ 10 s for 20 nm spots while suggesting ~ 40 s for 10 nm spots. Figure 7.7 shows the time evolution of total charge Q_{tot} and the number of spots in this region of area $l^2 = 0.01\ \mu\text{m}^2$. The total charge oscillates between

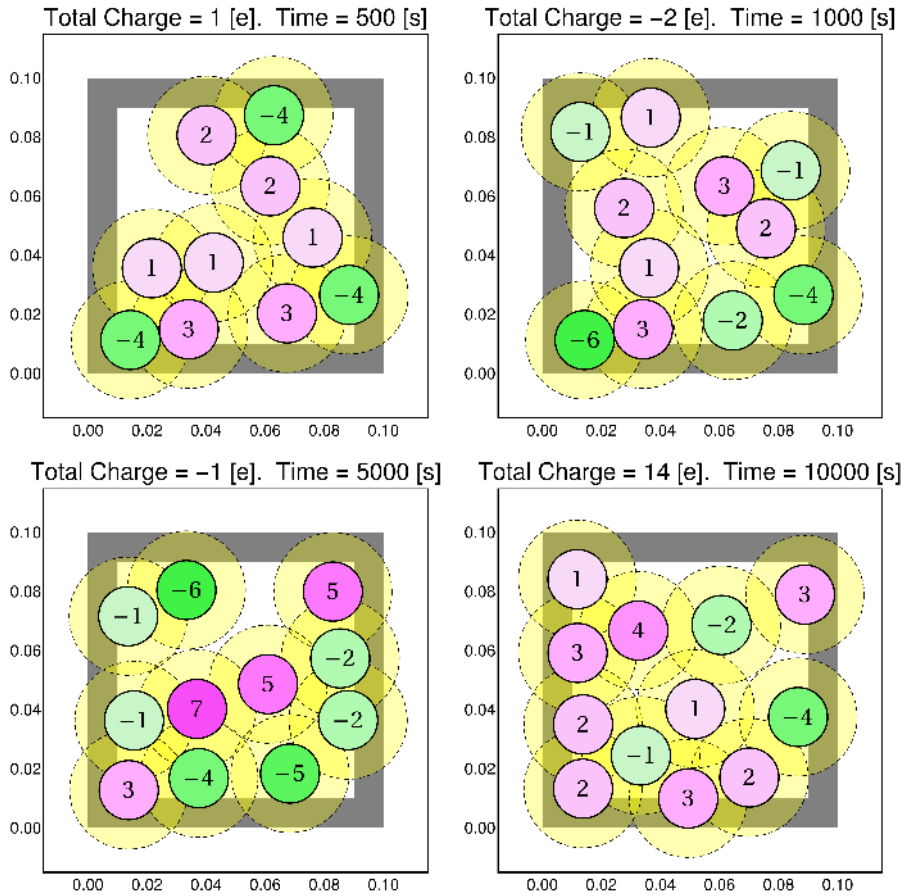

Figure 7.4: Snapshots of $l^2 = 0.01\,\mu\text{m}^2$ area at different times. Spots (of radius $r = 10$ nm) of different charges (denoted by the number written in the center of the spots) are generated randomly. The gray area represents the region where spot centers cannot occur.

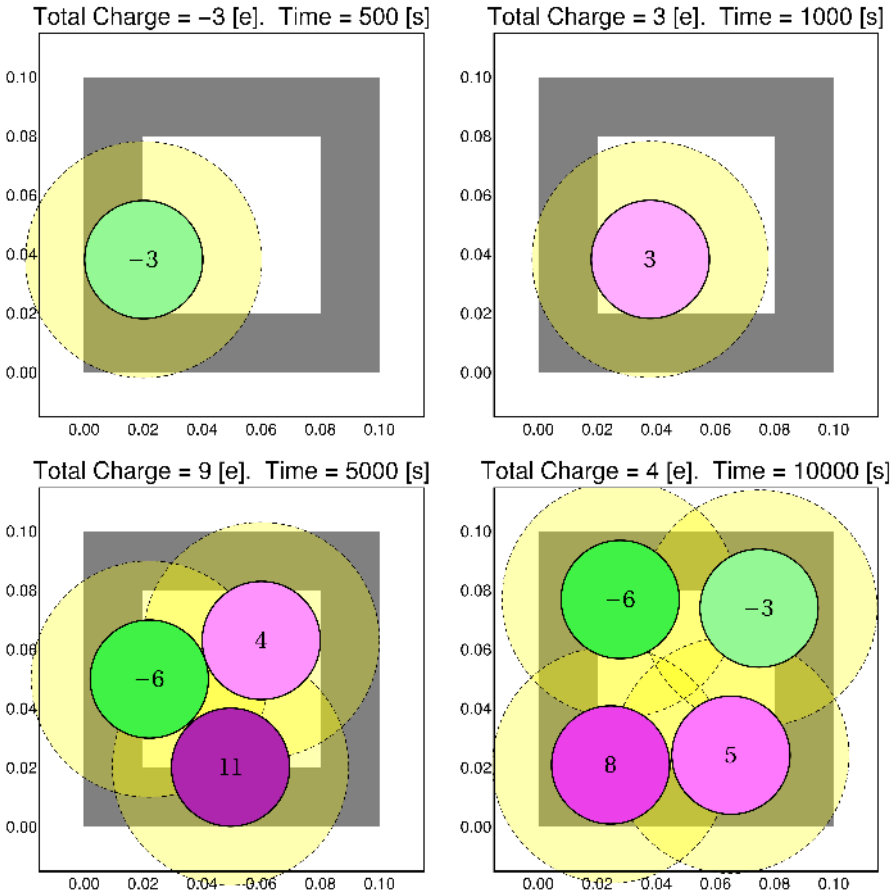

Figure 7.5: Snapshots of $l^2 = 0.01\,\mu\text{m}^2$ area at different times. Spots (of radius $r = 20$ nm) of different charges (denoted by the number written in the center of the spots) are generated randomly. The gray area represents the region where spot centers cannot occur.

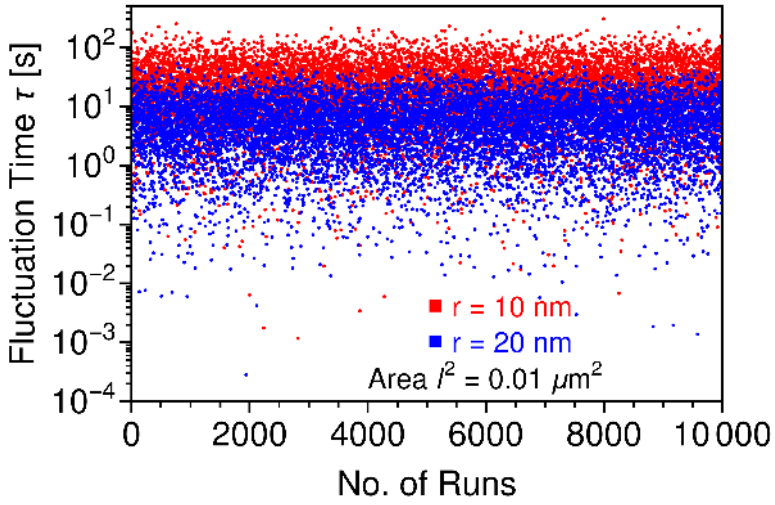

Figure 7.6: Fluctuation timescale of the spots of different sizes.

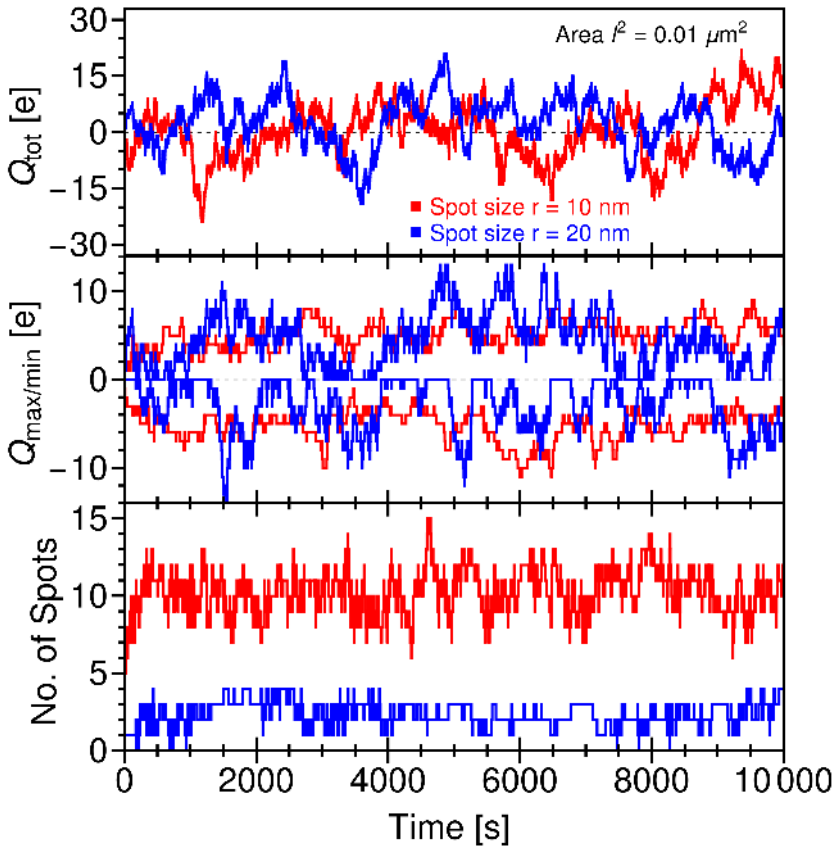

Figure 7.7: Time evolution of (top panel) total charge Q_{tot} and (bottom panel) number of spots in the $l^2 = 0.01\,\mu\text{m}^2$ area.

positive and negative values several times, and the region remains positive or negative for a significant time during the evolution. The middle panel shows the variation of maximum and minimum spot charges with time, and the discrete spots are noticed to acquire around $10e$ charges in several instances. For larger spots, the maximum and minimum spot charges become zero more frequently than smaller spots. The bottom panel represents the spot generation with time - it shows about 10 charged spots for $r = 10$ nm, while for $r = 20$ nm, the region becomes spotless and chargeless multiple times. The results demonstrate significant randomness, with dynamic charge density fluctuation, i.e., of the order of $\sim 10^{15}\, e$ m^{-2} in a given region, with both positive and negative values at the submicroscopic scale. It illustrates the fact that significant charge fluctuations can create large local vertical electric fields at microscopic scales.

Note, here the snapshots for microscopic region $l^2 = 0.01\ \mu$m^2 are illustrated. Multiple such coexisting regions could be considered on the lunar regolith, and the random 10000 events (Figure 7.6) may correspond to simultaneous simulations performed over 10000 l^2 regions. The simulation suggests that the overall effect of these random charge variations over a larger region tends to average out, effectively aligning with the mean charge density at the macroscopic scale ($\sigma_m \sim 10^8\, e$ m^{-2}) above the surface.

The degree of charge fluctuations above the lunar surface depends on two main factors, e.g., photoemission and photoelectron collection currents. Now, these two factors depend on several other factors, e.g., incoming solar irradiation (radiation and plasma), lunar surface parameters (regolith work function, quantum yield, and regolith temperature), and latitude θ. We have shown results only for a region of area $l^2 = 0.01\ \mu$m^2 located at $\theta = 0^\circ$ (equator). It is interesting to note that the probabilities P_{VUR}, P_{q_k}, and P_{ph} depend on the ratio of charging currents. Considering J_{ph} and n_0 varies approximately as $\cos\theta$, these probabilities are expected to remain the same with latitude (θ) - it suggests a similar degree of charge fluctuations with varying θ. Due to a reduction in photoemission and photoelectron density within the sheath, the frequency of charging events decreases with increasing θ. Therefore, charge spots are anticipated to sustain for longer at higher θ values.

7.2.3 Vertical electrostatic force

The electric field induced at the local charge spots may exert electrostatic force on nearby charged dust particles lying on the surface. Referring to Figure 7.8, the electric field at the center of the spherical dust due to a neighboring circular spot (radius r) carrying a

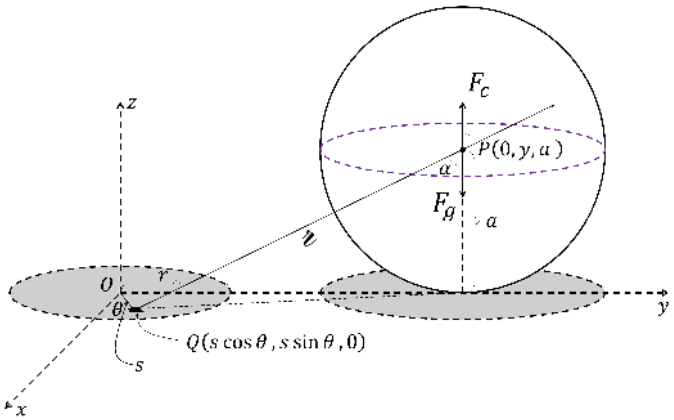

Figure 7.8: A dust particle of radius a, lying near a circular spot of radius r.

uniform surface charge density σ can be written as (Griffiths, 2017)

$$E_z = \frac{1}{4\pi\epsilon_0}\int \frac{dq}{\ell^2}\cos\alpha\,, \tag{7.17}$$

where ϵ_0 is the permittivity of free space. And

$$dq = \sigma s ds\, d\theta\,, \tag{7.18}$$

and

$$\ell^2 = s^2\cos^2\theta + (y - s\sin\theta)^2 + a^2\,, \tag{7.19}$$

and

$$\cos\alpha = \frac{a}{\ell}\,. \tag{7.20}$$

Substituting this in Eq. 7.17 the electric field at the center of the spherical dust due to a neighboring circular spot (radius r) carrying a uniform surface charge density σ can be written as

$$E_z = \frac{1}{4\pi\epsilon_0}\int_0^{2\pi}\int_0^r \frac{\sigma a s ds\, d\theta}{\left[s^2\cos^2\theta + (y - s\sin\theta)^2 + a^2\right]^{3/2}}\,. \tag{7.21}$$

If the dust particle has Q_d charge, then the vertical electrostatic force at the center of the dust particle can be written as

$$F_z = Q_d\, E_z\,. \tag{7.22}$$

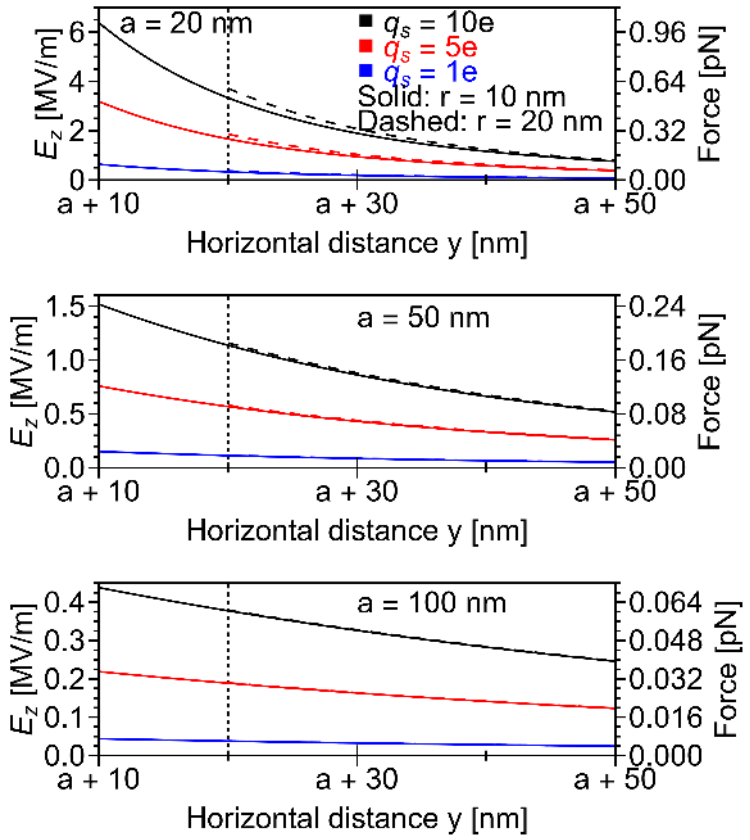

Figure 7.9: Vertical electric field at the center of a dust particle of radius a due to a circular spot of radius r as a function of the horizontal distance y. The right vertical axis represents the force on a dust particle with a single positive charge. Note: The values of $a + r$'s are different for each panel.

The vertical electric field at the center of the charged dust particle (given in Eq. 7.21) depends on q_s (spot charge), r, a, and y. Here, y represents the horizontal distance from the center of the spot to the point of contact of the spherical dust particle with the surface (see Figure 7.8). The minimum value of y is $a + r$, corresponding to the first nearest neighbor.

Figure 7.9 illustrates the vertical electric field at the center of a dust particle of radius a due to a circular spot of radius r as a function of y. For given q_s, r, and a, the closest spot (at $y = a + r$) exhibits maximum electric field and decreases with increasing y. Moreover, E_z increases with increasing q_s while it decreases with increasing a. The smaller spots in the vicinity of dust particles (i.e., smaller r) induce a large electric field, as shown in the vertical dashed line in Figure 7.9. Due to extended charge distribution, 20 nm spots show a slightly higher electric field compared to 10 nm spots (centered at the same location). The right vertical axis in Figure 7.9 represents the force on a dust particle with a single positive dust charge. As discussed, the charges on spots vary due to fluc-

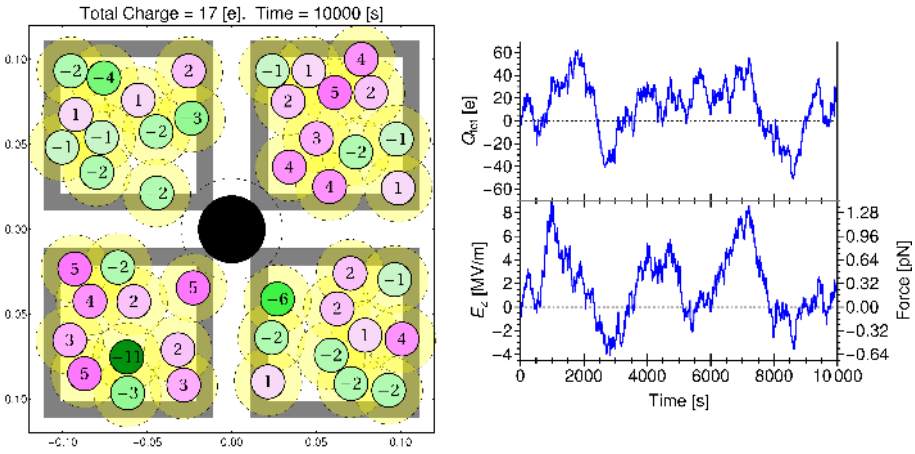

Figure 7.10: Vertical electric field at the center of a dust particle of radius a due to a circular multiple charged spots of radius r and different charges surrounded around the dust.

tuation (Figure 7.7), and thus, a 20 nm particle with a unit positive charge in the vicinity of a 10 nm spot with charges $1e$, $5e$, and $10e$ experiences a maximum electrostatic force of $\sim$ 0.1, 0.5, and 1.0 pN, respectively. Note that the dust particles are an inherent part of the surface, and undergo charging events similar to the charged spots. Thus, it is reasonable to assume that the instant charge on the dust particle also might vary similarly to the spots (Figure 7.7). Recently, Pacaud et al. (2025) conducted a series of experiments, taking JSC-1A lunar dust simulant and bombarding it with VUV, and measured the charge state of the dust. They reported that charges on the dust lying on the surface can be both positive and negative. These experimental observations may confirm the charge fluctuation on a microscopic scale, where, on a microscopic scale, photoemission and photoelectron collection randomly occur, and sub-microscopic dust can get both positive and negative charges. Hence, they may experience large Coulomb repulsion. For instance, if a 20 nm particle attains $10e$ charges, it experiences a force of $\sim$ 10 pN near the 10 nm spot. This force is greater than the force required to detach the dust particle from the surface with $S = 0.1$, $\beta = 10$ (the yellow line in Figure 7.1). Larger particles depict lower electrostatic repulsion; however, depending on varying dust and spot charges, it could be significant in detaching it from the regolith for a certain set of surface parameters viz., S, β (Figure 7.1). For instance, during temporal evolution, a 100 nm dust may acquire $25e$ and may feel an electrostatic force of $\sim$ 1.75 pN due to the nearest spot with charge $10e$.

As depicted (Figures 7.2, 7.4, and 7.5), multiple spots may coexist surrounding dust particles during random charging events. Such a random arrangement may cumulatively induce significantly high electrostatic repulsion and overcome the required force for dust detachment from the surface. An approximate scenario where dust is surrounded by cir-

cular charged spots is illustrated in Figure 7.10. The left panel shows a snapshot of fluctuating charged spots at ten thousand seconds, where randomly spread spots of different charges coexist with a total charge of $Q_{tot} = 17e$, and the black spot refers to positively charged dust. The top right panel displays the temporal evolution of total charge (Q_{tot}) in this region, which is noticed to oscillate between positive and negative values over time.

The cumulative electric field (and force) at the center of the dust particle are illustrated in the bottom panel. Though anticipated, they do not directly depend on Q_{tot}; instead, the electric field depends on individual spot charge and their distribution discretely. It is customary to think that only nearby spots significantly contribute to the cumulative field, but the results suggest that the contribution from other spots residing relatively far from the dust cannot be ignored. For example, the snapshot of the ten thousand seconds gives $\sigma \sim 1.4 \times 10^{15}\, e\, \mathrm{m}^{-2}$ and corresponding vertical electric field $E_z = \sigma/2\varepsilon_0 \approx 12.7$ MV m^{-1}. However, when the vertical electric fields produced by each individual charged spot at the center of the dust are combined, the overall effect results in a considerably weaker cumulative vertical electric field $E_z = 1.36$ MV m^{-1}. The maximum spot charge for this case is $5e$, and four such spots exist. The nearest $5e$ charged spot creates an electric field of 1.5 MV m^{-1}. On the other hand, the minimum spot charge is $-11e$, and it creates only -0.3 MV m^{-1} of the electric field because it resides significantly far from the dust. However, a nearby spot of $-6e$ charge creates an electric field of -1.2 MV m^{-1}. The total electric field created by positively and negatively charged spots is 4.52 MV m^{-1} and -3.16 MV m^{-1}, respectively. Consequently, when dust particles are surrounded by charged spots of the same sign, the strength of the repulsive vertical electric field and the resulting force are greatly amplified. For example, at time 840 seconds, the total charge of the area is $-1e$, but the charged dust particle experiences a vertical electric field of 5.45 MV m^{-1} due to the presence of similarly charged spots in its close proximity.

Over a larger area, the total effect of these random charge fluctuations tends to average out. So, the large fluctuating electric field is effective within a few scale lengths (vertical extent) of the microscopic region. As the areas become larger and larger, the random contributions are averaged out, and the effective field aligns with the macroscopic electric fields (~ 5 V m^{-1}) above the surface.

7.3 Summary

The dust detachment under electrostatic effects has been a long-standing quest, and the inherent mechanism is still unclear. The sunlit lunar regolith is characterized by a mean surface charge density of $\sigma_m \sim 5 \times 10^8\, e\ \mathrm{m}^{-2}$, and a photoelectron-dominated electron cloud resides in its vicinity as a photoelectron sheath. The electric field induced by the mean charge density is not strong enough to provide the necessary electrostatic force to lift dust particles off the lunar surface. We conceptualize that the surface charge density fluctuates locally on a microscopic scale due to the natural randomization connected with the charging events. Such natural fluctuations enhance the local electric field on the microscopic scale, possibly causing the detachment of sub-micron dust particles from the lunar surface. Monte-Carlo-type simulation based on the Markovian approach of statistical charge fluctuations and the discrete nature of the charging events is developed to demonstrate the conceptual basis. It reveals the following important findings

- The random creation/ annihilation of submicroscopic non-overlapping circular charged spots over time in a given microscopic region. As a result, a finite number of charge spots always exist at any point in time.

- The total charge of the microscopic region oscillates between positive and negative values several times and gives rise to reasonably large surface charge density $\sim 10^{15}\, e\ \mathrm{m}^{-2}$. This leads to the creation of a local electric field that is several orders of magnitude stronger than the average surface field.

- The distribution of charge spots determines the strength of the local electric field and the electrostatic force on adjacent dust particles

- Being an integral part of the regolith, the dust particles also might accumulate significant charge due to random fluctuations, and under the favorable arrangement of charge spots and dust particles randomly, a sufficient electrostatic repulsion could be induced leading to the dust detachment from the surface. The simulation suggests the possibility of electrostatic detachment of larger dust particles from the lunar surface.

Recent experimental measurements of Pacaud et al. (2025) reported that the charges on the dust lying on the surface can be both positive and negative under direct exposure to VUV photons. This may confirm the charge fluctuation on a microscopic scale, where,

on a microscopic scale, photoemission and photoelectron collection randomly occur, and sub-microscopic dust can get both positive and negative charges.

This study provides an accurate and compelling foundation for understanding the critical role that statistical charge fluctuations play in the detachment of dust particles from the lunar surface and other airless planetary bodies.

Chapter 8

Effect of surface topography

8.1 Introduction

Previous chapters presented significant insight into the plasma sheath around the Moon and advanced our understanding of its structure and variability using one-dimensional (1D) analytical and numerical simulations. The presence of surface relief results in non-trivial effects on surface charging and gives rise to complex electric potential and field structures on the surface and within the sheath (Poppe et al., 2012b). This chapter briefly discusses the influence of surface topography on the lunar plasma environment. In this context, let us first discuss the surface charging within a simple surface relief (a simple crater or a simple spherical depression) in the next section.

8.2 Physical scenario

Consider a simple crater of radius r and depth h over the Moon irradiated by sunlight as illustrated in the schematic (Figure 8.1). Following the schematic, the crater arc is a part of a virtual circle (in 2D) of radius R. It can easily be shown

$$R = r\left[\frac{1+(h/r)^2}{2(h/r)}\right] = \frac{D}{2}\left[\frac{1+4(h/D)^2}{4(h/D)}\right], \tag{8.1}$$

where $D = 2r$ is the diameter of the simple crater. And

$$\alpha_0 = \cos^{-1}\left[\frac{1-(h/r)^2}{1+(h/r)^2}\right] = \cos^{-1}\left[\frac{1-4(h/D)^2}{1+4(h/D)^2}\right], \tag{8.2}$$

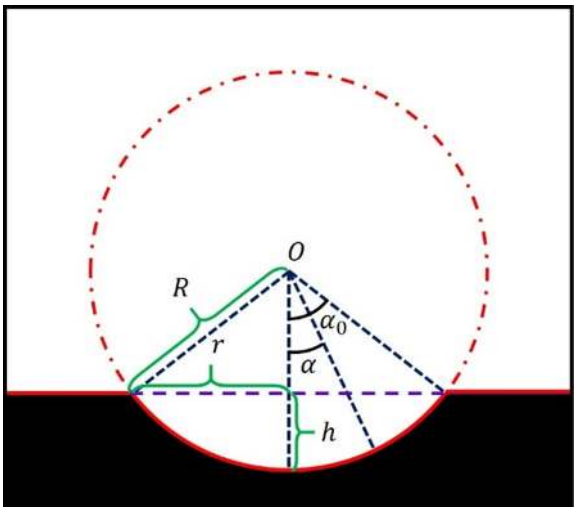

Figure 8.1: An schematic of 2D crater geometry.

Here, α_0 is the angle between the straight lines drawn from the center of the virtual circle (Figure 8.1). The solar illumination angle changes within the crater between $(-\alpha_0, \alpha_0)$.

8.3 Determination of crater's surface potential

The general concept of lunar surface charging is as follows: photoemission from the surface and accretion of ions to the surface take the surface at positive potential. On the contrary, due to the accretion of solar wind electrons, the surface acquires negative charges. These competing charging processes lead to the net charge buildup on the surface. The steady-state surface potential can be obtained by balancing the incoming solar wind plasma and photoemission fluxes. Mathematically, it can be presented as (Manka, 1973)

$$J_{\rm ph}(V_0) - J_{\rm se}(V_0) + J_{\rm si}(V_0) = 0\,, \tag{8.3}$$

$J_{\rm ph,se,si}$ are fluxes of photoemission, solar wind electron, and ion collections. This is the same flux balance equation given in Chapter 3 (Eq. 3.17); where V_0 is the surface potential. However, the mathematical expressions are different for different potential structures developed above it. Due to the lower mass of electrons, their accretion and photoemission dominantly decide the nature of the surface charge. The mathematical expressions considering Fermionic photoelectrons, kappa electrons, and cold ions are given by

$$\begin{aligned} J_{ph}(V_0) &= \cos\theta \int_{\lambda_{\rm min}}^{\lambda_{\rm max}} \left[\frac{\chi(\lambda) f_\lambda\, d\lambda}{\Phi(\xi_\lambda)}\right] \Phi\left(\xi_\lambda - \frac{eV_0}{kT_0}\right) \quad \text{for} \quad V_0 > 0\,, \\ &= \cos\theta \int_{\lambda_{\rm min}}^{\lambda_{\rm max}} \chi(\lambda) f_\lambda\, d\lambda \quad \text{for} \quad V_0 < 0\,. \end{aligned} \tag{8.4}$$

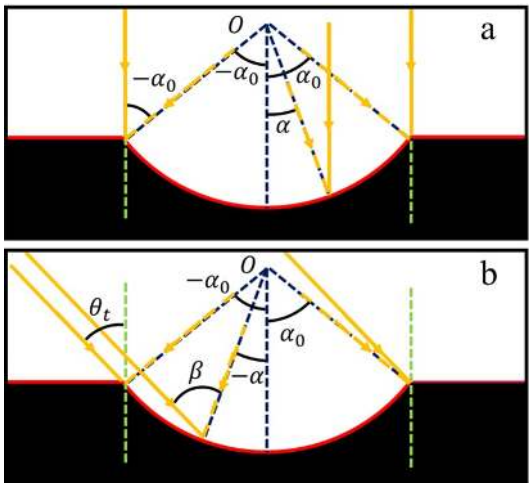

Figure 8.2: Effective photon flux on the crater's surface for (a) normal photon incidence and (b) oblique photon incidence.

$$\begin{aligned} J_{se}(V_0) &= \int_0^\infty \int_{-\infty}^\infty \int_{-\infty}^\infty f_\kappa(\mathbf{u})\, d^3\mathbf{u} \quad \text{for} \quad V_0 > 0\,, \\ &= \int_{\sqrt{-2eV_0/m_e}}^\infty \int_{-\infty}^\infty \int_{-\infty}^\infty f_\kappa(\mathbf{u})\, d^3\mathbf{u} \quad \text{for} \quad V_0 < 0\,. \end{aligned} \tag{8.5}$$

$$J_{si}(V_0) = n_{i\infty} u_{i\infty} \cos\theta = n_{i\infty} \sqrt{\frac{kT_e}{m_i}} M_x\,. \tag{8.6}$$

A detailed explanation of various terms of these equations is given in Chapter 3. For lower values of θ, photoemission flux dominates, and the surface acquires positive potential. For higher values of θ, the solar wind electron flux dominates—the surface acquires negative potential. The critical angle θ_c, for which the surface remains uncharged, and transition occurs using Eq. 8.3 can be given by

$$\cos\theta_c = \frac{J_{se}(V_0 = 0)}{\int_{\lambda_{\min}}^{\lambda_{\max}} \chi(\lambda) f_\lambda\, d\lambda + n_{i\infty} u_{i\infty}}\,. \tag{8.7}$$

We now apply this understanding to a simple crater under various illumination conditions.

8.3.1 Fully illuminated crater

For the normal photon incidence ($\theta = 0^\circ$), the effective photon flux depends on the inclination α (as shown in Figure 8.2a). It causes varying photoemission flux depending on inclination. Intuitively, the surface potential should be symmetric about the crater center

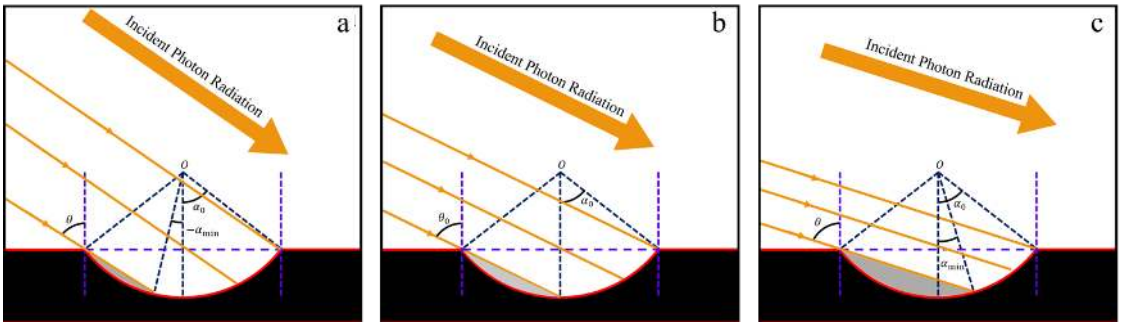

Figure 8.3: Illumination conditions on the crater's surface for (a) less than half-shadowed, (b) half-shadowed, and (c) more than half-shadowed crater.

for the normal photon incidence. In case $\alpha_0 < \theta_c$, the crater acquires a positive charge for normal photon incidence. The surface potential can be determined using the flux balance equation (Eq. 8.3). The constituent charging currents connected with photoemission and solar wind plasma are given by Eqs 8.4, 8.5, and 8.6. Here, θ in Eq. 8.3 will be replaced by α and varying α within the range $(-\alpha_0, \alpha_0)$ gives the surface potential within the crater.

In the case of oblique photon incidence, Figure 8.2b demonstrates that the light rays coming at an angle of inclination equal to or less than θ_t i.e., $\theta < \theta_t$, fully illuminates the crater. Here, θ_t is the angle of inclination of the incoming photons for which the rays are parallel to the tangent at the crater's flank edge (Figure 8.2b). It can be easily shown that

$$\theta_t = \frac{\pi}{2} - |\alpha_0| \,. \tag{8.8}$$

Here, θ in Eqs. 8.4 and 8.6 is to be replaced by β. Note, for $\beta < \theta_c$, the surface acquires positive potential, while for $\beta > \theta_c$, the surface acquires negative potential. In case $\beta = \theta_c$, the surface remains uncharged. In this case, the crater surface potential can be derived by solving the flux balance equation (Eq. 8.3) for each value of β varying in the range $(\theta + |\alpha_0|, \theta - |\alpha_0|)$. Here, $\theta + |\alpha_0|$ and $\theta - |\alpha_0|$ refer to the angles of solar inclination of the crater's left and right edges, respectively (Figure 8.2b).

8.3.2 Partially illuminated crater

For the illumination condition with $\theta > \theta_t$, some region on the leeward side of the crater floor is shadowed. The incoming plasma electrons and ions carry out the charging in the shadowed region and acquire a finite negative potential. Three kinds of scenarios are possible in the partially illuminated crater, as shown in Figure 8.3. Figure 8.3b illustrates that for a certain illumination angle $\theta_0 = (\pi - |\alpha_0|)/2$ the crater is half-shadowed. For

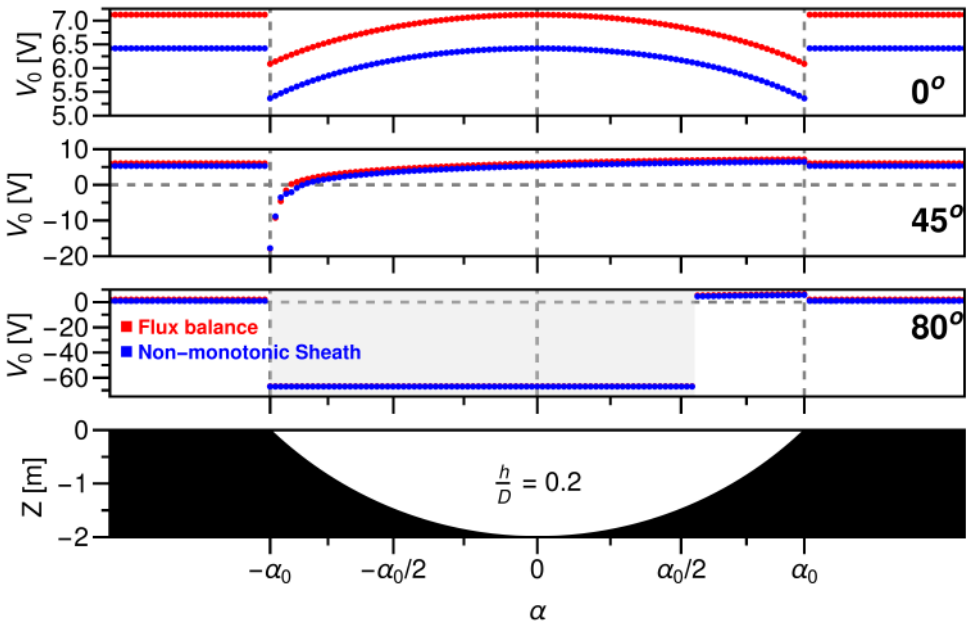

Figure 8.4: Surface potential structures within a simple crater with $h/D = 0.2$ under various illumination conditions. The red color points are derived from the flux balance (Eq. 8.3) and blue points are derived using the boundary conditions for Type A sheath discussed in section 3.4.1 of Chapter 3. Parameter Used: $J_{ph}(0) = 9.7\,\mu A\,m^{-2}$, $W_f = 5$ eV, $n_{i\infty} = 10\ \text{cm}^{-3}$, $T_e = 15$ eV, and $u_{i\infty} = 380\ \text{km s}^{-1}$.

$\theta_0 > \theta > \theta_t$ (Figure 8.3a), the more than half of the crater is illuminated. On the other hand, for $\theta > \theta_0$ (Figure 8.3c), less than half of the crater is illuminated. For a partially illuminated scenario, there is an angle $\alpha_{\min} = |\alpha_0| + 2\theta - \pi$ such that the region $(\alpha_{\min}, \alpha_0)$ is illuminated. For illumination condition $\theta_0 > \theta > \theta_t$, θ in Eq. 8.3 will be replaced by $(\theta + \alpha_{\min}, \theta - \alpha_0)$ between $(\alpha_{\min}, \alpha_0)$ and 90° between $(-\alpha_0, \alpha_{\min})$. On the other hand, for $\theta > \theta_0$, this will be $(\theta - \alpha_{\min}, \theta - \alpha_0)$ for the illuminated part.

8.3.3 Numerical results and discussions

In order to have a quantitative assessment of the effect of the simplest surface topography on the electrical environment around the moon, we need the value of α_0, which depends on the ratio of depth h and diameter D of the simple crater. Robbins et al. (2018) reported for simple craters the h/D varies between 0.1 to 0.2, so $h/D = 0.2$ is taken in this study to derive α_0. $\alpha_0 = 43.6°$ is used to derive the illumination angles at various locations on the crater floor; these illumination angles have been used as an input parameter on the charging currents, and using other plasma and solar radiation parameters, the surface potential profiles have been derived. The method of deriving surface potential presented herein only considers flux balance on the surface (Eq. 8.3). However, in section 3.4.1, the

surface potential for Type B and C sheaths has been determined considering flux balance and quasineutrality at infinity; additionally, for Type A, another condition comes from the zero electric field at potential minima and at infinity. Figure 8.4 illustrates the electric potential on the crater surface as a function of α. Different values of α indicate the locations on the crater floor, e.g., corresponds to the centre of the crater while $\alpha = \alpha_0$ refers to the crater's right side flank edge (Figure 8.1). Figure 8.4 shows slightly different surface potential values within the crater under various illumination conditions derived from flux balance and the same for Type A non-monotonic sheath due to the presence of a potential minimum within the Type A sheath.

In both cases, for normal photon incidence, the top panel of Figure 8.4 illustrates that the electric potential depicts symmetry about the crater center, where it takes maximum value at the center due to dominant photoemission. The surface potential reduces as we go towards the edge of the crater (i.e., α increase from zero to α_0). It can be understood as a decrease in effective photon flux, which reduces photoemission flux and surface potential. This change in surface potential indicates a tangential surface field directed toward the crater edge. In the case of normal incidence, the nature of the surface potential charge remains the same; however, the numerical values are expected to be changed for different parametric values.

For $\alpha_0 = 43.6^\circ$, $\theta_t = 46.4^\circ$. An oblique incidence with $\theta = 45^\circ$ fully illuminates the crater. The second panel from the top of Figure 8.4 shows the electric potential on the crater surface as a function of α for $\theta = 45^\circ$ solar illumination. Here, the effective photon flux is reduced by a factor of $\cos\beta$. It is noticed that a finite portion $(\beta > \theta_c)$ of the crater acquires negative potential. At $(\beta = \theta_c)$, the surface remains at zero potential. The positive potential is found maximum on the right edge of the crater at $\beta = \theta - |\alpha_0|$ - this location corresponds to the maximum photon and photoemission flux. The negative potential is maximum on the left edge of the crater-here, the contribution from photoemission is marginal. The figure suggests as we move from the left to the right edge of the crater, for $\beta > \theta_c$, the solar wind electron accretion flux dominates, and the surface acquires a negative charge. The photoemission dominates for $\beta \leq \theta_c$, and the surface acquires a positive charge. It is anticipated that the negatively and positively charged regions within the fully illuminated crater are sensitive to the surface, solar, and plasma parameters, i.e., on θ_c.

The third panel from the top of Figure 8.4 shows the crater's surface potential structure for illumination angle $\theta = 80^\circ$. As discussed in the section 8.3.2, the current angle is

greater than $\theta_0 = 68.2^\circ$. Less than half of the crater surface is illuminated, and the majority of the crater's surface is shadowed, as marked in the gray region in the figure. Due to dominant photoemission, the sunlit surface acquires positive potential; however, the darker region becomes negatively charged because of electron accretion from the solar wind/ambient plasma. So, the crater's surface experiences a significant shift in potential, transitioning from the illuminated to the darker side of this location. This potential shift due to topographic shielding within a very small region creates a sufficiently large electric field, which may have important implications for the electrostatic dust and volatile transport around this topographic region, especially in the polar region of the Moon.

The analytical model discussed so far can determine the charging of the fully and partially illuminated cater surface. For a fully illuminated crater two specific scenarios, viz., (i) normal and (ii) oblique photon incidences, have been discussed. On the other hand, for the partially illuminated crater, there exists (i) more than half, (ii) half, and (iii) less than half illuminated scenarios. For normal photon incidence, the craters acquire positive potential. The variation is found to be symmetric about the crater center. A symmetric photoelectron sheath is expected to form by trapping the photoelectrons in the vicinity. Due to the tangential variation in surface potential, the screening is likely to vary at different locations within the sheath. It could give rise to complex radial and tangential electric field structures within the sheath.

For fully illuminated oblique photon incidence, it has been found that in a finite region within the crater, due to the marginal photoemission flux depending on incident angle, the solar wind electron collection dominates, and the surface acquires negative potential/charge. It leads to an asymmetric potential distribution over the crater surface. In the illuminated region, a photoelectron sheath is anticipated (Type A & B), while in the negatively charged region, the screening is done by the solar wind ions, and a Debye type Type C sheath forms. The extent of this region depends on crater geometry, solar inclination, surface properties, and solar wind plasma parameters.

For partially illuminated cases, a photoelectron-free negatively charged region exists in the shadowed portion of the crater where the classical Debye sheath (Type C for $\theta = 90^\circ$) is anticipated. In the case of a partially illuminated crater, the asymmetric and discontinuous surface potential distribution results in the existence of a complex electric field structure, which might lead to complex dust/plasma transport within the crater.

The results presented herein are based on one-dimensional simulations used for different values of α. And α_0 in Eq. 8.2 depends on h/D ratio. So, the results are an-

ticipated to remain intact for small to large values of h and D, keeping h/D the same. However, three-dimensional effects are not taken into account while deriving those results. These effects, especially the horizontal variation of space charge densities within the sheath, become important when the topographic features are comparable to the sheath's Debye length. Under a typical plasma and solar irradiation condition, the considerable sheath thickness (few Debye lengths) of Type A, B, and C sheaths are typically around 12, 60 – 100, and 100 – 120 m. Our results are anticipated to be applicable when the crater sizes are much larger than the sheath thickness. As the sizes of the topographic features become comparable, the 1D solution has limited applicability in the exploration of the role of surface features on the sheath characteristics. Because due to the presence of surface topography, the horizontal components of potential structure become significant, and $\nabla^2 V$ cannot be replaced by d^2V/dx^2 as in Eq. 3.2. Along with that, in the terminator and polar region of the Moon, the craters and mountain-like surface features can obstruct the incoming plasma and radiation and create a 'mini-wake' like structure (Farrell et al., 2007, 2010; Mishra and Bhardwaj, 2020). These facts warrant further investigation into the influences of local reliefs in modifying the structure of the plasma sheath around the Moon.

8.4 Ongoing and future work

8.4.1 Spacecraft Plasma Interaction Software (SPIS)

Spacecraft Plasma Interaction Software (SPIS), an open-source 3D modeling tool, can be used to investigate the role of surface topography in the lunar plasma environment (Roussel et al., 2008; Hess et al., 2015). The simulation domain is a box composed of an open face through which solar wind plasma is injected, four lateral boundaries, and a lunar surface that can absorb plasma and emit photoelectrons. In SPIS, photoelectrons are considered to be Maxwellian Hess et al. (2015). Earlier chapters highlighted the importance of FD statistics in the distribution of lunar photoelectrons and the self-consistent mechanism of photoelectron generation. However, due to the complexity of the 3D scenario, SPIS was used for the initial study, which employed the particle-in-cell (PIC) method. 3D unstructured mesh representing lunar surface topography has been fed to SPIS with suitable input plasma and solar parameters to model the charging process.

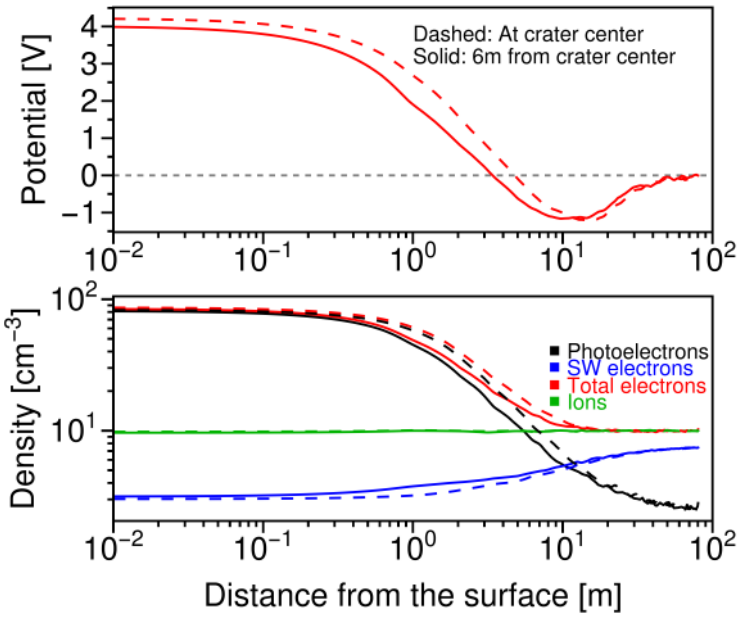

Figure 8.5: Altitude profile of electric potential (top) and charge density (bottom) profiles above the surface for normal illumination derived from SPIS. Solid Line: 6 m away from the crater center. Dashed Line: At the crater center. Different colors in the bottom panel indicate different sheath populations.

8.4.2 Preliminary results

For initial simulation purposes, a simple crater geometry with 2 m depth and 10 m diameter, located at the center of a flat surface with area 16×16 m^2 with unstructured meshing, has been taken into account. The surface has Lunar Mare properties and emits photoelectrons with $J_{ph} = 4.5\,\mu$A m^{-2} similar to Feuerbacher et al. (1972) and photoelectron temperature $T_p = 2.2$ eV. Above the surface exists an open face through which Maxwellian solar wind plasma with $n_e \sim n_i = 10$ cm^{-3} and $T_e \sim T_i = 15$ eV is injected with drift speed of 400 km s^{-1}. The sun's direction has been changed to create different illumination conditions above the crater. Figure 8.5 shows the potential and density profiles derived using SPIS using the input parameter discussed above and following the method discussed in Hess et al. (2021). The trends of these profiles are similar to Figure 3.11 discussed in Chapter 3. One discrepancy is that the potential is not smoothly going to zero, as was the case with the analytical results. This may be due to the force fully making the potential zero at the open boundary. Within 20 m above this surface, SPIS is giving desirable results. It is noticed that, at the center of the crater, the potential is slightly higher than the surface potential 6 m far from the crater center. This is due to the presence of a relatively dense photoelectron cloud within the spherical depression, creating higher potential minima,

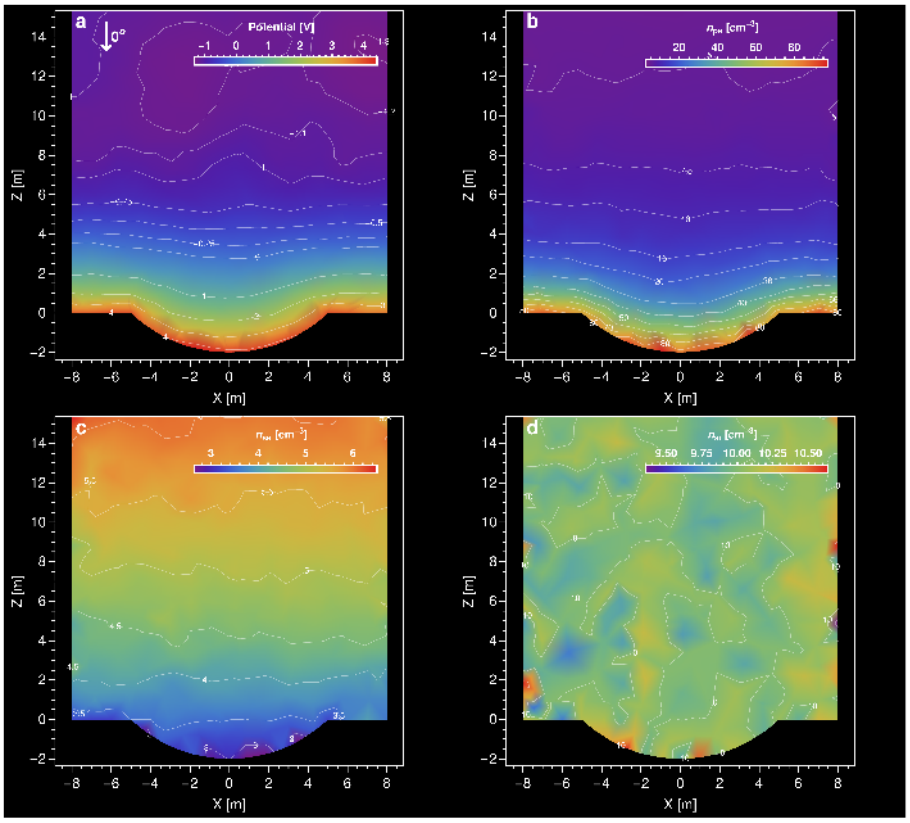

Figure 8.6: (a) The potential (b) photoelectron density (n_{pe}) (c) solar wind electron density (n_{se}), and (d) solar wind ion density (n_{si}) above a fully illuminated lunar crater with normal photon incidence derived from SPIS.

which reflect the incoming solar wind electrons and slightly reduce the incoming electron flux. Figure 8.6 illustrates the topographic effect on the photoelectron sheath due to a 10 m diameter and 2 m depth simple crater. The crater is located at the subsolar point, i.e., $\theta = 0^{\circ}$. Photons are coming normal to the flat surface. The potential profile within the sheath is shown in Figure 8.6a. The maximum surface potential value is found at the crater center. The potential gradually decreases as we go above altitudinally upward from the surface of the crater. Above some altitude, the potential started to take a negative value, indicating the existence of potential minima at some height above the crater. The depression in equipotential contours near the surface is anticipated due to the lower elevation of the crater surface than the surrounding flat surface and due to the lower photoemission from inside the crater. But above the surface, this contour depression reduces, indicating nearly uniform horizontal screening after a certain altitude. Photoelectrons primarily screen the effect of surface potential and are trapped due to potential minima. As a result, the equi-density contours of photoelectrons shown in Figure 8.6b closely resemble the equipotential contours in the potential profiles. Figure 8.6c shows the solar

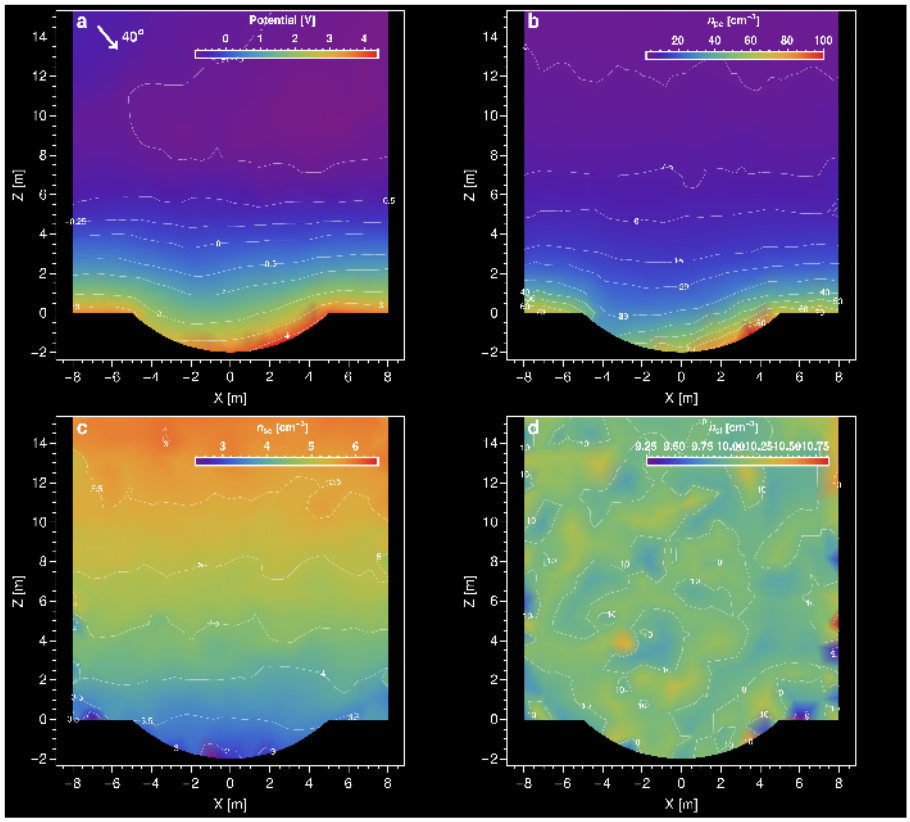

Figure 8.7: (a) The potential (b) photoelectron density (n_{pe}) (c) solar wind electron density (n_{se}), and (d) solar wind ion density (n_{si}) above a lunar crater with $\theta = 40°$ derived from SPIS.

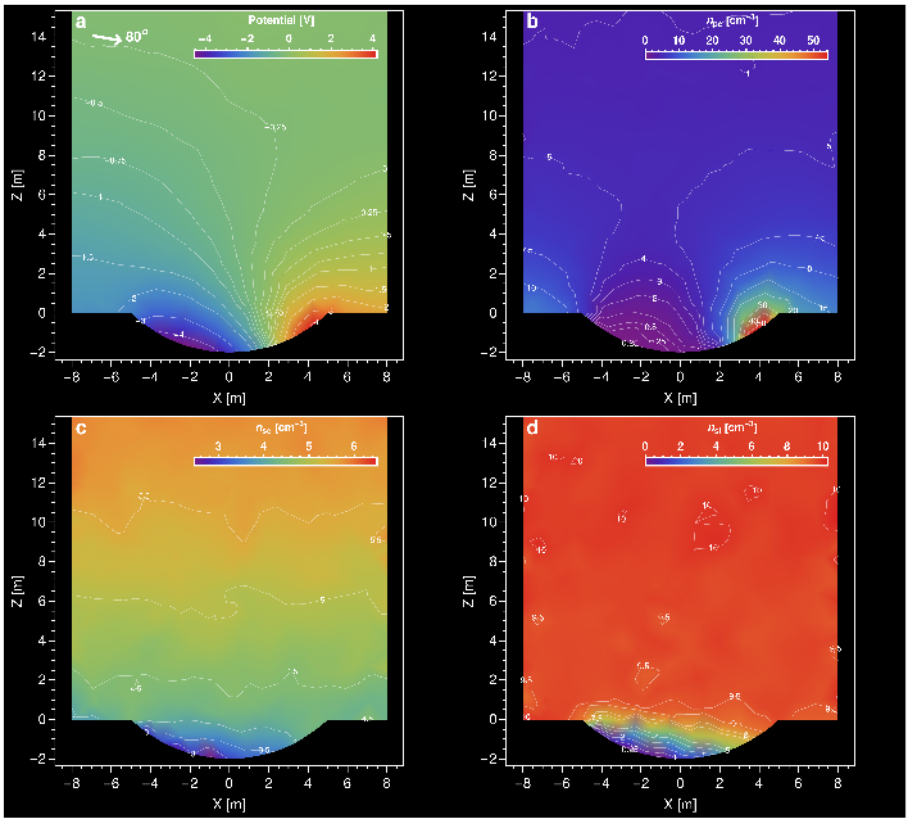

Figure 8.8: (a) The potential (b) photoelectron density (n_{pe}) (c) solar wind electron density (n_{se}), and (d) solar wind ion density (n_{si}) above a lunar crater with $\theta = 80°$ derived from SPIS.

wind electron density profile above the crater. The potential minima created significantly above the crate reflect the majority of the electrons. As a result, the solar wind electron density decreases near the crater surface, and variation in equi-density contours is not much seen. Due to higher inertia, the ion's motion experiences minimal variation within the sheath, resulting in a lack of significant ion density variation above the surface, as shown in Figure 8.6d.

The situation becomes complex for the 40° case as the local illumination angle becomes asymmetric around the crater floor. Figure 8.7a shows that the maximum surface potential shifted towards the right side in the location of larger photoemission. Here, the depression of equipotential contours becomes asymmetric near the surface. Above the crater, as altitude increases, this depression reduces, and some negative potential contours nearly parallel to the flat surface. The negative potential suggests the existence of potential minima. However, this potential minimum region is expected to develop due to the combined effects of the entire crater, highlighting the importance of 3D variations in the sheath parameter, which cannot be emphasized by 1D simulations. As discussed earlier, the photoelectrons shown in Figure 8.7b follow nearly the same trends of the potential structure near the surface. And ions density doesn't undergo much variation above the surface as shown in Figure 8.7d. Figure 8.7c shows the electron density profiles; due to similar reasons discussed earlier, variation in equi-density contours is not much seen.

A significantly different and more complex situation is illustrated in Figure 8.8 where the photon comes in 80°. This situation mimics terminator or polar region of the moon, where a small topographic feature can cast a long shadow due to the grazing solar illumination. The illuminated part of the crater with significant photoemission flux acquires a positive potential. The positive potential rapidly decreases and becomes zero towards the crater center as shown in Figure 8.8a. The positive region is dominated by photoelectrons as shown in Figure 8.8b. In the analytical study, it was assumed that the shadowed region would get uniform exposure to plasma and have a high negative potential. However, in the current scenario, the SPIS results suggest that plasma has been obstructed near the left edge of the crater. Solar wind electrons are noticed to be entered in the leeward side of the crater (see Figure 8.8c the electron density is around $\sim 3\ \mathrm{cm}^{-3}$) where the ion density is noticed to be very low $\sim$ 0.25 cm^{-3} as shown in Figure 8.8d. This creates a nearly ion-free electron region similar to a 'mini-wake' like structure as discussed by Farrell et al. (2007, 2010); Mishra and Bhardwaj (2020). In the scenarios discussed in Figures 8.6 and 8.7, clear existence of potential minima at some altitude have

been observed. However, for 80° case, the complex potential structure above the crater doesn't show any clear existence of potential minima. This may be due to the complex interplay between the vertical and horizontal distribution of sheath populations, as well as due mixed screening of Type A (photoelectron-dominated positively charged region) and Type C (solar wind electric rich region in the leeward side) sheath features.

The SPIS results are deemed to be in a steady state when the net current on the surface reaches zero. In the cases presented for 0° and 40°, a steady state is achieved within 100 seconds. The results shown here are for a time of 450 seconds. However, for 80°, the system didn't achieve zero net current after 2000 s. Although the photoemission-dominated illuminated region achieved a steady state quite early, the shadowed region on the leeward side of the crater didn't achieve a steady state. Because in the solar wind electron-rich region, no return current has been turned on in the simulation, which can balance with the negative solar wind electron current. In reality, this kind of scenario creates a more electrically complex picture. Because highly energetic electrons enter the leeward side of the crater and impact the crater surface. This leads to secondary electron emission, which has not yet been included in the current simulation. Negatively charged dust plays a crucial role in balancing the negative electron current in this region. According to Farrell et al. (2010), these negatively charged particles get accelerated by large local electric fields, potentially acting as a current source by removing excess negative charge. Additionally, Mishra and Bhardwaj (2020) argued that these charged dust particles act as field emission centers, generating electrons through quantum field emission. This process may provide a return current sufficient to establish a steady state in the electron-rich region. The significance of these findings highlights the critical need for further exploration into how surface topography influences the lunar plasma environment. A diverse range of mechanisms, interactions, and geometrical complexities may be incorporated into the simulation to provide a more comprehensive understanding of these phenomena, which could be taken up in future work. An improved understanding in this area could lead to significant advancements in the understanding of the lunar plasma environment.

8.5 Summary

This chapter investigates the effect of the simplest surface topography (a simple crater) in modifying the lunar photoelectron sheath. The presence of any surface relief modifies the local solar illumination angle around its vicinity. For example, the solar illumination angle

varies around the crater's floor, which changes the effective photoemission and positive surface charging. As a result, the potential structure is modified within the crater. Under normal photon incidence, a horizontally symmetric sheath structure around the crater center is anticipated. For oblique photon incidence, within a fully illuminated crater, the sheath structure becomes asymmetric, and some locations acquire negative potential due to higher local illumination and marginal photoemission. For a partially illuminated crater, the shadowed region acquires negative potential due to the dominant electron collection, and the illuminated region remains positive. A complex potential structure is anticipated in the sunlit-shadowed boundary. These analyses are carried out using 1D calculations by varying local illumination angles within the crater floor. The geometrical calculations suggest that the results should remain intact from any size of the simple crater with the same depth-to-diameter h/D ratio. However, the results are anticipated to be valid for the surface features with sizes larger than the sheath thickness of the lunar photoelectron sheath. For surface features that are equal to or larger than the local plasma, Debye length can generate horizontal effects where Poisson's equation can not be solved in one dimension. For those cases, the investigation of topographic effects on the lunar plasma environment has been initiated using an open-source 3D modeling tool named Spacecraft Plasma Interaction Software (SPIS). Some preliminary results have been presented. Although SPIS presumes Maxwellian photoelectrons, the modeling results can predict various features of the non-monotonic sheath. The results highlighted the importance of local illumination angle as predicted by the analytical results. Along with that, the adaption of PIC simulation within unstructured meshing of crater geometry, SPIS provides 3D potential and density profiles of various sheath populations, which takes care of both vertical and horizontal variations in the simulations. As a result, a 'mini wake' type of feature has been observed in the leeward side of the crater for 80° solar illumination.

SPIS can simulate various scenarios involving the lunar lander and its interactions with plasma and solar radiation. The study by Kuznetsov et al. (2018) examined the electrostatic charging of the Luna-Glob lander on the lunar surface using SPIS-DUST, considering various plasma and solar illumination conditions. This type of research is crucial for evaluating how the spacecraft may impact measurements from various instruments. The ability of SPIS to investigate this type of environment can be explored in greater depth and will be addressed in future studies. One of the main emphases of this thesis is to highlight the importance of FD statistics in deriving the photoelectron contribution and a self-consistent mechanism of their generation. The Maxwellian consideration of photo-

electrons in SPIS may limit the directed comparison of the results derived from the comprehensive analytical model presented in this thesis. While the current analytical model and SPIS photoelectron properties serve their purpose, implementing certain modifications could enhance their compatibility, allowing for a more direct and impactful comparison. This could be taken up as a future work.

Chapter 9

Summary, conclusion and future work

This thesis investigated the plasma sheath formation around the Moon and its implications. Plasma sheath is a non-neutral space charge region created in the vicinity of the lunar surface under dynamic interaction with high energetic UV radiation and Solar wind/ambient plasma collection.

In the dayside of the Moon, due to dominant UV-induced photoemission and subsequent solar wind/plasma collection, the surface acquires a finite amount of potential(primarily positive). The effect of the surface potential has been screened by a photoelectron-dominated non-neutral space charge region called the photoelectron sheath. On the nightside, photoemission is absent, a larger collection of solar wind/plasma electrons makes the surface negatively charged, and the effect of this negative charge and potential has been screened by an ion-dominated non-neutral space charge region called the Debye sheath. The sheath region exhibits an inherent potential structure that can be quantitatively estimated by solving the Poisson equation, which connects the potential structures with the population densities within the sheath. This potential structure exhibits an electric field structure that can mobilize the dust particle within this electrostatically active medium. Several analytical attempts have been carried out in order to characterize the plasma sheath structure around the Moon. However, several simplifications in the previous analysis have been noticed, which limit their applicability in the realistic lunar plasma scenario.

Lunar photoelectrons are a significant component characterizing the potential structures around sunlit Moon. Previous literature assumed a preexisting photoelectron

cloud in the vicinity of the sunlit lunar surface and assigned a simplified Maxwellian distribution to it. This simplified assumption ignores the self-consistent mechanism of photoelectron generation from the lunar surface and subsequent sheath formation. As a result, Maxwellian photoelectrons significantly differed from the photoelectron distribution experimentally measured from the lunar sample by Feuerbacher et al. (1972).

Chapter 2 of this thesis derived the characteristics of lunar photoelectrons considering the self-consistent generation of photoelectrons from the lunar surface using Fowler's photoemission theory (Fowler, 1929). In this course, observed EUV/UV solar spectrum (Chamberlin et al., 2020) is coupled with measured photoelectric efficiency of the lunar regolith (Feuerbacher et al., 1972; Willis et al., 1973). Latitude-dependent regolith temperature (Mishra and Bhardwaj, 2019) consistent with LRO-based Diviner instrument (Williams et al., 2017) is incorporated with FD-statistics of the electrons, to determine the availability of electrons within the surface lattice for absorption of photons and their subsequent emission. These aspects are used to derive the photoelectron flux from the lunar surface and their population densities. Combinations of these aspects feature a more realistic scenario and put forward a rather comprehensive approach in deriving the photoelectron distribution over the Moon. As the surface loses electrons via the photoemission process, the surface may acquire a finite positive potential. This positive potential creates a potential barrier that traps some part of the emitted photoelectrons in the close vicinity of the lunar surface. As a result, a significant difference in the derived photoelectron distribution function is noticed for the uncharged and charged lunar surface. The charged surface with an upward-directed electric field traps some of the emitted photoelectrons and characterizes three distinct charge populations (one free, two captured) and their distributions.

The derived photoelectron distribution function distinctly highlighted the effect of various high-energy spectral peaks of the observed solar spectrum. Hence, the effect of solar activity on the lunar photoelectron can be effectively characterized from this derived distribution. For typical solar flare, maxima, and minima conditions, the number densities and mean energy of photoemitted electrons are found to be $(533.66\,\mathrm{cm}^{-3}, 4.75\,\mathrm{eV})$, $(101.28\,\mathrm{cm}^{-3}, 4.46\,\mathrm{eV})$, and $(63.86\,\mathrm{cm}^{-3}, 4.42\,\mathrm{eV})$ respectively from uncharged lunar surface. The distribution of photoelectrons is significantly influenced by the potential of the lunar surface. The findings indicate that the steady-state photoelectron sheath captures almost 90% of the emitted photoelectrons due to the barrier created by the surface potential. Furthermore, the analysis indicates that different populations of photoelectrons

within the sheath exhibit distinct mean energies. However, when averaged, the mean energy of these different groups matches the mean energy of photoelectrons emitted from an uncharged surface. Additionally, the derived photoelectron distribution is reasonably consistent with the measurements made by Feuerbacher et al. (1972), although it shows considerable deviation from a Maxwellian distribution.

The derived photoelectron VDF is used in Chapter 3, where, in detail, sheath formation above the sunlit lunar surface has been discussed. A theoretical model describing the photoelectron sheath structure on the Moon's sunlit regolith has been developed. The model solves Poisson's equation within the sheath, accounting for the self-consistent nature of photoelectron generation from the lunar surface and the contribution of solar wind/plasma with kappa distributed electrons and cold ions. In steady-state, the quasineutrality at the sheath edge and flux balance are maintained, and these have been used to derive boundary conditions for Poisson's equation, viz., surface potential and potential minima. The analysis indicated that monotonic (Type B & C) and non-monotonic (Type A) sheaths prevails over the illuminated Moon (illustrated in Figure 3.1), with their occurrence being sensitive to parameters such as solar spectrum, solar wind/ambient plasma parameter, and lunar surface parameters.

Near the terminator with grazing photon incidence, the photoemission is marginal, and the surface acquires a negative charge due to dominant solar wind/ ambient plasma electron collection. The negative surface potential monotonically increases to zero at a vertical altitude of $\sim$ 100 m for a typical ambient plasma condition, forming a Debye-type Type C sheath. As one moves latitudinally away from the terminator, the photoemission flux increases, which transforms the Type C sheath structure to a non-monotonic Type A sheath where potential minima exist close to the surface. The potential minimum always yields negative values and occurs specifically at the surface $(x_m = 0)$ during the transition of the sheath from Type C to Type A. In the equatorial region within Type A sheath, the surface potential is noticed to be positive with sheath thickness typically around $\sim$ 60 m, whereas near the terminator, the vertical extent of the sheath can reach around $\sim$ 120 m for nominal solar wind plasma conditions. In addition to the Type A sheath, Poisson's equation also yields a monotonically decreasing sheath (Type B) solution. The Type B sheath solution is a photoelectron-dominated sheath with a smaller thickness, approximately $\sim$ 12 m, in contrast to the Type A sheath, where a double-layer structure is identified. Under typical solar wind conditions, the non-monotonic (Type A) sheath is observed to be stable in the terminator region, whereas both sheath types have equal likelihood of

occurrence near the equator region. It has also been observed that in exotic plasma conditions, when the Moon traverses Earth's magnetotail/magnetosheath, the Type A sheath becomes more stable, leading to situations where the entire sunlit Moon could have a negative potential. Furthermore, contrary to previous assumptions, this chapter concludes that high-energy photons from the solar spectrum, apart from the Lyman- α spike, also play a significant role in influencing the sunlit surface charge and the resulting sheath structure. Conclusively, Chapter 3 presented the formulation of a comprehensive photoelectron sheath model based on the self-consistent physics of photoelectron generation, realistic distribution of solar wind/plasma electrons, and ions. This model predicts the potential structure around the sunlit Moon and their possibility of occurrence.

The capability of this comprehensive model derived in Chapter 3 has been showcased in Chapter 4 by predicting the potential structure around Chandrayaan 3 landing site (Ch3 LS) as a case study during the 14-day sunlit passage. During the sunlit passage, Ch3 LS passes through the solar wind and Earth's magnetospheric plasma. The realistic scenario has been simulated using the plasma parameter data from the *ARTEMIS P2* spacecraft (former *THEMIS-C* probe) (Angelopoulos, 2011). During the sunlit passage, the local zenith angle θ_{sza} varies approximately between 70° and 90°. The model predicts Type C sheath with a negative surface potential for θ_{sza} close to 90°. The temporal existence of the Type C sheath around Ch3 LS is observed to last approximately one day, with half a day during local dusk and half a day during dawn. For other θ_{sza} values, the model predicted both Type A & B solutions. In comparison between Type A and Type B, the solution that has greater potential energy indicates a transient metastable solution that eventually converts into a lower energy, more stable configuration. Calculations from this model imply that the non-monotonic Type A sheath is a more stable potential that prevails over Ch3 LS during the sunlit passage. The calculations presented herein are in agreement with the space measurements of Halekas et al. (2008) in such physical conditions. The potential structure observed to be very dynamic throughout the passage of Ch3 LS, and the surface potential varies between 8 to -48 V, and the potential minimum between -0.5 to -55 V (at an altitude of 15 to 20 m). For exotic conditions, for instance, within Earth's magnetospheric plasma sheet, the surface potential varies from -297 to -386 V, and a potential minimum ranges from -304 to -392 V from $\theta_{sza} = 70°$ to 80° respectively. The implications of these findings have been thoroughly analyzed, offering valuable insights for interpreting the data related to the plasma environment acquired during the Chandrayaan 3 campaign or planning test trial for future lunar missions.

After giving a comprehensive discussion on the sunlit near-surface sheath plasma environment, Chapter 5 highlighted the plasma sheath formation around the lunar nightside. Solar radiation and streaming solar wind are obstructed on the dayside of the lunar surface. Space plasma currents from solar wind plasma expansion or currents from the Earth's magnetotail charge the lunar night side. Hence, the nightside plasma is very exotic, with typical plasma electron temperature varying between 100 to 2000 eV, and the density between 0.25 to 0.5 cm^{-3} (Stubbs et al., 2007; Halekas et al., 2008). As a result, the nightside surface acquires a negative potential due to the dominant plasma electron collection. This negative potential is screened by plasma ions, creating a Debye sheath in the vicinity. Due to higher electron temperature, the negative surface temperature achieves several kilovolts in magnitude. And lower plasma density takes a significantly large altitude, around a few kilometers, to screen the effect of this large negative potential. However, in reality, these high-energy primary electrons impacting the lunar surface generate electrons via secondary electron emission (SEE). The SEE experiments with the lunar sample indicated that for specific primary electron energies, the SEE yield exceeded unity (Horányi, 1996; Horányi et al., 1998). This fact highlighted that upon the bombardment of a single high-energy primary electron, the surface may lose more than one electron, effectively making the surface positively charged. And emitted secondary electrons may contribute to the screening of this positive potential, forming a sheath which is significantly different from the Debye sheath. This has been experimentally demonstrated by Wang et al. (2016a). Motivated by this experimental study, Chapter 5 provided an analytical formulation of an inverse sheath structure on the lunar nightside that is dominated by secondary electrons, under the assumption of Maxwellian primary and secondary electrons along with cold ions. For specific SEE yield values, there exists a temperature regime that allows the formation of an inverse sheath. In this sheath, secondary electrons dominate over primary plasma electrons by a factor of ten. Similar to the Debye sheath, the surface potential is shown to be unaffected by the density of the quasi-neutral plasma, as it solely influences the extent of screening. Under typical plasma conditions, in the presence of significant SEE, the surface of the lunar nightside develops a few positive potentials. In this scenario, an inverse sheath is observed, extending between 10 and 40 meters, rather than the Debye sheath, which typically has a large negative potential (measured in kilovolts) and can extend for kilometers vertically.

One of the direct implications of this potential structure is, the electric field within the sheaths can mobilize the dust particle above the lunar surface within this electrostat-

ically active medium. Dust particle undergoes electrostatic charging within the sheath by collecting the sheath constituents. Additionally, the dust is exposed to solar radiation, which causes photoemission. As a result, the charge on the dust changes over time while it moves within the sheath. The charged dust then experiences the influence of the inherent electric field, and its behavior is affected by the combined effects of gravity and electrostatic forces. Chapter 6 presented a detailed simulation of dust charging and dynamics within the lunar photoelectron sheath. In the estimation of dust charging currents and the electrostatic force, the sheath model discussed in Chapter 3 has been used. The steady-state charge of the dust has been estimated by setting the net current on the dust to zero. Results highlighted that the equilibrium dust charge varies altitudinally and latitudinally within the sheaths for all the Type A, B, and C potential structures. Estimates indicate that close to the surface, dust develops a finite negative potential primarily because of the collection of photoelectrons within the photoelectron-dominated Type A and B sheath structures. In contrast, at higher altitudes, dust acquires a finite positive potential due to the dominant photoemission induced by UV radiation. As a result, for Type A and B sheaths, certain-sized dust (below radius $\sim$ 125 nm) particles can be stably levitated at some altitudes where the upward-directed electrostatic force balances gravity. For the ion-dominated Type C sheath, due to grazing photon incidence, the surface acquires a finite negative potential, and the electric field is directed downward towards the surface. However, dust particles in this location get full solar illumination. Hence, dust particles in those locations acquire positive charges due to dominant ion collection and photoemission. The results suggested that dust cannot be stably levitated in the Type C sheath around the Moon. Although the steady-state results suggest the possibility of stable lunar dust levitation, a finite amount of time is required to achieve this condition. For this, the dust charge and trajectory of the dust particle is analyze over time by simultaneously solving the dust charging equation and equation of motion. It has been found that the dynamic condition does not always favor stable levitation. Results highlighted the existence of a small regime of initial conditions for which the dust particle proceeds towards the static levitation point by undergoing a periodic hopping trajectory. In other cases, the dust particles re-impact the surface after a single ballistic hop. In studying the dynamical evolution of the dust, the discrete nature of dust charging becomes important. In a rarefied lunar plasma scenario, the discrete, quantized, and random nature of charging yields significantly different dust dynamics compared to that obtained from continuous charging. To demonstrate this effect, a Monte Carlo protocol has been developed in

Chapter 6, revealing new findings and advancing the understanding of dust behavior in the lunar plasma environment.

In Chapter 6, the dust particles are launched from the lunar surface with the initial charge and velocity. But did not comment on how the dust particle gets detached from the surface in the first place. The dust particle lying on the charged lunar surface is subjected to gravity, cohesion, and electrostatic forces. If the electrostatic force exceeds the combined forces of cohesion and gravity, the dust particle detaches from the surface and lifts above. Previous chapters highlighted that the sunlit lunar surface has a typical electric field $\sim$ 5 to 10 V m^{-1}, which yields the mean surface charge density $\sim 5 \times 10^8\, e$ m^{-2}. Presuming the overlying dust particles acquire the same charge density, a 20 nm dust barely acquires a single electronic charge. It suggests that no dust particle could rise off the lunar surface for such a low charge density. In fact, the electrostatic lifting requires $\sim$ 5 orders of magnitude higher charge density and/ or dust charge. Laboratory experiments (Wang et al., 2016b) and space observation (Zook and McCoy, 1991), however, have demonstrated the possibility of electrostatic dust detachment induced by surface interaction with ambient plasma and solar irradiation. In Chapter 7, a possible mechanism of electrostatic dust detachment has been conceptualized. This chapter highlighted that the theory of charge fluctuation is a key to inducing this mechanism. It suggests that due to natural randomization associated with incident solar/plasma irradiation, the charge fluctuations at localized microscopic areas, which can generate a charge, on average, an order of magnitude higher than the mean charge. To consolidate the concept, a Markovian Monte Carlo protocol has been developed to simulate the random creation/ annihilation of sub-microscopic charged spots. These spots generate local electric fields and Coulombic repulsion, which can detach lunar dust particles from surfaces by overcoming gravity and Van der Waals adhesive forces. Signifying the role of electrostatic effects, this formulation explains the dust detachment from the lunar surface in the first place.

The thesis provided a comprehensive global structure of plasma sheath formation around the Moon and subsequent dust charging and dynamics. In Chapter 8, the effect of the surface topography on the lunar photoelectron sheath is briefly addressed. The presence of any surface relief modifies the local solar illumination angle around its vicinity, which can significantly modify the local plasma structures. For this, an analytical investigation was conducted to study the effect of the simplest surface topography (a simple crater) in modifying the lunar photoelectron sheath. These analyses are carried out using 1D calculations by varying local illumination angles within the crater floor. The 1D cal-

culations can provide some insight into the modification of the local potential structure. Like, for normal photon incidence, a symmetric sheath structure is expected around the crater center; for oblique incidence, the sheath becomes asymmetric, and certain areas may have negative potential due to higher local illumination and marginal photoemission. In a partially illuminated crater, the shadowed region can attain negative potential from dominant electron collection, while the illuminated region stays positive, creating a complex potential structure at the sunlit-shadowed boundary. However, 1D calculations cannot be performed when the topographic features become comparable to the local Debye length. For those cases, the investigation has been initiated using an open-source 3D modeling tool named Spacecraft Plasma Interaction Software (SPIS). Some preliminary results have been presented in this thesis. Although SPIS presumes Maxwellian photoelectrons, the modeling results can predict various features of the non-monotonic sheath. The SPIS results highlighted the importance of local illumination angle, as predicted by the analytical results, also providing 3D potential and density profiles of various sheath populations, which take care of both vertical and horizontal variations in the simulations. The capability of SPIS to study this kind of environment can be extensively explored and will be taken up in the future.

The work presented in this thesis significantly advances the understanding and improves the estimates of plasma sheath formation around the Moon and subsequent dust dynamics. However, there is a significant scope of future research in the following aspects:

- Application of the comprehensive model in the other airless planetary bodies: The Moon serves as a key reference for studying other planetary bodies without an atmosphere, because similar processes are expected to occur around other airless bodies exposed to similar space environments (Halekas et al., 2011b).

- Combining the analytical study with spacecraft data: Literature highlighted that ARTEMIS measurements can observe several signatures of the near-surface plasma sheath, especially some signatures of the non-monotonic sheath (Halekas et al., 2011a; Poppe et al., 2011). Apart from that, Xu et al. (2021), using ARTEMIS measurements, tried to constrain the photoemission yield of the lunar surface. However, their measurements of yields have uncertainty over four orders of magnitude. They expected that this may be due to the inadequately defined probability function for photoelectron energy. The analytical distribution of photoelectrons derived in this

thesis may be used to re-examine these ARTEMIS measurements, which might provide more adequate results.

- Conceptualizing test bed in-situ instrument for future lunar missions: The analytical studies have developed a significant understanding of the lunar plasma environment. But the quantitative estimates are sensitive to the input parameters. For example, the photoelectric yield of lunar regolith and the regolith work function are two significant parameters in characterizing the lunar photoelectrons. However, due to the possibility of contamination due to Earth's atmosphere, measurements from the lunar samples may not provide the actual values. Popel et al. (2014) conceptualized an experiment to measure the photoelectric properties of the lunar surface directly on the Moon for the future Luna 27 mission. The findings of this thesis related to lunar photoelectrons may be helpful in this aspect. The Langmuir probe is one of the adequate methods for measuring the in-situ local plasma parameters. The Rashid-1 rover and Chandrayaan 2/3 lander carried Langmuir probes to measure the local plasma environment (Clausen et al., 2025; Manju et al., 2020; Indian Space Research Organisation (ISRO), 2023a). Measurements were not performed on the probes of the Rashid-1 rover or Chandrayaan 2, and, as of now, detailed results from the measurements obtained on the Moon by Chandrayaan 3 are awaited. There is a strong possibility that Langmuir probes will be utilized in future lunar missions, and this thesis may help to define the specifications required for Langmuir probes (Hartzell et al., 2023).

- Lunar dust is an important component of the lunar complex plasma environment, posing significant challenges to space missions (Zakharov et al., 2020). The analytical studies carried out so far considered dust to be non-perturbing. That dust has been considered to be isolated, and its charge and emitted photoelectrons from it do not perturb the sheath. It would be interesting to derive the lunar plasma scenario when dust strongly perturbs the near-surface space plasma environment.

In conclusion, the findings of this thesis significantly enhance our understanding of plasma sheath formation around the Moon. The research provides accurate and realistic quantitative estimates of the sheaths and the subsequent dynamics of dust. It also provides deeper insight into the "microphysics" of electrostatic dust detachment. This study not only addresses critical gaps in the existing knowledge but also paves the way for future explorations in lunar studies.

Bibliography

Abbas, M., Tankosic, D., Craven, P., LeClair, A., and Spann, J. (2010). Lunar dust grain charging by electron impact: Complex role of secondary electron emissions in space environments. *The Astrophysical Journal*, 718(2):795–809. pages

Angelopoulos, V. (2011). The ARTEMIS Mission. *Space Science Reviews*, 165(1):3–25. pages

Bauer, S. J. (1973). *Physics of Planetary Ionospheres*, volume 6 of *Physics and Chemistry in Space*. Springer, Berlin, Heidelberg. pages

Berg, O., Richardson, F., and Burton, H. (1973). Apollo 17 preliminary science report. *NASA SP-330*, 16. pages

Berg, O., Richardson, F., Rhee, J. W., and Auer, S. (1974). Preliminary results of a cosmic dust experiment on the moon. *Geophysical Research Letters*, 1(7):289–290. pages

Bhardwaj, A., Dhanya, M., Alok, A., Barabash, S., Wieser, M., Futaana, Y., Wurz, P., Vorburger, A., Holmström, M., Lue, C., et al. (2015). A new view on the solar wind interaction with the moon. *Geoscience Letters*, 2(1):1–15. pages

Bohm, D. (1949). Minimum ionic kinetic energy for a stable sheath. *The Characteristics of Electrical Discharges in Magnetic Fields*, pages 77–86. pages

Bouchoule, A., editor (1999). *Dusty Plasmas: Physics, Chemistry, and Technological Impact in Plasma Processing*. Wiley. pages

Burinskaya, T. (2014). Influence of the solar wind on the distribution of the electric potential near the moon's surface. *Plasma Physics Reports*, 40(1):14–20. pages

Burinskaya, T. (2015). Non-monotonic potentials above the day-side lunar surface exposed to the solar radiation. *Planetary and Space Science*, 115:64–68. pages

Carroll, A., Hood, N., Mike, R., Wang, X., Hsu, H.-W., and Horányi, M. (2020). Laboratory measurements of initial launch velocities of electrostatically lofted dust on airless planetary bodies. *Icarus*, 352:113972. pages

Chamberlin, P. C., Eparvier, F. G., Knoer, V., Leise, H., Pankratz, A., Snow, M., Templeman, B., Thiemann, E. M. B., Woodraska, D. L., and Woods, T. N. (2020). The flare irradiance spectral model-version 2 (fism2). *Space Weather*, 18(12):e2020SW002588. e2020SW002588 10.1029/2020SW002588. pages

Chamberlin, P. C., Woods, T. N., and Eparvier, F. G. (2008). Flare irradiance spectral model (fism): Flare component algorithms and results. *Space Weather*, 6(5). pages

Chandran, S. R., Renuka, G., and Venugopal, C. (2013). Plasma electron temperature variability in lunar surface potential and in electric field under average solar wind conditions. *Advances in Space Research*, 51(9):1622–1626. pages

Chow, V. W., Mendis, D. A., and Rosenberg, M. (1993). Role of grain size and particle velocity distribution in secondary electron emission in space plasmas. *Journal of Geophysical Research: Space Physics*, 98(A11):19065–19076. pages

Clack, D., Kasper, J., Lazarus, A., Steinberg, J., and Farrell, W. (2004). Wind observations of extreme ion temperature anisotropies in the lunar wake. *Geophysical research letters*, 31(6). pages

Clausen, L. B. N., Bekkeng, T.-A., Els, S., Khoory, M. S., Sharaf, A. A., Adhikari, S., Eklund, A. J., Miloch, W. J., and Almarzooqi, H. (2025). The Langmuir Probe Instrument on Board the Rashid-1 Rover of the Emirates Lunar Mission. *Space Science Reviews*, 221(3):34. pages

Colwell, J. E., Batiste, S., Horányi, M., Robertson, S., and Sture, S. (2007). Lunar surface: Dust dynamics and regolith mechanics. *Reviews of Geophysics*, 45(2). pages

Colwell, J. E., Gulbis, A. A., Horányi, M., and Robertson, S. (2005). Dust transport in photoelectron layers and the formation of dust ponds on eros. *Icarus*, 175(1):159–169. pages

Colwell, J. E., Robertson, S. R., Horányi, M., Wang, X., Poppe, A., and Wheeler, P. (2009). Lunar dust levitation. *Journal of Aerospace Engineering*, 22(1):2–9. pages

Criswell, D. R. (1972). Lunar dust motion. In *Proceedings of the Lunar Science Conference, vol. 3, p. 2671*, volume 3, pages 2671–2680. pages

Cui, C. and Goree, J. (1994). Fluctuations of the charge on a dust grain in a plasma. *IEEE Transactions on plasma science*, 22(2):151–158. pages

Dove, A., Horanyi, M., Wang, X., Piquette, M., Poppe, A. R., and Robertson, S. (2012). Experimental study of a photoelectron sheath. *Physics of Plasmas*, 19(4). pages

Dove, A., Horányi, M., Robertson, S., and Wang, X. (2018). Laboratory investigation of the effect of surface roughness on photoemission from surfaces in space. *Planetary and Space Science*, 156:92–95. Dust, Atmosphere, and Plasma Environment of the Moon and Small Bodies. pages

Dukes, C. A. and Baragiola, R. A. (2013). Secondary electron emission from lunar soil: Yields, energy distributions, and charging effects. *Planetary and Space Science*, 89:36–41. pages

Dyadechkin, S., Kallio, E., and Wurz, P. (2015). New fully kinetic model for the study of electric potential, plasma, and dust above lunar landscapes. *Journal of Geophysical Research: Space Physics*, 120(3):1589–1606. pages

Eriksson, A. I., Boström, R., Gill, R., Åhlén, L., Jansson, S.-E., Wahlund, J.-E., André, M., Mälkki, A., Holtet, J. A., Lybekk, B., Pedersen, A., Blomberg, L. G., and The LAP Team (2007). RPC-LAP: The Rosetta Langmuir Probe Instrument. *Space Science Reviews*, 128(1-4):729–744. pages

Farr, B., Wang, X., Goree, J., Hahn, I., Israelsson, U., and Horányi, M. (2020). Dust mitigation technology for lunar exploration utilizing an electron beam. *Acta Astronautica*, 177:405–409. pages

Farr, B., Wang, X., Goree, J., Hahn, I., Israelsson, U., and Horányi, M. (2021). Improvement of the electron beam (e-beam) lunar dust mitigation technology with varying the beam incident angle. *Acta astronautica*, 188:362–366. pages

Farr, B., Wang, X., Goree, J., Hahn, I., Israelsson, U., and Horányi, M. (2022). Dust removal from a variety of surface materials with multiple electron beams. *Acta astronautica*, 200:42–47. pages

Farrell, W., Stubbs, T., Halekas, J., Killen, R., Delory, G., Collier, M., and Vondrak, R. (2010). Anticipated electrical environment within permanently shadowed lunar craters. *Journal of Geophysical Research: Planets*, 115(E3). pages

Farrell, W. M., Stubbs, T., Vondrak, R., Delory, G., and Halekas, J. (2007). Complex electric fields near the lunar terminator: The near-surface wake and accelerated dust. *Geophysical Research Letters*, 34(14). pages

Farrell, W. M., Stubbs, T. J., Delory, G. T., Vondrak, R. R., Collier, M. R., Halekas, J. S., and Lin, R. P. (2008). Concerning the dissipation of electrically charged objects in the shadowed lunar polar regions. *Geophysical Research Letters*, 35(19):L19104. pages

Feuerbacher, B., Anderegg, M., Fitton, B., Laude, L., Willis, R., and Grard, R. (1972). Photoemission from lunar surface fines and the lunar photoelectron sheath. In *Lunar and planetary science conference proceedings*, volume 3, page 2655. pages

Firefly Aerospace (2025a). Blue ghost mission 1: Ghost riders in the sky. https://fireflyspace.com/missions/blue-ghost-mission-1/. Accessed: 2025-05-20. pages

Firefly Aerospace (2025b). Blue ghost mission 1: Ghost riders in the sky. https://www.flickr.com/photos/fireflyspace/albums/72177720313239766/. Accessed: 2025-05-20. pages

Firefly Aerospace (2025c). Blue ghost mission 1: Live updates. https://fireflyspace.com/news/blue-ghost-mission-1-live-updates/. Accessed: 2025-05-20. pages

Flanagan, T. and Goree, J. (2006). Dust release from surfaces exposed to plasma. *Physics of plasmas*, 13(12). pages

Fowler (1967). *Statistical mechanics*. CUP Archive. pages

Fowler, R. H. (1929). Statistical mechanics: The theory of the properties of matter in equilibrium; based on an essay awarded the adams prize in the university of cambridge, 1923-24. pages

Fowler, R. H. (1931). The analysis of photoelectric sensitivity curves for clean metals at various temperatures. *Physical review*, 38(1):45. pages

Freeman Jr, J., Fenner, M., Hills, H., Lindeman, R., Medrano, R., and Meister, J. (1972). Suprathermal ions near the moon. *Icarus*, 16(2):328–338. pages

Freeman Jr, J. W., Balsiger, H., and Hills, H. (1970). Suprathermal ion detector experiment/lunar ionosphere detector. *Apollo 12-Preliminary Science Report*. pages

Fu, J. H. M. (1971). Surface potential of a photoemitting plate. *Journal of Geophysical Research*, 76(10):2506–2509. pages

Goertz, C. K. (1989). Dusty plasmas in the solar system. *Reviews of Geophysics*, 27(2):271–292. pages

Gold, T. (1955). The lunar surface. *Monthly Notices of the Royal Astronomical Society*, 115(6):585–604. pages

Gold, T. (1959). Dust on the moon. *Vistas in Astronautics*, 2:261–266. pages

Gold, T. (1962). Processes on the lunar surface. In *The moon*, volume 14, pages 433–440. pages

Golub', A. P., Dol'nikov, G., Zakharov, A. V., Zelenyi, L. M., Izvekova, Y. N., Kopnin, S., and Popel, S. I. (2012). Dusty plasma system in the surface layer of the illuminated part of the moon. *JETP letters*, 95:182–187. pages

Gosling, J. T., Hildner, E., Asbridge, J. R., Bame, S. J., and Feldman, W. C. (1977). Noncompressive density enhancements in the solar wind. *Journal of Geophysical Research (1896-1977)*, 82(32):5005–5010. pages

Grard, R. (1997). Photoemission on the surface of mercury and related electrical phenomena. *Planetary and Space Science*, 45(1):67–72. Mercury: The Planet and its Magnetosphere. pages

Grard, R. and Tunaley, J. (1971). Photoelectron sheath near a planar probe in interplanetary space. *Journal of Geophysical Research*, 76(10):2498–2505. pages

Griffiths, D. J. (2017). Introduction to electrodynamics. pages

Grobman, W. and Blank, J. (1969). Electrostatic potential distribution of the sunlit lunar surface. *Journal of Geophysical Research*, 74(16):3943–3951. pages

Guernsey, R. L. and Fu, J. H. M. (1969). Potential distribution surrounding a photoemitting plate in a dilute plasma. pages

Guernsey, R. L. and Fu, J. H. M. (1970). Potential distribution surrounding a photoemitting, plate in a dilute plasma. *Journal of Geophysical Research (1896-1977)*, 75(16):3193–3199. pages

Halekas, J., Brain, D., and Holmström, M. (2015). Moon's plasma wake. *Magnetotails in the solar system*, 207:149–167. pages

Halekas, J., Delory, G., Farrell, W., Angelopoulos, V., McFadden, J., Bonnell, J., Fillingim, M., and Plaschke, F. (2011a). First remote measurements of lunar surface charging from artemis: Evidence for nonmonotonic sheath potentials above the dayside surface. *Journal of Geophysical Research: Space Physics*, 116(A7). pages

Halekas, J., Delory, G., Lin, R., Stubbs, T., and Farrell, W. (2009a). Lunar Prospector measurements of secondary electron emission from lunar regolith. *Planetary and Space Science*, 57(1):78–82. pages

Halekas, J., Delory, G., Lin, R., Stubbs, T., and Farrell, W. (2009b). Lunar surface charging during solar energetic particle events: Measurement and prediction. *Journal of Geophysical Research: Space Physics*, 114(A5). pages

Halekas, J., Lin, R., and Mitchell, D. (2005). Large negative lunar surface potentials in sunlight and shadow. *Geophysical research letters*, 32(9). pages

Halekas, J., Saito, Y., Delory, G., and Farrell, W. (2011b). New views of the lunar plasma environment. *Planetary and Space Science*, 59(14):1681–1694. pages

Halekas, J., Saito, Y., Delory, G., and Farrell, W. (2011c). New views of the lunar plasma environment. *Planetary and Space Science*, 59(14):1681–1694. pages

Halekas, J. S., Delory, G. T., Lin, R. P., Stubbs, T. J., and Farrell, W. M. (2008). Lunar Prospector observations of the electrostatic potential of the lunar surface and its response to incident currents: LUNAR SURFACE ELECTROSTATIC POTENTIAL. *Journal of Geophysical Research: Space Physics*, 113(A9). pages

Halekas, J. S., Mitchell, D. L., Lin, R. P., Hood, L. L., Acuña, M. H., and Binder, A. B. (2002). Evidence for negative charging of the lunar surface in shadow: LUNAR SURFACE CHARGING. *Geophysical Research Letters*, 29(10):77–1–77–4. pages

Harada, Y. (2015). *Interactions of Earth's Magnetotail Plasma with the Surface, Plasma, and Magnetic Anomalies of the Moon*. Springer Theses. Springer Japan, Tokyo. pages

Hartzell, C., Zimmerman, M., and Hergenrother, C. (2022). An evaluation of electrostatic lofting and subsequent particle motion on bennu. *The Planetary Science Journal*, 3(4):85. pages

Hartzell, C. M. (2012). *The dynamics of near-surface dust on airless bodies*. PhD thesis, University of Colorado at Boulder. pages

Hartzell, C. M. (2019). Dynamics of 2d electrostatic dust levitation at asteroids. *Icarus*, 333:234–242. pages

Hartzell, C. M., Bellan, P., Bodewits, D., Delzanno, G. L., Hirabayashi, M., Hyde, T., Konopka, U., Thomas, E., Thomas, H. M., Hahn, I., and Israelsson, U. (2023). Payload concepts for investigations of electrostatic dust motion on the lunar surface. *Acta Astronautica*, 207:89–105. pages

Hartzell, C. M. and Scheeres, D. J. (2011). The role of cohesive forces in particle launching on the moon and asteroids. *Planetary and Space Science*, 59(14):1758–1768. pages

Hartzell, C. M. and Scheeres, D. J. (2013). Dynamics of levitating dust particles near asteroids and the moon. *Journal of Geophysical Research: Planets*, 118(1):116–125. pages

Heiken, G., Vaniman, D., and French, B. M. (1991). *Lunar sourcebook: A user's guide to the Moon*. Number 1259. Cup Archive. pages

Hess, S., Sarrailh, P., Matéo-Vélez, J., Villemant, M., Leclerq, L., Jeanty-Ruard, B., and Trouche, A. (2021). Spacecraft-plasma interaction software v6. *SPINE, Tech. Rep*. pages

Hess, S., Sarrailh, P., Matéo-Vélez, J.-C., Jeanty-Ruard, B., Cipriani, F., Forest, J., Hilgers, A., Honary, F., Thiébault, B., Marple, S., et al. (2015). New spis capabilities to simulate dust electrostatic charging, transport, and contamination of lunar probes. *IEEE Transactions on Plasma Science*, 43(9):2799–2807. pages

Hoffman, J., Hodges, R., Johnson, F., and Evans, D. (1973). Lunar atmospheric composition results from apollo 17. In *Lunar Planet. Sci. Conf*, volume 4, page 376. pages

Hones, Jr, E. W. (1985). Magnetic Reconnection in the Earth's Magnetotail. *Australian Journal of Physics*, 38(6):981–998. Publisher: CSIRO PUBLISHING. pages

Hood, L. and Williams, C. (1989). The lunar swirls-distribution and possible origins. In *IN: Lunar and Planetary Science Conference, 19th, Houston, TX, Mar. 14-18, 1988, Proceedings*

(A89-36486 15-91). Cambridge/Houston, TX, Cambridge University Press/Lunar and Planetary Institute, 1989, p. 99-113., volume 19, pages 99–113. pages

Hood, N., Carroll, A., Mike, R., Wang, X., Schwan, J., Hsu, H.-W., and Horányi, M. (2018). Laboratory investigation of rate of electrostatic dust lofting over time on airless planetary bodies. *Geophysical Research Letters*, 45(24):13–206. pages

Horanyi, M., Sternovsky, Z., Lankton, M., Dumont, C., Gagnard, S., Gathright, D., Grün, E., Hansen, D., James, D., Kempf, S., et al. (2015). The lunar dust experiment (ldex) onboard the lunar atmosphere and dust environment explorer (ladee) mission. *The Lunar Atmosphere and Dust Environment Explorer Mission (LADEE)*, pages 93–113. pages

Horányi, M., Szalay, J. R., and Wang, X. (2024). The lunar dust environment: concerns for moon-based astronomy. *Philosophical Transactions of the Royal Society A*, 382(2271):20230075. pages

Horányi, M. (1996). CHARGED DUST DYNAMICS IN THE SOLAR SYSTEM. *Annual Review of Astronomy and Astrophysics*, 34(1):383–418. pages

Horányi, M., Walch, B., Robertson, S., and Alexander, D. (1998). Electrostatic charging properties of Apollo 17 lunar dust. *Journal of Geophysical Research: Planets*, 103(E4):8575–8580. pages

Hughes, A. L., Colwell, J. E., and DeWolfe, A. W. (2008). Electrostatic dust transport on eros: 3-d simulations of pond formation. *Icarus*, 195(2):630–648. pages

Indian Space Research Organisation (ISRO) (2023a). Chandrayaan-3. https://www.isro.gov.in/ISRO_EN/Chandrayaan3_New.html. Accessed May 3, 2023. pages

Indian Space Research Organisation (ISRO) (2023b). RAMBHA-LP on-board Chandrayaan-3 measures near-surface plasma content. https://www.isro.gov.in/Ch3_Rambha-LP_near-surface_Plasma.html. Accessed: 2025-06-19. pages

Jackson, T. L., Farrell, W. M., Killen, R. M., Delory, G. T., Halekas, J. S., and Stubbs, T. J. (2011). Discharging of Roving Objects in the Lunar Polar Regions. *Journal of Spacecraft and Rockets*, 48(4):700–704. Publisher: American Institute of Aeronautics and Astronautics. pages

Jackson, T. L., Farrell, W. M., and Zimmerman, M. I. (2015). Rover wheel charging on the lunar surface. *Advances in Space Research*, 55(6):1710–1720. pages

Johansson, F. L., Odelstad, E., Paulsson, J., Harang, S., Eriksson, A. I., Mannel, T., Vigren, E., Edberg, N. J., Miloch, W., Simon Wedlund, C., et al. (2017). Rosetta photoelectron emission and solar ultraviolet flux at comet 67p. *Monthly Notices of the Royal Astronomical Society*, 469(Suppl_2):S626–S635. pages

Kureshi, R., Tripathi, K. R., and Mishra, S. K. (2020). Electrostatic charging of the sunlit hemisphere of the Moon under different plasma conditions. *Astrophysics and Space Science*, 365(2):23. pages

Kuznetsov, I., Hess, S., Zakharov, A., Cipriani, F., Seran, E., Popel, S., Lisin, E., Petrov, O., Dolnikov, G., Lyash, A., et al. (2018). Numerical modelling of the luna-glob lander electric charging on the lunar surface with spis-dust. *Planetary and Space Science*, 156:62–70. pages

Li, L., Zhang, Y., Zhou, B., and Feng, Y. (2016). Dust levitation and transport over the surface of the moon. *Science China Earth Sciences*, 59:2053–2061. pages

Lisin, E., Tarakanov, V., Petrov, O., Popel, S., Dol'nikov, G., Zakharov, A., Zelenyi, L., and Fortov, V. (2014). Effect of the solar wind on the formation of a photoinduced dusty plasma layer near the surface of the moon. *JETP letters*, 98(11):664–669. pages

Lisin, E., Tarakanov, V., Popel, S., and Petrov, O. (2015). Lunar dusty plasma: A result of interaction of the solar wind flux and ultraviolet radiation with the lunar surface. *Journal of Physics: Conference Series*, 653(1):012139. pages

Ma, X., Nykyri, K., Dimmock, A., and Chu, C. (2020). Statistical Study of Solar Wind, Magnetosheath, and Magnetotail Plasma and Field Properties: 12+ Years of THEMIS Observations and MHD Simulations. *Journal of Geophysical Research: Space Physics*, 125(10). pages

Manju, G., Pant, T. K., Sreelatha, P., Nalluveettil, S. J., Pradeep Kumar, P., Upadhyay, N. K., Hossain, M. M., Naik, N., Yadav, V. K., John, R., Sajeev, R., Ramalingam, J., George, P., Nandi, A., Mridula, N., Janmejay Jaiswal Rana, A. R. P., Srivastava, S., and Thampi, S. (2020). Lunar Near Surface Plasma Environment from Chandrayaan-2 Lander Platform:RAMBHA-LP payload. *Current Science*, 118(3):383. pages

Manka, R. H. (1973). Plasma and potential at the lunar surface. In *Photon and particle interactions with surfaces in space*, pages 347–361. Springer. pages

Mendis, D. A. and Rosenberg, M. (1994). Cosmic dusty plasmas. *Annual Review of Astronomy and Astrophysics, Volume 32, 1994, pp. 419-463.*, 32:419–463. pages

Mishra, S. (2020a). Role of photoelectric charge fluctuation in dust detachment from the lunar surface. *Physics of Plasmas*, 27(5). pages

Mishra, S. and Bhardwaj, A. (2019). Photoelectron sheath on lunar sunlit regolith and dust levitation. *The Astrophysical Journal*, 884(1):5. pages

Mishra, S. and Bhatt, A. (2023). Estimating optimum launch velocity of electrostatically detached dust particles over sunlit locations on moon. *Monthly Notices of the Royal Astronomical Society*, 519(1):85–90. pages

Mishra, S. and Misra, S. (2018). An analytical investigation: Effect of solar wind on lunar photoelectron sheath. *Physics of Plasmas*, 25(2):023702. pages

Mishra, S. K. (2020b). Photoelectron distribution on sunlit surface of the moon: A formalism. *Physics of Plasmas*, 27(8):082906. pages

Mishra, S. K. and Bhardwaj, A. (2020). Electrostatic charging of permanently shadowed craters on the Moon. *Monthly Notices of the Royal Astronomical Society: Letters*, 496(1):L80–L84. pages

Mishra, S. K., Misra, S., and Sodha, M. S. (2013). Charging kinetics of dust particles in a non-Maxwellian Lorentzian plasma. *The European Physical Journal D*, 67(10):210. pages

Mishra, S. K. and Sana, T. (2022). Mitigating massive triboelectric charging of drill in shadowed region of Moon. *Monthly Notices of the Royal Astronomical Society*, 512(4):4730–4735. pages

Neugebauer, M., Snyder, C., Clay, D., and Goldstein, B. (1972). Solar wind observations on the lunar surface with the apollo-12 alsep. *Planetary and Space Science*, 20(10):1577–1591. pages

Nitter, T. and Havnes, O. (1992). Dynamics of dust in a plasma sheath and injection of dust into the plasma sheath above moon and asteroidal surfaces. *Earth, Moon and Planets*, 56(1):7–34. pages

Nitter, T., Havnes, O., and Melandsø, F. (1998). Levitation and dynamics of charged dust in the photoelectron sheath above surfaces in space. *Journal of Geophysical Research: Space Physics*, 103(A4):6605–6620. pages

Němeček, Z., Pavlů, J., Richterová, I., Šafránková, J., and Vaverka, J. (2018). Secondary electron emission and its role in the space environment. *AIP Conference Proceedings*, 1925(1):020002. pages

O'Brien, B. J. and Reasoner, D. L. (1971). 10. charged-particle lunar environment experiment. *NASA SP.*, (272):193. pages

Opp, E., Hsu, H.-W., Wang, X., Deca, J., and Horányi, M. (2024). Electrostatic regolith size-sorting effects on surface spectra of airless bodies. *Icarus*, 421:116213. pages

Pacaud, R., Matéo-Vélez, J.-C., Hess, S., and Ranvier, S. (2025). Measurement of bipolar charge distribution of lunar dust simulant under vuv irradiation. *Planetary and Space Science*, page 106120. pages

Pagán Muñoz, J. H., Wang, X., Horányi, M., Kvon, V., Heijmans, L., Chaudhuri, M., Van De Kerkhof, M., Yakunin, A. M., Krainov, P., and Astakhov, D. (2024). Charging and mobilization of dust particles on a surface in plasma. *Physical Review Letters*, 133(11):115301. pages

Pagán Muñoz, J. H., Wang, X., Horányi, M., Kvon, V., Heijmans, L., Chaudhuri, M., van de Kerkhof, M., Yakunin, A. M., Krainov, P., and Astakhov, D. (2025). Electrostatic lofting conditions of single dust particles on a solid surface. *Physics of Plasmas*, 32(2). pages

Pierrard, V. and Lazar, M. (2010). Kappa distributions: theory and applications in space plasmas. *Solar Physics*, 267(1):153–174. arXiv:1003.3532 [physics]. pages

Popel, S., Golub', A., Kassem, A., and Zelenyi, L. (2022). Dust dynamics in the lunar dusty plasmas: Effects of magnetic fields and dust charge variations. *Physics of Plasmas*, 29(1):013701. pages

Popel, S., Kopnin, S., Golub', A., Dol'nikov, G., Zakharov, A., Zelenyi, L., and Izvekova, Y. N. (2013). Dusty plasma at the surface of the moon. *Solar System Research*, 47:419–429. pages

Popel, S., Zelenyi, L., Golub', A., and Dubinskii, A. (2018). Lunar dust and dusty plasmas: Recent developments, advances, and unsolved problems. *Planetary and Space Science*, 156:71–84. pages

Popel, S. I., Golub, A., Izvekova, Y. N., Afonin, V., Dol'nikov, G., Zakharov, A., Zelenyi, L. M., Lisin, E., and Petrov, O. F. (2014). On the distributions of photoelectrons over the illuminated part of the moon. *JETP letters*, 99(3):115–120. pages

Popel, S. I., Golub', A. P., Lisin, E. A., Izvekova, Y. N., Atamaniuk, B., Dol'nikov, G., Zakharov, A., and Zelenyi, L. M. (2016). Impacts of fast meteoroids and the separation of dust particles from the surface of the moon. *JETP letters*, 103:563–567. pages

Poppe, A., Halekas, J., Delory, G., Farrell, W., Angelopoulos, V., McFadden, J., Bonnell, J., and Ergun, R. (2012a). A comparison of artemis observations and particle-in-cell modeling of the lunar photoelectron sheath in the terrestrial magnetotail. *Geophysical research letters*, 39(1). pages

Poppe, A., Halekas, J. S., and Horányi, M. (2011). Negative potentials above the day-side lunar surface in the terrestrial plasma sheet: Evidence of non-monotonic potentials. *Geophysical Research Letters*, 38(2). pages

Poppe, A. and Horányi, M. (2010). Simulations of the photoelectron sheath and dust levitation on the lunar surface. *Journal of Geophysical Research: Space Physics*, 115(A8). pages

Poppe, A. R. (2011). *Modeling, theoretical and observational studies of the lunar photoelectron sheath*. PhD thesis, University of Colorado at Boulder. pages

Poppe, A. R., Piquette, M., Likhanskii, A., and Horányi, M. (2012b). The effect of surface topography on the lunar photoelectron sheath and electrostatic dust transport. *Icarus*, 221(1):135–146. pages

Prokopenko, S. and Laframboise, J. (1980). High-voltage differential charging of geostationary spacecraft. *Journal of Geophysical Research: Space Physics*, 85(A8):4125–4131. pages

Reasoner, D. L. and Burke, W. J. (1972a). Characteristics of the lunar photoelectron layer in the geomagnetic tail. *Journal of Geophysical Research*, 77(34):6671–6687. pages

Reasoner, D. L. and Burke, W. J. (1972b). Direct observation of the lunar photoelectron layer. In *Proceedings of the Lunar Science Conference, vol. 3, p. 2639*, volume 3, page 2639. pages

Rennilson, J. and Criswell, D. R. (1974). Surveyor observations of lunar horizon-glow. *The moon*, 10(2):121–142. pages

Rhodes, D. J., Farrell, W. M., and McLain, L., J. (2020). Tribocharging and electrical grounding of a drill in shadowed regions of the Moon. *Advances in Space Research*, 66(4):753–759. pages

Richardson, J. E., Melosh, H. J., and Greenberg, R. (2004). Impact-induced seismic activity on asteroid 433 eros: A surface modification process. *science*, 306(5701):1526–1529. pages

Richterová, I., Němeček, Z., Beránek, M., Šafránková, J., and Pavlů, J. (2012). Secondary emission from non-spherical dust grains with rough surfaces: Application to lunar dust. *The Astrophysical Journal*, 761(2):108. pages

Robbins, S. J., Watters, W. A., Chappelow, J. E., Bray, V. J., Daubar, I. J., Craddock, R. A., Beyer, R. A., Landis, M., Ostrach, L. R., Tornabene, L., et al. (2018). Measuring impact crater depth throughout the solar system. *Meteoritics & Planetary Science*, 53(4):583–637. pages

Rosenfeld, E. and Zakharov, A. (2020). Charge fluctuations on the sunlit surface of airless bodies and their role in dust levitation. *Icarus*, 338:113538. pages

Roussel, J.-F., Rogier, F., Dufour, G., Mateo-Velez, J.-C., Forest, J., Hilgers, A., Rodgers, D., Girard, L., and Payan, D. (2008). Spis open-source code: Methods, capabilities, achievements, and prospects. *IEEE transactions on plasma science*, 36(5):2360–2368. pages

Saito, Y., Nishino, M., Yokota, S., Tsunakawa, H., Matsushima, M., Takahashi, F., Shibuya, H., and Shimizu, H. (2014). Night side lunar surface potential in the earth's magnetosphere. *Advances in Space Research*, 54(10):1985–1992. Lunar Science and Exploration. pages

Schwan, J., Wang, X., Hsu, H.-W., Grün, E., and Horányi, M. (2017). The charge state of electrostatically transported dust on regolith surfaces. *Geophysical Research Letters*, 44(7):3059–3065. pages

Seitz, F. (1940). The modern theory of solids mcgraw-hill book company. *Inc., New York, London.[4]*. pages

Senshu, H., Kimura, H., Yamamoto, T., Wada, K., Kobayashi, M., Namiki, N., and Matsui, T. (2015). Photoelectric dust levitation around airless bodies revised using realistic photoelectron velocity distributions. *Planetary and Space Science*, 116:18–29. pages

Sheridan, T. (2013). Charging time for dust grain on surface exposed to plasma. *Journal of Applied Physics*, 113(14). pages

Sheridan, T. and Hayes, A. (2011). Charge fluctuations for particles on a surface exposed to plasma. *Applied physics letters*, 98(9). pages

Shodhan, S., Crooker, N. U., Fitzenreiter, R. J., Lepping, R. P., and Steinberg, J. T. (1999). Density enhancements in the solar wind. *AIP Conference Proceedings*, 471(1):601–604. pages

Shukla, P. K. and Mamun, A. A. (2002). Introduction to dusty plasma physics. *Plasma Physics and Controlled Fusion*, 44(3):395. pages

Sickafoose, A., Colwell, J., Horányi, M., and Robertson, S. (2001). Experimental investigations on photoelectric and triboelectric charging of dust. *Journal of Geophysical Research: Space Physics*, 106(A5):8343–8356. pages

Sickafoose, A., Colwell, J., Horányi, M., and Robertson, S. (2002). Experimental levitation of dust grains in a plasma sheath. *Journal of Geophysical Research: Space Physics*, 107(A11):SMP–37. pages

Singer, S. and Walker, E. (1962a). Electrostatic dust transport on the lunar surface. *Icarus*, 1(1-6):112–120. pages

Singer, S. and Walker, E. (1962b). Photoelectric screening of bodies in interplanetary space. *Icarus*, 1(1-6):7–12. pages

Sodha, M. and Mishra, S. (2014). Lunar photoelectron sheath and levitation of dust. *Physics of Plasmas*, 21(9). pages

Sodha, M. S. (2014). *Kinetics of Complex Plasmas*, volume 81 of *Springer Series on Atomic, Optical, and Plasma Physics*. Springer India, New Delhi. pages

Stern, S. A. (1999). The lunar atmosphere: History, status, current problems, and context. *Reviews of Geophysics*, 37(4):453–491. pages

Sternglass, E. (1954). The theory of secondary emission, sci. pap., 1772. pages

Sternovsky, Z., Chamberlin, P., Horanyi, M., Robertson, S., and Wang, X. (2008). Variability of the lunar photoelectron sheath and dust mobility due to solar activity. *Journal of Geophysical Research: Space Physics*, 113(A10). pages

Stubbs, T., Farrell, W., Halekas, J., Burchill, J., Collier, M., Zimmerman, M., Vondrak, R., Delory, G., and Pfaff, R. (2014). Dependence of lunar surface charging on solar wind plasma conditions and solar irradiation. *Planetary and Space Science*, 90:10–27. pages

Stubbs, T. J., Halekas, J. S., Farrell, W. M., and Vondrak, R. R. (2007). Lunar surface charging: A global perspective using lunar prospector data. *Dust in planetary systems*, 643:181–184. pages

Stubbs, T. J., Vondrak, R. R., and Farrell, W. M. (2006). A dynamic fountain model for lunar dust. *Advances in Space Research*, 37(1):59–66. pages

Szalay, J. R. and Horányi, M. (2015). The search for electrostatically lofted grains above the moon with the lunar dust experiment. *Geophysical Research Letters*, 42(13):5141–5146. pages

Tsytovich, V. N., Morfill, G. E., Vladimirov, S. V., and Thomas, H. M. (2008). *Elementary Physics of Complex Plasmas*, volume 731 of *Lecture Notes in Physics*. Springer, Berlin, Heidelberg. pages

Urey, H. C. and Korff, S. A. (1952). The planets: their origin and development. *Physics Today*, 5(8):12–12. pages

Vaniman, D., Reedy, R., Heiken, G., Olhoeft, G., and Mendell, W. (1991). The lunar environment. *Lunar Sourcebook*, pages 27–60. pages

Vaverka, J., Richterova, I., Pavlu, J., Safrankova, J., and Nemecek, Z. (2013). Numerical Calculation of an Equilibrium Dust Grain Potential in Lunar Environment. *IEEE Transactions on Plasma Science*, 41(4):740–744. pages

Vaverka, J., Richterová, I., Pavlu, J., Šafránková, J., and Němeček, Z. (2016). LUNAR SURFACE AND DUST GRAIN POTENTIALS DURING THE EARTH'S MAGNETOSPHERE CROSSING. *The Astrophysical Journal*, 825(2):133. pages

Vladimirov, S. V., Ostrikov, K., and Samarian, A. A. (2005). *Physics and Applications of Complex Plasmas*. Imperial College Press / World Scientific. pages

Walbridge, E. (1973). Lunar photoelectron layer. *Journal of Geophysical Research*, 78(19):3668–3687. pages

Wang, J., He, X., and Cao, Y. (2008). Modeling electrostatic levitation of dust particles on lunar surface. *IEEE transactions on plasma science*, 36(5):2459–2466. pages

Wang, X., Horanyi, M., Fisher, C., Eberwein, L., Deca, J., Knappmiller, S., Hansen, D., Levin, Z., Wing, R., Summers, D., et al. (2024). Electrostatic dust analyzer for dust transport measurements on the lunar surface. *The Planetary Science Journal*, 5(2):41. pages

Wang, X., Horányi, M., and Robertson, S. (2009). Experiments on dust transport in plasma to investigate the origin of the lunar horizon glow. *Journal of Geophysical Research: Space Physics*, 114(A5). pages

Wang, X., Horányi, M., and Robertson, S. (2010). Investigation of dust transport on the lunar surface in a laboratory plasma with an electron beam. *Journal of Geophysical Research: Space Physics*, 115(A11). pages

Wang, X., Horányi, M., and Robertson, S. (2011). Dust transport near electron beam impact and shadow boundaries. *Planetary and Space Science*, 59(14):1791–1794. pages

Wang, X., Pilewskie, J., Hsu, H.-W., and Horányi, M. (2016a). Plasma potential in the sheaths of electron-emitting surfaces in space. *Geophysical Research Letters*, 43(2):525–531. pages

Wang, X., Robertson, S., and Horányi, M. (2019). Plasma sheath formation at craters on airless bodies. *Journal of Geophysical Research: Space Physics*, 124(6):4188–4193. pages

Wang, X., Schwan, J., Hsu, H.-W., Grün, E., and Horányi, M. (2016b). Dust charging and transport on airless planetary bodies. *Geophysical Research Letters*, 43(12):6103–6110. pages

Whipple, E. C. (1981). Potentials of surfaces in space. *Reports on Progress in Physics*, 44(11):1197. pages

Wilcox, K. (2025). Scientists examine new data on unusual glow. https://appel.nasa.gov/2025/03/31/scientists-examine-new-data-on-unusual-glow/. Accessed: 2025-05-20. pages

Williams, J.-P., Paige, D., Greenhagen, B., and Sefton-Nash, E. (2017). The global surface temperatures of the moon as measured by the diviner lunar radiometer experiment. *Icarus*, 283:300–325. Lunar Reconnaissance Orbiter - Part II. pages

Willis, R., Anderegg, M., Feuerbacher, B., and Fitton, B. (1973). Photoemission and secondary electron emission from lunar surface material. In *Photon and particle interactions with surfaces in space*, pages 389–401. Springer. pages

Wolfram Research (2007a). RandomChoice. Wolfram Research. https://reference.wolfram.com/language/ref/RandomChoice.html. pages

Wolfram Research (2007b). RandomReal. Wolfram Research. https://reference.wolfram.com/language/ref/RandomReal.html. pages

Wolfram Research (2014a). RegionMeasure. Wolfram Research. https://reference.wolfram.com/language/ref/RegionMeasure.html. pages

Wolfram Research (2014b). RegionUnion. Wolfram Research. https://reference.wolfram.com/language/ref/RegionUnion.html. pages

Wolfram Research (2015). RandomPoint. Wolfram Research. https://reference.wolfram.com/language/ref/RandomPoint.html. pages

Wolfram Research (2017). RegionDifference. Wolfram Research. https://reference.wolfram.com/language/ref/RegionDifference.html. pages

Xu, S., Poppe, A. R., Harada, Y., Halekas, J. S., and Chamberlin, P. C. (2021). Lunar photoemission yields inferred from artemis measurements. *Journal of Geophysical Research: Planets*, 126(6):e2020JE006790. e2020JE006790 2020JE006790. pages

Yan, Q., Zhang, X., Xie, L., Guo, D., Li, Y., Xu, Y., Xiao, Z., Di, K., and Xiao, L. (2019). Weak dust activity near a geologically young surface revealed by chang'e-3 mission. *Geophysical Research Letters*, 46(16):9405–9413. pages

Yeo, L. H., Hood, N., Wang, X., and Horányi, M. (2022). Dust mobilization in the presence of magnetic fields. *Physical Review E*, 106(1):L013203. pages

Yeo, L. H., Wang, X., Deca, J., Hsu, H.-W., and Horányi, M. (2021). Dynamics of electrostatically lofted dust on airless planetary bodies. *Icarus*, 366:114519. pages

Zakharov, A. V., Zelenyi, L. M., and Popel', S. I. (2020). Lunar Dust: Properties and Potential Hazards. *Solar System Research*, 54(6):455–476. pages

Zhao, J., He, X., Yan, G., and Han, D. (2022). Kinetic particle simulations of plasma and dust environments at robotic construction sites near the lunar terminator. *Journal of Aerospace Engineering*, 35(6):04022095. pages

Zhao, J., Wei, X., Du, X., He, X., and Han, D. (2021). Photoelectron Sheath and Plasma Charging on the Lunar Surface: Semianalytic Solutions and Fully-Kinetic Particle-in-Cell Simulations. *IEEE Transactions on Plasma Science*, 49(10):3036–3050. Conference Name: IEEE Transactions on Plasma Science. pages

Zook, H. A. and McCoy, J. E. (1991). Large scale lunar horizon glow and a high altitude lunar dust exosphere. *Geophysical Research Letters*, 18(11):2117–2120. pages